UNIVERSITÉ DE GRENOBLE

THÈSE

Pour obtenir le grade de

DOCTEUR DE L'UNIVERSITÉ DE GRENOBLE

Spécialité : **Nanophysique**

Arrêté ministériel : 7 août 2006

Présentée par

Muhammad Zahid ISHAQUE

Thèse dirigée par **Jan VOGEL**
et codirigée par **Olivier FRUCHART**

préparée au sein **Institut Néel, CNRS**
et de **Ecole Doctrale de Physique, Grenoble**

Effets d'asymétrie structurale sur le mouvement de parois de domaines magnétiques induit par courant

Thèse soutenue publiquement le **le 31 Mai 2013**,
devant le jury composé de :

M. Alain MARTY
Directeur de recherche, INAC, SP2M-CEA Grenoble, Président
M. Vincent CROS
Directeur de recherche, CNRS/Thales, Palaiseau, Rapporteur
M. François MONTAIGNE
Professeur, Institut Jean Lamour, CNRS, Nancy Université, Rapporteur
Mme. Alexandra MOUGIN
Chargée de recherche, LPS, CNRS, Université Paris-Sud, Orsay, Examinateur
M. Jan VOGEL
Directeur de recherche, Institut Néel (CNRS/Université de Grenoble), Directeur de thèse
M. Olivier FRUCHART
Directeur de recherche, Institut Néel (CNRS/Université de Grenoble), Co-Directeur de thèse

Acknowledgments

Today, I feel myself purely satisfied when I look back at my decision of pursuing higher studies in Joseph Fourier University, Grenoble, France and being a part of the Micro and Nanomagnetism research team at Institut Néel. I honored the opportunity to study abroad, in a country where I not only interacted with intellectual and motivated individuals from around the world, but also the insight I gained by living in a foreign and fascinating nation.

No one walks alone on the journey of life, just where you start to thank those that joined you, walked beside you, and helped you along the way. First and foremost, I like to thank God for providing me this golden opportunity to learn. Then, I want to thank my parents and whole family whose love and prayers made me successful. I like to thank my wife who has helped make my life what it is today. I would like to extend my thanks to all my family and friends. I take immense pleasure in thanking Alain Fontaine and Alain Schuhl, directors of the Institut Néel (CNRS/UJF), Joël Cibert and Hervé Courtois, directors Department Nano, Institut Néel.

I would like to gratefully acknowledge the enthusiastic supervision of Dr. Jan Vogel, and Dr. Olivier Fruchart for having permitted me to carry out this work. I cannot say thank you enough for their tremendous support and help. I felt motivated and encouraged every time I attended their meetings. Without their encouragement and guidance this work would not have materialized.

I would like to express my thanks to all the people at Institut Néel and outside who have helped me and guided me to the right way: particularly Stefania Pizzini for her support throughout my thesis and helping me in Kerr microscopy measurements and preparing nanostripes by e-beam lithography, Nicolas Rougemaille and Jean-Christophe Toussaint for micromagnetic simulations, Laurent Ranno, who measured the electrical resistivity of epitaxial layers and assisted me in FMR measurements, Eric Mossang for doing XRD measurements, Dominique Berling from Mulhouse for anisotropy measurements, persons from Nanospectroscopy beamline at synchrotron Elettra, Italy, for XMCD-PEEM measurements, Valérie Guisset and Philippe David for their technical support regarding epitaxial growth by pulsed laser deposition, which were available all the time to resolve the technical issues, whenever the technical problems had happened and also for magnetic coating of AFM tips, Thierry Fournier, Thierry Crozes and Bruno Fernandez for nanofabrication, Edouard Wagner, Valérie Reita, Marlio Bonfim, Eric Eyraud, Richard Haettel, Laurent Del-Rey, Didier Dufeu, Daniel Lepoittevin for fabricating mechanical parts and their technical support during measurements, Patrick Belmain and Julien Michel from informatics department for their technical support, my colleagues Vo-Van Chi, Zoukaa Kassir-Bodon, Amina Kimouche, Georgeta Cuita, Sandrine Da-col, Ales Hrabec, Vojteh Uhlir, Luiz-Fernando Zanini, Nguyen Ngoc Viet, Cornelia Schwarz, Clement Bou-

vier, Fabien Jean, Svenja Perl and Van-dai Nguyen for spending a nice time with each other and fruitful discussions, the administrative teams who amicably and throughly occupied the administrative formalities of my finance and a lot of my missions, notably Véronique Fauvel, Sabine Gadal and Marielle Lardato Mathilde Mauro, Louise Infuso at the Nanosciences Departement; Sandrine Ferrari at the Ecole Doctorale de Physique de Grenoble.

I have the honour of showing my deep gratitude to the members of the jury commission, the reporters Vincent Cros, François Montaigne and the examiners, Alain Marty, Alexandra Mougin who accepted the invitation to evaluate my work and scheduled their time for my PhD defense.

I wish to express my deep sense of gratitude to Higher Education Commision, Pakistan for financial support for my Ph.D thesis and an additional support from the ANR-07-NANO-034 Dynawall project.

I also wish to express my gratitude to the officials and other staff members of CNRS who rendered their help during the period of my work. I am grateful to all my colleagues/friends, who were more than a family to me during my stay at the team. These were the beautiful memories and I will fondly remember them for the rest of my life

Thank you very much for your time.

Contents

Introduction

Spintronics, also known as magneto-electronics, deals with the spin dependent transport phenomena in solid state physics or in devices which utilize the electron's spin properties. After the discovery of the *"Giant-Magnetoresistance"* (GMR) effect, a well-known phenomena in spintronics, in 1988 [4][15], the developments in GMR devices made it possible to record smaller and smaller fields of smaller and smaller size data bits. This considerably increased the data storage density. Albert Fert and Peter Grünberg, the inventors of the GMR effect, were awarded the Nobel prize in physics in 2007.

Non-volatile information storage is mostly based on hard-disk drives in which each bit is stored using the direction of magnetization of uniformly magnetized grains in a magnetic thin film. To read/write the information, a reading/writing head moves over the magnetic disk. A small electromagnet is used to write the information and reading is done using giant magnetoresistive sensor. The main features of a magnetic memory are its storage density and the time needed to access the information. For conventional hard disk drives, the information access times are slow, of the order of milliseconds, due to large mass of the hard-disk. The storage density of hard-disks has followed the Moore's law, which predicts that the storage density doubles every two years. To increase the storage density, one needs to make data bits smaller and smaller. However, due to thermal stability, there will be a limit for decreasing the bit size further.

In 1990's, the concept of *"Magnetoresistive Random-Access Memory"* (MRAM) emerged, with fast information access time ($\sim$ nanoseconds) and non-volatility. Unlike for conventional RAM, data in MRAM is not stored as electric charge but by magnetic storage elements. Due to the extra circuitry required for reading and writing information, MRAM has much lower storage density as compared to conventional hard-disk drives. Work is in progress to increase the storage density of existing MRAMs.

Recently, a new type of a non-volatile memory device called *"Racetrack Memory"* [102] has been proposed based on the *"Spin Transfer Torque"* (STT) effect [118]. When an electric current passes through a magnetic material, due to the spin dependent scattering of the electrons it becomes spin polarised and it is possible that spin angular momentum of conduction electrons is transferred to localized magnetic moments, resulting in a spin-torque acting on the magnetization, called STT effect. The STT can result in switching of the magnetization or motion of a domain wall (DW).

In a racetrack memory, the magnetic information is stored in DWs in long nanostripes created horizontally or vertically on a Si substrate. A series of head to head or tail to tail DWs which corresponds to series of data bits can be moved along the electron flow direction in these nanostripes by spin polarized current. The information can be read/written by individual spintronic reading and writing nanodevices below each nanostripe. Unlike conventional hard-disk drives, no mechanical motion is involved. The information stor-

age density can be further increased by growing the nanostripes vertically, 3D racetrack memory, as the density of two dimensional devices are coming close to fundamental limits. It would combine the high storage density and low cost of hard-disks with fast speed of MRAM's. The typical current densities required to move DWs are rather high $\sim 10^{11}$-$10^{12}\,\mathrm{A/m^2}$. Low current densities to reduce power consumption and high DW velocities for fast information access time are required for practical applications. Especially, to assure reproducible and reliable DW motion, DW pinning in nanostripes has to be controlled.

Recent developments in lithographic techniques make it possible to study current-induced DW motion in magnetic nanostructures or nanostripes by spin-polarized current. In these nanostructures a single type of DW can be created as compared to complex DWs in continuous thin films. A significant part of the theoretical and experimental measurements with injected current were done on systems with an in-plane magnetization, particularly, permalloy (Py-$Fe_{20}Ni_{80}$). Since permalloy is a soft magnetic material, DWs move easily under applied magnetic field, and were also expected to move easily by electric current. The advantage of these systems is that as the DWs are quite large ($\sim 100\,\mathrm{nm}$), they are less sensitive to pinning on structural defects and roughness. Unfortunately, very high critical current densities $\sim 10^{12}\,\mathrm{A/m^2}$ are required for DW displacement. In contrast, perpendicularly magnetized systems exhibit narrower DWs ($\sim 10\,\mathrm{nm}$), that are more sensitive to pinning, however, numerical studies indicate that the current densities needed to move the DWs are smaller than in the in-plane geometry. Moreover additional effects such as Joule heating, Oersted field and interlayer coupling etc. in case of multilayer systems, makes the precise understanding of the STT effect difficult.

From the point of view of fundamental physics, the study of model systems (single crystalline, control of the magnetic anisotropy, etc.) should shed light on the remaining open questions. For technological aspects, new architectures (smooth films with less structural defects), possibly seeking new physical effects, may enhance the mobility of domain walls. Metallic single crystals cannot be used for current induced DW motion if the substrate is metallic, instead magnetic layers on insulating wafers like single crystalline sapphire can be used.

During my thesis, I deposited epitaxial Py films on single crystal sapphire(0001) substrates with and without Ir as a buffer layer. The Ir layer was used to study the effect of current-induced Oersted fields on DW motion, due to current passing through the Ir layer. The objective of my thesis was to investigate the effect of current induced Oersted fields on DW stability, chirality and mobility in Py/Ir bilayer nanostripes and to compare the results with Py single layers where the net Oersted field is zero. Moreover, I also studied the current induced DW motion in sputter-deposited Py/Pt bilayer samples. I will give a comparison of epitaxial and sputtered bilayer samples.

The composition of my thesis is as follows.

The first chapter deals with the basic concepts in the field of nanomagnetism. Then the theoretical and experimental results reported in the literature regarding field and current induced DW motion are described.

In the second chapter, I present my experimental results for the optimization of Py single layer and Py/Ir bilayer epitaxial growth by pulsed laser deposition (PLD). The magnetic characterization of Py films is also described in this chapter.

The third chapter is devoted to the description of the magnetic force microscopy (MFM) technique, as it is a technique I widely used to study my samples during my thesis. The MFM imaging of DW configurations in magnetic nanostripes prepared from

optimized Py films will also be described in this chapter. The optimization of magnetic tips by magnetic thin film coatings on non-magnetic Si tips for DW imaging without tip induced perturbation is also discussed in this chapter.

The fourth chapter describes the imaging of DW configurations in spin-valve nanostripes of different widths and thicknesses by MFM. Numerical simulations and analytical modeling was also done in our group to study these DW configurations. A spin-valve domain wall phase diagram is constructed on the the basis of the experimental results, numerical simulations and analytical modeling.

In the fifth and last chapter, I will present and explain my experimental results corresponding to the quasistatic field induced DW depinning and current-induced DW motion in Py single and Py/Ir, Py/Pt bilayer nanostripes. The effect of current induced Oersted fields on DW motion in bilayer nanostripes and other aspects i.e., Joule heating, DW pinning, DW auto-motion, DW transformation etc., and their influence on current-induced DW motion will also be discussed.

I will end my thesis with some final conclusions of my work.

Chapter 1

Theoretical background and literature overview

The purpose of this chapter is to give a brief introduction of basic concepts in nanomagnetism and the mechanisms of field and current induced domain wall (DW) motion in magnetic nanostripes. Later, these concepts will be used to explain our experimental results. The overview of theoretical and experimental advancements on field and current induced DW motion will also be given in this chapter. Finally I will end this chapter with the motivation and goals of my Ph.D experimental work.

1.1 The magnetic energies

The competition between the different energy terms determines the magnetic domain wall formation. The magnetic system tries to minimise the total energy. Here I will describe briefly these energies.

Zeeman energy

The Zeeman energy is the potential energy of a magnetic system in the presence of an external magnetic field. The magnetic moments in the magnetic material tend to align in the direction of the applied magnetic field. It can be expressed as

$$E_{\mathrm{Z}} = -\mu_0 \int_V \vec{M} \cdot \vec{H}_{\mathrm{ext}} \mathrm{d}V. \tag{1.1}$$

where H_{ext} = External field, M = Magnetization and V = Volume.

Exchange energy

The phenomenon where individual spin magnetic moments tend to couple with neighbours through electron orbitals within a material is known as the exchange interaction. This interaction tends to align the adjacent spins along the same direction. Depending on the nature of the material, if the magnetic moments tend to align parallel to each other, the material is called ferromagnetic. If they tend to align antiparallel, the material is said anti-ferromagnetic or ferrimagnet.

The exchange interaction is described by the Heisenberg hamiltonian:

$$\mathcal{H}_{\mathrm{ex}} = -\sum_{i \neq j} \mathcal{J}_{i,j} \vec{S}_i \cdot \vec{S}_j \tag{1.2}$$

where $\mathcal{J}_{i,j}$ is the exchange constant having units of energy. It is positive for ferromagnetic ordering and negative for antiferromagnetic ordering. The exchange interaction is extremely short range and only considered between nearest neighbour spins.

Magnetocrystalline anisotropy energy

In a crystalline magnetic material, the magnetization aligns preferentially along certain crystallographic directions. Therefore there are directions or planes in space along which a magnetic material is more easy to magnetize than others. The density of magnetocrystalline energy is usually small compared to the exchange energy.

If the crystal system has a single axis of rotational symmetry, the anisotropy of such crystals is called uniaxial anisotropy. The first term of the magnetocrystalline energy in the case of uniaxial symmetry is given by the following relation

$$E_{\mathrm{K}} = \int_V K_1 \sin^2(\theta) \mathrm{d}V \tag{1.3}$$

where θ is the angle between the magnetization and the easy axis and K_1 is the first order anisotropy constant, also represented by $\mathrm{K_u}$. It's unit is $\mathrm{J/m^3}$.

If the z axis is taken to be the main symmetry axis of the crystal, then

If $K_1 > 0$, the $\pm$ z directions form the easy axis. If $K_1 < 0$, this corresponds to an easy plane perpendicular to the symmetry axis.

Magnetic dipolar energy

Dipolar energy (often called magnetostatic or demagnetizing energy) is the energy resulting from the interaction of magnetic moments with each other in a given magnetic system. It can be expressed as

$$E_{\mathrm{d}} = -\frac{\mu_0}{2} \int_V \vec{H}_{\mathrm{d}} \cdot \vec{M} \mathrm{d}V. \tag{1.4}$$

The demagnetizing field is globally opposed to the magnetization which creates it. In bodies uniformly magnetized along the main axis of symmetry, this field can be calculated using the following relation:

$$\vec{H}_{\mathrm{d}} = -N\vec{M} \tag{1.5}$$

where N is the demagnetizing tensor along the considered direction such that $N_x + N_y + N_z = 1$.

1.2 Domain walls in thin films and nanostripes

In magnetic materials, the minimization of free energy takes place by the formation of magnetic domains. A magnetic domain represents a region of uniform magnetization

along some easy direction. The existence of magnetic domains was proposed by Pierre Weiss in 1907 [143]. He proposed that there are regions inside the magnetic material that are magnetized in different directions so that the net magnetization is nearly zero. It was experimentally confirmed in 1931 by directly visualizing the domains by Bitter technique. The regions separating the magnetic domains are called domain walls (DWs). Felix Bloch in 1932 analytically described these domain walls.

General picture of Bloch and Néel walls

The energies and the widths of DWs in thin films are very different from those in bulk material. Bloch DWs appear in bulk materials where sizes of magnetic material are considerably larger than the domain wall width. In bulk materials the north and south poles are very far apart in comparison to the wall width, so that the stray field energy is relatively small. In thin films, however, high magnetic stray fields exist, because the poles are at a distance equal to the film thickness. The high stray field energy results in a new type of wall, called Néel wall first predicted by L. Néel in 1955 [95].

Depending on the angle between two surrounding domains, there exist different types of DWs. For example 90°, 180° and 360° DWs. A 90° DW, separates two domains with mutually perpendicular magnetization, a 180° DW separates two antiparallel domains and a 360° DW separates two parallel domains, which forms due to combination of two 180° DWs. The simplest of all DWs is the 180° wall while other have more complicated structures.

The schematic representation of simple 180° Bloch and Néel walls is shown in Fig. 1.1. In the Bloch wall the DW magnetization rotates in the plane parallel to the DW [Fig. 1.1 (a)]. If the wall plane contains the anisotropy axis, the domain magnetizations are parallel to the wall. There are no magnetic charges inside the wall and the stray field energy is negligible. In the Néel wall, the DW magnetization rotates in the plane perpendicular to the DW [Fig. 1.1 (b)]. Contrary to the Bloch wall, here magnetic charges inside the wall result in a high stray field energy.

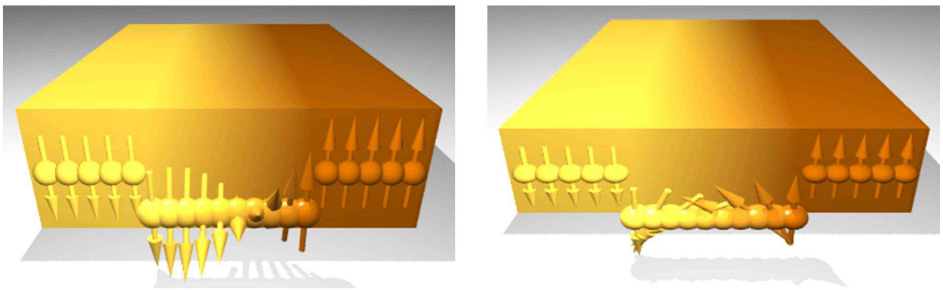

(a) (b)

Figure 1.1: Schematic representation of a 180° (a) Bloch wall (b) Néel wall in thin ferromagnetic films with perpendicular magnetization.

The number and size of the domains depends on the relative size of relevant magnetic energies. High magnetostatic energy and small exchange and anisotropy favor the existence of many small domains as the cost of DWs is relatively low and vice versa. The

magnetization in the DWs rotates continuously due to the strong short range exchange interaction.

In the absence of an applied field, the DW shape and width depend on the exchange and the anisotropy energy including shape anisotropy. The magnetization profile of a 1D Bloch wall is expressed as:

$$\varphi(y) = 0, \tag{1.6}$$

$$\theta(y) = \pm 2 \arctan \exp\left(\frac{y}{\Delta_0}\right), \tag{1.7}$$

where

$$\Delta_0 = \sqrt{\frac{A}{K}} \tag{1.8}$$

is the domain wall width. The domain wall width Δ_0 thus depends on the exchange and anisotropy constants A and K of the material. Systems with out of plane magnetization having strong uniaxial anisotropy usually contain narrow DWs, while systems with in-plane magnetization having weak in-plane uniaxial anisotropy exhibit wider DWs.

Domain walls in nanostripes

Since in this thesis I will discuss materials with in-plane anisotropy (Permalloy), I will explain here DWs in nanostripes with an in-plane anisotropy. Generally, two types of DWs are found in nanostripes of rectangular cross-section and in-plane anisotropy, as a result of the competition between exchange and demagnetizing energy. Depending on the thickness and width of the nanostripe, we can obtain transverse walls (TWs) or vortex walls (VWs). Fig. 1.2 shows the schematic representation of the transverse and vortex walls in nanostripes.

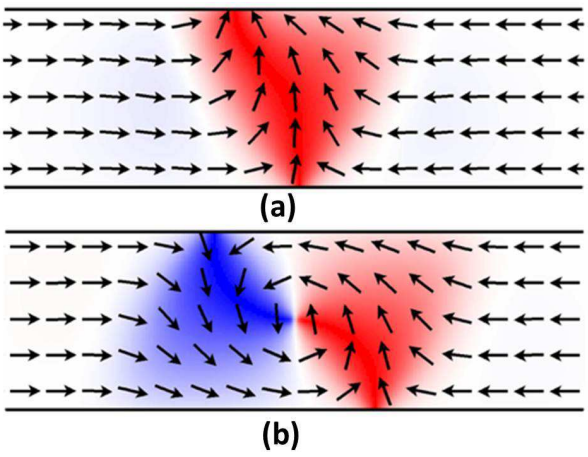

Figure 1.2: Schematic representation of head to head (a) Transverse and (b) Vortex walls in nanostripes in systems with an in-plane anisotropy [109].

The domains are pointing along the nanostripe axis, due to the shape anisotropy, in opposite directions and are separated by a DW. The magnetization in the DW has

a non-zero component transverse to the nanostripe. Due to the low magnetocrystalline anisotropy, the DW width is larger ($\sim 100\,\text{nm}$) in systems with an in-plane anisotropy as compared to systems with out of plane anisotropy ($\sim 10\,\text{nm}$).

Competing energies: Exchange vs dipolar energy

In VWs, the magnetization rotates in the form of concentric circles around the vortex core, where it points out of the nanostripe plane. Most of the energy is concentrated near the vortex core in the form of an exchange energy due to the large change of magnetization angle over a small distance. It also costs dipolar energy due to the out of plane magnetization at the vortex core. Due to the magnetization gradient the total energy of the VW slightly varies along the width of the stripe.

On the other hand in TWs, the cost in energy is proportional to the length of the wall along the nanostripe width because in contrast to a VW the magnetization gradient is almost constant in this direction. Therefore there is a critical width for which the TW energy is larger than that of the vortex wall as shown in Fig. 1.3 (a). It is also clear from this figure that the TW energy can also be higher for lower widths if the nanostripe thickness is higher. This can be related to the demagnetizing energy.

The DW width parameter Δ for both transverse and vortex walls increases with an increase in stripe width but it weakly depends on the stripe thickness. The transverse and vortex walls widths are very different from each other. For TW $\Delta = \text{w}/\pi$ and for VW $\Delta = 3\text{w}/4$. For asymmetric TWs, the DW width parameter increases with increasing stripe width and thickness [93].

Nakatani et al. [93] and R. D. McMichael et al [80] obtained the DW structure phase diagram as a function of the width and the thickness of nanostripes, for zero anisotropy soft magnetic nanostripes, using micromagnetic simulations. By comparing the energies of DWs in the nanostripes Nakatani et al. identify three different types of DWs, transverse walls, asymmetric transverse walls and vortex walls. The thickness and width range of nanostripes in which these DWs are more stable is shown in Fig. 1.3 (b).

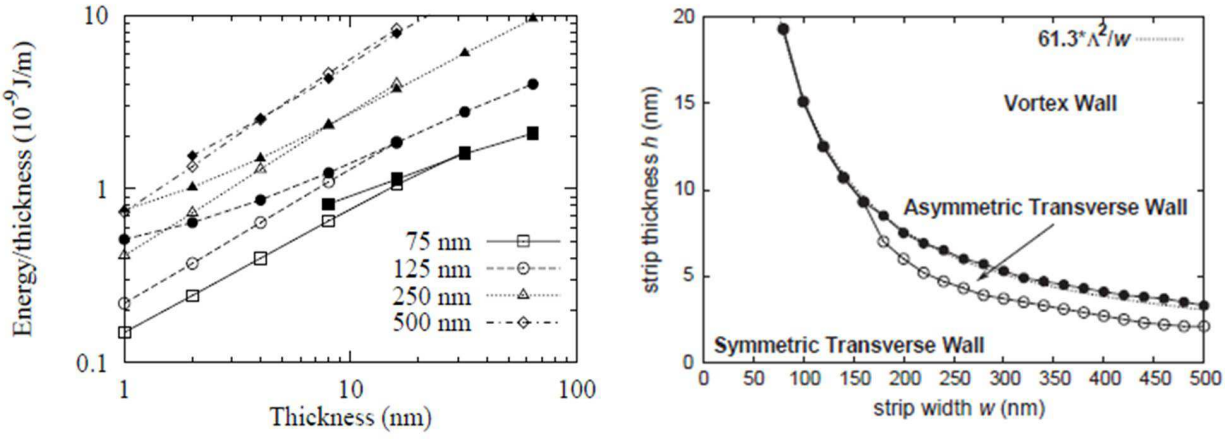

Figure 1.3: Phase diagram of DW structures in nanostripes with low in-plane anisotropy (reproduced from [93] and [80] respectively).

1.3 Field induced domain wall motion

1.3.1 Landau-Lifshitz and Landau-Lifshitz-Gilbert equation

Landau and Lifshitz in 1935, first described analytically the effect of a magnetic field on magnetization in bulk ferromagnetic systems under low applied fields [65]. They described the magnetization dynamics by the following relation called Landau-Lifshitz (LL) equation:

$$\frac{\partial \vec{M}}{\partial t} = -\gamma \vec{M} \times \mu_0 \vec{H}_{\text{eff}} - \frac{\lambda}{M_s}\left[\vec{M} \times \left(\vec{M} \times \mu_0 \vec{H}_{\text{eff}}\right)\right], \tag{1.9}$$

The first term in the above equation represents the precessional term and the second corresponds to damping, allowing relaxation to the field direction. H_{eff} is the effective local magnetic field resulting from external (applied magnetic field) and internal fields (representing the exchange, magnetocrystalline and magnetostatic energy). γ is the gyromagnetic ratio and λ represents the speed of the magnetization relaxation. The effective field provides the torque and the magnetization then precesses around the effective field with the Larmor angular frequency $\omega = \gamma \mu_0 H_{\text{eff}}$. Due to the energy dissipation the magnetization spirals towards the equilibrium position and finally aligns parallel to the effective field [Fig. 1.4 (a)].

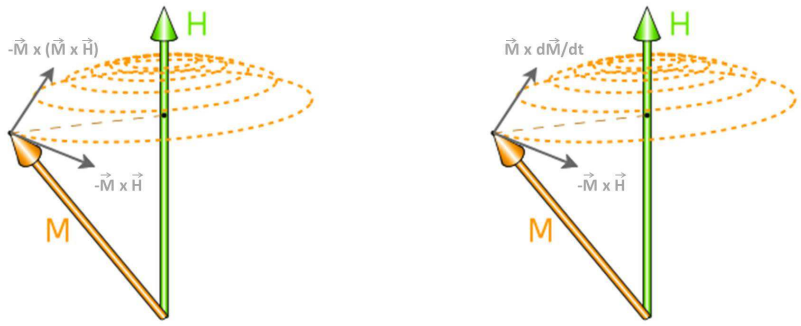

(a) (b)

Figure 1.4: Schematic representation of damped precessional motion of a magnetic moment in an effective magnetic field for (a) LL (b) LLG equation (Reproduced from [82]).

In 1955 Gilbert introduced another type of damping which is similar to a viscous force [37]. In 1974 Walker and Schryer derived a general 1D analytical solution for the motion of a 180° Bloch wall in an infinite anisotropic medium under uniform DC magnetic field. They considered the type of damping proposed by Gilbert using the Landau-Lifshitz-Gilbert (LLG) formalism [114]. The LLG equation is given by:

$$\frac{\partial \vec{M}}{\partial t} = -\gamma \vec{M} \times \mu_0 \vec{H}_{\text{eff}} + \frac{\alpha}{M_s}\left(\vec{M} \times \frac{\partial \vec{M}}{\partial t}\right) \tag{1.10}$$

where

$$\vec{H}_{\text{eff}} = \frac{1}{\mu_0} M_s \frac{\delta E}{\delta \vec{M}} \tag{1.11}$$

M_s is the saturation magnetization, α is the Gilbert damping parameter, proportional to the time variation of the magnetization, and is perpendicular to the magnetization trajectory.

The main difference between the Landau and Lifshitz (LL) and LLG formalism is the different way of considering damping. According to the LL form, the damping is perpendicular to the magnetization, while the LLG form considers that damping is not perpendicular to the effective torque but to the magnetization trajectory as shown in Fig. 1.4 (b).

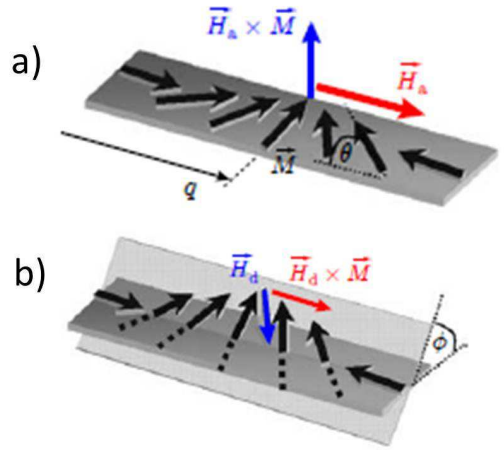

Figure 1.5: The schematic representation of the effect of an applied magnetic field (H_a) on a TW along the nanostripe (Reproduced from [9]).

The schematic representation of the effect of an applied magnetic field (H_a) on a TW along the nanostripe is shown in Fig. 1.5. The applied field exerts a torque $\vec{H}_a \times \vec{M}$ on the TW magnetization which cants the magnetic moments out of the plane [Fig. 1.5 (a)]. The resulting demagnetizing field exerts an additional torque $\vec{H}_d \times \vec{M}$, that moves the DW in the direction of the applied field [Fig. 1.5 (b)].

Domain wall mobility and Walker breakdown

Theoretical models using the LLG equation predicted two regimes of DW motion under magnetic field [114] [117]: a steady state regime with high DW mobility at low fields, in which the DW velocity increases linearly with increasing field. In this regime the DW velocity is expressed as $V = \mu H$ where μ is the DW mobility and is given by $\mu = \gamma\Delta/\alpha$ where γ is gyromagnetic ratio, Δ is the DW width parameter and α is the Gilbert damping parameter.

The second, precessional, regime corresponds to a lower DW mobility at high fields. In this regime the DW motion is governed by periodic DW transformations which results in the reduction of DW velocity. The critical field separating these two regimes was named *"Walker breakdown field"*, H_W. Walker also predicted that by further increasing the field above the Walker breakdown a second linear regime of lower mobility $\mu = \gamma\Delta(\alpha + \alpha^{-1})$ for $H > H_W$ should be obtained.

Fig. 1.6 shows the field dependence of the DW velocity. The domain wall velocity increases linearly with field up to the Walker breakdown. After the Walker breakdown

the velocity decreases due to the domain wall transformations. By further increasing the field above the Walker breakdown a second linear regime of lower mobility is obtained.

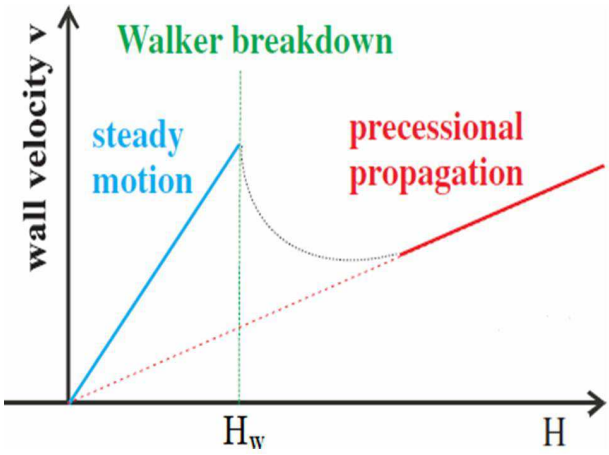

Figure 1.6: Field dependence of domain wall velocity, steady and precessional regimes [91].

1.3.2 One-dimensional model

The 1D model is applicable to narrow and thin nanostripes with a transverse size comparable to the exchange length. Mougin et al. studied analytically the Bloch wall dynamics under field [91]. They calculated the velocity of a single 180° Bloch wall in magnetic structure with reduced thickness and lateral dimension. They considered an out of plane magnetized track, supposed to be infinite and directed along the y direction as shown in the Fig. 1.7.

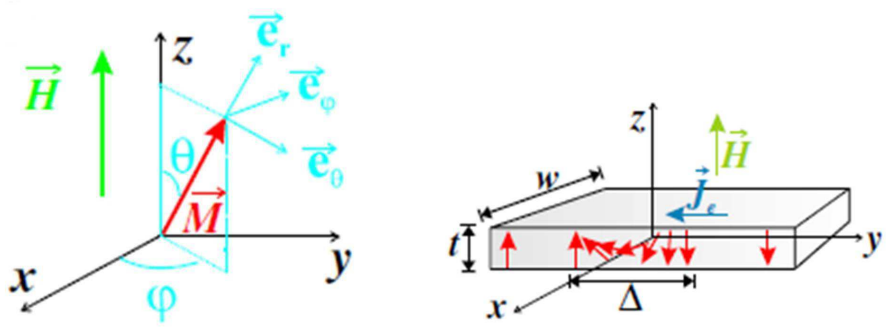

Figure 1.7: (a) Polar θ and azimuthal ϕ angles and the associated spherical coordinate system defining the orientation of the magnetisation $\vec{M}$ relative to a Cartesian axis system. (b) Sketch of a 180° domain wall in a track of width w and thickness t showing a perpendicular magnetic anisotropy(Reproduced from [91]).

The magnetization profile of the 1D Bloch wall along the y axis can be described as [91] :

$$\theta(y) = \pm 2 \arctan \exp\left(\frac{y - y_0}{\Delta}\right) \tag{1.12}$$

where y_0 represents the DW center at $\theta = \pi/2$.
The characteristic DW width Δ is given by

$$\Delta = \sqrt{\frac{A}{K_i + \frac{\mu_0}{2} M_s^2 (N_x \cos^2\varphi + N_y \cos^2\varphi - N_z)}} \tag{1.13}$$

where N_x, N_y and N_z are the DW demagnetizing factors, M_s the saturation magnetization, A and K_i are the exchange and intrinsic anisotropy constants.

The magnetization dynamics are described by the LLG equation (1.10). The different torques under an applied field acting on the magnetization, in spherical or polar coordinates, and the corresponding azimuthal DW velocities $\dot{\theta}$ and $\dot{\varphi}$ are related as [91] :

$$\dot{\theta} = -\frac{\gamma}{M_s}\Gamma_\theta, \tag{1.14}$$

$$\dot{\varphi} = -\frac{\gamma}{M_s}\Gamma_\varphi \tag{1.15}$$

where Γ_θ and Γ_φ are the azimuthal components of the total torque $\vec{\Gamma}$ given by

$$\vec{\Gamma} = \vec{\Gamma}_H + \vec{\Gamma}_D + \vec{\Gamma}_\alpha \tag{1.16}$$

The $\vec{\Gamma}_H$ is the torque due to the external field, $\vec{\Gamma}_D$ due to demagnetizing field and $\vec{\Gamma}_\alpha$ is the damping torque. The total polar and azimuthal torques are then calculated as [91]

$$\Gamma_\theta = M_s^2 (N_y - N_x) \sin\theta \sin\varphi \cos\varphi + \frac{\alpha M_s}{\gamma}\dot{\varphi} \sin\theta, \tag{1.17}$$

$$\Gamma_\varphi = -M_s^2 \sin\theta \cos\theta \left[N_x \cos^2\varphi + N_y \sin^2\varphi - N_z\right] - \frac{\alpha M_s}{\gamma}\dot{\theta} - M_s H \sin\theta. \tag{1.18}$$

Let us first consider the steady state motion in which the azimuthal angle ϕ does not change ($\dot{\varphi} = 0$), so the corresponding torque Γ_φ will also be zero. So putting $\Gamma_\varphi = 0$ and $\theta = \pi/2$ at the DW center (where the torque Γ_φ has an extremum) 1.18 gives :

$$\sin 2\varphi = \frac{2H}{\alpha M_s (N_y - N_x)} \tag{1.19}$$

This equation is valid only if [91]

$$H \leq \frac{\alpha M_s}{2} \mid N_y - N_x \mid \tag{1.20}$$

The maximum field for which the DW has a steady state motion is called the Walker field, which is given by:

$$H_{\mathrm{W}} = \frac{\alpha M_s}{2} \mid N_y - N_x \mid . \tag{1.21}$$

At the wall center where $\theta = \pi/2$, the steady DW velocity is given by [91]

$$v_{\mathrm{st}} = \frac{\gamma\Delta}{\alpha}H. \tag{1.22}$$

where

$$\mu_{\mathrm{st}} = \frac{\gamma\Delta}{\alpha}. \tag{1.23}$$

is called the DW mobility. The eq. 1.22 shows that the DW velocity is directly proportional to the applied field in the steady state regime.

Above the Walker field the domain wall is not stable and $\dot{\varphi} \neq 0$. This limiting case is called the *"Walker breakdown"*.

Above the Walker field, where $H > H_{\mathrm{W}}$, the azimuthal angle ϕ is no more constant and the domain wall oscillates and transforms periodically from one form to an other around the stripe axis. This is called the precessional regime. So, we can define the average DW velocity [91]

$$\bar{v}_{\mathrm{pr}} = \frac{\gamma\Delta\alpha}{1+\alpha^2}H. \tag{1.24}$$

The mobility in this regime is then defined as

$$\mu_{\mathrm{pr}} = \frac{\gamma\Delta\alpha}{1+\alpha^2}. \tag{1.25}$$

The eq. 1.24 shows that the DW velocity is again proportional to the applied field like in the steady state regime but with a lower DW mobility.

1.3.3 Micromagnetic simulations

Thiaville et al. computed the transverse and vortex wall velocity under field using micromagnetic simulations and a 1D model in a 300 nm wide and 5 nm thick Py nanostripe [123]. They considered both perfect and rough stripes with an edge roughness of 10 and 20 nm.

Fig. 1.8 (a) shows the computed transverse and vortex wall velocities both in linear and precessional regimes for perfect nanostripes. At low applied fields, both transverse and vortex walls move in steady-state conditions. The DW velocity increases with field. This is called a linear or steady state regime. The deformation of the DW structure describes the magnetization precession under the applied field (m_z and m_y components for transverse and vortex walls appears respectively). In case of asymmetric TW, magnetization rotation at the edge of the DW as well as at the half hedgehog vortex and half antivortex on the sample edges, increases with DW velocity. For the VW, the main deformation during motion is the progressive shift of the vortex core in the transverse y direction, that causes the change of the y moment of the VW. This displacement increases with field and hence DW velocity until the vortex core is expelled from the sample resulting in a transformation from VW into a TW. Fig. 1.8 (a) shows that in the first steady-state regime the VW moves more slowly than the TW, at the same field. The second steady-state regime of a VW is similar to that of a TW, because the end of the first steady state regime results into a TW structure, that can move in steady state conditions up to higher fields.

At the end of steady-state regime, at higher fields, the DW velocity drops abruptly called *"Walker breakdown"*. The DW magnetization components oscillate as well as DW

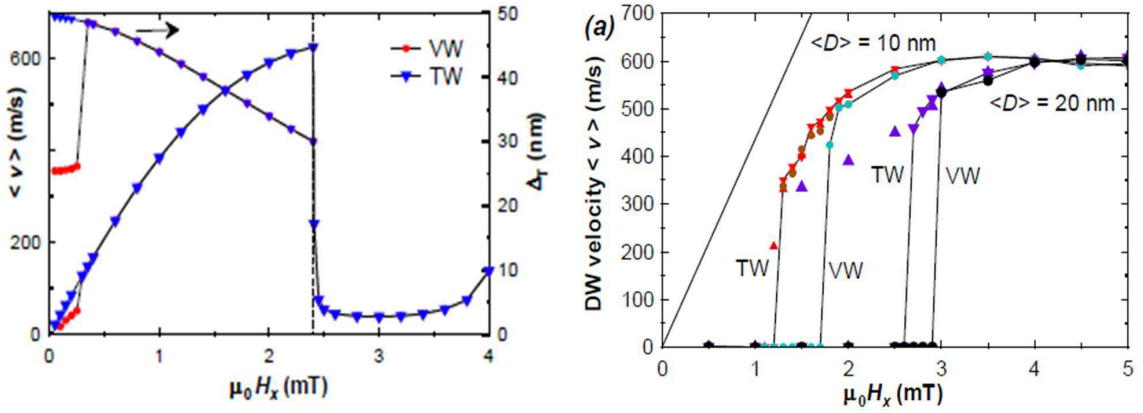

Figure 1.8: Computed velocity of transverse and vortex walls in a 300 nm *wide and* 5 nm *thick nanostripe under the field applied along the nanostripe axis. The damping constant is* $\alpha = 0.02$. *A transverse wall (TW, in fact an asymmetric transverse wall, triangular symbols) and a vortex wall (VW, circles) are compared. (a) perfect nanostripes, the VW velocity exist only upto* 60 m/s, *in the steady state regime (up to the dashed line), the Thiele domain wall width* Δ_T *is also plotted. (b) nanostripes with rough edges, two values of the average size of grains that are used to define the nanostripe edges are shown,* $< D > = 10$ *(smaller symbols) and* 20 nm *(larger symbols). For each case, the velocity in linear motion and the final velocity are indicated (calculations last* 50 ns*), showing the field window in which the DW motion is stochastic. The straight line shows the linear mobility of the TW extracted for a perfect nanostripe. Lines link the data points with the lower velocities (Reproduced from [123]).*

width and velocity. This results into continuous DW structural transformations, by the injection, expulsion, and displacement across the nanostripe width of single antivortices and vortices. The appearence of these structures during Walker breakdown is rather different from the predictions of the 1D model, where a precession of the DW magnetization is expected.

For rough nanostripes, the edge roughness corresponds to a mean grain diameter $< D >$. The calculated DW dynamics in the presence of such type of roughness are shown in Fig. 1.8 (b). The propagation fields from 1 to 3 mT can be simulated by their technique, limited by the grain and hence mesh size. To simulate smaller propagation field, smaller $< D >$ and hence smaller mesh sizes are required. So small velocities are not observed in their simulations. Fig. 1.8 (b) shows that a VW is more pinned than a TW but they observed the reverse for other sizes. The DW pinning is sensitive to the type of defects. Above the propagation field, the DW moves with an average velocity like in a perfect sample. The Walker breakdown in rough stripes is pushed to higher fields, not even visible in the simulations. This results from the energy dissipation at the nanostripe edge, preventing the appearance of vortex and antivortex structures at the stripe edges which were observed in perfect stripes.

The direct observation of DW transformations due to precessional motion beyond the Walker threshold was given by Hayashi et al [45][46]. They studied field induced DW motion in 200 and 300 nm wide and 10 nm thick FeNi nanostripes. FeNi show a large anisotropic magnetoresistance (AMR) and transverse and vortex DWs can be easily de-

tected and identified by resistance measurements. The periodic changes in DW structure were identified by corresponding discrete resistance levels using AMR. The nature of the DW structures corresponding to these discrete resistance levels was identified by Magnetic force microscopy. They also performed micromagnetic simulations to identify the origin of oscillations of DW resistance and confirmed that these oscillations are related to DW transformations.

1.3.4 Experiments

Most of the experimental studies regarding field induced DW motion were performed on Permalloy (Py - $Fe_{20}Ni_{80}$). A very small DW mobility $\sim 26 \times 10^3$ m/sT (2.6 m/sOe) was reported in 500 nm wide FeNi/Cu/FeNi trilayers nanostripes [100]. Ono et al. concluded that the low DW mobility in their nanostripes is due to an enhanced relative contribution of edge roughness to Gilbert damping. They calculated the damping parameter $\alpha = 0.63$ from the theoretical equation for DW mobility $\mu = \gamma\Delta/\alpha$, assuming $\Delta = 100$ nm. Such large values of alpha have also been reported in ultrathin Co films due to the presence of defects at the surface and interface [26]. Furthermore they suggest that edge effects in case of nanostripes should also be taken into account.

On the contrary, a high DW mobility under field was found by Atkinson et al. in 200 nm wide single layer FeNi nanostripes [3]. The DW mobility they found, of 30×10^4 m/sT (30 m/sOe), was about 10 times larger than the one found by Ono et al. Using the same expression as used by Ono et al. $\mu = \gamma\Delta/\alpha$, they obtained a value of α an order of magnitude lower, $\alpha = 0.053$. They suggested that confinement effects in the case of nanostripes do not significantly effect the Gilbert spin damping.

Beach et al. resolved the conflict between the contradictory results reported above [8]. They studied field induced DW motion in 600 nm wide and 20 nm thick NiFe nanostripes. They managed to experimentally observe both steady-state and precessional regimes of DW motion. At low fields $H < 0.4$ mT, the DW velocity increases linearly with field with a mobility of 25×10^3 m/sT (2.5 m/sOe) and at a critical field (the Walker field) of 0.4 mT it begins to decrease. Then for $H > 2$ mT the velocity increases again linearly with field but with a 10 times smaller mobility. So they suggested that the previous studies by Ono and Atkinson et al. were not necessarily contradictory, as they studied different regimes of DW motion. The low mobility observed by Ono et al. was found close to their high field value above Walker breakdown field. The high mobility observed by Atkinson et al. was comparable to their low field results.

Weerts et al. demonstrated that along with geometrical parameters of nanostripes and pulse amplitude the effect of the field pulse shape on field induced DW motion should also be taken into account [142]. They studied the effect of field pulse rise times on DW motion in 12 nm thick and 750 nm wide $Fe_{20}Ni_{80}$ nanostripes. They showed that for fast pulse rise time ~ 2 ns, the average DW velocity approaches the very high value of 500 m/s and decreases to 375 m/s for large pulse rise times of ~ 25 ns. The decrease of the average DW velocity may be due to the low effective field acting on the DW during the onset of pulse.

The influence of a transverse magnetic field on field induced DW dynamics was studied by S. Glathe et al. in 20 nm thick and 160 nm wide $Fe_{20}Ni_{80}$ nanostripes [111]. They found that a transverse field (H_{tr}) can influence the DW dynamics both below and above the Walker breakdown (WBD). They found that, for a certain value of (H_{tr}) where it increases

the DW width, it suppresses the WBD and therefore increases the average DW velocity and the high mobility regime continues up to higher fields. An increase in DW velocity of about three times ($\sim 4500\,\mathrm{m/s}$) was observed. This large value of the velocity could not be explained by the 1D model.

1.4 Current induced domain wall motion

The interaction of electric current with magnetization is well known from the 1950's and fully described by classical Maxwell equations. If we consider the solid state with many body quantum mechanical systems, many interesting new phenomenon can be found. Particularly in the last decade rapid progress has been made in the field of nanomagnetism and spin dependent transport.

1.4.1 Spin transfer torque

When an electric current passes through a ferromagnet it becomes spin polarised due to the spin dependent band structure. When these spin polarised electrons cross a magnetic domain wall in a ferromagnet, depending on the circumstances reflection, scattering and transfer of angular momentum to the lattice are the possible effects. This can result into different physical effects like a change of electrical resistance of the magnetic material or the motion of a DW.

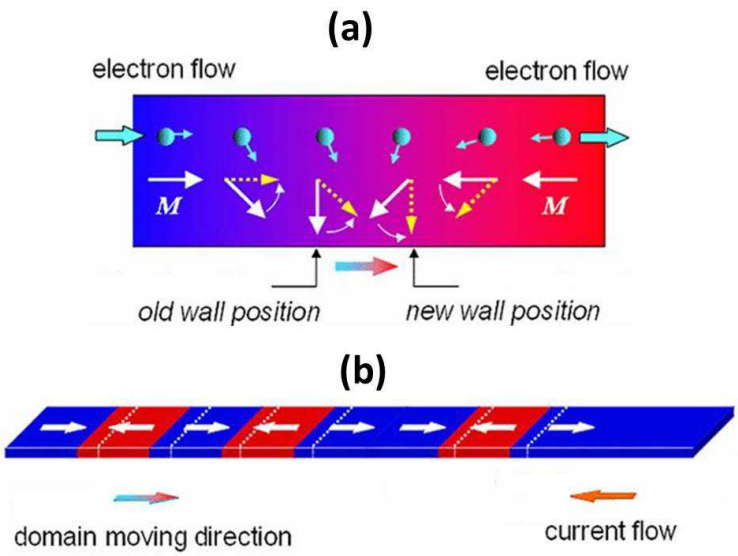

Figure 1.9: Schematic representation of the spin torque effect resulting in motion of (a) a single head to head transverse wall (b) multiple head to head and tail to tail domain walls along the electron flow direction.

L.Berger [10] [11] made the first studies of the interaction between current and a DW. Depending on the thickness of films, two different mechanisms were proposed to explain the interaction between current and DW. For thick films ($> 100\,\mathrm{nm}$), he proposed that due to an electric current DWs experience a dragging force called *"Hydromagnetic DW*

drag" due to the existence of the Hall effect [11]. The DW moves along the direction of charge carriers when the current density exceeds a certain value. Large Hall angle, small coercive field and large uniaxial anisotropy field enhance the DW drag effects.

For films with thickness $< 100\,\text{nm}$, the hydromagnetic drag force becomes negligible and *"s-d exchange interaction"* becomes dominant [12] [29]. This model takes into account the interaction of conduction electron spins and local magnetic moments. The s-d exchange field having non zero field gradient exerts a force on the magnetic moments of conduction electrons.

In 1996 Slonczewski [118] introduced for the first time the phenomenon of *"spin transfer torque"* (STT) in multilayers where two magnetic layers are separated by a non magnetic metallic spacer layer. He proposed that for magnetic materials in which the electric current is spin polarised it is possible that spin angular momentum of conduction electrons is transferred to localized magnetic moments, resulting in a spin torque acting on the magnetization, called STT. The schematic representation of the STT effect on a single head-to-head (HH) TW and multiple HH and tail-to-tail (TT) DWs in a nanostripe is shown in Fig. 1.9. Unlike field induced DW motion, both HH and TT DWs move in the same direction along the electron flow.

Modified LLG equation under adiabatic and non adiabatic spin torques

In 1998, Bazaliy et al. [6] derived analytically the equation of DW motion in the presence of a spin polarized current for continuously varying magnetization. They modified the LLG equation by adding an additional term for spin polarized current. Later in 2004 Li and Zhang [73] [74] also studied the DW dynamics analytically and numerically, under adiabatic spin torque conditions, assuming that the spin-polarization axis adiabatically follows the local magnetization direction. The modified LLG equation under adiabatic spin torque becomes:

$$\frac{\partial \vec{M}}{\partial t} = -\gamma \vec{M} \times \mu_0 \vec{H}_{\text{eff}} + \frac{\alpha}{M_s}\left(\vec{M} \times \frac{\partial \vec{M}}{\partial t}\right) - \left(\vec{u} \cdot \vec{\nabla}\right) \vec{M} \tag{1.26}$$

where $\vec{u}$ represents vector oriented along direction of electron motion and can be interpreted as an effective spin drift velocity given by:

$$\vec{u} = \frac{Pg\mu_{\text{B}}}{2eM_{\text{s}}}\vec{j}. \tag{1.27}$$

where $\vec{j}$ is the current density and P is the spin polarization.

They concluded that spin torque based on the adiabatic propagation of spin current can move the DW over a limited distance but is unable to move DW over large distance. They suggested to also consider the contribution from non-adiabatic spin torque.

Thiaville et al. in [126] studied the DW motion under the combined action of adiabatic and non-adiabatic spin torques by using micromagnetic simulations. They added a non adiabatic term represented by parameter β in the LLG equation. The new form of the LLG equation becomes:

$$\frac{\partial \vec{M}}{\partial t} = -\gamma \vec{M} \times \mu_0 \vec{H}_{\text{eff}} + \frac{\alpha}{M_s}\left(\vec{M} \times \frac{\partial \vec{M}}{\partial t}\right) - \left(\vec{u} \cdot \vec{\nabla}\right) \vec{M} + \frac{\beta}{M_{\text{s}}}\vec{M} \times \left[\left(\vec{u} \cdot \vec{\nabla}\right) \vec{M}\right]. \tag{1.28}$$

This equation explains reasonably well the DW velocities under spin polarized current as well as the variation of the DW propagation field under current. The non adiabatic torque has the same effect on the DW like an applied magnetic field. It cants the DW magnetization out of plane and the torque resulting from the demagnetizing field moves the DW forward.

1.4.2 1D model and micromagnetic modeling

The 1D model, normally adopted for a 1D Bloch wall, can be used to describe the transverse wall (TW) dynamics because it gives the good qualitative behaviour of TW dynamics. Using 1D model DW motion can be simply described by two parameters: its position y along the nanostripe and the DW magnetization angle ϕ. A third parameter can be the DW width Δ but it indirectly depends on the angle ϕ as shown in Fig. 1.7. The adiabatic and non-adiabatic spin torques $\vec{\Gamma}_u$ and $\vec{\Gamma}_\beta$ respectively acting on a DW are given by solving the eq. (1.28) using the 1D model [91]:

$$\vec{\Gamma}_u = \frac{M_s u}{\gamma}\frac{\sin\theta}{\Delta}\vec{e}_\theta, \tag{1.29}$$

$$\vec{\Gamma}_\beta = -\beta\frac{M_s u}{\gamma}\frac{\sin\theta}{\Delta}\vec{e}_\varphi. \tag{1.30}$$

The total polar and azimuthal torques Γ_θ and Γ_φ under field and current can be expressed as [91]:

$$\Gamma_\theta = 4\pi M_s^2(N_y - N_x)\sin\theta\sin\varphi\cos\varphi + \frac{\alpha M_s}{\gamma}\dot{\varphi}\sin\theta + \frac{M_s u}{\gamma}\frac{\sin\theta}{\Delta} \tag{1.31}$$

$$\Gamma_\varphi = -M_s H\sin\theta - \frac{\alpha M_s}{\gamma}\dot{\theta} - \beta\frac{M_s u}{\gamma}\frac{\sin\theta}{\Delta} + 4\pi M_s^2\sin\theta\cos\theta\left[N_z - N_y\sin^2\varphi - N_x\cos^2\varphi\right] \tag{1.32}$$

Let us first consider the steady state motion in which the azimuthal angle ϕ does not change ($\dot{\varphi} = 0$), so the corresponding torque Γ_φ will also be zero. So putting $\Gamma_\varphi = 0$ and $\theta = \pi/2$ at the DW center, eq. (1.32) gives [91] :

$$\sin 2\varphi = \frac{H + (\beta - \alpha)\frac{u}{\gamma\Delta}}{2\pi\alpha M_s|N_y - N_x|}. \tag{1.33}$$

This equation is valid only if

$$|H + (\beta - \alpha)\frac{u}{\gamma\Delta}| \leq H_{\mathrm{W}} \tag{1.34}$$

where the Walker field is defined as

$$H_{\mathrm{W}} = 2\pi\alpha M_s|N_y - N_x| \tag{1.35}$$

For a zero applied field, putting $H = 0$ in eq. (1.33) gives the Walker breakdown current density J_{W}, given by

$$J_{\mathrm{W}} = \frac{\alpha e M_s^2}{g\mu_{\mathrm{B}}P}\frac{\gamma\Delta}{|\beta - \alpha|}|N_y - N_x| \tag{1.36}$$

The DW velocity in the steady state below the Walker breakdown is given by [91] :

$$v_{\text{steady}} = \frac{\beta}{\alpha} u \tag{1.37}$$

Above the Walker breakdown, when $J \gg J_{\text{W}}$, the time average velocity over the period of precession of ϕ is expressed as [91]

$$\bar{v} = \frac{1 + \alpha\beta}{1 + \alpha^2} u \tag{1.38}$$

The equations (1.37 and 1.38) are qualitatively similar to the DW motion under low and high fields for a 180° Bloch wall [78][114], i.e., at low field the DW velocity is linearly proportional to the field and at the Walker breakdown its velocity decreases and at high field above the Walker breakdown the DW velocity again becomes linear with field. The only contribution to the domain wall velocity under current is the non-adiabatic part of the spin transfer torque. The effect of the non-adiabatic torque on the DW is similar to an applied field. It cants the DW magnetization out of the plane and the torque resulting from the demagnetizing field moves the DW forward. At low current densities, the spin transfer torque is balanced by an internal restoring torque. The DW magnetization tilts out of the easy magnetization plane but the DW does not move steadily under current. Above threshold, the internal torque is not sufficient and DW motion takes place, with a continuous precession of the DW magnetization.

Thiaville et al. computed the TW velocity using micromagnetic simulations in a 120 nm wide and 5 nm thick Py nanostripe as a function of current density, both for perfect and rough stripes [125]. They found finite propagation field and threshold current for DW motion in rough wires but not in perfect stripes. This indicates that threshold currents are extrinsic. They also studied the effect of the β parameter on the DW motion. Their results from micromagnetic simulations for TW dynamics for perfect nanostripes show a good agreement with analytical calculations using the 1D model. Their results for perfect nanostripes (Fig. 1.10) can be summarized as follows:

For $\beta = 0$, a high critical current density is required for DW motion and no motion is observed for $u < u_c = 600\,\text{m/s}$.

For $\beta < \alpha$, the DW motion starts for any finite value of u and the DW velocity increases linearly with current until a threshold and then again converges to u, the spin drift velocity.

For $\beta > \alpha$, the DW motion is characterized by two regimes: a steady state or stationary regime and a precessional regime.

In the steady state regime the DW velocity increases linearly with increase in current density until the Walker threshold current density. The velocity in this regime is described by the following relation $v = \beta u/\alpha$. In the precessional regime, the DW moves by continuous transformations between vortex and transverse walls resulting in a reduction of the DW velocity.

For $\beta = \alpha$, DW moves like a rigid body without transformation.

1.4.3 2D model and Vortex wall dynamics

The motion of a VW under current cannot be simply described by the 1D model. To describe the VW state we need an additional coordinate which represents the position of

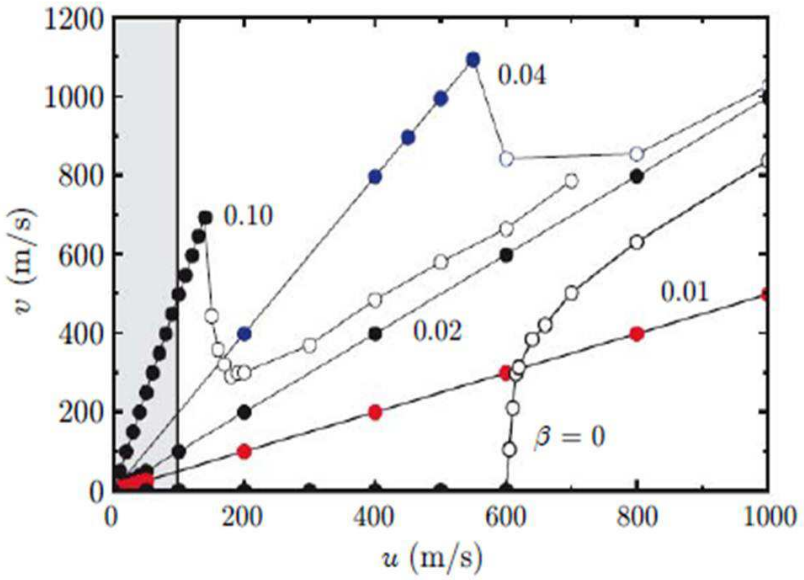

Figure 1.10: Transverse DW velocity computed from micromagnetic simulations in a 120 nm *wide and* 5 nm *thick Py nanostripe as a function of velocity u representing the current density for different values of the nonadiabatic parameter* β *and damping parameter* $\alpha = 0.02$*. The shaded area corresponds to the value of u used in experiments and open symbols shows nucleation of vortices (Reproduced from [125]).*

the vortex core. So we need at least a 2D model to describe a VW structure. Several models were proposed to describe the vortex wall internal structure and its dynamics. J. He et al. [47] introduced a 2D model for VW and analytically calculated its dynamical behaviour in terms of material parameters both under field and current.

Thiaville and Nakatani [124] performed detailed micromagnetic simulations by considering all the degrees of freedom of DWs for transverse and vortex wall motion under field and current. Here I will describe their results of DW motion under current for only VWs.

First, they considered only adiabatic spin torque and a perfect nanostripe. At very low current densities the VWs move and get deformed and finally stop like TWs. However VWs move a larger distance than TWs under the same current due to a larger structural characteristic time of a VW. The deformation of a VW occurs by displacement of the vortex core in the y direction towards the nanostripe edge.

The VW structure is stable only for low current densities $u < u_c = 60\,\mathrm{m/s}$. For intermediate current densities $u_{c,\mathrm{VW}} < u < u_{c,\mathrm{TW}}$, the VW transforms to a TW by expelling the vortex core, resulting in displacement of the DW position and finally the DW stops after transformation. The total DW displacement due to current is the sum of the DW displacement due to the transformation plus the TW displacement due to the current.

By considering perfect nanostripes and also a non-adiabatic torque in their simulations, they found identical velocities for vortex and transverse wall in the stationary regime. Above this regime, VW into TW transformation occurs due to the vortex core expulsion.

Fig. 1.11 shows the time evolution of a VW as a function of current density (u) for different values of β. The value of $u = 50\,\mathrm{m/s}$ corresponds to the linear regime of VW

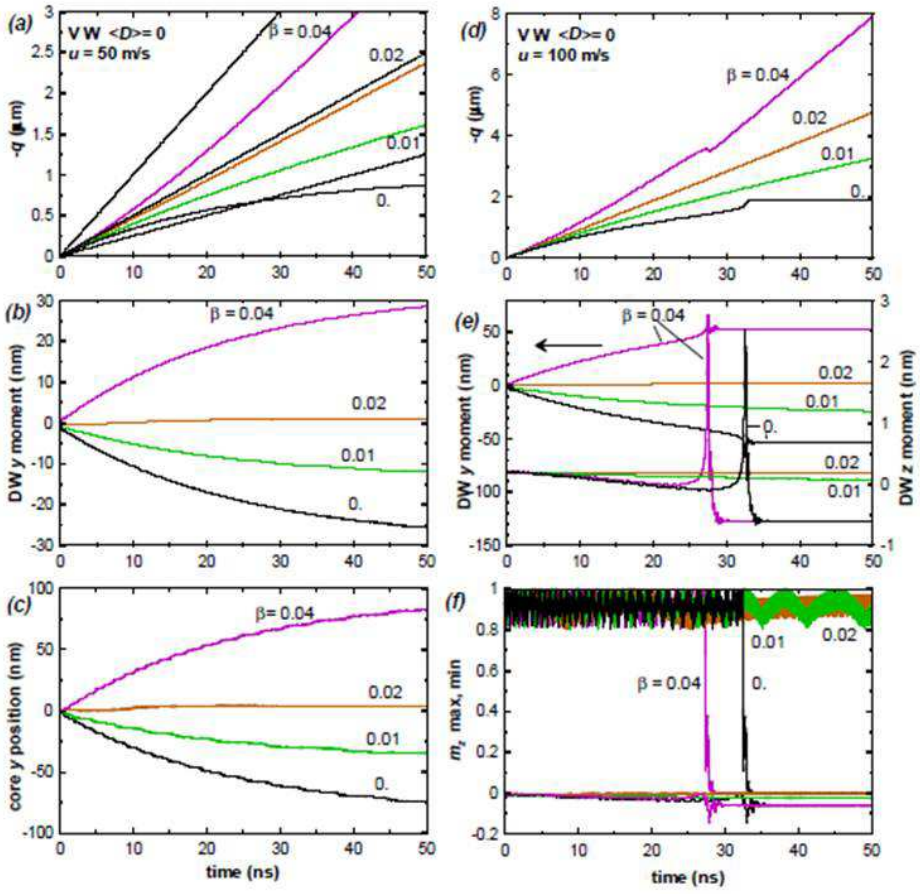

Figure 1.11: Time evolution of a VW in a 5 nm *thick and* 300 nm *wide perfect nanostripe under current, represented by equivalent current density u as a function of non adiabatic parameter β (α = 0.02). (a-c) corresponds to the VW linear regime for current densities u = 50* m/s *and (d-f) represents the VW above the Walker threshold for some values of β (Reproduced from [124]).*

without any transformation as shown in Fig. 1.11 (a-c). For $u = 100$ m/s, the VW motion corresponds to the linear regime only for $\beta = 0.01$ and 0.02. It is clear from Fig. 1.11 (b, e and c) that the VW y moment and the vortex core y position gradually change even in the linear regime of VW motion like for the TW. Only for $\beta = \alpha$, there is no change like for TW and it is almost double for $\beta = 0$ than that of $\beta = 0.01$. For $\beta = 0$ the change in VW y moment or core y position is opposite to that for $\beta = 0.04$. Fig. 1.11 (b) shows that the VW structural deformation has not reached the steady state value even after 50 ns so the corresponding VW velocities are far away from the linear regime. Since the DW initial velocity is u, the velocities obtained from Fig. 1.11 (a-d) then lie between the initial velocity $v = u$ and $v = \beta u/\alpha$.

After the end of the linear regime, the vortex is expelled and transforms to a TW. As the characteristic time of TW is shorter than VW, the velocities in the linear regime are different fort short times. However, the velocities obtained in the linear regime at long times for VWs are identical to the ones for TWs [Fig. 1.10].

1.4.4 Origin of the nonadiabatic parameter β

Several theoretical and experimental studies have been performed to find the origin and magnitude of the non-adiabatic parameter β resulting in partially contradictory results, but no final conclusion has been drawn yet. The presence of a non-adiabatic term is important in the sense that in its presence DW motion is possible for any finite current in a perfect system without any magnetic field. The difficulty in calculating β experimentally is to distinguish between intrinsic pinning and the extrinsic sources of pinning due to structural defects.

The non-adiabatic term has been proposed to be more dominant in narrow DWs where a high magnetization gradient occurs while a purely adiabatic contribution is expected in wide DW spin structures. Below I will summarize a few results regarding theoretical and experimental determination of the β parameter for both type of systems with in-plane and out of plane anisotropy, containing wider and narrower DWs respectively.

S. Zhang and Li predicted that a non-equilibrium conduction electron spin density connected to the mistracking of the conduction electron spins and the local magnetization direction after entering the DW, generates an additional torque [74]. This results into a non-equilibrium spin accumulation in the DW which is relaxed mainly by spin flip scattering. The non-equilibrium spin density induces a non-adiabatic torque which acts as an effective force on the DW. This torque is described by a coefficient $\beta = \tau_{ex}/\tau_{sf}$, where τ_{ex} is the Larmor precession period around the s-d exchange field and τ_{sf} is the spin relaxation time. The non-equilibrium current density also modifies the precession (gyromagnetic ratio γ) and damping parameter α in the LLG equation, so these terms should also be renormalized.

Tatara and Kohno [121][122] show that a non-adiabatic torque remains present for wider DWs and decreases strongly with DW width. They have shown that both α and β arise from spin relaxation processes and generally β is not equal to α. Garate et al [34] derived the β parameter directly from the band structure of real materials. They found that both α and β have the same qualitative dependence on disorder although their ratio depends on details of the band structure.

M. Eltschka et al. [22] experimentally derived β by investigating thermally activated vortex and transverse DW motion in $Fe_{20}Ni_{80}$ nanostripes. They showed that this purely thermal motion can be well described by the Arrhenius law by considering the DW as a quasi-particle in a 1D landscape. The values of β calculated for transverse and vortex walls are $\beta_t = 0.01 \pm 0.004$ and $\beta_v = 0.02 \pm 0.073$ respectively. The larger value for a VW as compared to a TW is related to the high magnetization gradient at the vortex core. The larger value of β for a VW indicates that higher velocities should be possible for VWs.

Much higher values of β were observed for systems with out of plane anisotropy and inversion asymmetry [85]. I. M. Miron et al., measured experimentally the non-adiabatic component of the spin torque in a AlOx/Co/Pt system with inversion asymmetry. They reported that the value of the β parameter can be as high as 1 in this system, approaching the maximum value predicted by the existing theories [85].

1.4.5 Experiments

After the prediction of current induced DW motion by the STT effect, it has attracted considerable attention during the last decade and a large number of experimental studies have been performed to confirm and better understand this effect. Here I will give brief description of some of the experimental results in this field. During my thesis I worked on systems with an in-plane anisotropy, I will discuss in details such type of systems.

Systems with in-plane anisotropy

$Fe_{20}Ni_{80}$ (Permalloy - Py) is a very soft magnetic material having small coercive field. The DWs in Py can be moved with a very small magnetic field. Due to this low DW propagation field, it is expected that DWs in Py can be moved with low current densities. For this reason, most of the studies were focused on Py. Experimental results indicate a large spread in DW velocities observed for the same type of materials. Here I will describe some of these experiments indicating diverse results and the origin of these discrepancies.

Initially the current induced DW motion was studied in continuous magnetic thin films. Hung and Berger studied DW motion in $Fe_{19}Ni_{81}$ thin films of thickness between 14 and 86 nm [54]. They observed a DW displacement by current both under magnetic field and without field. They found that for films of thickness < 35 nm containing Néel walls and for thickness 35 to 86 nm containing cross-tie walls, the DWs move along the charge carriers (electrons). They explained the observed DW displacements by s-d exchange forces induced by conduction electrons. The low values of current density of 5×10^{11} A/m^2 required to move DWs agree with theoretical predictions based on s-d exchange [12][29].

E. Salhi and L. Berger observed Bloch wall displacements in $Fe_{19}Ni_{81}$ films of thickness $\cong 263$ nm [112]. They observed DW displacements for very low critical current density of $\cong 1.3 \times 10^{10}$ A/m^2, about 20 to 200 times lower than for Néel or cross-tie walls predicted earlier by Hung and Berger [54]. They suggested that the observed Bloch wall motion was caused by precession of wall spins under *"s-d exchange torque"*, applied by conduction electrons passing through the wall.

The study of current induced DW motion in magnetic nanostructures or nanostripes became only possible after the developments in lithography techniques to make nanostructures. J.Grollier et al. [39] have shown for the first time that DC current can switch the magnetic configuration of a 5 nm thick Py layer in a Py/Cu/Co spin valve structure by moving a DW pinned by a 500 nm wide constriction in a 1 µm wide nanostripe. The direction of DW displacement was reversed by reversing the direction of the DC current.

Large spread in domain wall velocities observed for Py

A large spread in DW velocities was observed for Py in experiments. DW velocities that were one or two orders of magnitude lower than predicted by theory, as well as velocities higher than the spin angular momentum transfer rate, have been reported. I will describe here some of these experiments revealing this discrepancy. Later, I will also list some experiments resolving this discrepancy.

The DW motion was studied quantitatively by Yamaguchi et al. in 10 nm thick and 240 nm wide L-shaped $Fe_{19}Ni_{81}$ nanostripes [145]. They investigated the DW displacement as a function of intensity and duration of the current pulses. They observed DW

displacements proportional to the pulse duration, which supports that the DW displacement was due to the spin transfer torque. They observed a very low DW velocity $\sim$ 3 m/s under current pulses of duration 500 ns and current density 1.2×10^{12} A/m^2. They suggested that detailed experiments with different thickness and width of nanostripes are required to know the origin of the low DW velocity.

Very high DW velocity exceeding the spin angular momentum transfer rate under zero magnetic field was reported by M. Hayashi et al. [45] in similar 10 nm thick and 300 nm wide $Fe_{19}Ni_{81}$ nanostripes. This shows that the DW is moving faster than the rate of spin angular momentum transfer, i.e. $v_{1D} = (\beta/\alpha)u$ with $\beta > \alpha$. A DW velocity of 110 m/s was obtained for a current density of 1.5×10^{12} A/m^2. They suggested that some other mechanism such as linear momentum transfer effect should also be considered to explain the velocities larger than the momentum transfer rate. The maximum DW velocities reported in previous measurements were 10 to 100 times lower than the one allowed by the spin angular momentum transfer rate.

The origin of the large spread in domain wall velocities

Different origins of this discrepancy were reported by different groups i.e., M. Klaui et al. have also observed very low DW velocities of ~ 0.3 m/s for 1 µs long current pulses of current density of 2.2×10^{12} A/m^2 [60]. They observed that both head to head and tail to tail DWs move along the direction of the electron flow in 500 nm wide and 10 nm thick Py nanostripes. The velocity decreased with subsequent current pulses and finally the DW stopped moving after injection of a few pulses. They observed the DW deformation from vortex to transverse spin structure after injection of a few current pulses by high resolution spin polarized electron microscopy. That was the first experimental evidence of DW transformations due to the current. They related the reduction of the DW velocity to DW deformation.

The periodic DW transformations from vortex to transverse walls and vice versa by injection of current pulses were also observed by Heyne et al. [48] in 1500 nm wide and 8 nm thick Py nanostripes. After each transformation, the vortex core showed the same chirality and direction of core displacement which is the evidence of the spin torque effect.

A DW that changes its structure is predicted to undergo a displacement by itself, the so called "*automotion*". J. Y. Chauleau et al. [19] demonstrated the phenomenon of automotion experimentally in Py nanostripes with in-plane magnetization by transforming an asymmetic metastable transverse DW into a vortex DW under spin transfer torque. They observed DW displacements more than three times larger than under spin transfer torque only for 1 ns current pulses. They suggested that to calculate the real DW velocities, the DW displacement due to automotion should be excluded. They also studied field induced DW transformation and automotion and concluded that automotion is independent of the type of excitation used for DW transformation. Their results agree well with micromagnetic simulations. The phenomenon of automotion also applies well to systems with perpendicular magnetization. However, due to the small size of DWs in these materials due to the strong anisotropy, the observation of the wall structure is more difficult. Therefore, to investigate the real effect of spin transfer torque on DW displacement, DW structure transformations should be checked by imaging.

In addition to DW transformations due to spin torque, M. Klaui et al. [61] also observed continuous transformations of VWs to double and triple vortices and vice versa

due to DW pinning and joule heating in 28 nm thick and 1 µm wide nanostripes. They found that the velocity is related to these transformations and decreases with increasing number of vortices.

Most of the experiments focussed on the current induced depinning of DW from material defects and artificially created pinning sites and find velocities one or two orders of magnitude lower than predicted in theory. This suggests that most of the transferred angular momentum is dissipated by local excitations instead of driving DW. G. S. D. Beach et al. [7] used an external magnetic field to cancel pinning and identified the contribution of spin torque to the velocity of freely propagating DWs. They found that the DW velocity increases in proportion with current by an amount predicted by theories. They observed a DW velocity of $\sim 35\,\mathrm{m/s}$ at a current density of $6 \times 10^{11}\,\mathrm{A/m^2}$ in 20 nm thick 600 nm wide Py nanostripes. This velocity is about 10 times larger than reported in pinning dominating experiments. These values of DW velocity agree well with theoretically predicted values of DW motion due to spin torque effects. So it means that DW pinning does not allow to extract quantitative information on the spin torque effect on DWs, as most of the energy is dissipated in depinning of DWs.

An influence of the current pulse rise time on DW velocity was also reported by L. Heyne et al. [49] in Py nanostripes. They observed high DW velocities of 130 m/s, of the order of the spin angular momentum transfer rate $u = 120\,\mathrm{m/s}$, in agreement with the theory assuming β close to α. They used very short pulses of 3 ns of very fast rise time $\sim$ 100 ps for a current density of $1.8 \times 10^{12}\,\mathrm{A/m^2}$. They also observed DW transformations under these very short nanosecond pulses. They proposed that this efficiency is not related to the quality of Py sample but rather to the fast pulse rise time because in their previous studies they obtained very low DW velocities $\sim 1\,\mathrm{m/s}$ in the same type of Py samples for pulse rise times larger than 1 µs.

Domain wall inertial effects

As it is reported that DWs exhibits inertial effects when driven under field [78], the theories predict that DWs should also exhibit inertial effects when driven by current [73][126][121]. The inertial response of the DW depends on the relative magnitude of adiabatic and non-adiabatic torques. Their relative contribution can be quantified by the ratio β/α. L. Thomas et al. [128] reported that DW displacement is directly proportional to pulse length even for very short current pulses of a few nanoseconds by studying 20 nm thick and 200 nm wide Py nanostripes. Inertia causes a delay of the constant velocity motion at the beginning of the pulse but this is compensated by the inertia at the end of the pulse (DW keeps moving when pulse has stopped). The total displacement is thus proportional to the pulse length despite the inertia.

Other systems with in-plane anisotropy

In parallel to Py single layers, other systems with an in-plane anisotropy were also studied. I will explain here few of these systems. S. M. Seo et al. [115], recently analytically studied current induced DW motion in the presence of the spin hall effect (SHE) in FM/NM bilayers, where NM is non magnetic metallic layer having strong spin orbit coupling (SOC) responsible for the SHE and FM is the metallic ferromagnetic layer having in-plane anisotropy. Their results show that SHE has a significant effect on transverse DW

motion. The DW motion can be represented by two threshold current densities J_{WB} and J_{rev}, where J_{WB} is the threshold for DW chirality switching and J_{rev} is the threshold for reverse DW motion due to SHE. For current density $J_{rev} < J < J_{WB}$ such that $J_{WB} > J_{rev}$ and $\alpha > \beta$, the DWs move against the electron flow with high speeds $\sim 300\,\mathrm{m/s}$, for a certain chirality. They also performed micromagnetic simulations and their results are in agreement with their analytical model. Their results show that by proper tuning of spin orbit coupling and hence SHE, very efficient CIDW motion can be achieved.

The relation between damping parameter α and the non-adiabatic parameter β was studied by T.A.Moore et al. [88]. By artificially varying α they studied its effect on β. They modified α by doping Py with Ho with different compositions resulting in different values of α. They measured values of α by ferromagnetic resonance. The value of α increases with Ho concentration. Then they measured the current induced DW velocity below the Walker breakdown in 20 nm thick and 1500 nm wide pure Py nanostripes and nanostripes with Ho doping. Since $v = (\beta/\alpha)u$ below the Walker breakdown, they found that β scales with α and concluded that spin relaxation, which leads to non-adiabatic torque, and angular momentum dissipation that causes damping, both have the same origin.

Critical current densities of one order of magnitude lower than for single Py layers have been reported in Py based spin-valve nanostripes. J. Grollier et al. observed the back and forth DW motion between two pinning centers with very low DC current densities, $\sim 10^{11}\,\mathrm{A/m^2}$, in 300 nm wide Py/Cu/Co spin valve nanostripes [38]. They found their results consistent with the spin torque mechanism introduced by Berger and Slonczewski [118][13].

Very low critical current densities of $8 \times 10^{10}\,\mathrm{A/m^2}$ have also been reported in Py/Cu/Co spin-valve nanostripes under zero field by C. K. Lim et al. [75]. These values are about an order of magnitude lower than reported in Py single layers [43]. They observed DW displacements for very short 0.4 ns current pulses along the conduction electrons flow. However, the DW displacements were found independent of current pulse duration and the direction of the DW displacements were opposite to the conduction electrons for higher current densities.

The critical current density can be further reduced by replacing Py in spin valve nanostripes by CoFeB [66]. CoFeB is a very soft amorphous magnetic material. A critical current density of $1 \times 10^{10}\,\mathrm{A/m^2}$ at zero field, about two orders of magnitude smaller than in single Py nanostripes, was observed.

Recently very large DW velocities of up to 600 m/s have been found in Py/Cu/Co spin-valve nanostripes for very short 3 ns current pulses at current densities of $4 \times 10^{11}\,\mathrm{A/m^2}$ [137]. They also partially explained the previously reported problems in this type of system. They relate the reduction of critical current densities partially due to vertical spin currents caused by the local spin accumulation in Cu spacer layer below the DW region [59]. They also show that DW displacements do not scale with current pulse durations because of the pinning. The DWs move with high DW velocities, but only in between two pinning sites, which makes it difficult to determine accurate DW velocities. They identify possible sources of pinning, among which the dipolar interaction between Py and Co layers due to anisotropy inhomogeneties in the Co layer is found to be dominant.

Systems with out-of-plane anisotropy

Although high DW velocities up to 150 m/s have been reported in Py nanostripes [42], there are some drawbacks of using Py for applications. Often, the DW displacements are not reproducible and DW depinning from thermally stable positions is difficult. Usually a high critical current density $\sim 1 \times 10^{12}\,\mathrm{A/m^2}$ is required to depin and propagate the DW. This high current density can cause a large temperature rise due to joule heating resulting in nucleation and annihilation of DWs or DW transformations. The DW structural transformations due to Walker breakdown limits its maximum velocity.

Micromagnetic simulations and experimental results predicted that using systems with strong perpendicular anisotropy, these problems can be overcome [57][33]. Recently high efficiency of current induced DW depinning has been reported in materials with out of plane anisotropy [24][63]. The DWs in these systems are narrower due to strong perpendicular anisotropy. The torque which is proportional to magnetization gradient should be stronger. But due to the narrow width $\sim 10\,\mathrm{nm}$ of these DWs, pinning could be more effective in these systems as compared to systems with in-plane anisotropy where the DW width is $\sim 100\,\mathrm{nm}$.

T. A. Moore et al. [89] reported high DW velocities of 130 m/s at current densities of $1.8 \times 10^{12}\,\mathrm{A/m^2}$ in an AlOx/Co/Pt system with strong perpendicular anisotropy. The inversion asymmetry of their system is expected to enhance spin torque through increase in the spin flip rate.

Mihai Miron et al. [83] proposed that strong effective magnetic fields of 1 T for current densities of $1 \times 10^{12}\,\mathrm{A/m^2}$ can be induced in a ferromagnetic metal films lacking structure inversion symmetry through the *"Rashba effect"*. They show that an electric current flowing in the uniformly magnetized Co layer in an AlOx/Co/Pt system with inversion asymmetry and perpendicular anisotropy produces an effective transverse magnetic field, the so called "$Rashba field$" (H_R). The H_R combines with s-d exchange interaction, that couples the conduction electron spin with the local magnetization. This results into an effective s-d exchange field H_{sd}, which depends on current density and produces a torque on the local magnetization. Spin orbit effects at metal surfaces increase in the presence of heavy atoms [85][86] and surface oxidation [84]. Here Pt as a heavy metal and AlOx as an oxide play a role to enhance the Rashba spin orbit interaction.

In the same AlOx/Co/Pt system later, Mihai Miron et al. [84] reported high DW velocities of 400 m/s with current density of $1 \times 10^{12}\,\mathrm{A/m^2}$. The Rashba field in this system acts along the hard axis and stabilizes the Bloch DW chirality meaning that the DW can be moved without being transformed for higher current densities. On the other hand, an enhancement of the non-adiabatic spin torque is reported in this type of systems which facilitates to depin the DW (β/α is also rather high) and hence the DW mobility.

1.5 Domain wall pinning

The precise control of DW motion is very important for logic and memory devices based on current induced DW motion. However, the stochastic nature of DW motion due to intrinsic (structural defects) and extrinsic (roughness) DW pinning is the major challenge for practical applications [134][107]. Usually artificial pinning sites in the form of curved nanostripes or notches of different shapes are created in the nanostripes to control the

DW motion by pinning and depinning DWs across them using current or magnetic field pulses [44][56].

Previous studies have reported that critical current densities for current induced DW motion scaled with DW depinning field. These critical current densities can be reduced by reducing the edge roughness of nanostripes. G. Malinowski et al. have obtained low DW depinning fields of 0.2 to 0.3 mT due to low edge roughness by using an Ar ion milling process to pattern the nanostripes instead of using conventional lift-off technique [77]. As compared to other similar samples having higher pinning, they reported very low critical current densities of 4×10^{11} A/m^2 in 25 nm thick and 900 nm wide Py nanostripes. They also suggested that current densities larger than the critical current densities can result into DW transformations instead of DW depinning, affecting the DW motion.

In the case of the precessional regime beyond the Walker breakdown, nanostripe edge roughness can play an important role in DW dynamics, as the DW transformation occurs at the edges of nanostripes by an injection of anti-vortices. Y. Nakatani et al. [92], using micromagnetic simulations, reported that high DW velocities can be achieved by suppressing the Walker breakdown for nanostripes with rough edges. They explained that for sufficiently rough edges, according to simulations, the nucleation of an anti-vortex at the edges is suppressed and the wall continues moving with maximum velocity without transformation. Their results show that roughness larger than exchange length is suitable. For Py the exchange length is about 9 nm. However, edge roughness also causes DW coercivity. Therefore they propose to optimise the edge roughness to get the best DW propagation properties.

Along with the edge roughness and other intrinsic material defects in nanostripes, the field induced depinning of DWs also depends on structure and chirality of the DWs [44]. M. Hayashi et al. studied the depinning of transverse and vortex DWs of two different chiralities pinned at the same nano-constrictions in 10 nm thick and 100-300 nm wide Py nanostripes. They found different field induced depinning fields for all four type of DWs but nearly the same critical depinning current for all DWs.

The dependence of DW depinning threshold current on different factors has been reported by different groups. S. Lepadatu et al. [70] studied the effect of the shape of the pinning profile on threshold depinning current density. They created different triangular notches, in single 20 nm thick and 1400 nm wide Py nanostripes, by keeping the width of the wire and notch depth constant and varying only the notch angle. They found that the threshold current density increases linearly with notch angle. They confirmed their results by micromagnetic simulations.

The temporal effect of current pulses on DW motion was studied by L. Bocklage et al. both experimentally and theoretically [16]. They investigated this effect in 20 nm thick and 380 nm wide Py nanostripes having a notch with a depth about 120 nm. Their results show that the current pulses with fast rise times, smaller than the damping time (a few nanoseconds), can result into efficient depinning of DWs. No dependence on the pulse length was observed. They suggested that their results should be independent of the origin of pinning either due to material defects or artificial pinning sites and also independent of the structure of the DWs.

W. C. Uhlig et al. [134] observed the strong influence of random pinning sites due to material defects on CIDW motion. They studied both vortex and transverse DWs in wider and narrower nanostripes respectively. They observed the distortion of DWs at low currents without moving the DW and for large currents the DW releases and moves along

the direction of electron flow until it gets pinned by another pinning site.

1.6 Other effects

1.6.1 Joule heating

Since a significant Joule heating due to current pulses has been observed in experiments [144], this should be quantitatively measured and its effect on DW motion should be considered to compare experimental and theoretical results.

The thermal excitations can reduce the energy barrier of a pinned DW. D. Ravelosona et al. [24] observed the thermally assisted efficient depinning of narrow Bloch DWs in thin films with perpendicular anisotropy. This efficiency of DW depinning was found an order of magnitude higher than reported in films with an in-plane anisotropy. They suggested that this high efficiency is due to the fact that in previous experiments the critical current density was determined by observing 3D Néel wall motion on the micrometer scale, resulting in a measured critical current density above the real threshold value [145][75]. On the other hand, they observed 1D Bloch wall motion on the nanometer scale in the presence of thermal fluctuations below the threshold current density.

Unlike Ravelosona et al., M. Laufenberg et al. observed an increase of critical current density with temperature [69]. This is also in contradiction to a decrease of critical field in the field driven case. They studied both field and current induced DW motion in 34 nm thick and 110 nm wide Py ring shape nanostripes between 2 and 300 K and concluded that intrinsic spin torque efficiency is reduced with increase in temperature, may be due to thermally excited spin waves. The decrease in current polarization has been reported from 0.75 ± 0.05 to 0.58 ± 0.02 over the temperature range 80 to 340 K in Py nanostripes [149]. Different temperature dependencies of spin-up and spin-down conductivities reveal the the strong impurity scattering of spin down electrons. The decrease in magnetic moment with rise in temperature has also been reported [130]. This decrease in spin polarization and magnetic moment with temperature can result into an increase of critical current density for DW motion.

Yamaguchi et al. [144] studied the effect of Joule heating in 10 nm thick and 240 nm wide $Fe_{19}Ni_{81}$ nanostripes. They observed an increase in sample temperature up to 830 K, which is close to the Curie temperature, for current densities of $7.5 \times 10^{11}\,\mathrm{A/m^2}$. After further increasing the current density, they observed a multidomain structure by MFM, which is the indication that temperature has increased above the Curie temperature. This shows that for good dissipation of heat the substrate should be a good thermal conductor as well as bad electrical conductor to avoid a short circuit.

1.6.2 Oersted field

V. Uhlir et al. [136][138] performed first time resolved XMCD-PEEM measurements on Py/Cu/Co and CoFeB/Cu/Co spin valve nanostripes. They gave the first direct evidence of the effect of the current induced magnetic Oersted field on the magnetic configuration of magnetic nanostripes. They observed a large tilt in Py and CoFeB magnetization transverse to the nanostripes. They showed that this effect cannot be quantitatively explained by only Oersted field and shape anisotropy, but is caused by the combination

of Oersted field and strong dipolar interactions due to the different magnetic layers in spin-valve nanostripes. They suggested that this internal transverse field may contribute to the enhancement of the spin torque efficiency in the Py layer. The transverse Oersted field might stabilize transverse DWs, preventing DW transformations. This can result in suppression of the Walker breakdown resulting in an increase in DW velocity, like it was observed for field induced DW motion in spin-valve nanostripes in the presence of a transverse magnetic field [111][18].

The objective of my thesis is to first grow the single crystal epitaxial permalloy and supermalloy layers with less structural defects and surface or interface roughness to reduce pinning and hence threshold current density to move DWs. Secondly, to investigate the effect of magnetic Oersted field on DW stability, chirality and mobility in asymmetric FM/NM bilayers, where FM is a ferromagnetic layer (permalloy or Supermalloy) and NM is a non-magnetic layer (in our case Ir or Pt). Unlike spin valves, the absence of Co layer will allow us separating the effect of the Oersted field from flux-closure magneto-static interactions with the Co underlayer, and also avoiding the effects of spin accumulation in the spacer layer on the domain wall motion.

1.7 Practical applications

Beside fundamental investigations, the use of magnetic DWs in logic [2] and memory [102] devices has been proposed. In magnetic logic devices initially proposed by D. Allwood et al. [2] domain walls can propagate through complex networks of nanostripes by applying an external magnetic field. The logics 1 and 0 were defined as the magnetization pointing along and opposite to the DW propagation direction respectively. They proposed that any computational calculation can be performed by considering NOT, AND or OR and other complicated logic systems.

Another type of memory called domain wall *"Racetrack Memory"* proposed by S. S. P. Parkin [102] has stimulated the research in the field of current induced DW motion. In this memory the magnetic information is stored in DWs in long nanostripes created horizontally or vertically on a Si substrate as shown in Fig. 1.12. Individual nanoscale reading and writing heads are created below each nanostripe to read or write the information. The information can be read from the stored bit by reading the tunnel magnetoresistance of a magnetic tunnel junction in contact with the racetrack. The writing of the information is done by the stray field of a DW below the bit. Highly reliable and controlled forward and backward motion of DWs, which represents the databits, along the racetrack is required. Especially, to assure reproducible and reliable DW motion, DW pinning in nanostripes has to be controlled. Low current densities and high DW velocities at zero magnetic field are required for future applications.

There are several advantages of the racetrack memory over the conventional hard disk drives. There is no mechanical movement involve as in hard disks. The heavy mass of the hard disk limits its speed. The information accessing time is very small, $\sim$ nanoseconds, as compared to milliseconds in harddisks. The power consumption is very low because no coils are required to produce magnetic fields for magnetization switching but instead magnetization is switched directly by applying short nanosecond current pulses. Very high magnetic storage density can be achieved by realizing 3D magnetic memory by making vertical racetracks.

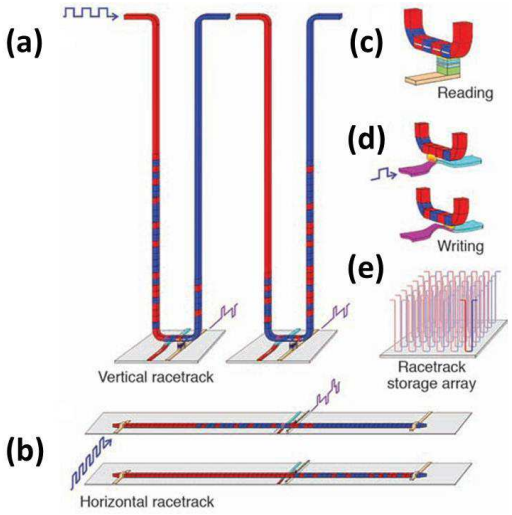

Figure 1.12: Picture of the domain wall racetrack memory. (a) vertical racetrack, (b) horizontal racetrack, (c) reading data by reading the tunnel magnetoresistance of a magnetic tunnel junction in contact with the racetrack. (d) writing data by the stray field of a domain wall below the magnetic bit. (e) concept of vertical racetrack storage array built on a chip for high density data storage (Reproduced from [27]).

The solid state memories (RAM) are fast but are volatile unlike the racetrack memory. On the other hand solid state FLASH memories are non-volatile but have a limited number of cell overwritings unlike racetrack memory in which information can be read or write for an unlimited number of times.

Chapter 2

Growth and characterization of epitaxial permalloy films

Permalloy (Py = $Fe_{20}Ni_{80}$) is an alloy with low anisotropy, very high magnetic permeability and significant magnetization ($\mu_0 M_S = 1T$). Py is in priniciple an interesting material for current-induced domain wall (DW) motion because of its soft magnetic properties. However, pinning of DWs was shown to be important as discussed in chapter 1. Most of the Py thin films so far studied are polycrystalline. The magnetic properties of these polycrystalline films are affected by the influence of grain boundaries. The aim of my work was to improve the crystalline quality of these films, by suppressing/reducing grain boundaries using epitaxial growth. Single crystalline epitaxial films with less structural defects, surface or interface roughness and small coercive field can reduce the DW pinning and hence increases the DW mobility. The additional advantage of these films is that, the improved crystalline quality may facilitate the understanding of fundamental physical phenomena.

Several techniques have been employed for thin film and multilayer growth. These include sputter deposition (SD), chemical vapor deposition (CVD), molecular beam epitaxy (MBE) and pulsed laser deposition (PLD). The latter has the capability to produce high quality thin films of various kinds of materials [21] and to preserve the stoichiometry of compound materials while being compatible with ultra high vacuum (UHV), unlike SD.

Single crystal fcc (100) and (110) Py films have been epitaxially grown on single crystal MgO(100) and MgO(110) substrates [51]. These Py films were deposited at 350 °C using MBE. The Py films were found almost strain relieved for a thickness above 5 nm. The Py (100) films showed very soft magnetic behaviour with a coercive field of ~ 0.15 mT, compared to about 0.6 mT for Py (110) films.

M.Ohtake et al. [99] have also reported fcc (110) single crystal and fcc (111) bicrystal epitaxial Py growth on MgO(110) and MgO(111) single crystal substrates at 300 °C using MBE. A large increase of coercive field was observed when films were grown at a higher temperature of 500 °C. The trenches between the Py islands due to high temperature growth may pin the domain walls resulting in an increase of the coercive field.

We studied the epitaxial growth by PLD under UHV and magnetic properties of fcc Py(111) single layers and Py(111)/Ir(111) bilayers on single crystal Al_2O_3(0001) (sapphire) substrates. Fcc(111) supermalloy (Su-Py) single layer and Su-Py(111)/Ir(111) bilayer films with negligible magnetostriction were also epitaxially grown on single crystal sapphire. We used two types of sapphire substrates with miscut angles of 0.25° and

0.05°. The notation Py/Ir denotes Py deposited on Ir. A similar notation will be used throughout the thesis to describe which is the bottom or top layer.

The alloy composition of Py is Fe 20% and Ni 80% and of supermalloy is Fe 15.5%, Ni 81.6% and Mo 2.8%. The base pressure of the UHV system is 3×10^{-11} torr. The substrate was degassed for 1 h, both in the analysis chamber at 500 °C and then in the deposition chamber at 660 °C, before initial deposition under UHV conditions for all samples. The temperature was measured by a thermocouple calibrated with an optical pyrometer. The deposition rate of Ir and Py films was 0.08 nm/min and 0.1 nm/min, respectively, for all the samples. The thicknesses were measured by a quartz microbalance calibrated using Rutherford back scattering.

The surface structure and epitaxial orientation of the films were determined in-situ by Reflection high energy electron diffraction (RHEED). The topography was measured in-situ by Scanning tunneling microscopy (STM). The magnetic properties were measured ex-situ by SQUID magnetometry, Kerr magnetometry and microscopy, Ferromagnetic resonance (FMR) and Transverse bias initial inverse susceptibility and torque (TBIIST) measurements.

2.1 Epitaxial growth of Py single layers

In sapphire(0001), the (0001) planes are hexagonal. The a-axis and c-axis lattice constants of this hexagonal plane are 0.4758 nm and 0.1299 nm respectively. The Py is a face-centered cubic transition metal with a bulk lattice constant of 0.355nm. Py(111) can be epitaxially grown on sapphire(0001) because Py(111) is also a hexagonal plane. The in-plane lattice constant of Py(111) is 0.434 nm with an in-plane lattice mismatch of about 8.78% with the a-axis lattice constant of sapphire(0001).

The nature of the interface between the thin film and substrate plays an important role on the subsequent film growth. The lattice mismatch between the elements of the film and the substrate and the bonding strength at the interface for corresponding planes decide whether the interface is coherent, semi-coherent or incoherent [40]. For a coherent interface, the lattice mismatch results into strain in the total film. For semi-coherent interfaces the lattice mismatch is compensated partially or fully by introducing misfit dislocations. This results into partially or fully relaxed films. For incoherent interfaces the dislocation core of the misfit dislocation is completely delocalized.

We deposited 5, 10 and 20 nm thick single Py layers directly on sapphire(0001) substrates with a miscut angle of 0.25° at room temperature (RT), and annealed them at 350°C for 30 minutes. During annealing, the RHEED patterns seemed to become two dimensional (2D) at about 250 °C, and they kept improving with further annealing until at 350 °C a very narrow streak pattern was obtained.

Fig. 2.1 (a-b) shows RHEED patterns along the [11-2] Py azimuth before and after annealing. The very fine RHEED streaks indicate 2D epitaxial Py on sapphire (0001). The in-plane epitaxial relationship between sapphire (0001) and Py determined by RHEED is Al_2O_3[11-20] // Py[11-2] and Al_2O_3[1-100] // Py[1-10]. The cubic in-plane lattice constant calculated from RHEED measurements for Py[1-10] and Py[11-2] are 0.354 and 0.353 nm which are in good agreement with the Py bulk value of 0.355 nm. This also shows that Py films are mostly strain relieved in this thickness range [32].

The STM images for 10 nm Py on sapphire with a miscut angle of 0.25 ° are shown in

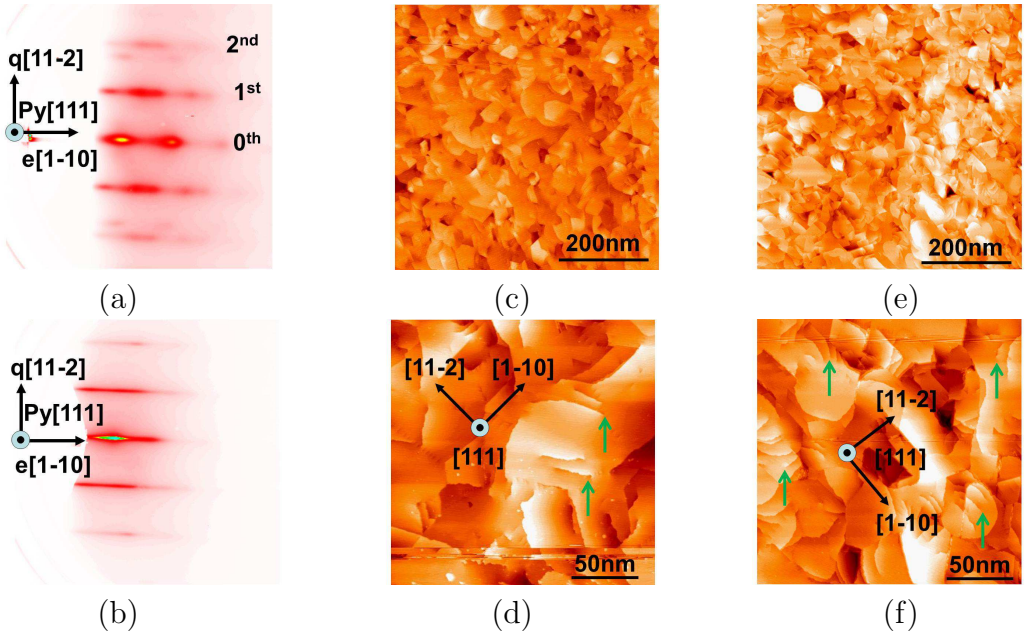

Figure 2.1: (a,b) RHEED patterns along the Py [11-2] azimuth, before and after annealing respectively. The STM images of Py 10 nm *on* Al_2O_3*(0001) with a miscut angle of (c,d) 0.25° (e,f) 0.05°, deposited at RT and annealed at* 350 °C. *The green arrows indicate the emerging screw dislocations.*

Sample thickness (nm)	Miscut angle (°)	Growth temperature (°C)	Average roughness (nm)	RMS roughness (nm)	Screw dislocation density ($/m^2$)
Py10	0.25	RT, anneal 350	0.086	0.113	$\sim 8 \times 10^{16}$
Py20	0.25	same	0.103	0.132	$\sim 1.3 \times 10^{17}$
Py10	0.05	RT, anneal 350	0.107	0.142	$\sim 2.3 \times 10^{17}$

Table 2.1.1: Summary of the epitaxial Py growth on Al_2O_3*(0001) with miscut angles of 0.25° and 0.05°.*

Fig. 2.1 (c-d). The Py surface is very flat with a high density of atomic steps. There are some emerging screw dislocations, with a density of about 8×10^{16} /m^2, in the 10nm thick Py layer, indicated by green arrows in the STM image. The density of screw dislocations increases slightly with an increase in the Py thickness. For Py 20 nm the density of screw dislocations is about 1.3×10^{17} /m^2.

The periodical misfit dislocations appear at the film/substrate interface due to the lattice mismatch between film and substrate. Fcc films are sensitive to screw dislocations due to the possibility of introducing stacking faults. These screw dislocations cause a residual roughness in the films. The average and root mean square (rms) roughness in 600 nm^2 for 10 nm Py is 0.086 and 0.103 nm and for 20 nm Py 0.103 and 0.132 nm respectively. The roughness slightly increases with an increase in the Py thickness. Removing screw dislocations requires bulk mobility, thus much higher temperatures. The absence of screw dislocations and epitaxial twins has been reported for epitaxial growth

of Mo(110) on sapphire(11-20) [31] and fcc Ir(111) on sapphire(0001) [20] by annealing at high temperature $\sim 800\,^{\circ}$C. For Py, this temperature is well above the curi temperature.

To study the effect of the vicinality of the sapphire substrate on the Py growth and its magnetic properties we also deposited Py on less vicinal sapphire with a miscut angle of 0.05°. The Py was deposited under the same conditions as before. The STM images in Fig. 2.1 (e,f) show the average and rms roughness for 10 nm Py films 0.107 and 0.142 nm respectively. This value of roughness is slightly higher than for those on sapphire with a miscut angle of 0.25°. The density of screw dislocations in this Py film $\sim 2.3 \times 10^{17}\,/\mathrm{m}^2$ is also almost double which can increase the residual roughness. It has been reported that use of vicinal substrate can favour the step-flow mode of crystal growth, resulting in more macro-steps during growth. This can reduce the dislocation density [41]. Table 2.1.1 summarises the Py growth on both sapphires with the miscut angles of 0.25° and 0.05°.

2.2 Epitaxial Py/Ir bilayer growth

In order to study the effect of an Oersted field on current induced domain wall motion in Py nanostripes, we also prepared epitaxial Py/Ir bilayers. The current passing through the Ir layer generates an Oersted field which can change the domain wall chirality, stability and mobility.

Before optimizing the Py growth on Ir, 9 nm of Ir was deposited on sapphire (0001) with a miscut angle of 0.25°. The bulk lattice parameter of Ir(111) is 0.384 nm and like Py(111), Ir(111) is also a hexagonal plane with an in-plane a-axis lattice constant of 0.470 nm. Therefore, Ir can be grown more easily on sapphire(0001) than Py due to the smaller lattice mismatch of 1.2% (compared to 8.78% for Py). The Ir was deposited according to the optimised procedure developed in our group for epitaxial Ir growth [20]. The Ir was grown at about 345 °C and annealed at 900 °C for 45 minutes. RHEED streaks [Fig. 2.2 (a)] indicate 2D epitaxial Ir(111). The in-plane epitaxial relationship between sapphire and Ir determined by RHEED is Al_2O_3[11-20] // Ir[11-2] and Al_2O_3[1-100] // Ir[1-10].

Fig. 2.2 (c) shows the STM image of a 9 nm Ir layer directly grown on sapphire. The image shows atomically flat Ir terraces whose width is limited by the miscut angle of the sapphire.

Subsequently, 5, 10 and 20 nm Py layers were deposited at RT on such Ir/sapphire surfaces and were annealed at 350 °C, like for Py directly on sapphire, to have a flat 2D surface. I could not perform RHEED and STM measurements on this sample, but the magnetic characterization shows a large increase of the coercive field, almost 5 times as large as for Py directly grown on similar sapphire with a miscut angle of 0.25°, at the same temperature.

A possible explanation is that, annealing the sample at a relatively high temperature of about 350 °C may leads to interdiffusion between Py and Ir at the interface. A second possibility may be the higher roughness of Py on Ir as compared to the Py directly grown on sapphire. The crystalline quality of Py/Ir can also be different from Py alone and result in an increase of the coercive field.

To know the origin of the enhancement of the Py/Ir coercive field, we deposited again 5, 10 and 20 nm Py films on atomically flat Ir/sapphire with a sapphire miscut angle of

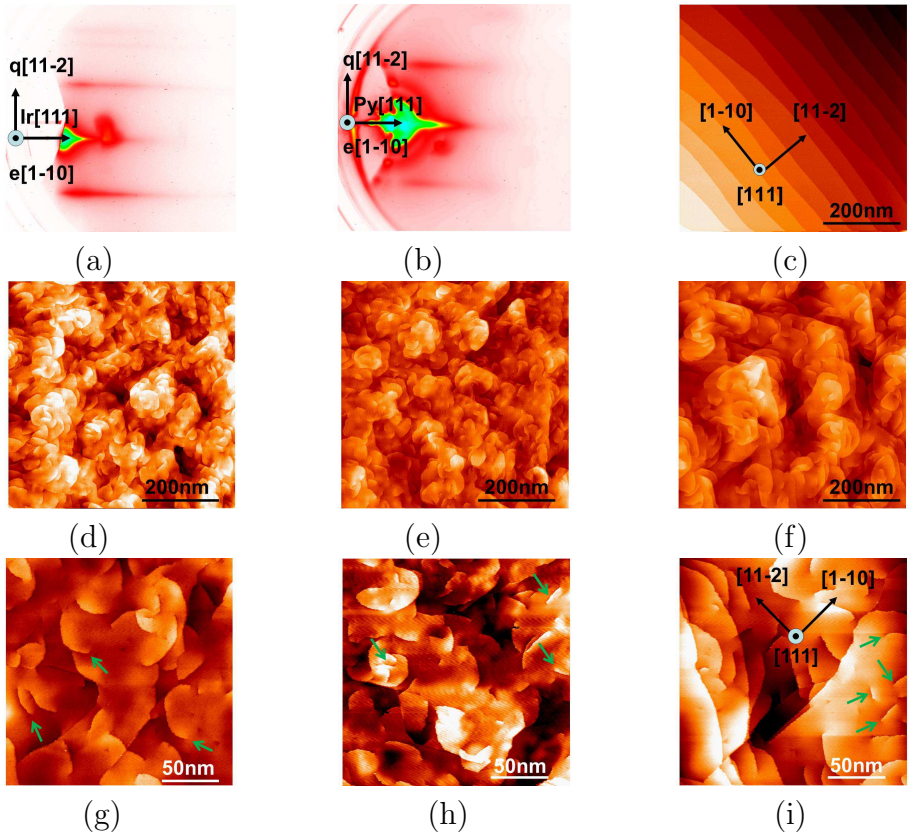

Figure 2.2: (a,b) RHEED patterns along Ir [11-2] and Py/Ir [11-2] azimuths, annealed and non-annealed respectively (c) STM image for Ir(9 nm)/Al_2O_3(0001) deposited at 345 °C and annealed at 900 °C and STM images of (d,g) Py 5 nm (e,h) Py 10 nm (f,i) Py 20 nm deposited on Ir(9 nm)/Al_2O_3(0001) at RT and annealed at 200 °C. The substrate is sapphire with a miscut angle of 0.25°. The green arrows indicate the emerging screw dislocations.

Sample thickness (nm)	Miscut angle (°)	Growth temperature (°C)	Average roughness (nm)	RMS roughness (nm)	Screw dislocation density ($/m^2$)
Ir9	0.25	345, anneal 900	Terraces	Terraces	No
Py5/Ir	0.25	RT, anneal 200	0.096	0.119	$\sim 1.3 \times 10^{17}$
Py10/Ir	0.25	same	0.112	0.139	same
Py20/Ir	0.05	same	0.151	0.192	same

Table 2.2.1: Summary of the epitaxial Ir and Py/Ir growth on Al_2O_3(0001) with a miscut angle of 0.25°.

0.25°. The Py was deposited at RT but annealed at 200 °C to avoid intermixing due to high temperature (350 °C) annealing. The RHEED streaks pattern [Fig. 2.2 (b)] shows 2D epitaxial Py on Ir/sapphire. The in-plane epitaxial relation determined by RHEED reveals that, as expected, the fcc lattices of Ir and Py adopt parallel directions with Al_2O_3[11-20] // Ir[11-2] // Py[11-2] and Al_2O_3[1-100] // Ir[1-10] // Py[1-10].

The STM images of Py 5, 10 and 20 nm are shown in Fig. 2.2 (d-i). Up to a thickness

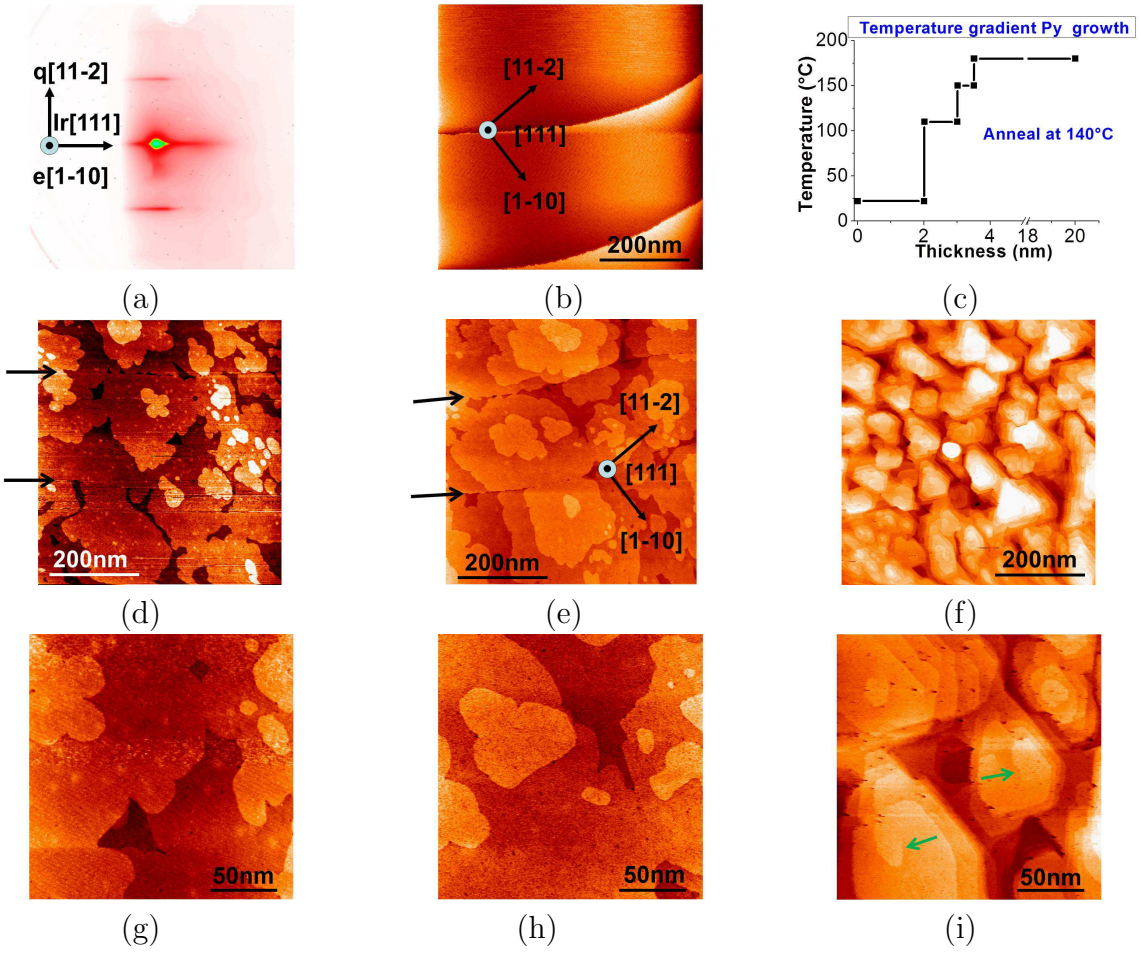

Figure 2.3: (a) RHEED pattern along the Ir [11-2] azimuth, (b) STM image of Ir(9 nm)/Al_2O_3(0001) deposited at 345 °C and annealed at 900 °C and STM images of (d,g) Py 5 nm, (e,h) Py 10 nm and (f,i) Py 20 nm deposited on Ir(9 nm)/Al_2O_3(0001), using a temperature gradient RT-180 °C and annealed at 140 °C. The sapphire miscut angle is 0.05°. The green arrows indicate the emerging screw dislocations.

Sample thickness (nm)	Miscut angle (°)	Growth temperature (°C)	Average roughness (nm)	RMS roughness (nm)	Screw dislocation density ($/m^2$)
Py5/Ir	0.25	Temp grad, RT-180 anneal 140	0.081	0.123	No
Py10/Ir	0.25	same	0.089	0.117	No
Py20/Ir	0.25	same	0.355	0.461	$\sim 1 \times 10^{16}$

Table 2.2.2: Summary of epitaxial Py/Ir growth on Al_2O_3(0001) with a miscut angle of 0.05° using a temperature gradient RT-180 °C and annealed at 140 °C.

of 10 nm, the surface is relatively flat containing few screw dislocations, but at higher thickness (20 nm) these images reveal mounds with their top not flat. The density of screw dislocations is $\sim 1.3 \times 10^{17}$ /m^2. This is slightly higher than for Py directly grown

on the same sapphire ($\sim 8 \times 10^{16}$ /m^2), for the same thickness. This could be due to a larger strain relaxation of Py grown on Ir instead of directly on sapphire, although Py on Ir was annealed at lower temperature (200 °C vs. 350 °C). The smaller lattice mismatch (7.66%) between Ir and Py, as compared to Py and sapphire (8.78%), can also cause more relaxation in Py films deposited on Ir.

The average and rms roughness in a 600 nm^2 image for Py 10 nm are 0.112 and 0.141 nm, while for Py 20 nm they are 0.151 and 0.192 nm, respectively. This increase in the roughness may be due to the annealing at lower temperature, 200 °C as compared to 350 °C for Py grown directly on sapphire. However, even at 350 °C we could not get rid of the residual roughness due to screw dislocations for Py on sapphire. The Ir and Py/Ir growth on sapphire with a miscut angle of 0.25° is summarised in table 2.2.1.

Since we obtained very small coercive fields for Py deposited on less vicinal sapphire, with a miscut angle of 0.05°, we continued optimizing Py growth on Ir on these substrates. The Ir was deposited using the optimised procedure explained above. RHEED streaks, shown in Fig. 2.3 (a), confirm the epitaxial 2D growth of the Ir layer. We get atomically flat 300 nm wide Ir terraces as shown in STM Fig. 2.3 (b). The larger size of the Ir terraces as compared to the previous Ir sample is in agreement with the smaller miscut angle of the sapphire substrate.

As shown above, deposition of Py on Ir/sapphire at RT and post annealing at 200 °C leads to a residual roughness that is higher than for Py films directly grown on sapphire under the same conditions. On the other hand, Py deposition at RT and annealing at a higher temperature of 350 °C results in a large coercive field. We therefore decided to grow Py using a temperature gradient. In the following, all Py/Ir bilayer samples were prepared on the less vicinal sapphire with a miscut angle of 0.05 °.

Py layers of thicknesses 5, 10 and 20 nm were deposited using a temperature gradient from RT to 180 °C on Ir/sapphire. Starting at RT, 2 nm Py was deposited, then 1 nm at 110 °C, 0.5 nm at 150 °C and the rest at 180 °C until the final thickness. Finally, the samples were annealed at 140 °C for 12 h as shown in Fig. 2.3 (c) schematically. Fig. 2.3 (d-i) shows STM images which reveal very flat Py surfaces with large terraces (300 nm wide for 5 and 10 nm of Py). However, there are grooves in the Py surface at the buried Ir steps, as indicated by green arrows in the STM images. The 20 nm Py films show mounds with a flat top surface together with few screw dislocations ($\sim 1 \times 10^{16}$ /m^2).

Using this temperature gradient thus allowed me to get rid of residual roughness due to screw dislocations, but induced grooves in the Py layer above buried Ir steps. These grooves at the steps indicate a very high mobility of the deposites adatoms. This suggests that the initial temperature for the growth should be lower, to decrease the adatoms mobility. On the other hand, for larger thickness ($\sim$ 20 nm) three-dimensional growth with mounds was observed [see Fig. 2.3 (f,i)], indicating that the final growth temperature should be higher to reduce the roughness. The average and rms roughness in the 600 nm^2 image for Py 10 nm are 0.089 and 0.117 nm and for Py 20 nm they are 0.354 and 0.460 nm, respectively. The table 2.2.2 gives the summary of the Py/Ir growth using a (RT-180 °C) temperature gradient.

To avoid the grooves in the Py surface at buried Ir steps Py was grown again on Ir/sapphire using a temperature gradient RT-300 °C. The temperature was raised slowly to reduce the mobility of the adatoms at Ir steps and the final temperature of 300 °C might help to reduce the roughness for the higher thickness. First 2 nm Py was grown at RT, then 1 nm at 60 °C, 1.5 nm at 110 °C, 1 nm at 160 °C, 1 nm at 220 °C and then until

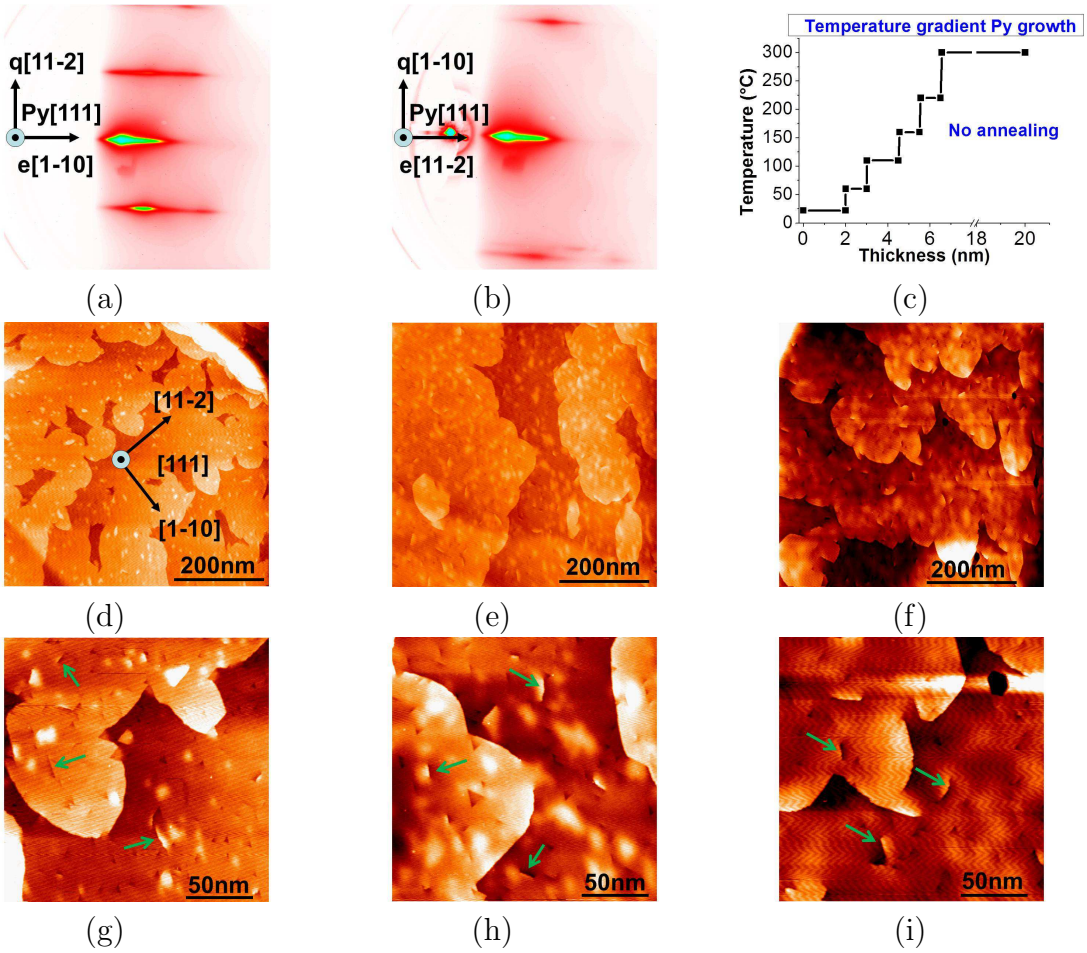

Figure 2.4: (a,b) RHEED patterns along the Py [11-2] and [1-10] azimuths, (c) Schematic of temperature gradient for Py growth and STM images for (d,g) Py 5 nm*, (e,h) Py* 10 nm *and (f,i) Py* 20 nm *deposited on Ir(*9 nm*)/Al_2O_3(0001) using the temperature gradient RT-*300 °C*, without annealing. The green arrows indicate screw dislocation loops.*

Sample thickness (nm)	Miscut angle (°)	Growth temperature (°C)	Average roughness (nm)	RMS roughness (nm)	Screw dislocation density ($/m^2$)
Py5/Ir	0.05	Temp grad, RT-300 No annealing	0.068	0.106	$\sim 8 \times 10^{16}$
Py10/Ir	0.05	same	0.062	0.078	same
Py20/Ir	0.05	same	0.068	0.092	same

*Table 2.2.3: Summary of the epitaxial Py/Ir growth on Al_2O_3(0001) using the temperature gradient RT-*300 °C*, without annealing.*

20 nm at 300 °C without annealing [Fig. 2.4(c)].

Fig. 2.4(a-b) shows very fine RHEED streaks showing epitaxial 2D Py. I got rid of the problem of Py growth at Ir steps but at the cost of emerging screw dislocation loops with a density of $\sim 8{\times}10^{16}/m^2$. The STM images show very flat Py surfaces with 300 nm

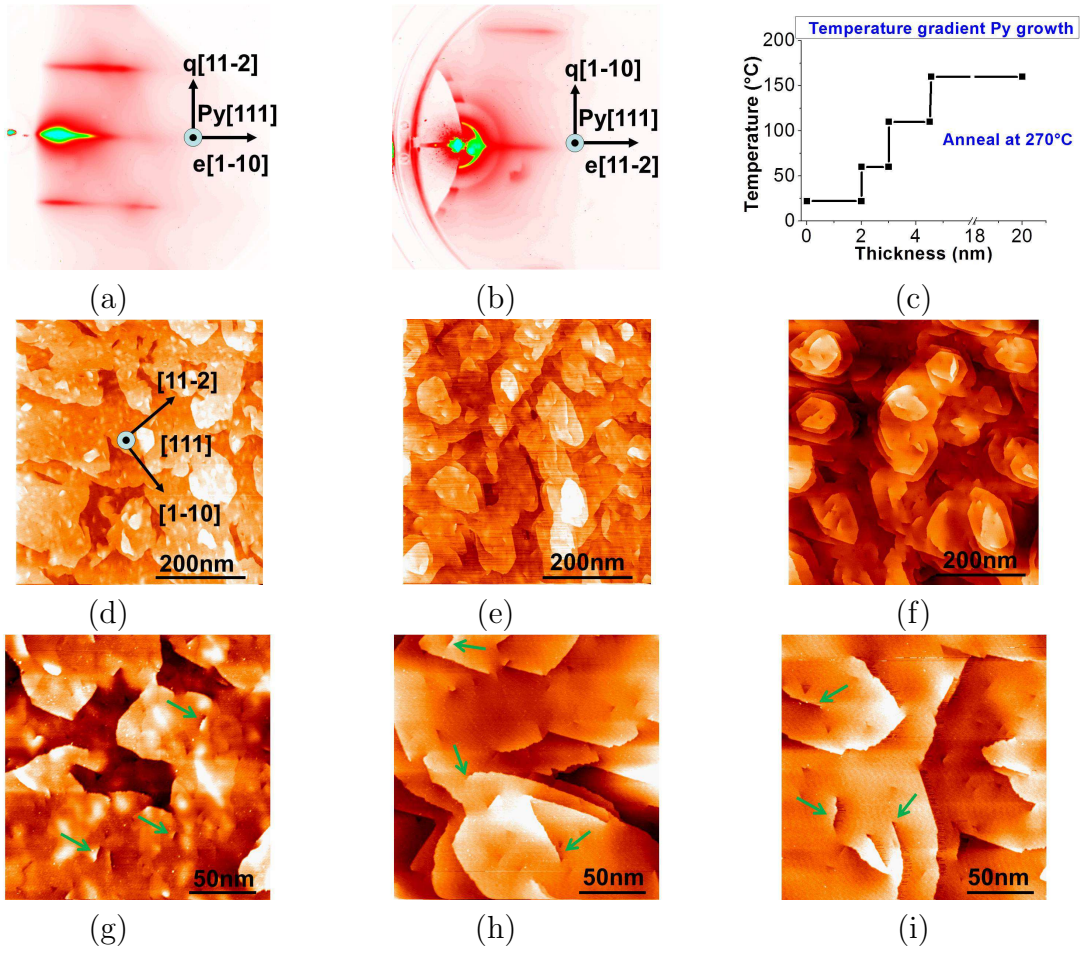

Figure 2.5: (a,b) RHEED patterns along the Py [11-2] and [1-10] azimuths, (c) Schematic of temperature gradient for Py growth and STM images (d,g) Py 5 nm*, (e,h) Py* 10 nm *and (f,i) Py* 20 nm *deposited on Ir(*9 nm*)/Al_2O_3(0001) using the temperature gradient RT-*160 °C *and annealed at* 270 °C*. The green arrows indicate screw dislocation loops.*

Sample thickness (nm)	Miscut angle (°)	Growth temperature (°C)	Average roughness (nm)	RMS roughness (nm)	Screw dislocation density (/m^2)
Py5/Ir	0.05	Temp grad, RT-160 anneal 270	0.069	0.090	$\sim 1.3 \times 10^{17}$
Py10/Ir	0.05	same	0.079	0.101	same
Py20/Ir	0.05	same	0.116	0.142	same

*Table 2.2.4: Summary of the epitaxial Py/Ir growth on Al_2O_3(0001) using a temperature gradient RT-*160 °C *and annealed at* 270 °C*.*

wide Py terraces as shown in Fig. 2.4(d-i). The average and rms roughness in a 600 nm^2 image for Py 5 nm are 0.068 and 0.106 nm and for Py 5 nm they are 0.062 and 0.078 nm respectively, which is even 29% less than for Py directly grown on sapphire. The Py/Ir growth using a (RT-300 °C) temperature gradient is summarised in table 2.2.3.

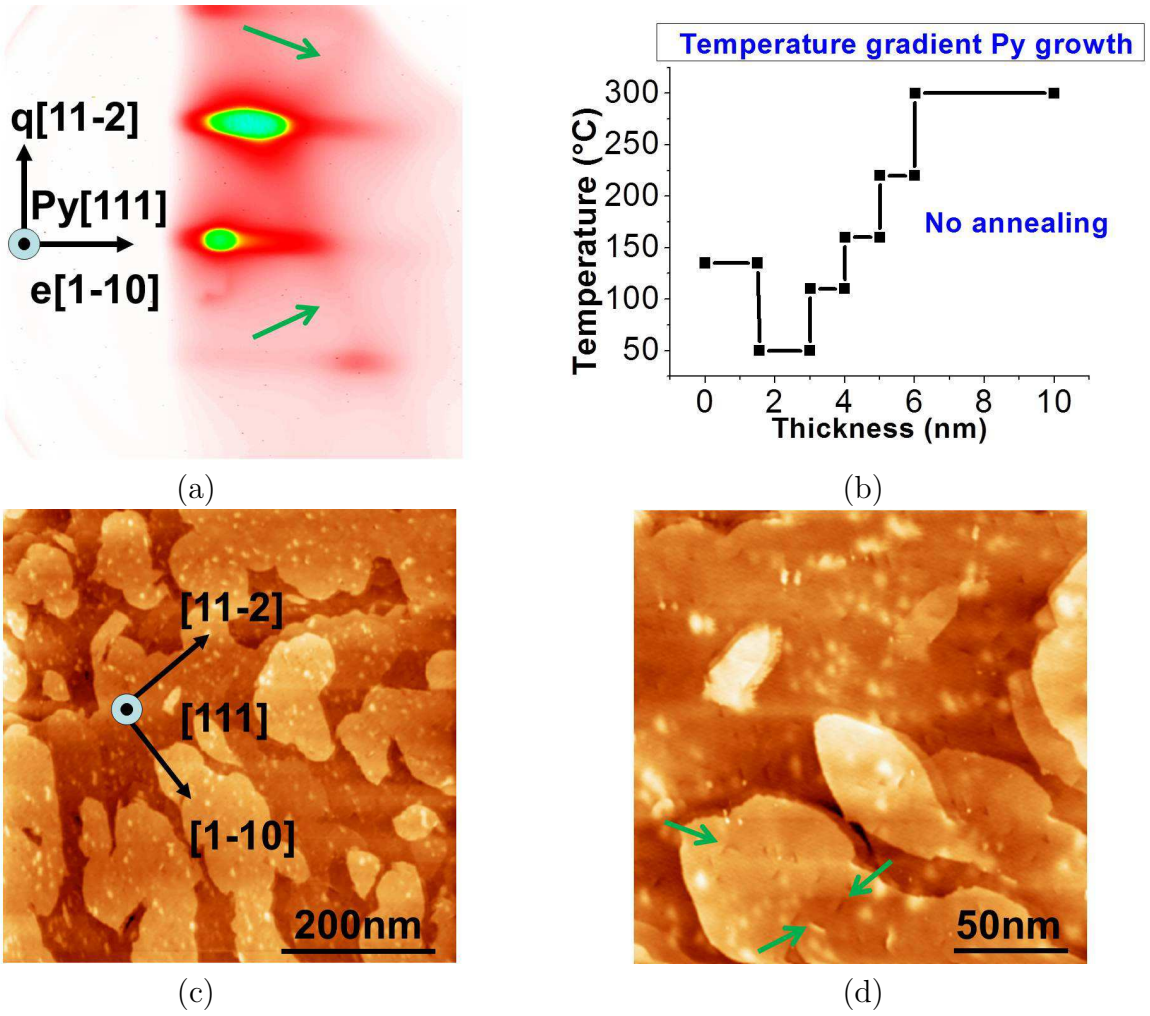

Figure 2.6: (a) RHEED patterns along the Py [11-2] azimuth, (b) Schematic of temperature gradient for the Py growth (c,d) STM image of Py 5 nm *deposited on Ir(*9 nm*)/Al_2O_3(0001) with a temperature gradient 50-*300 °C *without annealing. The green arrows show screw dislocation loops.*

Sample thickness (nm)	Miscut angle (°)	Growth temperature (°C)	Average roughness (nm)	RMS roughnes (nm)	Screw dislocation density (/m^2)
Py5/Ir	0.05	Temp grad 50-300 No annealing	0.073	0.090	$\sim 5\times10^{16}$
Py10/Ir	0.05	same	0.078	0.098	same

Table 2.2.5: Summary of epitaxial Py/Ir growth on Al_2O_3(0001) using a temperature gradient from 50 to 300° C without annealing.

A gradual rise of temperature up to 300 °C during growth, without annealing, results thus in the appearance of screw dislocation loops although the Py surface is very flat. Depositing Py at intermediate temperature using a temperature gradient and annealing

at higher temperature ($\sim 300\,^{\circ}$C) might help to dissociate these screw dislocations. We therefore deposited again Py on Ir/sapphire, using a temperature gradient RT-160 °C and followed by annealing at 270 °C.

First 2 nm Py was grown at RT, 1 nm at 60 °C, 1.5 nm at 110 °C and then until 20 nm at 160°C. Finally the sample was annealed at 270°C for 30 minutes [Fig. 2.5 (c)]. RHEED streaks in Fig. 2.5 (a-b) indicate 2D epitaxial Py. The terrace size reduced down to 100 to 150 nm, along with screw dislocations with a density of $\sim 1.3 \times 10^{17}$ /m^2, as shown in Fig. 2.5(d-i). The average and rms roughness in a 600 nm^2 image for Py 10 nm are 0.079 and 0.101 nm and for Py 20 nm they are 0.116 and 0.142 nm respectively. This value of roughness is almost the same as for Py grown directly on similar sapphire. The table 2.2.4 gives the summary of Py/Ir growth using a (RT-300 °C) temperature gradient.

Both procedures, gradually increasing the temperature during growth to 300 °C without annealing or depositing using a lower temperature gradient and post annealing at 270 °C, could not reduce the density of screw dislocations. This indicates that the screw dislocations are introduced in the very beginning of the Py growth due to the lattice mismatch with the substrate. We therefore decided to start the Py growth at temperature higher than RT to decrease the initial roughness and strain. The rather high final temperature of 300 °C can reduce the Py roughness and lead to better strain relaxation, resulting in a layer by layer growth as described below.

Py growth was started at 135 °C with 1.5 nm, then Py deposition was stopped for ten minutes to cool down the sample. After ten minutes the Py deposition was again started with a deposition of 1.5 nm at 50 °C, then 1 nm at 110 °C, 1 nm at 160 °C, 1 nm at 220 °C and finally up to 10 nm at 300 °C, without annealing at the end as shown in Fig. 2.6 (b) schematically. The RHEED streaks reveal 2D epitaxial Py as shown in Fig. 2.6 (a). The green arrows on the RHEED patterns indicate the kikuchi lines, which are further evidences of the good quality of the surface.

The STM image for Py 5 nm, with 150 to 200 nm wide terraces together with screw dislocation loops at a density of $\sim 5 \times 10^{16}$ /m^2, is shown in Fig. 2.6 (c,d). The screw dislocations loops are highlighted by green arrows. The average and rms roughness in the 600 nm^2 image for Py 5 nm are 0.047 and 0.056 nm, respectively, which is less than for Py directly grown on sapphire and all the previous Py/Ir samples. The good Py surface quality, as compared to the previous samples, made us chose this process as the final optimised process for the Py/Ir growth. This process using a (50-300 °C) temperature gradient for Py growth is summarised in table 2.2.5.

A texture analysis using XRD was carried out to study the crystalline structure of the optimised Ir and Py films. The θ-2θ scan [Fig. 2.7 (a)] shows that both Ir and Py films are fcc (111) textured. The XRD pole figure [Fig. 2.7 (b)] shows six-fold Ir and Py symmetry around fcc(111). The six-fold symmetry instead of the three-fold for fcc(111) films is the evidence of two epitaxial twins rotated by 180 °C around [111] in both Ir and Py films.

Fig. 2.8 (a-d) shows the XRD texture peaks and peak line profiles along the Ir(200) and Py(200) directions respectively. The Bragg diffraction angles show that both Ir and Py are (111) textured. The sharp and identical high intensity peaks show the good epitaxy of the Ir and Py films on sapphire(0001). The texture line profiles show the spread of $\sim 1^{\circ}$ at full width half maximum of the profile peak. Moreover, this spread is almost the same for Ir and Py, which indicates that there is no degradation of the epitaxy of Py films on Ir/sapphire.

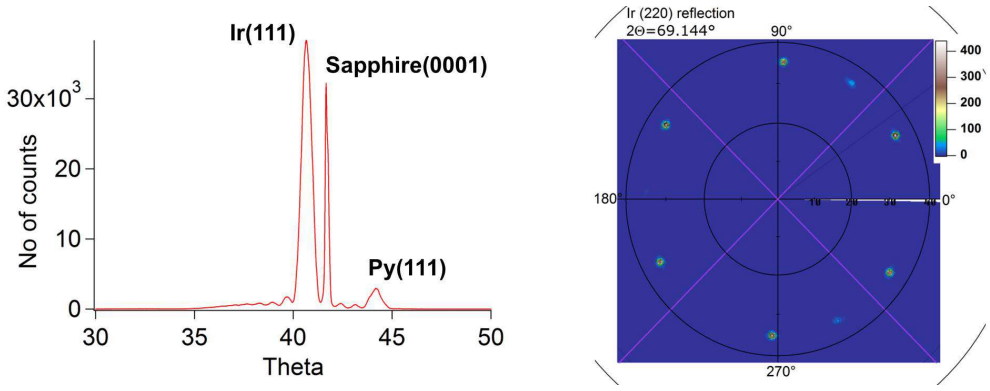

(a) (b)

Figure 2.7: XRD (a) θ-2θ scan (b) Pole figure Ir(220) reflection of Au(2nm)/Py(10nm)/Ir(10nm)/Al_2O_3(0001) epitaxial film.

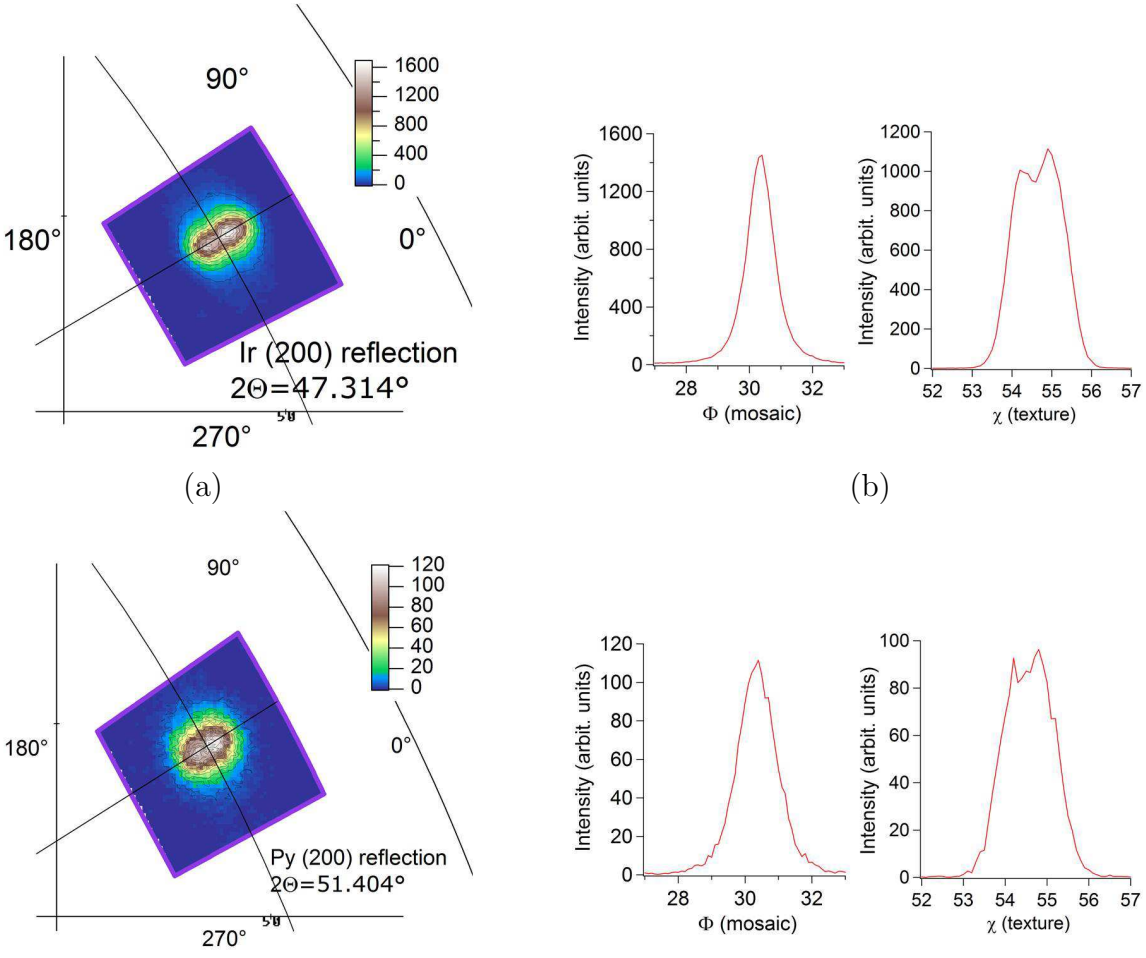

(a) (b)

(c) (d)

Figure 2.8: XRD texture (a,b) Ir(200) reflection (c,d) Py(200) reflection of Au(2nm)/Py(10nm)/Ir(10nm)/Al_2O_3(0001) epitaxial film.

In conclusion, we studied the epitaxial Py growth on sapphire (0001)and Ir/Sapphire with the sapphire miscut angles 0.25° and 0.05° as a function of temperature. We prepared very flat, epitaxial Py single and Py/Ir bilayer films. The Py films on sapphire were deposited at RT and annealed at 350 °C. The minimum temperature required to have a 2D Py surface is 300 °C. The 2D Py films on sapphire with a miscut angle of 0.25° reveal a high density of atomic steps together with a density of screw dislocations of $\sim 8 \times 10^{16}$ /m^2. The Py films on less vicinal sapphire with a miscut angle of 0.05° show a lower density of atomic steps, but a larger density of screw dislocations ($\sim 2.3 \times 10^{17}$ /m^2). The rms roughness for 10 nm Py films is $\sim$ 0.1 nm.

The Py films on atomically flat epitaxial Ir/sapphire were prepared using different temperature gradients. The temperature gradient RT-180 °C results into flat Py terraces. However, the high mobility of the adatoms at the Ir steps due to the fast increase of temperature results in grooves above the buried Ir steps and 3D mounds for higher thickness. A slower increase of temperature from RT to 300 °C eliminates grooves and results into flat terraces, but introduces screw dislocation loops. The deposition of Py using a slow increase of temperature during growth up to 160 °C, followed by annealing at 270 °C, reduces the terrace size and induces screw dislocations with almost the same density as for Py directly grown on sapphire.

Finally, the best growth process was to start the Py deposition at a temperature of 135 °C instead of RT, and ending at 300 °C using a slow rise of temperature. This gives us very flat Py surfaces with 150 to 200 nm wide terraces, together with only a small number of screw dislocation loops. The higher temperature at the beginning of the growth can reduce the initial roughness by strain relaxation, resulting in a layer by layer growth, while the rather high final temperature can decrease the roughness for larger thicknesses.

2.3 Epitaxial Su-Py and Su-Py/Ir bilayers growth

Thin films with non-zero magnetostriction, like Py, can induce magneto-elastic anisotropy. In magnetic nanostripes, the magnetization is along stripe direction due to shape anisotropy. The magneto-elastic anisotropy can result into local variation of the magnetization direction in nanostripes. This can effect the DW motion. The increase of DW velocity by decreasing magneto-elastic energy has been observed in CoFeNiSiB and CoFeSiB microwires, with different composition [150][108]. The adjustment of the film composition seems necessary to minimize magnetostriction. That's why we also prepared supermalloy (Su-Py) films with negligible magnetostriction to avoid magneto-elastic anisotropy.

Epitaxial fcc(111) Su-Py and Su-Py/Ir bilayers were grown on sapphire (0001) with the small miscut angle of 0.05°. Like Py, the 5, 10 and 20 nm Su-Py films were deposited directly on sapphire at RT and annealed at 350 °C for 30 minutes. Fig. 2.9 (a) shows RHEED pattern along the Su-Py [-1-12] azimuth. Very narrow RHEED streaks pattern indicate 2D epitaxial Su-Py films. The in-plane epitaxial relationship between sapphire (0001) and Su-Py determined by RHEED is Al_2O_3[11-20] // Su-Py[-1-12] and Al_2O_3[1-100] // Su-Py[1-10].

Fig. 2.9 (b) shows the AFM image of Su-Py directly grown on sapphire. The average and rms roughness in 2 µm image for Su-Py 10 nm are 0.147 and 0.194 nm respectively. The AFM was made ex-situ just after removing the sample from the deposition chamber.

Like Py/Ir bilayers, Su-Py/Ir bilayers were also prepared to study the effect of an

Oersted field on current induced domain wall motion. The 5, 10 and 15 nm Su-Py films on Ir/sapphire were grown using a temperature gradient 50-300 °C, according to the final optimised procedure for Py growth on Ir/sapphire. The schematic representation of growth procedure is shown in Fig. 2.9 (c)

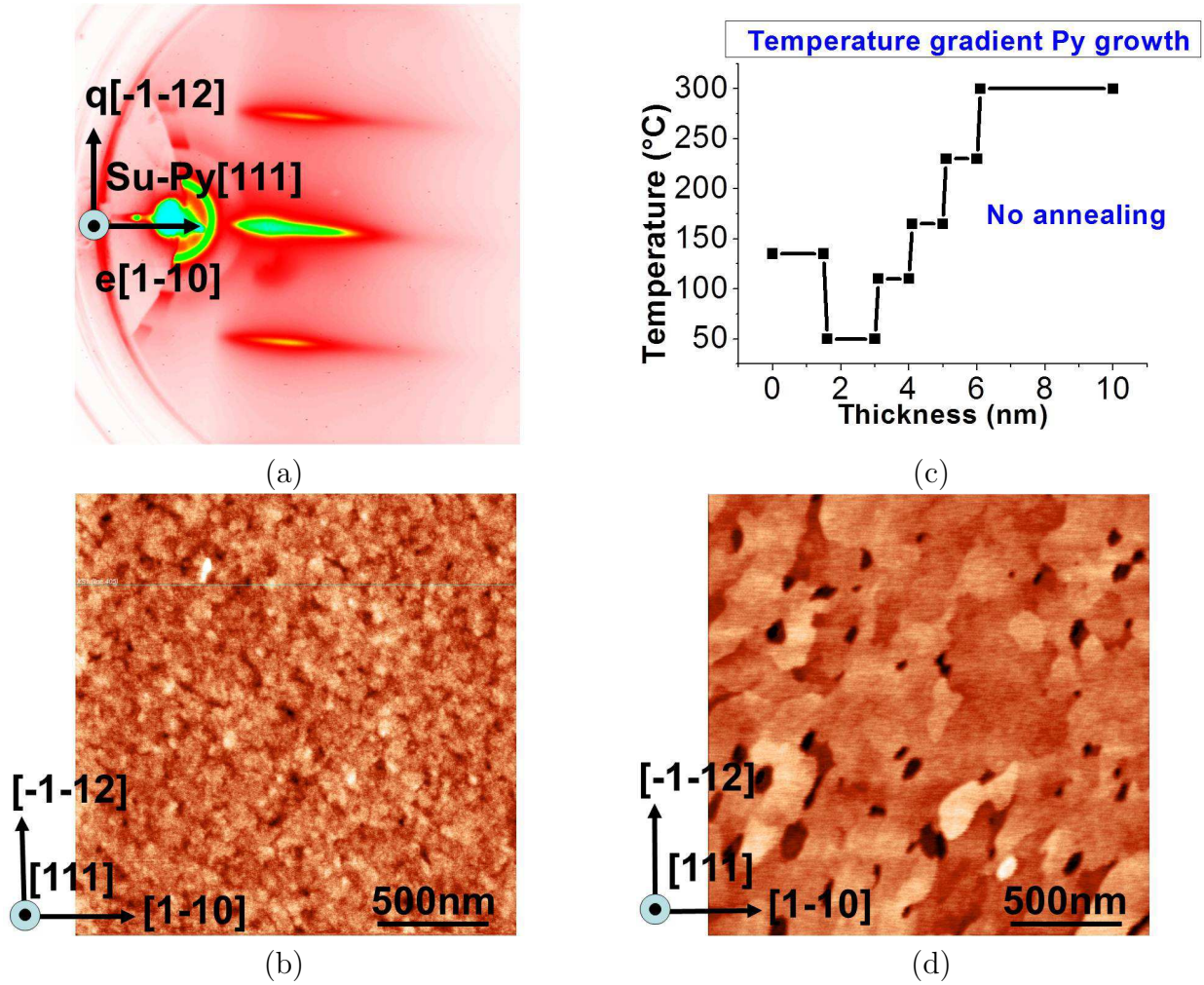

Figure 2.9: ZI31 (a) RHEED streaks pattern along the Su-Py [-1-12] azimuth deposited on $Al_2O_3(0001)$ with a miscut angle of 0.05°. Atomic force microscopy images (b) Su-Py(10 nm)/$Al_2O_3(0001)$ deposited at RT and annealed at 350 °C and (d) Su-Py(15 nm)/Ir(10 nm)/$Al_2O_3(0001)$ deposited using a temperature gradient 50-300 °C, without annealing. (c) Schematic of temperature gradient for the Su-Py/Ir growth.

The Ir was deposited on sapphire according to the optimised procedure as described above. The Su-Py growth was started at intermediate temperature 135 °C until 1.5 nm, then stopped for ten minutes to cool down the sample. After ten minutes the deposition was restarted growing 1.5 nm at 50 °C, then 1 nm at 110 °C, 1 nm at 165 °C, 1 nm at 230 °C and finally until 15 nm at 300 °C, without annealing at the end.

Fig. 2.9 (d) shows the AFM image of 15 nm thick Su-Py grown on Ir/sapphire. The AFM was performed ex-situ under ambient conditions just after removing the sample from the UHV chamber. The average and rms roughness in the 2 µm image for Su-Py 15 nm are 0.240 and 0.307 nm, respectively, which is slightly higher than for Su-Py 10 nm

Sample thickness (nm)	Miscut angle (°)	Growth temperature (°C)	Average roughness (nm)	RMS roughness (nm)	Screw dislocation density ($/m^2$)
Su-Py10	0.05	RT,anneal 350	0.147	0.194	No high resolution
Su-Py15/Ir	0.05	Temp grad 50-300 No annealing	0.240	0.307	No high resolution

Table 2.3.1: Summary of epitaxial Su-Py and Su-Py/Ir growth on Al_2O_3(0001) with a miscut angle of 0.05 °

Sample thickness (nm)	Miscut angle (°)	Growth temperature (°C)	Terrace width (nm)	RMS roughness (nm)	Screw dislocation density ($/m^2$)
Py10	0.25	RT, anneal 350	High step density	0.113	$\sim 8\times10^{16}$
Py10	0.05	RT,anneal 350	Low step density	0.142	$\sim 2.3\times10^{17}$
Py10/Ir	0.25	RT, anneal 200	High step density	0.141	$\sim 1.3\times10^{17}$
Py10/Ir	0.05	Temp grad, RT-180 anneal 140	200-300	0.117	$\sim 1\times10^{16}$
Py10/Ir	0.05	Temp grad, RT-300 No annealing	200-300	0.078	$\sim 8\times10^{16}$
Py10/Ir	0.05	Temp grad, RT-160 anneal 270	100-200	0.101	$\sim 1.3\times10^{17}$
Py10/Ir	0.05	Temp grad, 50-300 No annealing	150-200	0.098	$\sim 5\times10^{16}$
Su-Py10	0.05	RT, anneal 350	Low step density	0.194	$\sim 1.3\times10^{17}$
Su-Py15/Ir	0.05	Temp grad, 50-300 No annealing	150-200	0.307	$\sim 2.3\times10^{17}$

Table 2.3.2: Summary of epitaxial Py, Su-Py and Py/Ir, Su-Py/Ir growth on Al_2O_3(0001) with miscut angles 0.25° and 0.05°.

directly grown on sapphire due to the higher thickness. The epitaxial Su-Py and Su-Py/Ir growth is summarised in table 2.3.1.

In conclusion, we prepared very flat epitaxial Su-Py and Su-Py/Ir bilayer films on sapphire(0001). Table 2.3.2 provides the summary of the epitaxial growth of all Py and Su-Py samples deposited on sapphire with miscut angles of both 0.25° and 0.05°.

2.4 Coercivity of Py single and Py/Ir bilayers

In epitaxial magnetic films, the magnetic properties strongly depend on the orientation and the substrate temperature during growth [98]. Different studies have been performed for epitaxial growth of Py thin films on different substrates with different orientations and temperatures. Small coercive fields of 0.15 and 0.6 mT, measured at 10 K, have been reported for single crystal epitaxial fcc(100) and fcc(110) Py 25 nm films respectively. The films were grown on single crystal MgO(100) and MgO(110) substrates at 350 °C using MBE [51].

We have measured the coercivity of fcc(111) Py single and Py(111)/Ir(111) bilayer films of thicknesses 5, 10 and 20 nm, described in the previous sections. The longitudinal magneto-optical Kerr effect (MOKE) was used to measure the coercivity of these layers. The MOKE hysteresis loops for different in plane directions were measured at RT and 11 Hz frequency for all samples.

Py single layers

Fig. 2.10 (a,b) shows the MOKE hysteresis loops along the easy axis direction, related to the step direction (will be discussed later) for Py 10 nm deposited directly on sapphire (0001) with miscut angles of 0.25° and 0.05° respectively, using the optimised growth process. Fig. 2.10 (a) shows a coercive field of 0.5 mT along the easy axis for Py 10 nm deposited on sapphire with a miscut angle of 0.25°. The 5 and 20 nm Py films (not shown here) showed similar behaviour with almost the same coercive field. The Py films deposited on the less vicinal substrate with a miscut angle of 0.05° show a smaller coercive field 0.1mT, as shown in Fig. 2.10 (b). This coercive field is smaller than the one of 0.15 mT reported in the literature for epitaxial single crystal films on a MgO(100) substrate[51]. The coercive field is even slightly smaller ($\sim$ 0.08 mT) for Py 5 nm. In addition, this coercive field is almost 5 times smaller than for Py grown on more vicinal sapphire with the miscut angle of 0.25°. Interestingly, the difference of substrate miscut angle is also a factor 5.

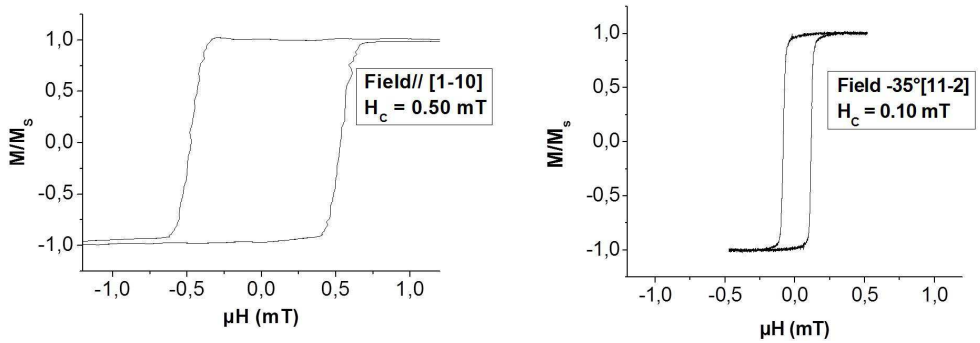

Figure 2.10: Longitudional MOKE loops along the easy axis for Au(2nm)/Py(10nm)/Al_2O_3(0001) deposited at RT and annealed at 350 °C *with two different substrate miscut angles (a) 0.25° (b) 0.05°.*

Sample thickness (nm)	Miscut angle (°)	Growth temperature (°C)	RMS roughness (nm)	Coercive field (mT)
Py5	0.25	RT, anneal 350	-	0.47
Py10	0.25	same	0.113	0.50
Py20	0.25	same	0.132	0.53
Py5	0.05	RT, anneal 350	0.151	0.08
Py10	0.05	same	0.142	0.1

Table 2.4.1: Summary of Py coercivity deposited on $Al_2O_3(0001)$ with miscut angles 0.25° and 0.05°.

As both Py films were prepared using the same growth procedure and the only difference is the miscut angle of the substrate, this reveals that the vicinality of the substrate plays an important role in the magnetic properties of Py films. One possible origin of the difference in coercive field can be a difference in strain: the more vicinal substrate can cause more step induced strain in the Py films than the less vicinal. Another reason could be a difference in surface roughness, but we observed that the value of the residual roughness in Py films on less vicinal sapphire is about 20% higher than on more vicinal sapphire. This would mean that an increase in roughness would induce a decrease in coercive field, which is unlikely here.

I will show in the next section that both films exhibit a weak step induced uniaxial anisotropy. The Py films on sapphire with a miscut angle of 0.25° show an anisotropy that is about three times larger than for Py on sapphire with a miscut angle of 0.05°. This increase of anisotropy may result in an increase of the coercive field. The Py coercivity measurements are summarised in the table 2.4.1.

Py/Ir bilayers

I also measured the coercive fields of the Py/Ir bilayers. Fig. 2.11 shows longitudinal MOKE hysteresis loops along the easy axis for Py/Ir bilayers deposited at different temperatures.

Fig. 2.11 (a) reveals a large coercive field of 2.4 mT for Py 10 nm deposited at RT and annealed at 350 °C on Ir/sapphire with the sapphire miscut angle 0.25°. The coercive field increases with an increase in Py thickness and hence in roughness (not shown here). For Py 5 and 20 nm the coercive fields are 1.6 and 3.0 mT. The coercive field of 2.4 mT for the Py10 nm/Ir bilayer is almost 5 times larger than for single layer Py 10 nm grown directly on similar sapphire at the same temperature. This large increase in coercive field is may be due to the inter-diffusion of Ir with Fe or Ni during annealing at 350 °C.

Fig. 2.11 (b) shows MOKE hysteresis loop along the easy axis for Py/Ir layer deposited on less vicinal sapphire with a miscut angle of 0.05°, using temperature gradient RT-150 °C without annealing. The coercive field of 0.4 mT is about 6 times lower than for Py/Ir deposited on more vicinal sapphire of miscut angle 0.25°.

Keeping in mind the effect of vicinality of sapphire on coercive field we further optimised the Py/Ir bilayer growth only on less vicinal sapphire with the miscut angle 0.05° to have further low coercive field, using different temperature gradients. Fig. 2.11 (c) shows

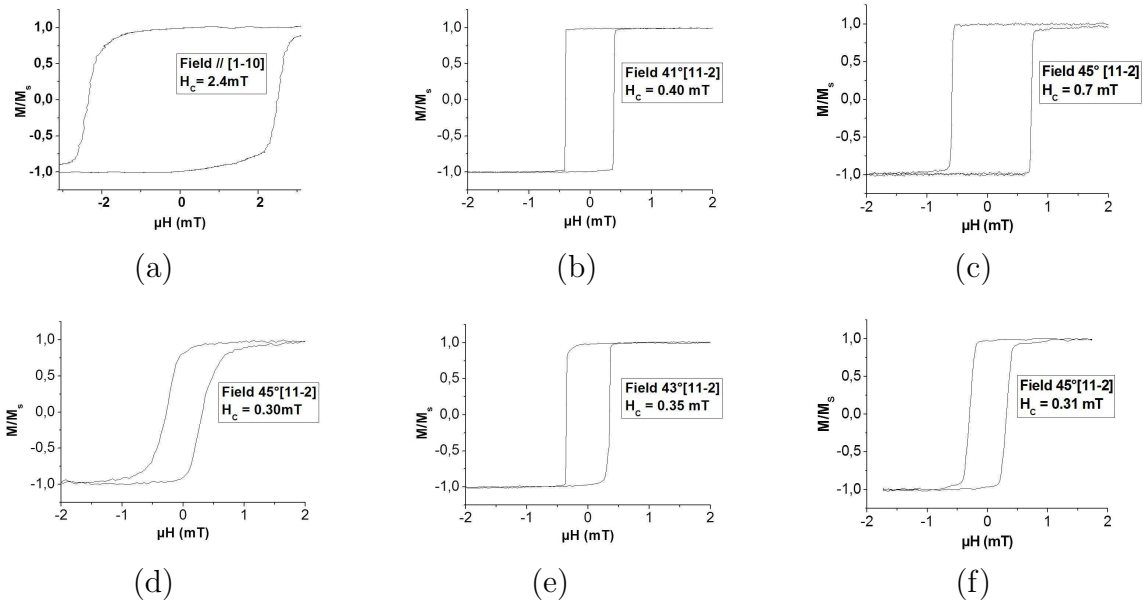

*Figure 2.11: Longitudinal MOKE loops along the easy axis for Au(*2 nm*)/Py(*10 nm*)/Ir(*9 nm*)/Al*$_2$*O*$_3$*(0001) with Py deposited at different temperatures (a) RT and annealed at* 350 °C *(b) Temperature gradient RT-*150 °C*, without annealing (c) Temperature gradient RT-*180 °C *and annealed at* 140 °C *(d) Temperature gradient RT-*300 °C *without annealing (e) Temperature gradient RT-*160 °C *and annealed at* 270 °C *(f) Temperature gradient 50-*300 °C*, without annealing, on two different sapphires with miscut angles (a) 0.25° and (b to f) 0.05°.*

MOKE hysteresis loop along easy axis for Py deposited using temperature gradient from RT to 180 °C and annealed at 140 °C. The coercive field is even higher (0.7 mT) than for previous sample (0.4 mT). This can be due to the grooves observed at the buried Ir steps in the Py layer topography of this sample, which can pin the DW resulting higher coercive field. The large value of the coercive field, observed for Py 20 nm (1.3 mT) is consistent with the Py topography with four times higher roughness for Py 20 nm than for Py 5 and 10 nm.

To address this issue of high coercive field due to Py grooves at Ir steps we deposited Py on Ir/sapphire using temperature gradient from RT to 300 °C without annealing. This results into a small coercive field (0.30 mT) along the easy axis for Py 10 nm as shown in Fig. 2.11 (d). The value of the coercive field for Py 5 and 20 nm is 0.26 and 0.29 mT respectively. Almost the same value of coercive field for all Py thicknesses 5, 10 and 20 nm is justified with Py topography which shows almost the same small roughness for all Py thicknesses.

Fig. 2.11 (e) shows MOKE hysteresis loops along the easy axis for Py deposited on Ir/sapphire using temperature gradient RT-160 °C and annealing at $\sim$ 270 °C. This gives a coercive field of 0.35 mT even slightly higher than for the previous sample (0.30 mT), may be due to the slightly higher residual roughness observed as compared to the previous sample.

The MOKE hysteresis loop along the easy axis direction for the final optimised sample deposited using temperature gradient 135-300 °C, shows a small coercive field (0.31 mT) as

Sample thickness (nm) (nm)	Miscut angle (°)	Growth temperature (°C)	RMS roughness (nm)	Coercive. field (mT) (mT)
Py5	0.25	RT, anneal 350	No STM	1.8
Py10	0.25	same	same	2.4
Py20	0.25	same	same	3.0
Py5/Ir	0.05	Temp grad RT-150 no anneal	No STM	0.4
Py10/Ir	0.05	same	same	0.4
Py20/Ir	0.05	same	same	0.5
Py5/Ir	0.05	Temp grad RT-180 anneal 140	0.123	0.7
Py10/Ir	0.05	same	0.117	0.7
Py20/Ir	0.05	same	0.461	1.3
Py5/Ir	0.05	Temp grad RT-300 no annealing	0.106	0.26
Py10/Ir	0.05	same	0.078	0.24
Py20/Ir	0.05	same		0.50
Py5/Ir	0.05	Temp grad RT-160 anneal 270	0.090	0.29
Py10/Ir	0.05	same	0.101	0.35
Py20/Ir	0.05	same		0.38
Py5/Ir	0.05	Temp grad 50-300 No annealing	0.090	0.31
Py10/Ir	0.05	same	0.098	0.30

Table 2.4.2: Summary of coercive fields of epitaxial Py/Ir deposited on $Al_2O_3(0001)$.

shown in Fig. 2.11 (f). This is consistent with the sample's topography with a very smooth surface and a small density of dislocation loops as compared to the previous samples. However, this value of the coercive field is still about 3 times higher than for single Py (0.1 mT) directly deposited on similar sapphire. The Py/Ir coercivity measurements are summarised in table 2.4.2.

In conclusion, both Py single and Py/Ir bilayer films deposited on more vicinal sapphire with the miscut angle 0.25° exhibits 5 or 8 times higher coercive fields respectively than deposited on the sapphire with miscut angle 0.05°. Secondly, the higher coercive field for Py/Ir films (0.3 mT) as compared to single Py films on similar sapphire can be related to the different roughness and strain induced uniaxial anisotropy (will be explained in next section 2.5) in Py single and Py/Ir bilayers.

2.5 Anisotropy of Py single and Py/Ir bilayers

The cubic (111) epitaxial metallic films exhibit three-fold symmetry of the [1-10] and [11-2] directions in the (111) plane. Magnetic cubic (111) films show no magneto-crystalline anisotropy and should have the same magnetic behaviour along the [1-10] and [11-2] di-

rections. However, there exist some other types of magnetic anisotropies in magnetic thin films like shape anisotropy, strain induced anisotropy and surface or interface anisotropy [30].

The strain induced uniaxial anisotropy has been observed in sputtered bi-epitaxial 200 nm thick Py (111) films deposited onto epitaxial Nb(110) with and without Cu(111) buffer layer on hcp-sapphire (11-20) [76]. A two times higher magnetic anisotropy was found in Py films directly grown on Nb as compared to deposited on Nb with Cu as a buffer layer. The difference of anisotropy strength was related to the strain relaxation in the 20 nm thick Cu buffer layer between Nb and Py. They suggested that the uniaxial strain due to the lattice mismatch between Py and Nb is responsible for the uniaxial anisotropy.

The change of local symmetry of step atoms as compared to the surface atoms can induced magnetic step anisotropy. The anisotropy energies per step atom are of the same order of magnitude as the magnetic energies per surface atom [1]. We studied the step induced magnetic anisotropy of the epitaxial fcc(111) Py and Py/Ir bilayer films deposited on sapphire(0001) with low (miscut angle 0.05°) and high (miscut angle 0.25°) density of atomic steps with atomically flat terraces. Longitudinal MOKE was used to study the anisotropy. The hysteresis loops were measured along different in plane directions at RT and 11 Hz frequency.

Py single layers

Figs. 2.13(a-c) show the longitudinal MOKE hysteresis loops along different in-plane directions for Py 10 nm on sapphire(0001) with a miscut angle of 0.25 °. The hysteresis loops reveal a weak uniaxial magnetic anisotropy with a slightly easier axis along the [1-10] azimuth, although we expect three or six-fold symmetry due to two epitaxial twins rotated by 180 ° around the [111] direction in our fcc(111) Py films. The Py 5 and 20 nm films show the same behaviour with an easy axis along the [1-10] azimuth.

To determine precisely the strength of the uniaxial anisotropy and the direction of the easy axis we applied the technique of Transverse bias initial inverse susceptibility and torque (TBIIST) under constant transverse bias field using a longitudinal MOKE setup [14] as shown in Fig. 2.12. The measurements were performed by Dominique Berling at Mulhouse.

The Py thin films are subject to two mutually orthogonal fields, the longitudinal sweep field H_L and a transverse static bias field H_B. The static bias field should be large enough so that Py is uniformly magnetized and displays no hysteresis, always remaining in the direction with the minimum energy. The magnetization component m_L versus H_L in terms of M_S is measured around $m_L = 0$. This gives two quantities χ^{-1} and ΔH related to the 1st and 2nd angular derivative of E_a respectively. This in turns gives two determinations of magnetic anisotropy energy $E_a(\theta)$ from χ^{-1} and ΔH respectively. A Fourier analysis then resolves the different symmetries of magnetic anisotropy.

We first studied the 5 and 10 nm Py thin films deposited on sapphire with a miscut angle of 0.25°. Fig. 2.13(d) shows the TBIIST measurements for the Py 10 nm thin film. It can be seen that both χ^{-1} and ΔH show prominent oscillations congruent with a uniaxial two-fold symmetry. The maxima and minima of the χ^{-1} plot versus in-plane polar angle θ correspond to the hard 17° ± 7° and easy axes -73° ± 7° of the fcc(111) Py film respectively. The Kerr reference axis is taken along the [11-2] azimuth. The

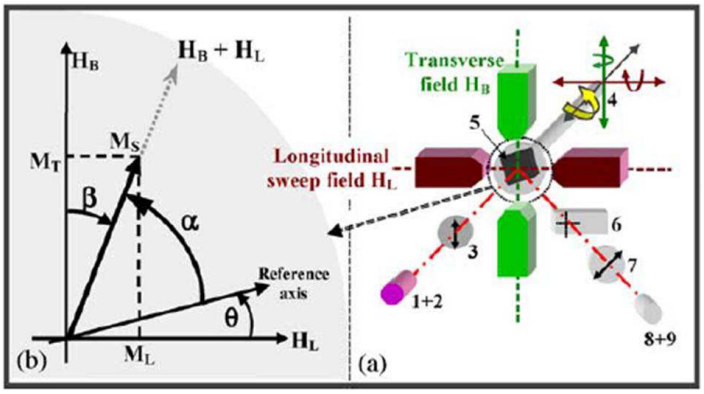

Figure 2.12: Experimental setup: (a) MOKE measurement apparatus: 1-Laser, 2-Focusing aspherical lens, 3-Polarizer, 4-Sample holder, 5-Sample, 6-Photoelastic modulator, 7-Analyzer, 8-Focusing lens and 9-Detector, (b) magnetization orientation α and in-plane sample rotation polar angle θ are defined with respect to an arbitrary reference axis in the film plane. (b) β corresponds to the angle between the transverse field and magnetization vector (reproduced from [14]).

easy and hard axis positions are quite consistent with the in-plane longitudinal MOKE hysteresis loops shown before. The value of the uniaxial anisotropy constant determined from TBIIST measurements for this sample is $2K_u/M_S = 0.156 \pm 0.055$ mT.

The Kerr microscopy images Fig. 2.13(f-h) of 10 nm Py film show the nucleation and propagation of big DWs along the easy axis with negligible pinning under a small applied field of ~ 0.5 mT. This indicates that there are few structural defects and small surface or interface roughness in these epitaxial layers. The big and uni-directional DWs confirm the presence of uniaxial anisotropy. The arrows in the images indicate the easy axis direction determined by TBIIST. The Atomic force microscopy (AFM) image in Fig. 2.13 (e) shows that the easy axis is almost perpendicular to the sapphire step direction.

The Py 5 nm films show similar behaviour to Py 10 nm films. The value of the uniaxial anisotropy constant $2K_u/M_S = 0.182 \pm 0.040$ mT is slightly higher than for Py 10 nm. The direction of the easy axis is almost perpendicular to the sapphire step direction, like for Py 10 nm. The decrease in the strength of the uniaxial anisotropy with increase of the Py thickness can be related to the decrease in the step-induced uniaxial strain upon increasing thickness.

We also studied the strength and direction of the uniaxial anisotropy for Py films deposited on less vicinal sapphire with a miscut angle of 0.05°, for Py films of thickness 5 and 10 nm. Fig. 2.14 shows the longitudinal MOKE hysteresis loops (a-c) along different in-plane directions for Py 10 nm. The Py was deposited at RT and annealed at 350 °C. These loops reveal a weak uniaxial magnetic anisotropy with a slightly easier axis at $\sim$ -35° with respect to the [11-2] azimuth.

The TBIIST measurements give a value of the easy axis direction at 34°, consistent with the MOKE hysteresis loops. The value of the uniaxial anisotropy constant is $2K_u/M_S$

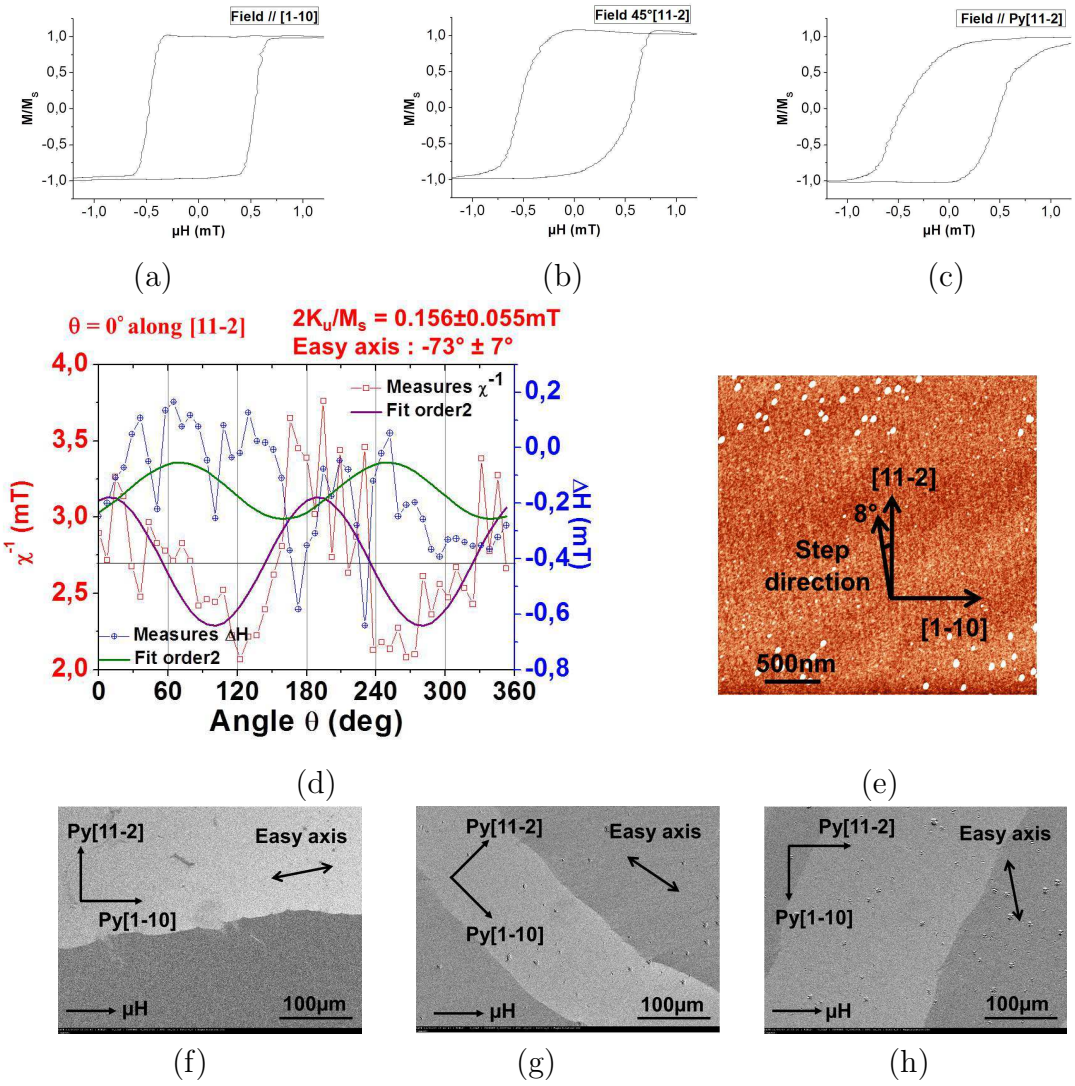

Figure 2.13: (a-c) Longitudional MOKE loops (d) TBIIST data, χ^{-1} and ΔH versus in-plane polar angle θ (e) Topography (AFM) of sapphire with a miscut angle of 0.25° (f-h) Kerr microscopy for different in-plane directions of Au(2 nm)/Py(10 nm)/Al_2O_3(0001), Py deposited at RT and annealed at 350 °C. The arrows on the Kerr microscopy images indicate the easy axis direction determined by TBIIST.

= 0.06 ± 0.01 mT. As expected, the magnitude of the unaxial anisotropy constant is smaller than for Py deposited on the sapphire with a miscut angle of 0.25°. The Kerr microscopy images show relatively small and not well oriented DWs, as shown in the Fig. 2.14 (g-i), which is consistent with the small value of the uniaxial anisotropy in this sample. Contrary to the Py deposited on more vicinal sapphire, the direction of the easy axis ∼ -34° is along the sapphire step direction, as shown in the AFM image in Fig. 2.14 (e).

The value of the uniaxial anisotropy constant for Py 5 nm on similar sapphire is $2K_u/M_S$ = 0.92 ± 0.010 mT, which is as expected slightly higher due to higher strain than for Py 10 nm. The easy axis direction (-17°) is slightly different than for 10 nm Py

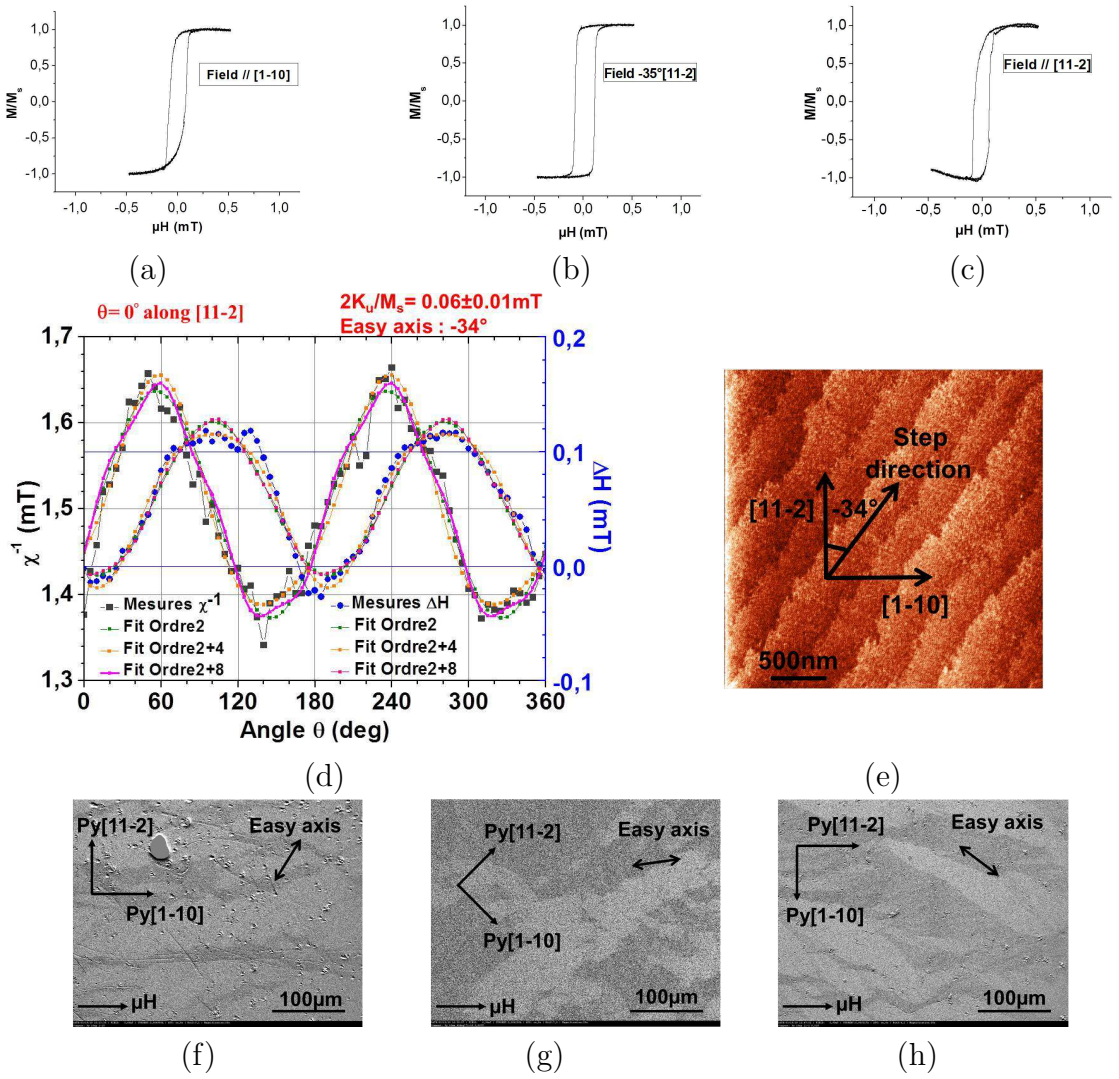

Figure 2.14: (a-c) Longitudional MOKE loops (d) TBIIST data, χ^{-1} and ΔH versus in-plane polar angle θ (e) Topography (AFM) of sapphire with a miscut angle of 0.05° (f-h) Kerr microscopy for different in-plane directions of Au(2 nm)/Py(10 nm)/Al_2O_3(0001), Py deposited at RT and annealed at 350 °C. The arrows on Kerr microscopy images indicate the easy axis direction determined by TBIIST.

film but again almost along the sapphire step direction.

In conclusion, we observed an about 3 times smaller uniaxial anisotropy for Py grown on sapphire with a small miscut angle of 0.05° than for sapphire with a relatively large miscut angle of 0.25°. This shows that the anisotropy strength is directly related to the atomic step density of the sapphire substrate. Moreover, the strength of the uniaxial anisotropy decreases with the increase in Py thickness due to decrease in the step-induced uniaxial strain.

The direction of the easy axis is almost perpendicular to the sapphire steps for a miscut angle of 0.25°, and along the sapphire steps for a miscut angle of 0.05°, with slight variation of easy axis direction with Py thickness. The strength of the anisotropy could

be even higher if measured without annealing the Py layers, due to higher strain.

Py/Ir bilayers

The Py/Ir bilayers were also deposited on sapphire with miscut angles of 0.25° and 0.05° at different temperatures, as described in section 2.2. We performed the magnetic anisotropy measurements to study the influence of the vicinality of the sapphire and growth temperature on the anisotropy.

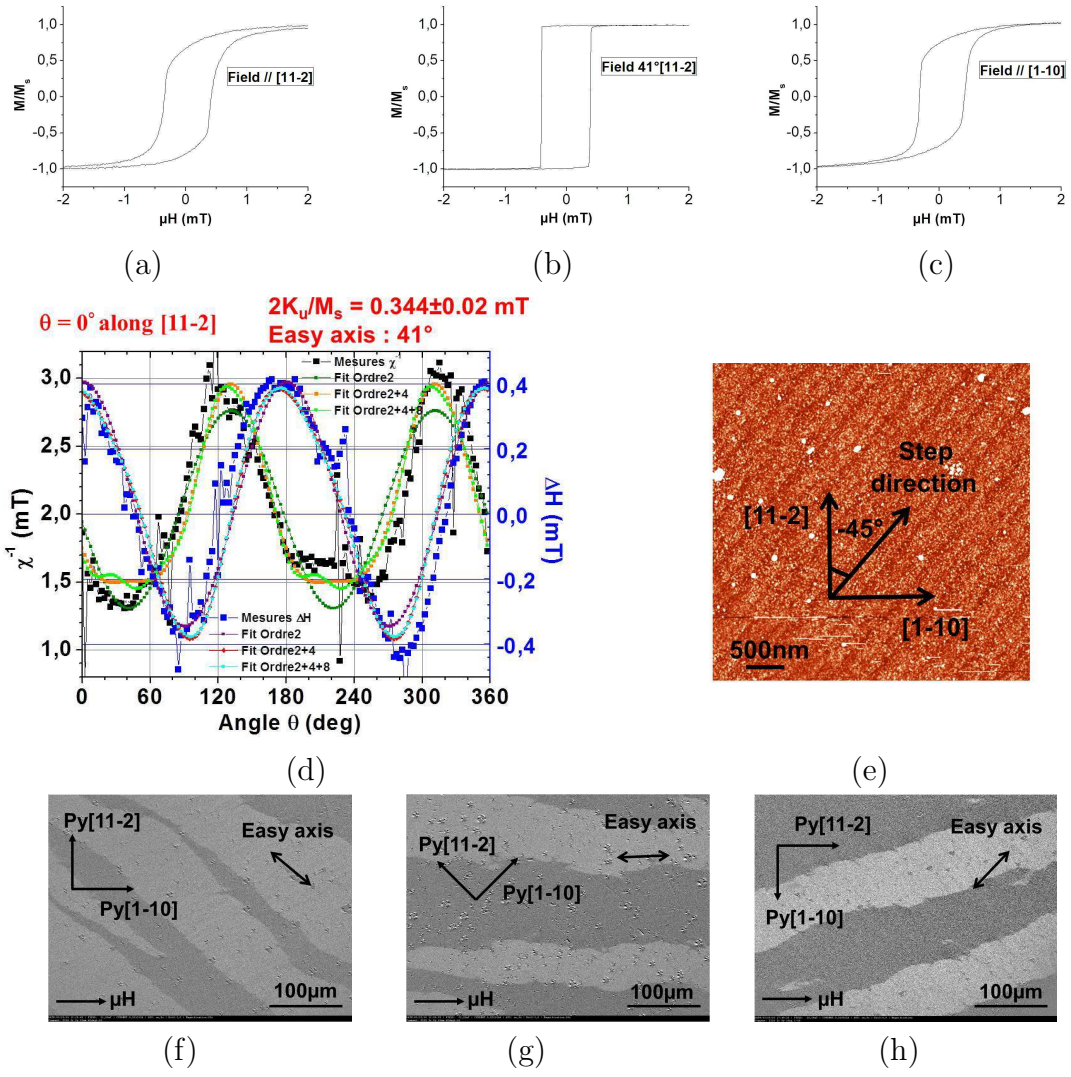

Figure 2.15: (a-c) Longitudional MOKE loops (d) TBIIST data, χ^{-1} and ΔH versus in-plane polar angle θ (e) Topography (AFM) of sapphire with a miscut angle of 0.05° (f-h) Kerr microscopy for different in-plane directions of Au(2 nm)/Py(10 nm)/Ir(9 nm)/Al_2O_3(0001), Py deposited using a temperature gradient RT-150 °C without annealing. The arrows on the Kerr microscopy images indicate the easy axis direction determined by TBIIST.

First we measured the Py/Ir bilayer deposited on sapphire with a miscut angle of 0.25° at RT and annealed at 350 °C, like for the Py single layer as described above. The MOKE hysteresis loops for different in-plane directions for Py 10 nm (not shown) show very weak

uniaxial anisotropy with an easy axis along the [1-10] azimuth. The easy axis direction is again perpendicular to the sapphire step direction like for single Py layer deposited on similar sapphire. The Kerr microscopy images (not shown) show nucleation of very small domains in random directions. The high coercive field of $\sim 2.4\,\mathrm{mT}$ and random nucleation of small domains show that there is more disorder in this sample than in Py directly grown on sapphire.

To improve the crystalline quality, the Py growth was optimised using different temperature gradients during deposition, as described in section 2.2. We performed TBIIST anisotropy measurements for all samples prepared during optimization of the Py/Ir growth. As already described in section 2.4, both single Py and Py/Ir bilayers reveal smaller coercive fields when deposited on less vicinal sapphire with a miscut angle of 0.05°, so we further optimised the Py growth on Ir only on this type of sapphire. The anisotropy measurements described below are thus all for Py/Ir bilayer samples deposited on this type of sapphire.

We started by depositing 5, 10 and 20 nm Py films on Ir/sapphire using a temperature gradient from RT to 150 °C without annealing. Longitudinal MOKE and TBIIST measurements were performed for all these three thicknesses of Py. Fig. 2.15(a-c) shows the longitudinal MOKE loops along different in-plane directions for Py 10 nm. These loops reveal a weak uniaxial magnetic anisotropy with an easy axis at 41° with respect to the [11-2] azimuth. Fig. 2.15 (d) shows the TBIIST measurements for Py 10 nm, indicating more precisely the easy axis position of 41 ° and the value of the uniaxial anisotropy constant $2K_u/M_S = 0.364 \pm 0.040\,\mathrm{mT}$. This value of the anisotropy constant is about 6 times higher than for Py 10 nm directly grown on similar sapphire at RT and annealed at 350 °C. This indicates that high temperature annealing can significantly reduce the step induced uniaxial anisotropy by reducing the uniaxial strain.

The Atomic force microscopy (AFM) image in Fig. 2.15 (e) shows that the easy axis is almost perpendicular to the sapphire step direction. The uni-directional big domain walls nucleate and propagate along the easy axis with a small field of $\sim 0.4\,\mathrm{mT}$, as shown in Fig. 2.15 (f-h). The arrows in the Kerr images indicate the easy axis direction determined by TBIIST.

The values of the uniaxial anisotropy for Py 5 and 20 nm films are $2K_u/M_S = 0.344 \pm 0.02\,\mathrm{mT}$ and $2K_u/M_S = 0.392 \pm 0.01\,\mathrm{mT}$. Unlike Py single layers, for Py/Ir bilayers the anisotropy slightly increases with increasing the Py thickness and hence the roughness. The direction of the easy axis also varies slightly with increasing the Py thickness, but it is almost perpendicular to the sapphire step direction for all thicknesses.

For all other Py/Ir bilayer samples, the easy axis is found almost perpendicular to the sapphire step direction. The strength of the uniaxial anisotropy varies from sample to sample due to different temperature gradients during the growth. A maximum value of the anisotropy of $2K_u/M_S = 0.522 \pm 0.02\,\mathrm{mT}$ was obtained for Py deposited with a temperature gradient from RT to 180 °C and annealed at 140 °C. This sample shows atomically flat Py terraces and the absence of screw dislocations.

A minimum value of the anisotropy, $2K_u/M_S = 0.096 \pm 0.025\,\mathrm{mT}$, was observed for Py deposited with a temperature gradient from RT to 300 °C, without annealing afterwards. This sample also shows a flat Py surface but contains screw dislocation loops. Moreover, like the previous sample this sample shows a quadratic magneto-optical contribution to the Kerr signal, with a 3-fold cubic(111) in-plane symmetry, indicating again a good crystalline quality.

Both temperature gradients during growth lead thus to the same easy axis direction, perpendicular to the sapphire step direction. Both samples show good crystalline quality and small roughness. The 6 times lower uniaxial anisotropy in the latter sample is thus probably related to a better strain relaxation for the Py growth using a larger temperature gradient RT-300 °C. The strain relaxation can decrease the step induced uniaxial anisotropy. The Kerr microscopy images (not shown) show very small domains with random nucleation in the latter sample, confirming the small uniaxial anisotropy.

The anisotropy measurements of all Py single and Py/Ir bilayers deposited on sapphire with miscut angles of 0.25° and 0.05° are summarised in table 2.5.1.

Sample thickness (nm)	Growth temp (°C)	Miscut angle (°)	Step orientation (°)	Easy axis (°)	Anisotropy strength (mT)
Py 5	RT, anneal 350	0.25	8	-81 ± 14	0.182 ± 0.04
Py 10	same	0.25	8	-73 ± 7	0.156 ± 0.055
Py 5	RT, anneal 350	0.05	-34	-17	0.092 ± 0.01
Py 10	same	0.05	-34	-34	0.06 ± 0.01
Py 5/Ir	Temp. gradient RT-150	0.05	-45	48	0.344 ± 0.02
Py 10/Ir	same	0.05	-45	41	0.364 ± 0.04
Py 20/Ir	same	0.05	-45	56	0.392 ± 0.01
Py 10/Ir	Temp. gradient RT-180 anneal 140	0.05	-45	37	0.522± 0.02
Py 10/Ir	Temp. gradient RT-300	0.05	-45	40 ± 10	0.096± 0.025
Py 5/Ir	Temp. gradient RT-160 anneal 270	0.05	-45	0 ± 5	0.131 ± 0.02
Py 10/Ir	same	0.05	-45	-60 ± 6	0.151 ± 0.01
Py 20/Ir	same	0.05	-45	30 ± 6	0.197 ± 0.017

Table 2.5.1: Summary of anisotropy measurements on Py single and Py/Ir bilayers on Al_2O_3(0001) with miscut angles of 0.25 ° *and* 0.05 °.

Finally, we can conclude that the microscopic origin of the weak uniaxial magnetic anisotropy may come from the asymmetry of the in-plane uniaxial strain of the Py film exerted by the residual density of sapphire steps. Some important results from the measurements above are summarised below.

- The strength of uniaxial anisotropy in Py single layers directly grown on sapphire

at RT and annealed at 350 °C increases with increase in the substrate miscut angle. The direction of the easy axis is along or perpendicular to the sapphire step direction for miscut angles 0.05° and 0.25° respectively and changes slightly with a decrease of the Py thickness.

- Contrary to Py single layer deposited on sapphire with a miscut angle of 0.25°, at RT and annealed at 350 °C, the Py/Ir bilayer deposited on similar sapphire under the same conditions, shows very small anisotropy. The very small domains observed in Kerr microscopy images reveal more disorder in this sample.

- Py/Ir bilayers deposited on sapphire with a miscut angle of 0.05° using different temperature gradients show different values of the uniaxial anisotropy. This indicates that the growth temperature also plays an important role on the strength of strain induced uniaxial anisotropy, together with the sapphire miscut angle. In contrast to Py single layers deposited on similar sapphire, the direction of the easy axis is mostly perpendicular to the sapphire step direction and changes slightly with the change of Py thickness.

In conclusion, I have shown that for Py and Py/Ir there is always some residual anisotropy due to strain induced by substrate steps. Ideally, we would like that when we make stripes, the only anisotropy is shape anisotropy to be sure that the magnetization is homogeneous, along the stripe direction. So in order to avoid any strain induced contribution, we prepared supermalloy films with negligible magnetostriction.

2.6 Coercivity of Supermalloy single and Supermalloy/Ir bilayers

The Su-Py (FeNiMo) is a very soft magnetic material with a low magnetization saturation field, very high permeability and zero magnetostriction. J. F. Bobo et al. [81] produced single crystal epitaxial (001) Su-Py (Fe 18%, Ni 79%, Cu 1% and Mo) films on single crystal MgO(001) substrates. These films show a very small coercive field (less than 0.1 mT) and four-fold cubic in-plane anisotropy with the easy axis along the (100) direction. The coercive field slightly increases with increase in the Py thickness due to strain relaxation of the Py films.

We produced epitaxial Su-Py(111) and Su-Py(111)/Ir(111) bilayer films on single crystal sapphire(0001) with a miscut angle of 0.05°. The target which we used for Su-Py deposition contains Fe(16.5%) Ni(86.5%)Mo(2.8%). Superconducting quantum interference device (SQUID) magnetometry at RT was performed to measure the coercive field of both Su-Py and Su-Py/Ir layers.

Fig. 2.16 (a,b) shows the SQUID hysteresis loops along different in-plane directions for supermalloy (Su-Py) directly grown on sapphire at RT and annealed at 350 °C. The very small coercive field of 0.02 mT, smaller than the one reported in literature (0.1 mT) [81]), shows the very soft behaviour of Su-Py films. The coercive field is almost an order of magnitude smaller than for our epitaxial Py (~ 0.1 mT). The same shape of the hysteresis loops, with almost 100% remanence along both in-plane orthogonal Su-Py azimuths [1-10] and [-1-12], shows the isotropic behaviour of single layer Su-Py films.

Fig. 2.16 (c,d) shows the SQUID hysteresis loops along different in-plane directions for Su-Py grown on Ir/sapphire(0001), using a temperature gradient of 50-300 °C without annealing. The very small coercive field of 0.07 mT shows the very soft behaviour of Su-Py/Ir films with respect to Py/Ir bilayer films (0.3 mT) deposited on similar sapphire under the same conditions. The similar hysteresis loops along both in-plane orthogonal [1-10] and [-1-12] azimuths indicate isotropic behaviour of the Su-Py/Ir bilayer films.

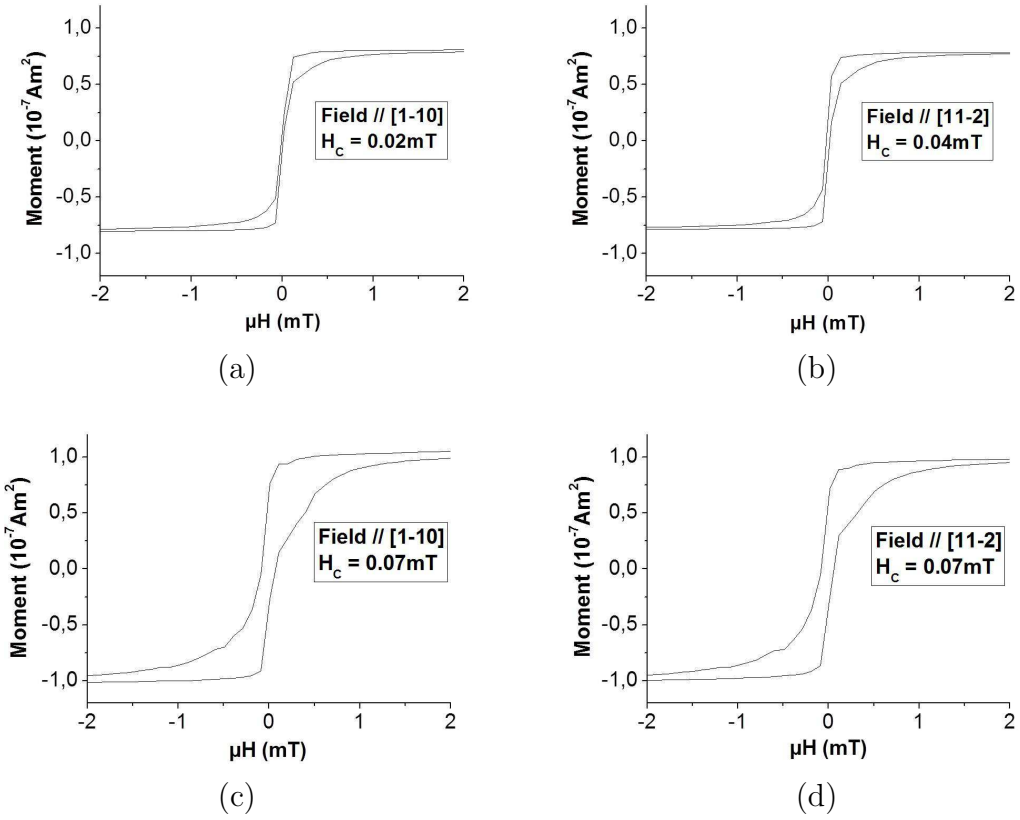

Figure 2.16: Squid hysteresis loops along different in-plane directions for (a,b) Au(2 nm)/Su-Py(10 nm)/Al_2O_3(0001) deposited at RT and annealed at 300 °C and (c,d) Au(2 nm)/Py(10 nm)/Ir(9 nm)/Al_2O_3(0001) deposited using a temperature gradient of 50-300 °C without annealing. The sapphire miscut angle is 0.05°.

Sample thickness (nm)	Miscut angle (°)	Growth temperature (°C)	RMS roughness (nm)	Coercive field (mT)
Su-Py10	0.05	RT, anneal 350	0.194	0.02
Su-Py15/Ir	0.05	Temp grad 50-350 no annealing	0.307	0.07

Table 2.6.1: Summary of coercivities of Su-Py and Su-Py/Ir deposited on Al_2O_3(0001) with a miscut angle of 0.05°.

In conclusion, we prepared very soft Su-Py single and Su-Py/Ir bilayer films on single crystal sapphire with a miscut angle of 0.05°. Both Su-Py and Su-Py/Ir films show very small coercive fields, 0.02 mT and 0.07 mT respectively. In contrast to Py films, both single and bilayer Su-Py films show isotropic behaviour without step-induced uniaxial anisotropy, indicating vanishing magnetostriction in these films. Due to the extremely soft magnetic behaviour, a low domain wall propagation field is expected in these films. Table 2.6.1 gives the summary of the coercivity of Su-Py and Su-Py/Ir layers.

2.7 Measurement of Gilbert damping constant of Py and Su-Py layers

Ferromagnetic resonance (FMR) is commonly used in the study of thin ferromagnetic films to determine magnetic properties such as the g-factor, magnetization, magnetic anisotropy constant and intrinsic Gilbert damping constant. These magnetic properties can be studied from the resonance peak position and shape of FMR spectra. Knowing these quantities is important to model magnetization dynamics. For high frequency magnetic recording fast magnetization reversal plays an important role. The switching time strongly depends on the value of the Gilbert damping constant α.

We calculated the value of α for Py thin films, which is related to the line width of the FMR spectra. The line width of FMR also gives information about magnetic inhomogeneities in the thin film, like non-homogeneity of the film thickness or local variations of magnetic anisotropy. We studied the out of plane angular dependence of FMR both experimentally and numerically using the Landau-Lifshitz-Gilbert (LLG) equation. The value of α is then calculated analytically from the line width spectra of FMR.

Smit and Belgers were the first to derive a general form of the magnetic resonance frequency (ω) for anisotropic ferromagnets from the magnetic free energy given by [120]

$$(\frac{\omega^2}{\gamma^2}) = \frac{1}{M_s^2 sin\theta^2}(F_{\theta\theta}F_{\phi\phi} - F_{\theta\phi}^2)$$

This equation does not hold for θ=0, where ω cannot be obtained. Another drawback of their equation is the mixing of different terms in the free energy. Later, L. Baselgia et al [5] proposed another equation to avoid this mixing. Their equation works well for all magnitudes and directions of H including $\theta = 0$, and is written as :

$$(\frac{\omega^2}{\gamma^2}) = \frac{1}{M_s^2}(F_{\theta\theta}(\frac{F_{\phi\phi}}{sin^2\theta} + \frac{cos\theta}{sin\theta}F_\theta) - (\frac{1}{sin\theta}F_{\theta\phi} - \frac{cos\theta}{sin^2\theta}F_\phi)^2)$$

For a film with in-plane anisotropy (shape+ uniaxial), with the effective field along z, the resonance frequency is given by :

$$\omega^2 = \mu_0^2\gamma^2[(H0_z + (D_y - D_z)M_s)(H0_z + (D_x - D_z)M_s) - \frac{\alpha^2\omega^2}{\mu_0^2\gamma^2}]$$

For a film with only shape anisotropy, the in-plane components D_z=D_x=0 and the out-of-plane component $D_y = 1$. The resonance frequency becomes

$$\omega^2 = \mu_0^2\gamma^2[(H_{res} + M_s)(H_{res}) - \frac{\alpha^2\omega^2}{\mu_0^2\gamma^2}]$$

$$\omega^2(1+\alpha^2) = \mu_0^2\gamma^2[(H_{res}+M_s)(H_{res})]$$

The resonance field can be written as

$$B_{res} = \frac{\sqrt{((\mu_0 M)^2 + 4 * \frac{\omega^2(1+\alpha^2)}{\gamma^2})} - \mu_0 M}{2}$$

If the FMR resonance line has a Lorentzian shape

$$f(B) = \frac{A}{\frac{(B-B_r)^2}{D^2}+1}$$

where A = Line amplitude, B_r = Line center and 2D = Full width at half maximum (FWHM)

Then the line derivative is given by

$$\frac{df}{dB} = \frac{-2A(B-B_r)}{D^2(\frac{(B-B_r)^2}{D^2}+1)^2}$$

The resonance field B_r and FWHM are calculated numerically and are also determined experimentally as a function of angle from in-plane to out-of-plane of the film.

The peak to peak width of the line derivative from the FMR measurement is given by

$$\Delta B_{pp} = \frac{2D}{\sqrt{3}} = \frac{FWHM}{\sqrt{3}}$$

If we know the value of the peak to peak width from the FMR experiment, then we can calculate the FWHM from the above equation. The value of α is then calculated analytically from the full width at half maximum (FWHM) from the model:

$$\Delta H = \frac{\alpha}{d\omega/dH}\frac{\gamma}{M_s}(F_{\theta\theta} + \frac{1}{sin^2\theta}F_{\phi\phi})$$

It has been reported that the interaction between the itinerant electrons and the spin waves is increased significantly in the vicinity of a NM/FM interface, where NM is a non-magnetic metal and FM is a ferromagnetic metal. This can result into the local enhancement of α [13][119]. Since spin-orbit effects at metal surfaces increase in the presence of heavy atoms [68], the strength of the interaction at a NM/FM interface is higher for metals with strong spin orbit coupling, resulting in higher value of α. A relatively large value of α (~ 0.019) has been found for Pt(5 nm)/Py(10 nm)/Pt(5 nm) thin films due to the strong spin orbit coupling of the Pt layer [86]. This value of α further increases by decreasing the thickness of Py, since it is mainly an interface effect.

We considered Py single layer, Py/Ir bilayer and Su-Py single layer thin films on sapphire(0001) substrates with sapphire miscut angle of 0.05°. These films were capped

by 2 nm Au to protect from oxidation. We investigated this effect by studying the Py/Ir bilayers, where Ir is a heavy metal. As the capping layer of Au is also a heavy metal, it can also effect the value of α.

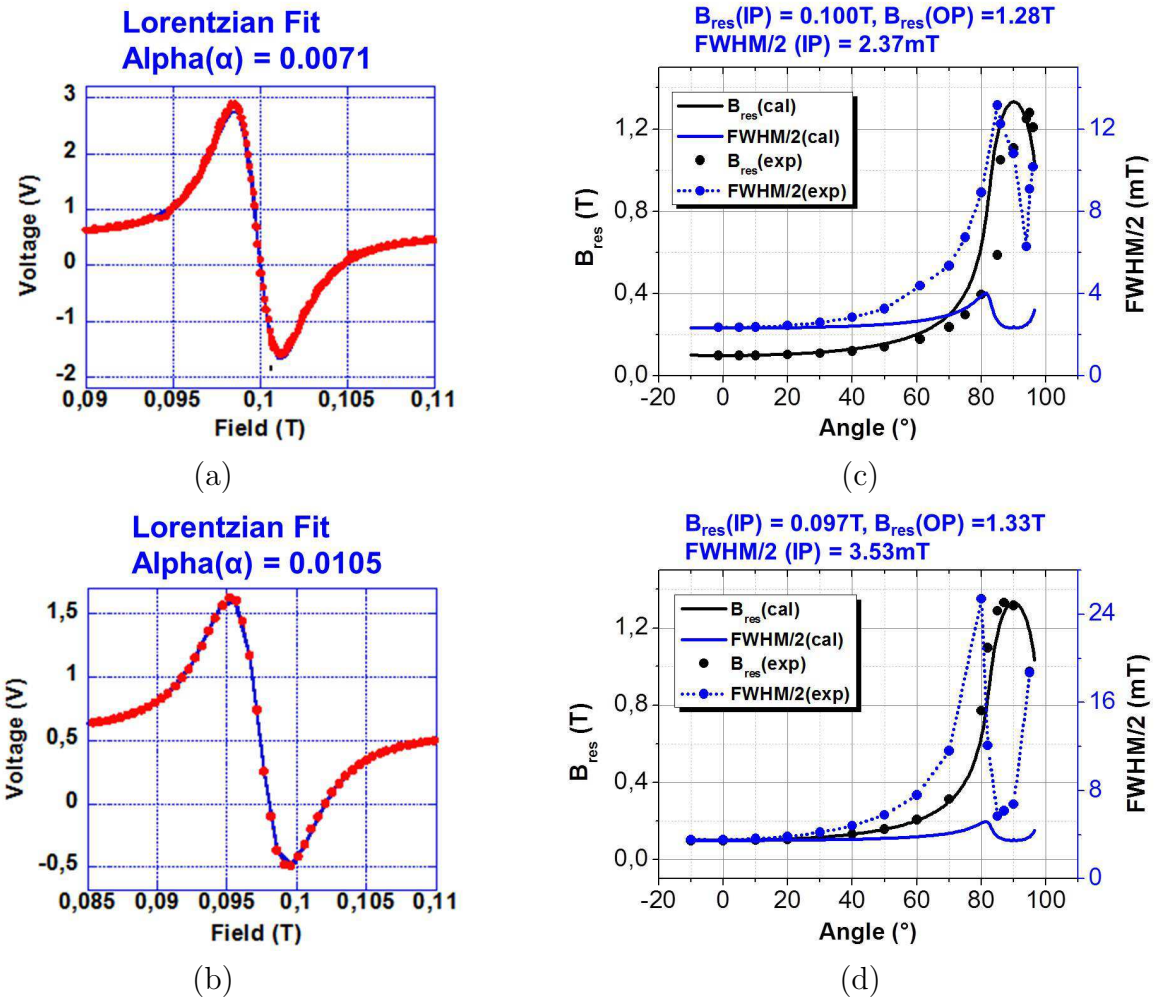

Figure 2.17: (a,b) In-plane FMR spectra (The red points and solid blue line correspond to experimental data and a lorentzian fit, respectively) and (c,d) the out-of-plane angular dependence of B_r and FWHM/2 for Au(2 nm)/Py(10 nm)/Al_2O_3(0001) and Au(2 nm)/Py(10 nm)/Ir(9 nm)/Al_2O_3(0001) respectively with sapphire miscut angle 0.05°. The solid disks are the experimental data points and solid lines are the calculated values using the parameters g = 2.1, ($D_x = D_z = 0$, $D_y = 1$), K = 0 and $\mu_0 M_S = 1$ T.

Fig. 2.17 (a,b) shows the in-plane FMR spectra for Au(2 nm)/Py(10 nm)/Al_2O_3(0001) and Au(2 nm)/Py(10 nm)/Ir(9 nm)/Al_2O_3(0001) respectively. The horizontal axis indicates the applied DC magnetic field and the vertical axis shows the signal in arbitrary units. The red points and solid blue lines correspond to experimental data and the lorentzian fit, respectively. The shape of the resonance curve is perfect Lorentzian. The out-of-plane angular dependence of B_r and FWHM/2 for Py(10 nm) and Py(10 nm)/Ir(9 nm) are shown in Fig. 2.17 (c,d). The solid circles are the experimental data points and solid lines are the calculated values using the parameters g = 2.1,($D_x = D_z = 0$, $D_y = 1$), K = 0 and $\mu_0 M_S = 1$ T

We calculated the value of α from a fit with the derivative of a perfect Lorentzian function. The α measured for Py (10 nm) directly grown on sapphire is 0.0071 which is almost the same as for bulk Py. This shows that the FWHM of the resonance curve reveals negligible extrinsic contributions from magnetic inhomogeneities. This indicates the good quality and magnetic homogeneity of the Py films. The value of α is slightly higher than reported in the literature, which are 0.0060 for 10 nm Py [62] and 0.0065 for 3 nm Py thin films [87].

The value of α calculated for Py(10 nm)/Ir(10 nm) grown on sapphire(0001) is $\sim$ 0.0105. The 30% increase in value of alpha for Py grown on an Ir buffer layer is in agreement with the theoretical predictions and experimental results reported in the literature for the enhancement of α at the NM/FM interface [86][119].

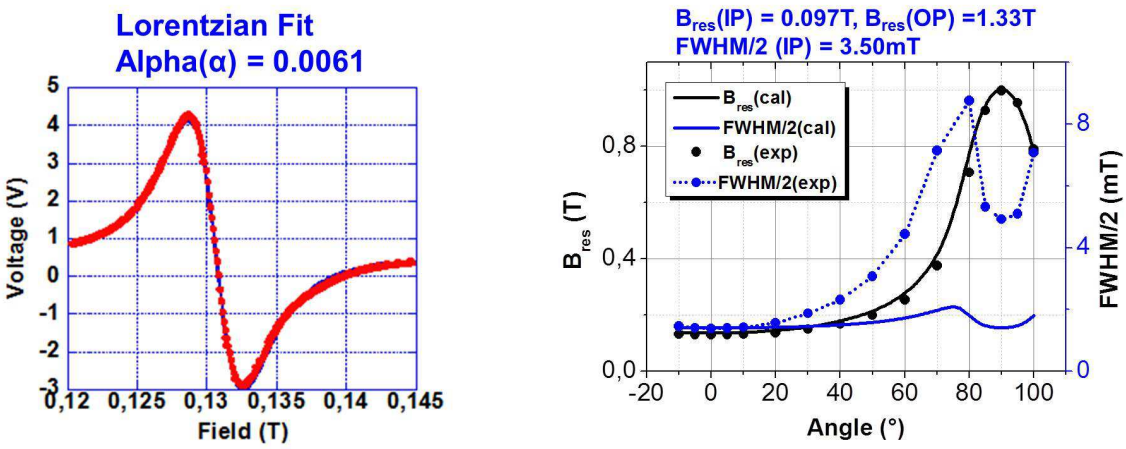

(a) (b)

Figure 2.18: (a) In-plane FMR spectra (The red points and solid blue line correspond to experimental data and lorentzian fit respectively) and (b) The out-of-plane angular dependence of FWHM/2 and B_r for Au(2 nm)/Su-Py(10 nm)/Al_2O_3(0001) with sapphire miscut angle 0.05°, Su-Py deposited at RT and annealed at 350 °C. The solid circles are the experimental data points and solid lines are the calculated values using the parameters g = 2.1, ($D_x = D_z = 0$, $D_y = 1$), $K = 0$ and $\mu_0 M_S = 0.67$ T.

The out-of-plane angular dependence of B_r and FWHM/2 for both Py and Py/Ir show that for $\theta = 0°$, the experimental data is best-fitted and near $\theta = 90°$ there is small disagreement. There could be some magnetic inhomogeneities like small variations of the thickness from one end to the other end of the films or local variations of the magnetization due to strain induced anisotropy etc. There could also be a small angular misalignment of the DC magnetic field or the sample. As for in-plane, these small variations have little effect on B_r and FWHM/2, so we got the perfect lorentzian curve, however for out-of-plane, these can have a significant effect. This indicates that our films are magnetically homogeneous. A better set-up with perfectly aligned magnetic field and sample can overcome this small disagreement.

The saturation magnetization of Su-Py ($\mu_0 M_S = 0.67$ T) is lower than for Py ($\mu_0 M_S = 1$ T), and the value of α can be different than for Py. We also determined the value of α for Su-Py, in the same way as for Py. Fig. 2.18 (a) shows the in-plane FMR spectra for Au(2 nm)/Su-Py(10 nm)/Al_2O_3(0001). The red points and solid blue line show the

experimental data and the lorentzian fit respectively. The shape of the resonance curve is perfect lorentzian. The out of plane angular dependence of B_r and FWHM/2 are shown in Fig. 2.17 (b). The solid circles are the experimental data points and solid lines are the calculated values using the parameters g = 2.1,($D_x = D_z = 0$, $D_y = 1$), K = 0 and $\mu_0 M_S$ = 0.67 T. Again the out-of-plane angular dependence of B_r is fitted well for both in-plane and out-of-plane directions of the film, however, with a small disagreement for FWHM/2 for out-of-plane direction, like for Py layers described above.

The value of α calculated from a fit with the derivative of a perfect Lorentzian function for Su-Py is ~ 0.0061. This value of α is close to that of Py ~ 0.0071, although Su-Py has a lower saturation magnetization than Py.

2.8 Summary of epitaxial growth and magnetic characterization

In conclusion, we studied the epitaxial Py growth on sapphire (0001)and Ir/Sapphire with the sapphire miscut angles 0.25° and 0.05° as a function of temperature. We prepared very flat, epitaxial Py single and Py/Ir bilayer films with less structural defects and surface or interface roughness. The LMOKE hysteresis loops measured at RT and 11 Hz frequency along different in plane directions show very soft magnetic behaviour of Py films with coercive fields of 0.1 and 0.3 mT respectively for Py and Py/Ir films respectively deposited on sapphire with a miscut angle of 0.05°. Both Py single and Py/Ir bilayer films deposited on more vicinal sapphire with the miscut angle 0.25° exhibits 5 or 8 times higher coercive fields respectively than deposited on the sapphire with miscut angle 0.05°. For Py and Py/Ir there is always some residual anisotropy due to strain induced by substrate steps. The strength of anisotropy increases with increase in sapphire miscut angle. For Py films deposited at different temperature gradients on similar sapphire, we observed smaller anisotropy for higher temperature gradient growth due to strain relaxation of the films and vice versa. In order to avoid any strain induced contribution, we prepared Su-Py films with negligible magnetostriction on sapphire with a miscut angle of 0.05°. Both Su-Py and Su-Py/Ir films show an order of magnitude smaller coercive fields, 0.02 mT and 0.07 mT respectively as compared to Py films. In contrast to Py films, both single and bilayer Su-Py films show isotropic behaviour without step-induced uniaxial anisotropy, indicating vanishing magnetostriction in these films. We calculated the value of Gilbert damping parameter α for both Py and Su-Py thin films using FMR technique. We calculated the value of α from a fit with the derivative of a perfect Lorentzian function. The α calculated for Py (10 nm) directly grown on sapphire is 0.0071 which is almost the same as for bulk Py. This indicates the good quality and magnetic homogeneity of the Py films. Slightly higher value of $\alpha \sim 0.0105$ was calculated for Py(10 nm)/Ir(10 nm) bilayer films due to strong spin-orbit coupling of Ir. The value of α calculated for Su-Py is ~ 0.0061. This value of α is close to that of Py ~ 0.0071, although Su-Py has a lower saturation magnetization than Py and there is also Mo in Su-Py which should increase the value of α due to higher spin-orbit coupling.

The table 2.8.1 summarises the epitaxial growth and magnetic properties of all the Py single and Py/Ir bilayers for an optimised Py thickness of 10 nm.

Sample thickness (nm)	Growth temp (°C)	Miscut angle (°)	Coercivity (mT)	Step orientation (°)	Easy axis (°)	Anisotropy strength (mT)
Py 10	RT, anneal 350	0.25	0.5	8	-73 ± 7	0.156 ± 0.055
Py 10	RT, anneal 350	0.05	0.1	-34	-34	0.06 ± 0.01
Py 10/Ir	Temp grad RT-150 no anneal	0.05	0.4	-45	41	0.364 ± 0.04
Py 10/Ir	Temp grad RT-180 anneal 140	0.05	0.7	-45	37	0.522± 0.02
Py 10/Ir	Temp grad RT-300 no anneal	0.05	0.28	-45	40 ± 10	0.096± 0.025
Py 10/Ir	Temp. gradient RT-160 anneal 270	0.05	0.35	-45	-60 ± 6	0.151 ± 0.01
Py 10/Ir	Temp. gradient 50-300 no anneal	0.05	0.31	-45	-	-
Su-Py10/Ir	RT, anneal 350	0.05	0.02	-45	-	-
Su-Py15/Ir	Temp grad 50-300 no anneal	0.05	0.07	-45	-	-

Table 2.8.1: Summary of Py and Su-Py epitaxial growth and magnetic characterization on $Al_2O_3(0001)$ with miscut angles 0.25° and 0.05°.

Chapter 3

Magnetic force microscopy

In this chapter the working principles of atomic and magnetic force microscopy and the modelization of the cantilever dynamics and magnetic force will be presented. Then magnetic tip stray field-induced perturbations of domain walls in nanostripes will be discussed. Consequently, I will describe in detail the optimization of magnetic thin film coatings on AFM silicon tips to have low moment magnetic tips to minimize the tip induced DW perturbations.

3.1 Atomic force microscopy

Principle of operation

Magnetic force microscopy is derived from the atomic force microscopy (AFM), so first I will explain its principle of operation. AFM uses a flexible cantilever with a sharp tip at its end. The cantilever is usually made of Si or Si_3N_4 with a radius of curvature of the tip from a few nanometers to tens of nanometers.

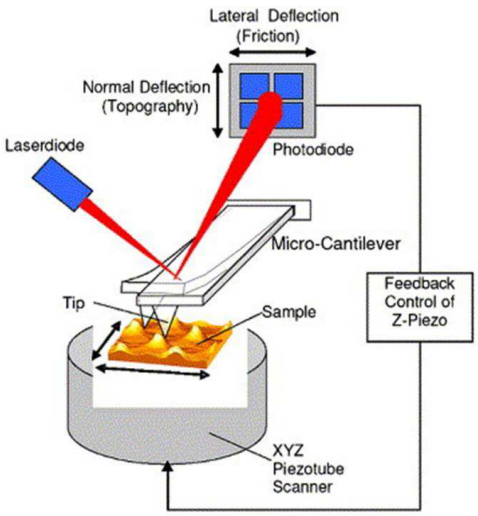

Figure 3.1: Principle of operation of atomic force microscopy [106].

The tip is scanned laterally close to the sample surface within a few nanometers and interacts with the sample, which results in modification of the cantilever dynamics. The

magnitude of the deflection is measured in real time by a laser that reflects at an oblique angle from the very end of the cantilever onto a position-sensitive detector. Fig. 3.1 shows the schematic representation of AFM working principle. Depending on the mode of operation different type of forces are measured i.e., Van der Waals, mechanical, electrostatic, friction, capillary and magnetic (using magnetic tips) forces etc.

3.1.1 Modes of operation of AFM

Static or Contact mode

In contact mode the tip is in contact with the surface through the adsorbed fluid layer on the sample surface. The tip predominately experiences repulsive forces resulting in tip deflection. These short range repulsive forces $\sim 10^{-6}$ - 10^{-8} N are sufficient to generate tens of nanometers of cantilever deflection. The surface topography results in changes of tip-sample force and hence deflection. By keeping a constant cantilever deflection using a feedback loop the force between the probe and the sample is maintained constant and an image of the surface is obtained through the adjustment of the height of the sample.

This mode of operation is useful when contact is required, for example when electric properties or friction analysis are sought. It is not useful for imaging soft samples because the sample surface can be damaged, however imaging samples in liquids can resolve this problem. However, the combination of lateral and normal forces reduces the resolution and is liable to increase the wear of the tip.

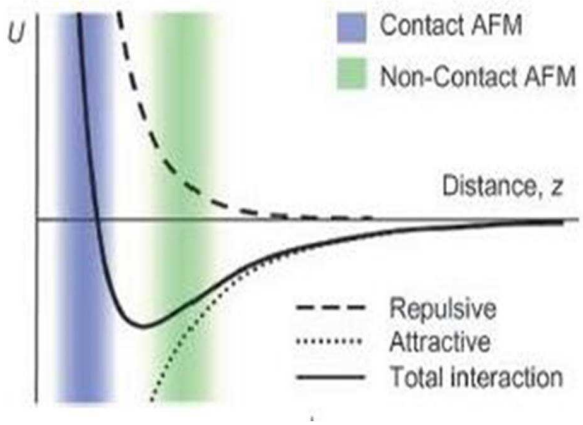

Figure 3.2: Force between the tip and the sample surface atoms versus tip-to-sample distance curve [ParkAFM].

Dynamic or non-Contact mode

In non-contact mode the cantilever is driven to oscillate close to the sample surface at its resonant frequency. Tip-sample forces influence the AC motion of the cantilever, with an impact on both phase and amplitude response. The most common way for imaging topography in this mode is with a constant excitation of the cantilever and feedback on the amplitude. Using again a feedback loop to keep the amplitude constant the surface topography can be measured. Generally, the resolution is lower under ambient conditions

because the occurence of a layer of adsorbed fluid. The best imaging conditions are met under vacuum.

Fig. 3.2 shows the force between the tip and the sample surface atoms as a function of the tip-sample distance. A spatial resolution of 50 nm can be normally achieved with conventional tips, however by using very sharp tips a resolution down to 25 nm is also possible. As I did all my topographic and magnetic measurements in non contact mode, I will discuss in detail this mode.

3.2 Magnetic force microscopy

Magnetic force microscopy (MFM) is a technique for imaging magnetization patterns with high resolution, some tens of nanometers. Very little sample preparation is required as compared to other magnetic imaging techniques. One drawback of MFM is the difficulty to interpret MFM contrast. Secondly, the mutual interaction between the tip and the sample can perturb the tip or sample magnetization. For the best resolution and a reduced mutual interaction, a small amount of magnetic material on the tip is required. However, the small amount of material decreases the MFM signal and hence reduces the tip sensitivity.

Principle of operation

This technique is derived from AFM and uses a very sharp magnetic tip attached to a flexible cantilever. Normally CoCr thin film coatings on Si cantilevers are used as magnetic tips. Generally, imaging is done using a two pass technique. During the first pass, the tip is scanned in tapping mode to measure the surface topography. In the second pass, the tip is lifted to a selected height (10-500 nm) and follows the same topography path, assuming that Van der Waals forces can be neglected, and long-range forces of other physical origin are measured, such as electric or magnetic in case of MFM. The tip interacts with the stray field arising from the magnetic sample. The effect of this interaction is measured as a function of the sample position. Fig.3.3 shows the schematics of the two-pass MFM technique.

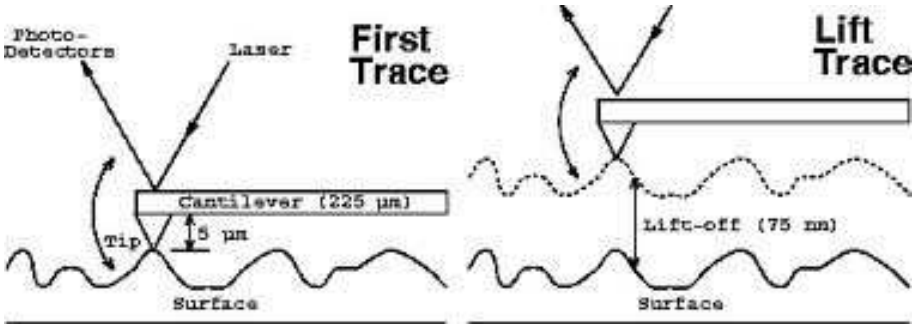

Figure 3.3: Magnetic force microscopy working principle (two pass technique). The first pass gives surface topography and second pass results in magnetic image [M. J. Donahue].

In the following, I will first derive equations to describe the physics of MFM, then present specificities and developments related to the imaging of soft magnetic materials.

3.2.1 Modelling of the cantilever motion

A cantilever can be considered a damped harmonic oscillator and can be described by the following equation

$$m\frac{\mathrm{d}^2z}{\mathrm{d}t^2} + b\frac{\mathrm{d}z}{\mathrm{d}t} + kz = 0 \tag{3.1}$$

where m is the effective mass of the cantilever, b is the viscous damping constant and k is the spring constant of the cantilever.

The angular resonant frequency of oscillation of the cantilever is given by

$$\omega_0 = \sqrt{\frac{k}{m}} \tag{3.2}$$

In the presence of a force F, exerted by the sample on the tip, the eq. (3.1) can be written as

$$m\frac{\mathrm{d}^2z}{\mathrm{d}t^2} + m\frac{\omega_0}{Q}\frac{\mathrm{d}z}{\mathrm{d}t} + (k - \frac{\mathrm{d}F}{\mathrm{d}z}) = F_0 \tag{3.3}$$

assuming a slow spatial variation i.e., a linear regime. F_0 is a constant responsible for the deflection of the cantilever, $Q = m\frac{\omega_0}{b}$ is the quality factor and $k - \frac{\mathrm{d}F}{\mathrm{d}z}$ is the effective spring constant.

In the presence of an external driving force $F_\mathrm{d}\cos(\omega t)$, the steady state solution of eq. (3.3) can be written as

$$z = A(\omega)\cos[\omega t + \phi(\omega)] \tag{3.4}$$

where the amplitude of oscillation $A(\omega)$ and the phase $\phi(\omega)$ are given by

$$A(\omega) = \frac{F_d/(k - \frac{\mathrm{d}F}{\mathrm{d}z})}{\sqrt{[(\omega^2/\omega_0^2 - 1)^2 + \omega^2/\omega_0^2Q^2]}} \tag{3.5}$$

and

$$\tan\phi(\omega) = Q/(\omega/\omega_0 - \omega_0/\omega) \tag{3.6}$$

The angular resonant frequency determined by both the spring constant and the force gradient is then given by

$$\omega_0 = \sqrt{\frac{k - \mathrm{d}F/\mathrm{d}z}{m}} \tag{3.7}$$

It is clear from the above expression that the resonant frequency decreases for attractive interactions (i.e., $\frac{\mathrm{d}F}{\mathrm{d}z} < 0$ gives $\omega_0 > 0$) and increases for repulsive interactions (i.e., $\frac{\mathrm{d}F}{\mathrm{d}z} > 0$ gives $\omega_0 < 0$). The effect of an attractive force gradient on amplitude $A(\omega)$ and phase $\phi(\omega)$ is shown in Fig. 3.4.

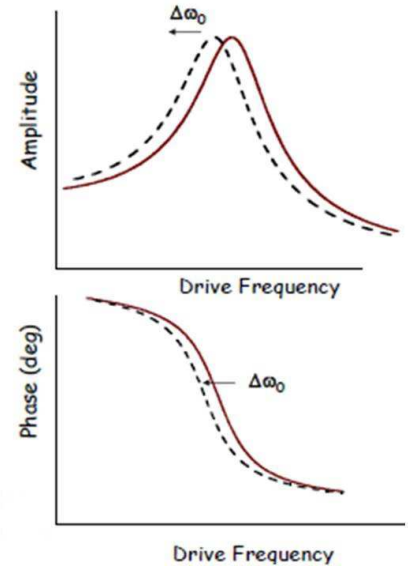

Figure 3.4: Amplitude and phase of a simple harmonic oscillator. The dotted lines correspond to the effects of the gradient of an attractive force that decreases the resonant frequency and a phase lag between the cantilever drive and response greater than 90°. The effects of the gradient of repulsive force (not shown) will shift the resonant frequency to a higher value and a phase lag less than 90° [Fig. produced by B. Moskowitz].

An attractive force gradient shifts the resonant frequency towards lower values and induces a phase lag between the cantilever drive and response greater than 90° (dotted lines), while a repulsive force gradient (not shown) shifts the resonant frequency towards higher values and causes a phase lag smaller than 90°. In practice, the cantilever is excited at a fixed frequency (i.e., its resonant frequency) and the MFM signal consist of the measured phase. With our convention, a negative phase shift (dark contrast) means attractive forces, while a positive phase shift (bright contrast) means repulsive forces.

The shift in the cantilever phase due to the force gradients can be simplified based on a first order expansion of eq. (3.7)

$$\Delta\Phi = -\frac{Q}{k}\frac{\mathrm{dF}}{\mathrm{dz}} \tag{3.8}$$

This equation shows that the phase signal depends on the force gradient, the quality factor and the spring constant of the cantilever.

3.2.2 Magnetic forces and force gradients

The magnetic force between the tip having a magnetic moment $\mathbf{m^t}$ and the stray field $\mathbf{H^s}$ from a sample is given by the following expression

$$\mathrm{F} = \nabla_r[\mathbf{m^t} \cdot \mathbf{H^s}] \tag{3.9}$$

where μ_0 is the magnetic permeability of the free space.

Usually AFM or MFM cantilevers move along one specific direction and are relatively stiff along other directions. Thus the only component of the magnetic force between a MFM tip and the stray field from a sample along this direction (z is relevant) is given by

$$F_z^t = \frac{\partial}{\partial \mathrm{z}}[\mu_0 \mathbf{m^t} \cdot \mathbf{H^s}] \tag{3.10}$$

and the force gradient becomes

$$\frac{\partial F_z^t}{\partial z} = \frac{\partial^2}{\partial z^2}[\mu_0 \mathbf{m^t} \cdot \mathbf{H^s}] \tag{3.11}$$

If the tip magnetic moment is a constant point dipole and does not change under the influence of the sample stray field and also the tip stray field does not alter the distribution of magnetization in the sample, then eqs. (3.10) and (3.11) can be simplified :

$$F_z^t = \mu_0 m_x^t \frac{\partial H_x^s}{\partial z} + \mu_0 m_y^t \frac{\partial H_y^s}{\partial z} + \mu_0 m_z^t \frac{\partial H_z^s}{\partial z} \tag{3.12}$$

and the force gradient becomes

$$\frac{\partial F_z^t}{\partial z} = \mu_0 m_x^t \frac{\partial^2 H_x^s}{\partial z^2} + \mu_0 m_y^t \frac{\partial^2 H_y^s}{\partial z^2} + \mu_0 m_z^t \frac{\partial^2 H_z^s}{\partial z^2} \tag{3.13}$$

If the tip is magnetized along the z-axis, then $m_x = m_y = 0$ and eqs. (3.12) and (3.13) can be written as

$$F_z^t = \mu_0 m_z^t \frac{\partial H_z^s}{\partial z} \tag{3.14}$$

and

$$\frac{\partial F_z^t}{\partial z} = \mu_0 m_z^t \frac{\partial^2 H_z^s}{\partial z^2} \tag{3.15}$$

In practice, the magnetic tip is not a point dipole. Another model for a MFM tip is a monopole, we can then write the magnetic force gradient as

$$\frac{\partial F_z^t}{\partial z} = \mu_0 m_z^t \frac{\partial H_z^s}{\partial z} \tag{3.16}$$

Here z is along the oscillation direction, not necessarily the direction perpendicular to the sample surface. In that case a refrential axis (x′, y′, z′) must be applied, which mixes $\frac{\partial H_z^{s\prime}}{\partial z'}$ and $\frac{\partial H_z^{s\prime}}{\partial x'}$ in eq. (3.16), and $\frac{\partial^2 H_z^{s\prime}}{\partial z'^2}$, $\frac{\partial^2 H_z^{s\prime}}{\partial x'^2}$ and even $\frac{\partial^2 H_z^{s\prime}}{\partial x' \partial z'}$ in eq. 3.15.

3.2.3 Magnetic force microscopy image formation

Based on a monopole or dipole model for the tip, in MFM we measure the force or force gradient due to the stray field arising from the magnetic charges in the sample. The interaction between the magnetic tip and the sample can be attractive or repulsive, depending whether the stray fields from the tip and the sample are parallel or antiparallel to each other.

Fig. 3.5(a) shows the schematics of repulsive and attractive interactions between the tip and the positive and negative magnetic charges of charged head-to- head (HH) and

tail-to-tail (TT) domain walls (DWs). The red arrows indicate the direction along which the tip is magnetized. Conventionally, the attractive and repulsive interactions are coded as black and white contrast respectively, which is consistent with the choice of sign for ϕ in eq. (3.6).

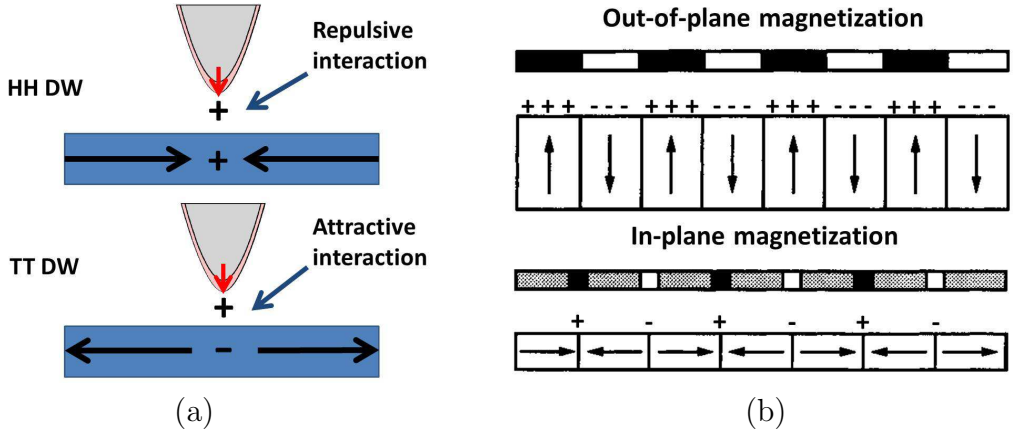

Figure 3.5: Schematics (a) tip-sample repulsive and attractive interactions. (b) Magnetic force microscopy charge image formation for systems with out-of-plane and in-plane magnetization giving magnetic domains and domain walls (transition between domains) contrast (black and white) respectively [52].

For systems with out-of-plane magnetization the MFM image reflect the surface charges, i.e., the domain image if we neglect the influence of the bottom charges as shown in the Fig. 3.5(b) top image. The black and white contrast corresponds to up and down domains. On the other hand, for systems with in-plane magnetization we get the transition (domain wall) between two opposite domains as shown in the Fig. 3.5(b) bottom image. Here black and white contrast gives the positively and negatively charged HH and TT DWs respectively. In this chapter I will describe MFM imaging of that nature because I did magnetic imaging of DWs in soft magnetic material permalloy (Py) with in-plane magnetization.

3.2.4 Magnetic tip-sample mutual perturbations

Magnetic force microscopy is a technique commonly used for imaging magnetic materials with a rather high coercivity where it can be assumed that the magnetic tip does not change the distribution of magnetization in the sample. However, the tip stray field can change the distribution of magnetization in the case of soft magnetic materials. Reversible and irreversible changes due to the tip stray field have been reported in the literature. For reversible changes, e.g., DW distortion or local magnetization distribution of the sample, the sample recovers its initial state as soon as the tip stray field is removed [79][28]. That can be detrimental, or on the reverse can be used, e.g., for imaging ultrathin films with out-of-plane magnetization where mutual interaction is always attractive. In contrast, for irreversible changes, e.g., DW transformation, DW propagation and tip induced switching, the initial magnetic state cannot be recovered after removal of the tip stray field [35][72].

Here, we illustrate tip-sample interactions on DW configurations in 15 nm-thick Py nanostripes, deposited on sapphire(0001) substrate and capped by 2 nm Au. The nanos-

tripes of width between 200-500 nm were patterned by combined electron-beam lithography and ion-beam etching techniques at Nanofab, Institut Néel, by Stefania Pizzini. Images were taken with commercial so-called low moment (LM) Asylum tips. The resonance frequency of these cantilevers ranges between 60 to 80 kHz. The spring constant values of the cantilevers are between 0.5 and 4.4 N/m. The cantilevers are 240 µm long, 30 µm wide and 2.7 µm thick. The outer tip radius is 20±7 nm with a $Co_{80}Cr_{20}$ coating of 15 nm. During all scans, the cantilever amplitude of oscillation is set to ∼ 100 nm during the first pass and ∼ 75 nm during the second pass. The vertical tip to sample distance ΔZ during each scan was kept at ∼ 10 nm for all DWs imaging.

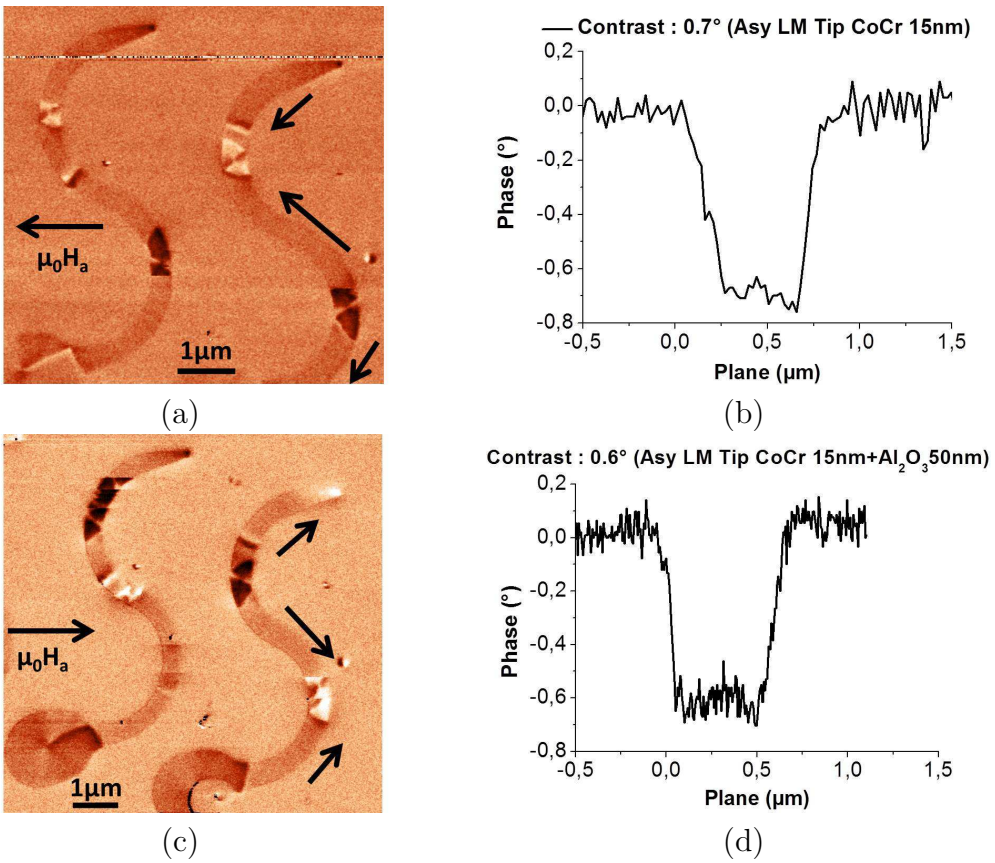

Figure 3.6: Magnetic force microscopy images of vortex walls and phase contrast respectively in 400 and 500 nm *wide nanostripes with (a,b) commercial low moment Asylum tips (c,d)* 50 nm *Al_2O_3 coated Asylum low moment tips. The cantilever amplitude of oscillation is set to* ∼ 100 nm *during the first pass and* ∼ 75 nm *during the second pass and imaging was done at a lift height of* 10 nm.

The HH and TT DWs were created at the bends of stripes, by applying a magnetic field of ∼ 50 mT transverse to the stripes. As we imaged a soft magnetic material (Py) with a hard magnetic tip, we can assume that the tip magnetic configuration remains unaffected while the sample magnetic configuration can change. Before imaging, the tips were magnetized along the tip pyramid axis with a permanent magnet. We observed vortex walls (VWs), as also predicted in the DW phase diagram in nanostripes of these dimensions [93].

Fig. 3.6(a) shows the HH and TT VWs in 15 nm thick and 400 and 500 nm wide Py

nanostripes, represented by white and black contrast respectively. The direction of magnetization in the nanostripes is represented by the black arrows. The fast scan direction is transverse to the stripes while slow scanning from bottom to the top of the stripes. The tip is magnetized along the pyramidal direction so that it is sensitive to the z component of the sample's stray field. For HH positively charged DWs the tip-DW should have repulsive interaction and for TT negatively charged DWs, this interaction should be attractive.

Consistent with literature reports [36][35], we observed tip-induced magnetization reversal, repelling, snatching and dragging of DWs due to tip-DW interaction. In Fig. 3.6(a), the tip snatches the TT VW in 400 nm (left) nanostripe due to the attractive interaction, then drags it until it gets pinned. In the upper half of the same nanostripe, the tip repels down the HH DW after some point, consistent with the tip-DW repulsive interaction. The MFM phase contrast of DWs is shown in Fig. 3.6(b).

Our first attempt to reduce the tip-DW interaction was to deposit 50 and 70 nm Al_2O_3 on commercial LM Asylum tips. Fig. 3.6(c) shows the HH and TT VWs in 400 and 500 nm wide Py nanostripes imaged by LM Asylum tips capped by 50 nm Al_2O_3. The Al_2O_3 capping results in lowering the DW contrast from 0.7 to 0.6° as shown in Fig. 3.6(d) but still the tip repels, snatches and drags the DWs due to tip-DW repulsive and attractive interactions. The tip drags the TT black DW in 400 nm wide stripe (left) and at some point it snatched away moving out of the stripe due to the attractive tip-DW interaction. This results in reversal of the stripe magnetization as indicated by black contrast at the sharp edge of the nanostripe as compared to white contrast in a 500 nm wide nanostripe (right) where DW do not move out of the stripe [Fig. 3.6(c)]. Thus, beyond the loss of spatial resolution, another route needed to be explored.

3.2.5 Optimization of magnetic thin film coatings

We developed our own LM magnetic tips to reduce further the tip magnetic moment and hence its stray field to minimize the tip-induced perturbations. For this purpose, we deposited $Co_{80}Cr_{20}$ alloy thin films of different thicknesses on conventional non-magnetic Si cantilevers and tips. I will describe here the qualitative and the quantitative analysis of the tip coatings, and the tip-DW interactions with respect to the thickness of a $Co_{80}Cr_{20}$ coating.

3, 5, 7.5 and 10 nm $Co_{80}Cr_{20}$ thin films were deposited by RF sputtering on commercial Asylum 240TS silicon tips. After $Co_{80}Cr_{20}$ deposition, the films were capped by 5 or 10 nm of SiO_2 for protection against oxidation. The thin film depositions covers the tip, the cantilever as well as the tip substrate. The physical dimensions, resonance frequency and spring constant of the Asylum 240TS silicon cantilevers are the same as for Asylum LM cantilevers as described above, except for a small tip radius of 9±2 nm because of the initial absence of $Co_{80}Cr_{20}$ deposition. After different $Co_{80}Cr_{20}$ coatings between 3 to 10 nm, the tip radius is expected to be between 10 and 20 nm.

Imaging and analysis

Fig. 3.7(a) shows HH and TT VW images in 400 and 500 nm wide and 15 nm thick Py nanostripes. The images were taken with a coating of 10 nm $Co_{80}Cr_{20}$ plus 10 nm of SiO_2. Only in some cases we observed tip-sample perturbations. The sudden appearance of a

sharp contrast of a HH VW in a 500 nm wide nanostripe in the left image of Fig. 3.7(a) indicates that it has been repelled by the tip due to repulsive interaction. As expected, the DW contrast decreased from 0.7 to 0.5° due to lower (10 nm) $Co_{80}Cr_{20}$ coating as compared to the 15 nm for LM commercial tips [Fig. 3.7(b)].

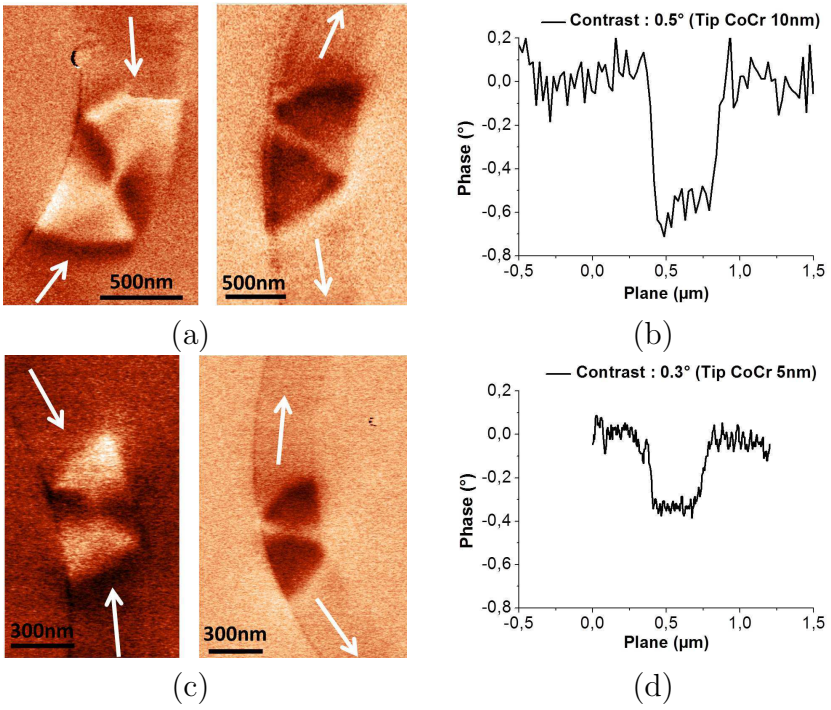

Figure 3.7: Magnetic force microscopy images of vortex walls and phase contrast respectively in (a,b) 400 and 500 nm *wide nanostripes taken with* $Co_{80}Cr_{20}$(10 nm)/SiO_2(10 nm) *tips (c,d)* 300 nm *wide nanostripes taken with* $Co_{80}Cr_{20}$(5 nm)/SiO_2(10 nm) *tips. The cantilever amplitude of oscillation is set to* ∼ 100 nm *during the first pass and* ∼ 75 nm *during the second pass and imaging was done at a lift height of* 10 nm.

To reduce further the tip-DW interaction we imaged again the DWs using tips coated with 5 nm $Co_{80}Cr_{20}$ and 10 nm of SiO_2. Fig. 3.7 (c) shows DWs imaged by these tips. We did not observe any tip-induced DW perturbations and get very nice unperturbed VW images. We repeatedly image the DWs to verify the tip-DW interaction. All the nanostripes of widths between 200 to 500 nm show unperturbed DWs. The DW contrast was decreased to about ± 0.3° as compared to ± 0.5° for 10 nm $Co_{80}Cr_{20}$ tips as shown in Fig. 3.7 (d).

In rare cases, we still observed weak tip-DW interactions with 5 nm $Co_{80}Cr_{20}$ tips. That's why we imaged the DWs again by 3 nm $Co_{80}Cr_{20}$ plus 5 nm SiO_2 coated tips. We did not observe any tip induced perturbation but as expected obtained relatively weak DW contrast ∼ 0.15° as shown in Fig. 3.8.

The experimental results regarding tip-DW interaction and DW contrast as a function of different $Co_{80}Cr_{20}$ coatings is summarized in table 3.2.1. The force gradient is calculated using the following equation.

$$\Delta\Phi = -\frac{Q}{k}\frac{\mathrm{dF}}{\mathrm{dz}} \tag{3.17}$$

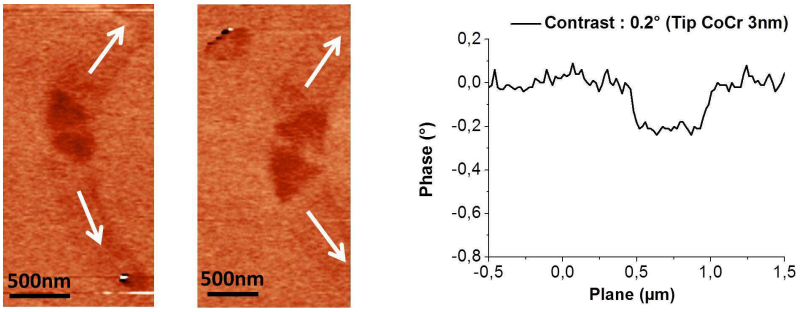

(a) (b)

Figure 3.8: Magnetic force microscopy images of (a) vortex walls and (b) phase contrast in 300 and 500 nm *wide nanostripes with* $Co_{80}Cr_{20}$*(*3 nm*)/*SiO_2*(*5 nm*) tips. The cantilever amplitude of oscillation is set to* ∼ 100 nm *during the first pass and* ∼ 75 nm *during the second pass and imaging was done at a lift height of* 10 nm.

where the DW contrast $\Delta\Phi$ is measured directly from the MFM phase profiles of the DW images. The spring constant k of the cantilever is $\approx 2\,\mathrm{N/m}$. The quality factor Q is calculated by the following relation

$$Q = \sqrt{3}\frac{f_{\mathrm{res}}}{\Delta f} \tag{3.18}$$

where Δf is the full width at half maximum of the cantilever resonance frequency. The quality factor Q calculated for our tips in air when the tip approaches the surface is $Q \approx 200$.

The force gradient calculated experimentally from eq. 3.17 is $\sim 10^{-4}\,\mathrm{N/m}$. We also calculated the force and force gradient directly from the following relations :

$$\mathrm{F} = \mu_0 m_z^t \frac{\partial H_{\mathrm{d}}}{\partial \mathrm{z}} \tag{3.19}$$

where $\mathrm{H_d} \sim \frac{t}{w}\,\mathrm{M_s}$ is the demagnetizing field of the nanostripe of thickness t and width w. $\mathrm{M_s}$ is the saturation magnetization of the magnetic material of the nanostripe.

Putting the value of $\mathrm{H_d}$ in eq. 3.19 and differentiating with respect to w, we get

$$\mathrm{F} \sim \mu_0 m_z^t \frac{\mathrm{t}}{2w^2} M_{\mathrm{s}} \tag{3.20}$$

and the force gradient becomes

$$\frac{\partial F}{\partial z} \sim \mu_0 m_z^t \frac{\mathrm{t}}{3w^3} M_{\mathrm{s}} \tag{3.21}$$

The calculated values of force and force gradient from eqs. 3.20 and 3.21 for a 500 nm wide nanostripe and 10 nm $Co_{80}Cr_{20}$ coated tips are $\sim 10^{-12}\,\mathrm{N/m}$ and $10^{-6}\,\mathrm{N/m}$ respectively. Hence, we can calculate the DW contrast by the following relation

$$\Delta\Phi = \frac{Q}{k}\frac{\partial^2 H_{\mathrm{d}}}{\partial \mathrm{z}^2} \tag{3.22}$$

or

$$\Delta\Phi \sim \frac{Q}{k}\frac{\mathrm{t}}{3w^3}M_\mathrm{s} \tag{3.23}$$

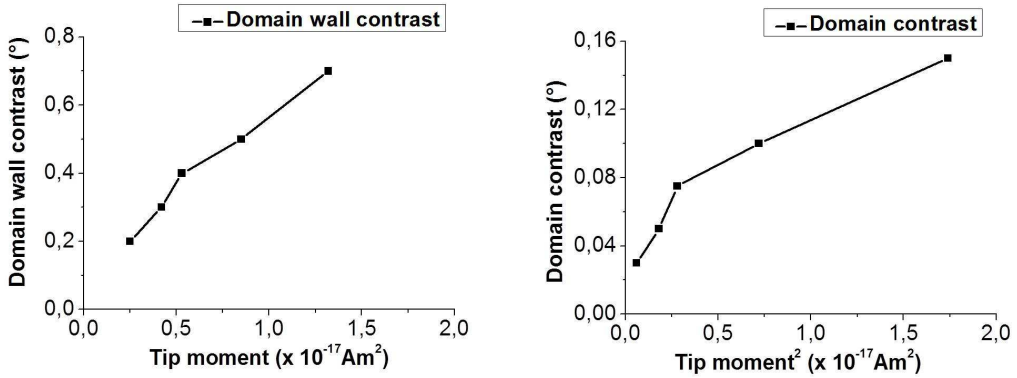

(a) (b)

Figure 3.9: Magnetic force microscopy (a) domain wall contrast (b) domain contrast, as a function of tip magnetic moment and tip moment square respectively (tip moments corresponding to different thicknesses of $Co_{80}Cr_{20}$ thin film coatings). Domain wall contrast is proportional to tip moment and domain contrast is proportional to the square of the tip moment. The cantilever amplitude of oscillation is set to $\sim 100\,\mathrm{nm}$ *during the first pass and* $\sim 75\,\mathrm{nm}$ *during the second pass and imaging was done at a lift height of* $10\,\mathrm{nm}$.

The approximate value of DW contrast, arising from the stray field of DW charges, calculated from eq. 3.23 is $\sim 0.01°$, which is comparable with the experimental value determined by MFM. The DW contrast is proportional to the tip magnetic moment as shown in Fig. 3.9(a). On the other hand in the neutral part of the nanostripe where magnetization is uniform and no stray field is present, the MFM tip's stray field makes the sample magnetization non-uniform. As a result, the sample's stray field interacts with tip's stray field resulting in mutual or so called domain contrast. In this case, the tip domain interaction is always attractive and we get always dark contrast in neutral parts of nanostripes as shown in all MFM images. The domain contrast decreases with decreasing moment of the tip [Fig. 3.9(b)] and is proportional to the square of the tip moment.

In conclusion, we developed low moment magnetic tips for MFM, by depositing thin $Co_{80}Cr_{20}$ films on non-magnetic Si tips to minimize the tip-induced perturbations in the soft magnetic sample. The commercially available low moment tips were not suitable for our very soft Py samples. Very strong attractive and repulsive tip-sample interactions were observed with commercial tips resulting in snatching, dragging and repelling of DWs. Our home-coated 3 and 5 nm $Co_{80}Cr_{20}$ tips show no or very little tip-sample interaction. These tips are suitable to study current induced DW motion in soft magnetic nanostripes.

Tip	Asylum LM CoCr15 nm	Asylum LM CoCr15 nm+ Al_2O_3(50 nm)	AC240TS CoCr10 nm	AC240TS CoCr5 nm	AC240TS CoCr3 nm
Volume $V=\pi r^2 t$ $\times 10^{-23}\,m^3$	1.1	1.1	0.71	0.35	0.21
Moment $m_z^t=\pi r^2 t M_s$ $\times 10^{-17}\,A\,m^2$	1.32	1.32	0.85	0.42	0.25
Force calculated (10^{-13} N)	4.1	4.1	1.7	0.42	0.15
Force grad. calculated (10^{-6} N/m)	0.53	0.53	0.23	0.06	0.02
Domain contrast (°)	0.15	0.12	0.1	0.05	0.03
DW contrast (°)	0.7	0.6	0.5	0.3	0.15
Force grad. experiment. (10^{-4} N/m)	1.22	1.05	0.872	0.523	0.262
Tip-DW interaction	DW snatching dragging and repelling	DW snatching dragging and repelling	DW snatching and repelling	no perturbation	no perturbation

Table 3.2.1: Summary of the tip-DW interactions and DW contrast as a function of commercial low moment magnetic tips and different $Co_{80}Cr_{20}$ thicknesses for home-coated low moment tips. The cantilever amplitude of oscillation is set to ~ 100 nm *during first pass and* ~ 75 nm *during second pass and imaging was done at a lift height of* 10 nm.

Chapter 4

Micromagnetics in spin-valve nanostripes

A system in which two ferromagnetic (FM) layers are separated by a thin non-magnetic metal is called *"Spin-valve"*. Spin-valves exhibit interesting physical phenomena that are important for applications. An example is the *"Giant-Magnetoresistance"* (GMR) effect, which is used in magnetic read heads based on spin-valves. Another is the spin transfer torque effect, the inverse of the giant magnetoresistance effect, which is also an important development in spintronics. We studied experimentally the micromagnetics in Py/Cu(3.5,5 nm)/Co spin-valve nanostripes of width between 100 to 600 nm. Micromagnetic simulations and analytical modeling were also done to compare with the experimental results. In this chapter I will first describe the interlayer coupling in spin-valves, then different results from literature and finally my results with consequences of interlayer coupling.

4.1 Interlayer coupling

In spin valves, the two ferromagnetic layers can be coupled through different types of interactions i.e., exchange [17] or magnetostatic interactions [96]. If FM layers are directly attached or separated by a very thin ≤ 1 nm metallic layer, the exchange interaction is dominant. This interaction is used in synthetic ferrimagnets to increase the coercive field of some layers without changing the remanence magnetization, to act as reference layers [97].

For spacer layers thicker than 3 to 5 nm, the magnetostatic interactions often dominate. These interactions can result into a local decrease of the nucleation barrier for magnetization reversal [141] or demagnetization of one of the layers [129]. They may also play a role in the decrease of the critical current in spin-valve systems for current induced domain wall (DW) motion. [38][67].

4.1.1 Interlayer exchange interactions

The exchange interaction between two ferromagnetic layers can be mediated by a non-magnetic spacer through conduction electrons [17]. The magnetic layer interacts with the conduction electrons of the spacer layer resulting in spin polarization of conduction

electrons, which travel across the spacer layer and interact with other magnetic layer resulting in exchange interaction. This interaction is also known as *"RKKY"* coupling after the name of the scientists Ruderman, Kittel, Kasuya and Yoshida, who discovered this effect [110][58][147]. The exchange coupling oscillates between ferromagnetic or antiferromagnetic with the thickness of the spacer layer and a period depending on the spacer layer material [101][105]. The strength of the exchange coupling decreases very fast with the distance between the magnetic layers. The magnetic coupling through thin layers of Ru, Cu and Cr oscillates with periods, $P_{Cu} \simeq 10\,\text{Å}$ [103], $P_{Ru} \simeq 12\,\text{Å}$ [104] and for Cr with much longer period, $P_{Cr} \simeq$ 18-21 Å [104] in Co/Cu, Co/Ru and Co/Cr superlattices respectively. The exchange coupling can be described by the following assumed relation [63]

$$H_{\text{exch}} = \frac{J_1}{M_s t_f t_s^2} \sin[\frac{2\pi(t_s + \phi)}{\Lambda}] \tag{4.1}$$

Eq. 4.1 shows that the variable parameters describing the exchange coupling are the amplitude J_1 of the interlayer coupling, the period Λ and phase ϕ for a fixed spacer and a free layer of certain thickness. Levy, Maekawa and Bruno describe the J_1 by the following expression [71]

$$J_1 = J_0 \exp(-2K_F^2 \sigma_{\text{LMB}}) \tag{4.2}$$

where J_0 is the amplitude in the case of perfect interfaces and σ_{LMB} corresponds to the interface roughness. k_F is the wavevector of electrons at the Fermi level. In our case the thickness of the metallic spacer layer is 3.5 and 5 nm, so interlayer exchange coupling is negligible.

4.1.2 Interlayer magnetostatic interactions

Néel was the first to consider the magnetic dipolar coupling between the two magnetic layers due to rough interfaces, the so-called Néel *"orange peel"* coupling. In the model of Néel, a sinusoidal roughness profile is considered, and the orange-peel coupling field in case of infinite magnetic film thickness is defined as [63][113]

$$H_N = \frac{\pi^2 h^2 \mu_0 M_s}{2\lambda t_f} \exp(\frac{-2\pi\sqrt{2} t_s}{\lambda}) \tag{4.3}$$

where h and λ are the amplitude and wavelength of the roughness profile as shown in Fig. 4.1(a). t_f and t_s are the thicknesses of free and spacer layer, and M_s is the saturation magnetization of the free layer. H_N and H_M are the fields due to Néel and magnetostatic couplings. Eq. 4.3 shows that the Néel coupling depends on the grain size and associated roughness of the the layers as well as the thickness of spacer and magnetic layers. The sign of the coupling results from an interplay between the magnetostatic, the exchange and the anisotropy energy.

In magnetic thin films, the magnetic poles are at a distance equal to the film thickness resulting in high magnetic stray fields. Free poles are then formed on the wall surface instead of film surface [Fig. 4.1(b)]. For systems of reduced dimensions the magnetic poles generated at the surfaces influence the interactions within the layer and between the two ferromagnetic layers. For two FM layers separated by a thin nonmagnetic layer,

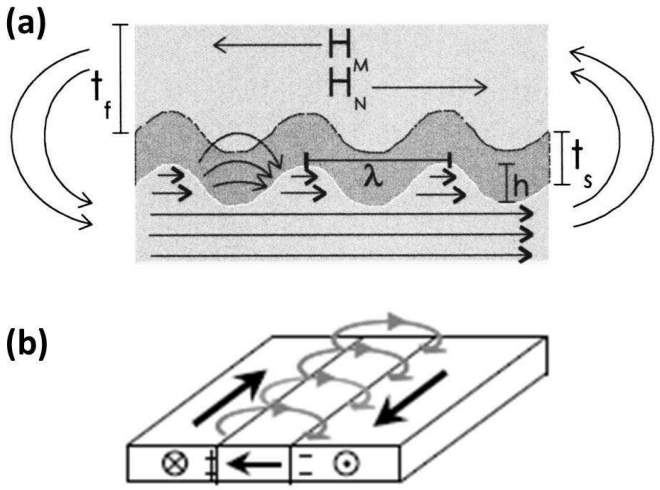

Figure 4.1: Schematics of (a) orange peel coupling between two ferromagnetic layers separated by a non-magnetic spacer [113] (b) DW stray field arising from surface charges from a Néel wall in a thin film.

the stray-field of a DW in one layer will exert a local force in the region above the domain wall in the second layer giving rise to another local type of coupling.

In continuous films, the influence of domain wall stray fields in one layer on the static domain configuration of another layer has been reported by different groups. The influence of the magnetostatic stray fields from Ni domain walls on the Co domain pattern in epitaxially grown Co/Cu/Ni trilayers on Cu(001) have been studied by W. Kuch et al. [64]. The study of as-grown magnetic domain images of the Co (magnetized in-plane) and Ni (magnetized out-of-plane) layers show a lateral displacement of the Co DW position compared to the Ni domain walls. The Co DW displacement was found equivalent to displacement under 25 mT external magnetic field. They confirmed their results by performing micromagnetic simulations.

J. Vogel et al. observed the nucleation of reversed Py domains above Co domain walls in magnetic tunnel junction-like Py(4 nm)/Al_2O_3(2.6 nm)/Co(7 nm) continuous trilayers due to the stray fields generated by domain walls present in the hard magnetic Co layer [141]. The Co domain wall stray field acts as a transverse bias field that locally decreases the energy barrier for nucleation, significantly increasing the local switching speed. They confirmed their results by micromagnetic simulations. They suggested that the effect of domain wall stray fields can be controlled by manipulating the width and position of the domain wall. This allows increasing the local speed and reproducibility of magnetic switching. This effect can be very important for current induced DW motion in trilayers for future Racetrack memory [27].

They have also reported that the stray fields associated with the domain walls in Co and Py layers can lead to an antiparallel coupling between the local Co and Py moments [140]. For domain walls parallel to the easy magnetization axis, this interaction is limited to the DW region itself. For strongly charged (HH or TT) DWs, the antiparallel coupling dominates the interaction over radial distances up to several micrometres from the centre of the DW.

The stray fields of DWs sweeping back and forth during repeated switching of one

of the FM layers can demagnetize the other magnetic layer, even if it is much harder magnetically [129]. L. Thomas et al. proposed a model for a quantitative mechanism of the demagnetization of a hard FM layer due to repeated reversal of a neighbouring soft FM layer, separated by a spacer layer in Co or $Fe_{60}Ni_{40}/Al_2O_3/Co_{75}Pt_{12}Cr_{13}$ trilayer thin films systems. They showed that an interlayer magnetostatic coupling is induced by large stray fields from DWs in the soft (Co or $Fe_{60}Ni_{40}$) layer during its repeated switching and a hard magnetic layer ($Co_{75}Pt_{12}Cr_{13}$) with a Al_2O_3 spacer layer, resulting in demagnetization of the hard layer. They showed that this effect strongly depends on the thickness of the hard and the spacer layers.

In case of spin-valve nanostripes, a magnetostatic coupling between two FM layers also takes place. J. M. B. Ndjaka et al., using micromagnetic simulations, studied the effect of a TW in a Py layer on a initially uniformly magnetized Co layer coupled through a Cu spacer in Py(4 nm)/Cu(L)/Co(4 nm) spin-valve nanostripes [94]. They varied the thickness (L) of the Cu layer in simulations. At equilibrium, the stray field from DWs in the Py layer gives rise to a so-called *"quasi wall"* in the Co layer. They also studied the DW dynamics under moderate field and observed that both the TW and the quasi wall move with the same speed. The effect of the Co layer on the DW dynamics is that the stray field from the quasi wall makes the TW in the Py wider due to the flux closure and hence increases its velocity, however, to a moderate extent. They also suggested that the DW velocity may decrease if the Gilbert damping parameter in the Co layer increases.

We studied the coupling between Co and Py layers separated by a non-magnetic (Cu) layer of thickness 3.5 and 5 nm, both in continuous films and in nanostripes. In the case of nanostripes, the Co layer was initially uniformly magnetized along the nanostripe length and Py layer hosts a DW. For these thicknesses of the Cu spacer layer, the magnetostatic coupling is dominant, so I will describe in detail this interaction.

4.2 Domain wall Phase diagram in spin-valve nanostripes

In our group Nicolas Rougemaille et al. [109] investigated the transverse versus vortex phase diagram of HH DWs in Py/Cu/Co spin-valve nanostripes [Fig. 4.2(a)] with an in-plane anisotropy, combining numerical simulations and analytical modeling. This work extended the phase diagram, already known for single layer Py nanostripes [80][93]. The Co layer is initially set as uniformly magnetized along the nanostripe direction while the Py layer contains a DW. The stability of the TWs in spin-valves is found extended to a range of larger Py thickness as compared to a single layer, due to the magnetostatic coupling with Co layer, which acts as a partial magnetic mirror.

Numerical simulations

The material parameters used for Co and Py are $\mu_0 M_{\mathrm{Co}} = 1.7593\,\mathrm{T}$, $A_{\mathrm{Co}} = 30\,\mathrm{pJ/m}$, $\mu_0 M_{\mathrm{Py}} = 1.0053\,\mathrm{T}$, $A_{\mathrm{Py}} = 10\,\mathrm{pJ/m}$ and zero magneto-crystalline anisotropy in both layers. No exchange coupling is considered between Co and Py layers. The HH transverse or vortex walls were created in Py under different initial conditions, with the Co layer uniformly magnetized. Like Py single layers, in spin-valves, the transverse and vortex

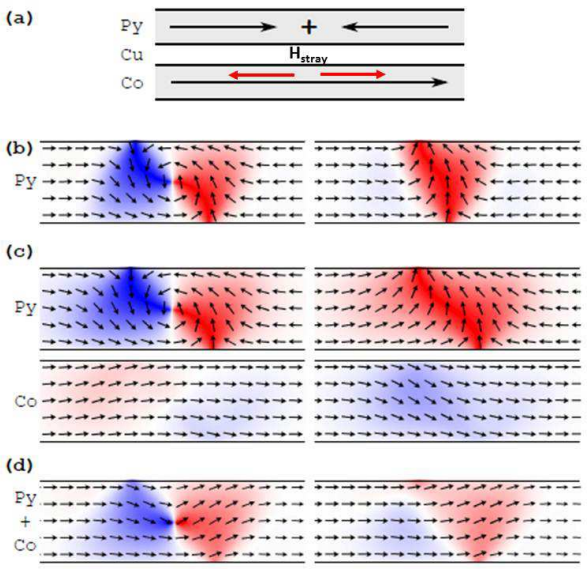

Figure 4.2: (a) The schematic representation of a head-to-head domain wall in a Py layer and associated stray field (red arrows) acting on a uniformly magnetized Co layer in a spin-valve. The black arrows indicate the direction of magnetization in the Py and Co layers. Plain views of a vortex and a transverse wall in a 300 nm *wide (b) Py (*5 nm*) single layer (c) Py(*5 nm*)/Cu(*5 nm*)/Co(*5 nm*) spin-valve nanostripe. (d) thickness integrated maps of magnetization from (c). The red (blue) colour indicates the positive (negative) transverse component of the magnetization, normalized to the magnetization of the layer under focus in (b) and (c), and to half the magnetization of Co in (d). Reproduced from [109].*

walls exist together as metastable states for a large range of geometrical parameters. The micromagnetic simulations show that VWs in both single Py layer and spin-valves are qualitatively similar while TWs were found different in spin-valves. In a single layer Py, TWs are symmetric for small thickness and width [Fig. 4.2(b)], while going towards higher thickness and width, the TW becomes asymmetric. This reduces the magnetostatic energy by spreading the magnetic charges as shown in Fig. 4.2(c).

In spin-valves, the stray field from a DW in the Py layer results in a quasi-wall in the Co layer [Fig. 4.2(c)], which in turn creates a stray field acting on the Py layer. This magnetic screening effect lowers the energy as compared to a single Py layer [94]. The stray field arising from the DW in Py is preferentially parallel or antiparallel to the initial direction of magnetization of Co, depending whether the left or right side of the DW is considered. Thus, the magnetic configuration of Co is expected to be asymmetric and so should be the stray field arising from Co and acting on the Py layer. A TW in a spin valve is therefore expected to be always asymmetric by nature, due to the unidirectional magnetization in the Co. Both the VW and TW have larger widths in a spin-valve, which is associated with the emergence of tails because the decrease of magnetostatic energy allows to reduce exchange energy through an increase of the DW width [53].

The flux closure between the Py and Co layers can be described by the map of the magnetization M_{int} integrated over the two layers along their normal [Fig. 4.2(d)][109].

$$M_{\text{int}} = \frac{1}{t_{\text{Co}} + t_{\text{Py}}} \int M(z)dz \tag{4.4}$$

This shows that the flux is better closed than in a single layer TW, while avoiding the cost associated with the vortex core in a single layer VW. The DW tails of the individual layers [Fig. 4.2(c)] also compensate. As the share of magnetostatic energy is larger in a TW than in a VW [80], the interlayer flux closure lowers the energy of the TW more than that of the VW. This suggests that the TW should be the ground state in a larger range of geometrical parameters in a spin valve than in a single layer. This is verified by the simulations with varying the Py thickness t_{Py} and width w for t_{Co}=t_{Cu}=5 nm as shown in Fig. 4.3. In single Py layer both transverse asymmetric left and right DWs are the lowest energy states while in spin-valves there is only one type of asymmetric TWs having the lowest energy due to the unidirectional magnetization in the Co layer.

Analytical modeling

For Py single layers, McMichael and Donahue calculated numerically the transverse and vortex wall energy as a function of nanostripe width and thickness. They found that TWs have a lower energy than VWs for small values of t and w and suggest a phase boundary of the form [80] :

$$tw = C\Delta_d^2 \tag{4.5}$$

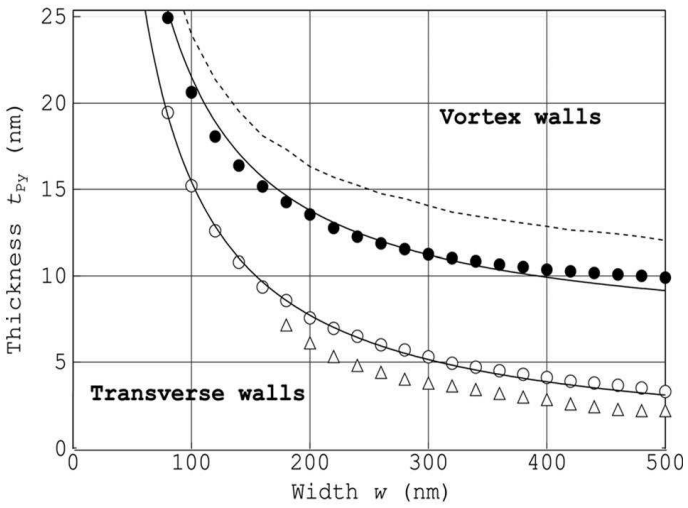

Figure 4.3: Phase diagram of head-to-head domain walls in stripes, with the boundary between symmetric and asymmetric TWs (Open Triangles), and TW and VW (Open circles) in a single layer, and asymmetric TW and VW in a spin valve (Full disks). The dotted line corresponds to the phase boundry with thickness translation t_{sh} ($t_{Cu} = 0$) [109].

where $\Delta_d = \sqrt{\frac{A}{K_d}}$ is the dipolar exchange length, $K_d = \frac{\mu_0}{2} M_s^2$ is the dipolar constant, and C is a constant. The numerical value of C $\approx$ 61-64 must be provided by simulations [80][93]. The above scaling law (eq. 4.5) can be adopted taking into account accordingly using partial flux closure in spin-valves to refine the magnetostatic energy [109] :

$$w(t - t_{\mathrm{sh}}) \approx C\Delta_{\mathrm{d}}^2 \tag{4.6}$$

with the same C value. This suggests that the phase diagram for a spin valve may be derived from that of a single layer, shifted towards higher thicknesses by a value t_{sh}. This is in good agreement with the results of numerical simulations as shown in Fig. 4.3. An empirical scaling law is found for t_{sh} [109] :

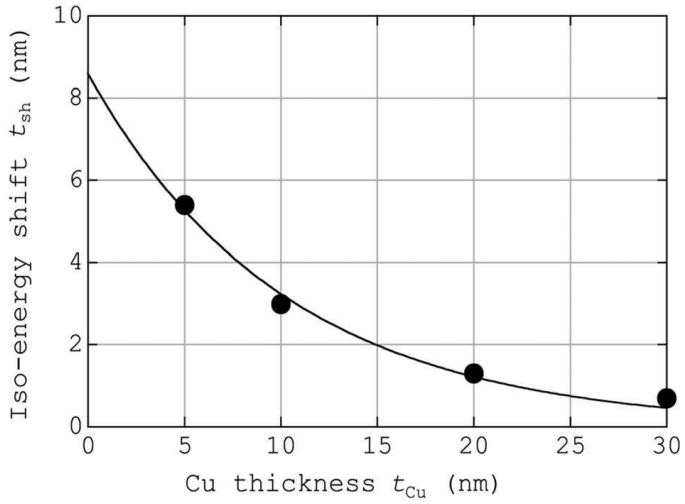

Figure 4.4: Thickness shift t_{sh} of the iso-energy line in a spin valve compared to a single layer, for $w = 100\,\text{nm}$ and $t_{Co} = 5\,\text{nm}$ [109].

$$t_{\text{sh}} = t_{\text{Co}} \frac{M_{\text{Co}}}{M_{\text{Py}}} \exp\left(-\frac{t_{\text{Cu}}}{t_0}\right) \tag{4.7}$$

where $t_0 \approx 10\,\text{nm}$ is derived from Fig. 4.4, which shows the thickness shift of the iso-energy line in a spin valve compared to a single layer, for $w = 100\,\text{nm}$ and $t_{\text{Co}} = 5\,\text{nm}$. The iso-energy line in spin valves is shifted towards a larger thickness with respect to single layers, by a value decreasing approximately exponentially with the spacer thickness.

4.3 Experimental results

4.3.1 Experimental details

The epitaxial Py 15 nm single layer, epitaxial Py(15, 20 nm)/Cu(3.5 nm)/Co(5 nm) and sputtered Py(15, 20 nm)/Cu(5 nm)/Co(5 nm) spin-valves were deposited on sapphire(0001) and Si substrates respectively. S-shaped nanostripes of different thicknesses and widths between 200-600 nm were patterned by combined electron-beam lithography and ion-beam etching techniques by Stefania Pizzini. A strong field of 30 mT transverse to the nanostripes was applied to create DWs at the bends of the nanostripes. This field was large enough to have DWs in both single Py and spin-valve Py layer, because it was optimized experimentally by switching the Py magnetization in nanostripes under transverse field. The demagnetizing field for Co layer is higher than Py, so we expect no DW in the Co layer. The imaging of DWs in spin-valves was thus performed with uniformly magnetized Co.

We applied MFM to observe the DW configurations in nanostripes. 5 nm $Co_{80}Cr_{20}$ home coated magnetic tips were used for imaging DWs. The tips were capped with 10 nm SiO_2 to protect against oxidation.

We also performed high spatial resolution (< 40 nm), x-ray photo emission electron microscopy combined with x-ray magnetic circular dichroism (XMCD-PEEM) measurements to see individually the magnetic configuration of Py and Co layers. The measurements were done at the Nanospectroscopy beamline at the synchrotron ELETTRA (Trieste, Italy). Element selective magnetic imaging was done using XMCD, with the x-ray energy tuned to the maximum of the Fe L_3-absorption-edge (707 eV) for the Py layer and of the Co L_3-edge (778 eV) for the Co layer. The x-ray absorption results in transition of a core-electrons to the empty levels above the Fermi surface, leaving behind empty core levels which are then filled by electrons relaxing from higher energy levels. The difference of energy is provided to Auger electrons which are emitted out of the atoms resulting in secondary electron emission which is proportional to X-ray absorption. These secondary electrons emitted from the material for a fixed circular polarization provide us a map of the magnetization in the sample. Lorentz microscopy was also performed by Aurélien Masseboeuf at LEMMA/INAC/CEA, Grenoble to clarify the magnetization processes in nanostripes.

4.3.2 Results and discussion

The coupling field or strength between two layers can be accurately determined by the measurement of the shift of the free-layer minor hysteresis loop. Before patterning nanostripes, we performed quasistatic hysteresis loops using Kerr magnetometry to study the coupling between continuous Py (free layer) and Co (pinned layer) layers in spin-valves. Fig. 4.5(a-b) shows the magnetization hysteresis loops along the easy axis, taken at 11 Hz frequency, for spin-valves with Py thickness 15 and 20 nm respectively. The two steps in hysteresis loops (black curves) corresponds to the reversal of free (small coercive field) and the pinned layers (large coercive field) of the spin-valves. The Py minor loops (red curves) show a shift of about 0.4 mT with respect to zero field attributed to orange-peel coupling strength.

Fig. 4.6(a) shows the VW (left) in a 300 nm wide and 15 nm thick Py nanostripe. The other Py nanostripes of similar thickness and of widths between 200 and 600 nm also contain VWs. This is in agreement with the DW phase diagram for single Py layers which also predicts VWs for this type of thickness and width of Py nanostripes [93]. The MFM image shows a DW contrast of $\pm$ 0.3° with a 5 nm $Co_{80}Cr_{20}$ tip. The imaging was done with a cantilever oscillation amplitude $\sim$ 100 nm in the first pass and $\sim$ 75 nm in the second pass with a lift height of 10 nm.

On the contrary, we observed asymmetric transverse walls in the spin-valve nanostripes of similar Py thickness and widths between 200 and 600 nm. Fig. 4.6(a) shows the asymmetric TW (right) in a 600 nm wide Py(15 nm)/Cu(5 nm)/Co(5 nm) spin-valve nanostripe taken with the same 5 nm $Co_{80}Cr_{20}$ tip under the same imaging parameters as for single Py layer nanostripe as described above. A DW contrast of $\pm$ 0.15° was observed for TWs in spin-valve nanostripes. As in MFM we measure the stray field, the 50% decrease in the DW contrast as compared to VWs in single Py layers is the confirmation of the partial flux closure between the Py and Co layers due to the antiparallel coupling as predicted in the spin-valve phase diagram.

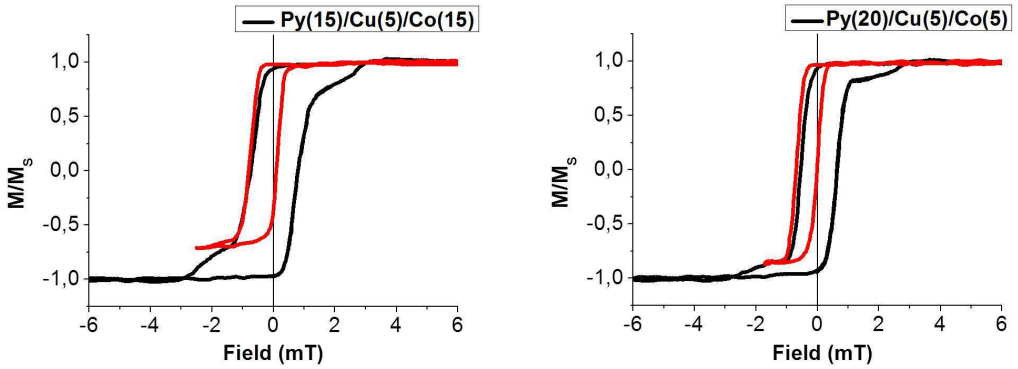

(a) (b)

Figure 4.5: Quasi-static hysteresis loops along the easy axis of (a) Py(15 nm)/Cu(5 nm)/Co(5 nm) and (b) Py(20 nm)/Cu(5 nm)/Co(5 nm) continuous spin-valve films obtained by longitudinal Kerr magnetometry at 11 Hz frequency. The minor loops for the Py layer taken along the easy axis are represented by red curves. These loops show a shift of 0.4 mT with respect to zero field, which is the direct measure of the coupling strength between Py and Co layers.

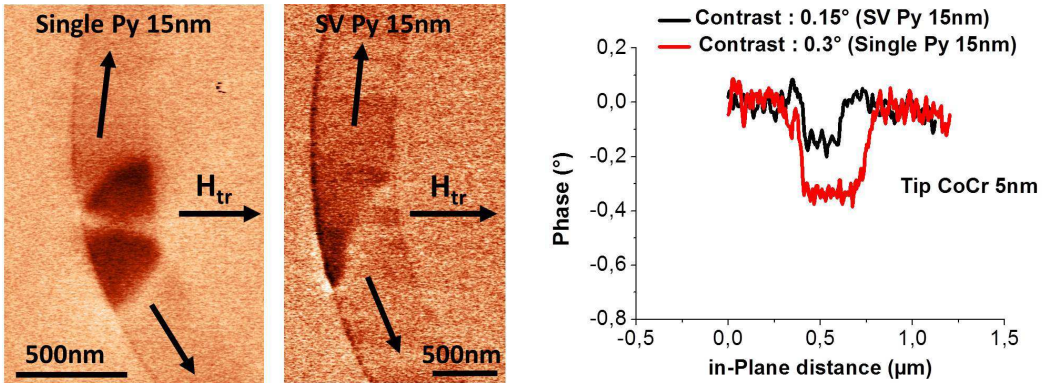

(a) (b)

Figure 4.6: Magnetic force microscopy (a) images of a vortex and an asymmetric transverse wall (b) magnetic phase contrast of domain walls, in a 15 nm thick and 300 nm wide Py single layer and 600 nm wide Py(15 nm)/Cu(5 nm)/Co(5 nm) S-shaped spin-valve nanostripe respectively taken with a 5 nm $Co_{80}Cr_{20}$ magnetic tip using the same imaging parameters. The cantilever amplitude of oscillation is set to ∼ 100 nm during the first pass and ∼ 75 nm during the second pass and imaging was done at a lift height of 10 nm.

For spin-valve nanostripes with larger Py thickness (20 nm), we observed both asymmetric TWs and VWs. For nanostripe widths between 200 and 400 nm we observed only asymmetric TWs while for 500 and 600 nm wide nanostripes both asymmetric transverse and vortex walls were found. Fig. 4.7 shows both asymmetric transverse and vortex walls in 600 nm wide Py(20 nm)/Cu/Co(5 nm) spin-valve nanostripes with Cu thickness 3.5 and 5 nm respectively.

Fig. 4.8 shows both the experimental and simulated phase diagram for a single Py layer and Py/Cu/Co spin-valve nanostripes for different Py thicknesses and nanostripe widths.

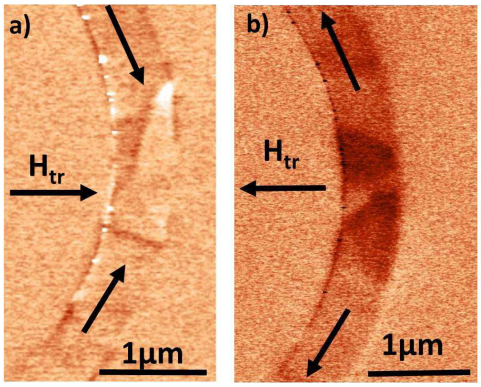

Figure 4.7: Magnetic force microscopy images (a) asymmetric transverse wall (b) vortex wall, in a 600 nm *wide Py(*20 nm*)/Cu/Co(*5 nm*) spin-valve nanostripe with Cu thickness 3.5 and* 5 nm *respectively, taken with a* 5 nm $Co_{80}Cr_{20}$ *magnetic tip. The black arrows indicate the direction of transverse field applied to create domain walls. The imaging parameters were same as for previous sample.*

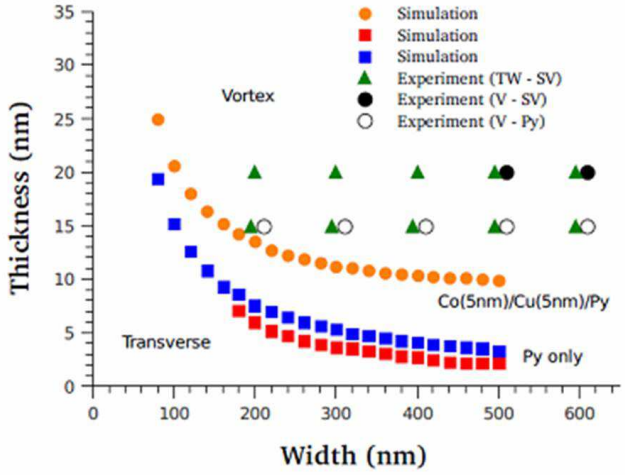

Figure 4.8: Simulated phase diagram for Py and Py/Cu/Co spin-valves nanostripes, together with some experimental points. The numerical simulations show the phase boundary between symmetric and asymmetric transverse walls (red squares), and transverse and vortex walls (blue squares) in a single Py layer, and asymmetric transverse and vortex walls in a spin-valve (filled orange disks). The experimental points indicate the observation of TWs (green triangles and filled black disks) and VWs (blank circles) for the different samples.

In our experimental results, we find mainly TWs, even where VWs are expected. These are the metastable TWs stabilized through the application of the transverse magnetic field. Nevertheless, TWs are found in a larger area in spin-valves compared to single layers, confirming the model and simulations.

Fig. 4.9 shows the XMCD-PEEM image of an asymmetric transverse wall in a Py layer and the Co layer without a DW, in a 600 nm wide Py(15 nm)/Cu(5 nm)/Co(5 nm) spin-valve stripe. As explained in section 4.2, the stray field of a DW in a Py layer can perturb a uniformly magnetized Co layer resulting a quasi-wall in the Co layer. We could not see

the DW in Co due to the thicker Py layer as the secondary electrons we use in PEEM to obtain the map of magnetization cannot escape from the material, and are absorbed by the Cu and Py layers due to higher thicknesses. But we can see the white magnetic contrast in the Co XMCD opposite to Py XMCD (black) at the side of the stripe, at the position where the DW is located in the Py layer. The appearence of this contrast at the nanostripe edge is shown schematically in Fig. 4.9 (c).

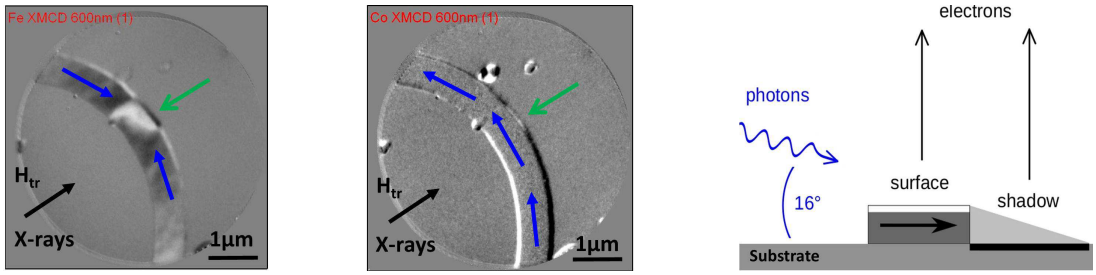

(a) (b) (c)

Figure 4.9: XMCD-PEEM image (a) asymmetric transverse wall in a Py layer (b) Co layer without a domain wall, in 600 nm *wide Py(*15 nm*/Cu(*3.5 nm*)/Co(*5 nm*) S-shaped spin-valve nanostripe. The black arrows indicate the direction of transverse field applied to create domain walls and the direction of the incoming x-rays. The blue arrows show the magnetization direction in the nanostripes. (c) Schematic of appearence of opposite contrast at the nanostripe edge for Co XMCD, at the position where the DW is located in the Py layer represented by green arrows in XMCD-PEEM images.*

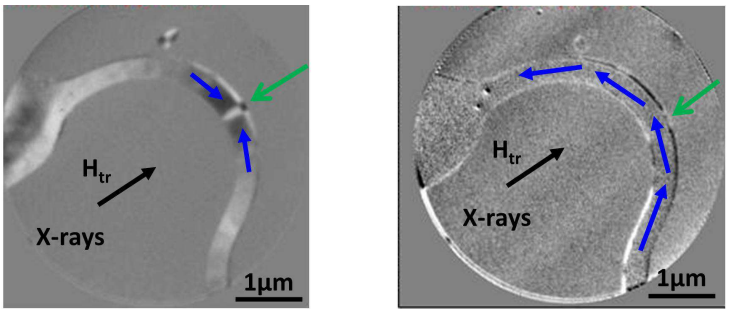

(a) (b)

Figure 4.10: XMCD-PEEM images of narrow domain walls in the Py layer of a 300 nm *wide Py(*15 nm*/Cu(*3.5 nm*)/Co(*5 nm*) S-shaped spin-valve nanostripe with also a domain wall in the Co layer (a) XMCD image of the Py layer, containing a narrow transverse wall (b) XMCD image of the Co layer. The black arrows indicate the direction of the transverse field applied to create domain walls and the direction of the incoming x-rays. The blue and green arrows show the magnetization direction and position of domain walls in the nanostripes.*

For magnetic imaging, we take two images, one with left and one with right circularly polarized x-rays, and then we take the asymmetry (the dfference divided by the sum of the two images). This increases the magnetic contrast and decreases the topographic contrast. The photons of one chirality are absorbed by the magnetic material giving black or white contrast, while the photons of other chirality are transmitted and are absorbed

by the substrate resulting in emission of the electrons from the substrate giving opposite contrast at the nanostripe edge. Like we observed in MFM, this is again the evidence of the local antiparallel coupling of Py and Co layers in the DW region.

The magnetic imaging of DWs was also performed by creating DWs, both in Co and Py layers. For this purpose we applied a strong enough field transverse to the stripes such that the Co layer also hosts a DW. This results in a much better flux closure between Py and Co layers resulting in narrow DWs. Fig. 4.10(a-b) shows the XMCD-PEEM images of narrow TWs in a Py and a Co layer respectively. Again, except on the sides of the stripe, we can not see the DW in Co layer due to the higher Cu and Py thicknesses.

In conclusion, we have investigated transverse versus vortex DW phase diagram in spin-valve nanostripes, using numerical simulations and analytical modeling. The Co layer is initialized uniformly magnetized while the Py layer contains a DW. MFM imaging confirms the numerical results and shows that the range of stability of TWs is shifted towards higher thickness as compared to single Py layers due to a magnetostatic screening effect between the two ferromagnetic layers. Secondly, the transverse walls are always asymmetric in spin-valves to a larger extent than in single layers.

Chapter 5

Field and current induced domain wall motion

5.1 Quasistatic field induced domain wall depinning in magnetic nanostripes

The precise control of DW pinning and depinning from artificially created pinning sites in magnetic nanostripes is very important for future spintronic devices based on DW propagation e.g., *"Racetrack Memory"* [102]. The DW depinning from natural defects or artificial pinning sites in magnetic nanostripes has been studied by several groups, both in systems with in-plane [134][55] and out-of-plane magnetization [25][23], under field and an electric current. The DW depinning revealed stochastic behaviour in these results.

5.1.1 Samples and experimental details

We studied the quasi-static field-induced DW depinning from natural defects in epitaxial Py single, Py/Ir bilayer and sputter-deposited Py/Pt bilayer nanostripes. Both Py and Py/Ir films were deposited on sapphire(0001) substrate of miscut angle 0.05° and were capped by 2 nm Au to protect against oxidation. Py/Pt films were sputter-deposited on a naturally oxidized Si substrate and were capped by Al(2 nm)/Cu(3 nm). S-shaped, 12 µm-long Py (15 nm) single layer and 20 µm long Py(10 nm)/Ir(10 nm) and Py(15 nm)/Pt(10 nm) bilayer nanostripes were prepared by combined electron-beam lithography and ion-beam etching techniquesa. The width of nanostripes is between 100 to 500 nm. The S-shape was choosen to nucleate the DWs at the bends of nanostripes under applied transverse field. The HH and TT DWs were created by applying an in-plane magnetic field (H_{tr}) $\sim$ 50 mT transverse to the nanostripes. MFM was used to observe the DW configurations before and after applying a quasistatic pulse of magnetic field.

We used an electromagnet to apply field pulses of few seconds duration in order to depin the DW. The field was calibrated using a Hall probe. Different field amplitudes were used to find the minimum field required to depin the DW. Below I will describe the results obtained for both Py single and bilayer nanostripes.

5.1.2 Field induced DW depinning in epitaxial Py nanostripes

First, we studied the field induced depinning of DWs in 12 µm long S-shaped Py(15 nm) nanostripes. We observed VWs in these nanostripes as predicted by the DW phase diagram [93]. Fig. 5.1(a) shows the topography of 400 and 500 nm wide stripes. The MFM images of the HH and TT vortex walls at the bends of these stripes represented by white and black MFM contrast respectively are shown in Fig. 5.1(b).

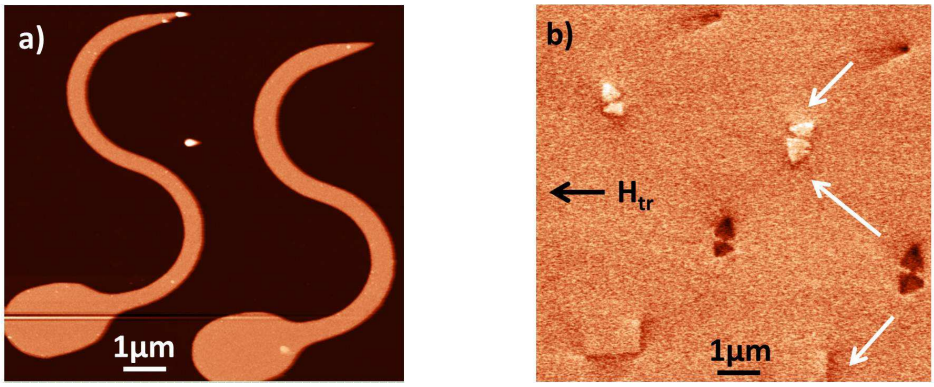

Figure 5.1: 400 and 500 nm *wide Au(2nm)/Py(15nm)/Al_2O_3(0001) nanostripes (a) The AFM topography (b) MFM images of the HH and TT vortex walls at the bends of the stripes represented by white and black MFM contrast respectively. The VWs were created by applying an in-plane magnetic field (H_{tr})* $\sim$ 50 mT *transverse to the stripes, in the direction indicated by the black arrow. The white arrows show the direction of magnetization in the nanostripe.*

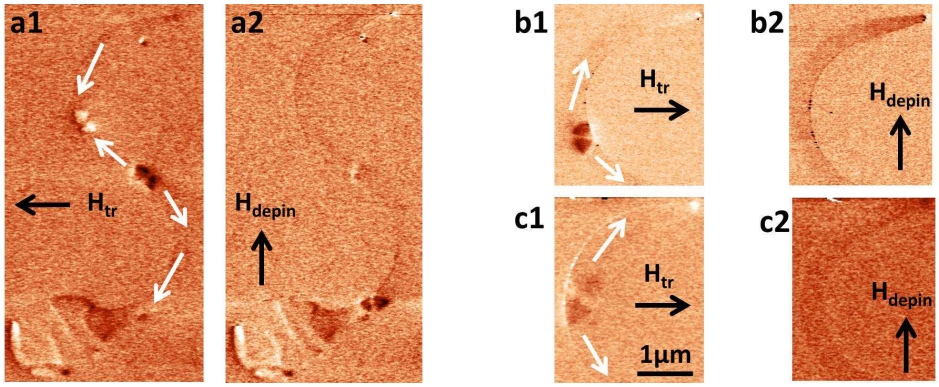

Figure 5.2: MFM images of (a1,a2) HH and TT vortex walls in a 300 nm *wide stripe before and after applying a longitudional magnetic field of* $\sim$ 2.5 mT *along the stripes. (b1,b2) and (c1,c2) TT vortex walls in 400 and* 500 nm *wide stripes respectively, before and after applying a longitudional magnetic field of* $\sim$ 2 mT.

Fig. 5.2(a1) shows the initial configurations of HH and TT vortex walls in a 300 nm wide nanostripe. After applying a longitudional magnetic field (H_{depin}) of 2.5 mT these DWs moved in opposite directions, as expected. The (white) HH wall moved upward towards the nanostripe sharp end. This is clear from the change of the contrast from black to white at the end of the stripe as shown in Fig. 5.2(a2). The (black) TT wall

moved downward and got pinned near the bottom end of the stripe where it was slightly damaged topographically.

Similarly, Fig. 5.2(b1,c1) shows the initial configuration of TT VWs in one bend of 400 and 500 nm wide stripes respectively. After applying a 2 mT longitudional magnetic field (H_{depin}), both DWs moved along the magnetic field towards the sharp end of the stripes, reversing the magnetic contrast from white to black as shown in Fig. 5.2(b2,c2).

In summary, we observed a stochastic behaviour of the field-induced DW depinning, as also reported in literature. Slightly different depinning fields were observed for similar nanostripes of same width and thicknesses at different nanostripe positions near the center of nanostripe bends. This could be due to different projection of longitudional fields at different positions due to the nanostripes curvature and different pinning potentials at different positions due to the edge roughness or intrinsic material defects. The DWs in 400 and 500 nm wide stripes exhibit depinning fields of almost the same magnitude. For these stripes, the depinning field ranges between 1.5 and 2.5 mT. In 300 nm wide nanostripes slightly higher depinning fields between 2 and 3 mT were found. The average depinning field for 400 and 500 nm stripes is thus about 2 mT while for 300 nm wide stripes, it is $\sim$ 2.5 mT.

5.1.3 Field induced DW depinning in epitaxial Py/Ir and sputtered Py/Pt bilayer nanostripes

We also studied the DW depinning in 20 µm long, 300-400 nm wide S-shaped epitaxial Py(10 nm)/Ir(10 nm) and sputtered Py(15 nm)/Pt(10 nm) bilayer nanostripes. In these stripes, initially all DWs were transverse when prepared under in-plane magnetic field transverse to the stripes. These metastable TWs can be transformed to VWs and vice versa by applying a magnetic field. In these samples we were close to the DW phase boundary and metastable transverse and vortex walls can exist together.

The DWs in epitaxial Py/Ir samples revealed a similar stochastic behaviour as in single epitaxial Py layers. The average DW depinning field is also almost the same, $\sim$ 2 mT for 400 nm wide stripes and $\sim$ 2.5 mT for 300 nm wide stripes. The sputtered Py(15 nm)/Pt(10 nm) bilayer nanostripes, however, showed smaller depinning field between 0.5 and 1 mT for 400 and 500 nm wide stripes and between 1 and 1.5 mT for 300 nm wide stripes, thus average depinning fields of 0.75 mT and 0.12 mT respectively. These depinning fields are almost one half of the epitaxial samples.

The micromagnetic simulations predict the DW depinning field $\sim$ 0.1 mT for 5 nm thick and 120 nm wide rough nanostripes with roughness parameter $D = 10$ nm (corresponds to the grain size) and Gilbert damping parameter α=0.01 [127]. In our case, the relatively higher DW depinning field $\sim$ 2 and 2.5 mT for 400 and 300 nm wide stripes respectively and α=0.01, indicates the presence of DW pinning due to the nanostripe edge roughness or intrinsic material defects.

The possible explanation is that our films are not purely single crystalline but instead epitaxial bi-crystalline, with two fcc (111) epitaxial twins rotated by 180° with respect to each other around the ¡111¿ planes. The size of the grains in our epitaxial bi-crystal samples is relatively large with respect to the polycrystalline samples and comparable to the stripe width (See chapter2 STM images Py and Py/Ir growth). This explains that the effect on DW pinning may be quite strong. Moreover, the DW depinning fields in our continuous films before patterning are an order of magnitude lower than for nanostripes

(See chapter2 section 2.5). On the other hand sputtered samples showed almost the same depinning field as predicted by micromagnetic simulations for rough nanostripes with roughness parameter $D = 10\,\text{nm}$. This shows the weaker DW pinning of sputtered samples as compared to the epitaxial samples.

5.2 Important current effects in nanostripes

We are interested in studying the DW motion in nanostripes, related to the spin polarization of conduction electrons, but other current-induced effects have to be taken into account as well. The most important of those are the Joule heating and the Oersted field. Before presenting my experimental results regarding current-induced DW motion I will first describe these effects.

5.2.1 Joule heating

The high current densities required to move DWs can cause significant Joule heating in samples. Joule heating may result in an increase of the critical current density needed to move the DWs [69] by decreasing spin polarisation [149] and magnetic moment [130]. On the other hand, it may assist the DW depinning because thermal excitations may reduce the energy barrier of a pinned DW [24]. At very high temperature, above the Curie temperature, the nucleation of multi-domains has also been reported [144].

Joule heating strongly depends on the current density, the current pulse duration, the resistivity of the sample, the thermal conductivity of the underlying substrate and contacts and geometry. The resistivity of the sample increases with heating, resulting in a decrease of the current density when using voltage pulses as we did in our experiments. To accurately determine the value of the current density required to move DWs, the effect of Joule heating must therefore be taken into account. The choice of substrate is very important to minimize the Joule heating. The substrate should be a good electrical insulator to avoid short circuiting and a good thermal conductor for better heat dissipation during and after the current pulse.

We used sapphire(0001) single crystal substrate to epitaxially grow the Py films. Sapphire is a very good electric insulator but a relatively poor heat conductor as compared to a naturally oxidised Si substrate. The thermal conductivities for Si and sapphire are 148 W/mK and 23 W/mK respectively at RT. The RT electrical resistivity of Si is $3.2 \times 10^5\,\Omega/\text{cm}$ and that of sapphire is $10^{14}\,\Omega/\text{cm}$. We also studied some sputter-deposited samples on naturally oxidised Si substrates. We observed significant Joule heating for samples on sapphire, but negligible Joule heating on naturally oxidised Si for similar current densities.

We used current densities between 3 and $4.3 \times 10^{12}\,\text{A/m}^2$, for Py single layers deposited on sapphire. The current pulses were recorded by an oscilloscope, which shows that there is a 13 to 40% decrease in the pulse amplitude at the end of the current pulses of different current densities and pulse lengths, as shown in Fig. 5.3(a,b). This indicates significant Joule heating which depends on the current density as well as the pulse length.

Yamaguchi et al. estimated the sample temperature of 20 µm long, 10 nm thick and 240 nm wide L-shaped Py nanostripes deposited on thermally oxidized Si substrate by measuring the sample resistance during the application of a current pulse. They measured

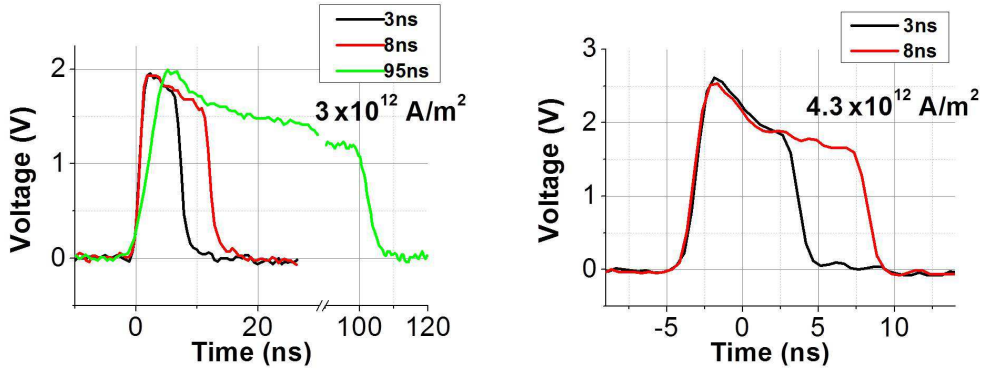

(a) (b)

Figure 5.3: Effect of Joule heating on current pulse amplitude at current densities of (a) $3 \times 10^{12}\,\mathrm{A/m^2}$ *and (b)* $4.3 \times 10^{12}\,\mathrm{A/m^2}$ *in* 12 µm *long and 300-*400 nm *wide Au(*2 nm*)/Py(*15 nm*)/Al*$_2$*O*$_3$*(0001) nanostripes. 13 to 40% decrease in the pulse amplitude at the end of the current pulses for different current densities and pulse lengths is observed.*

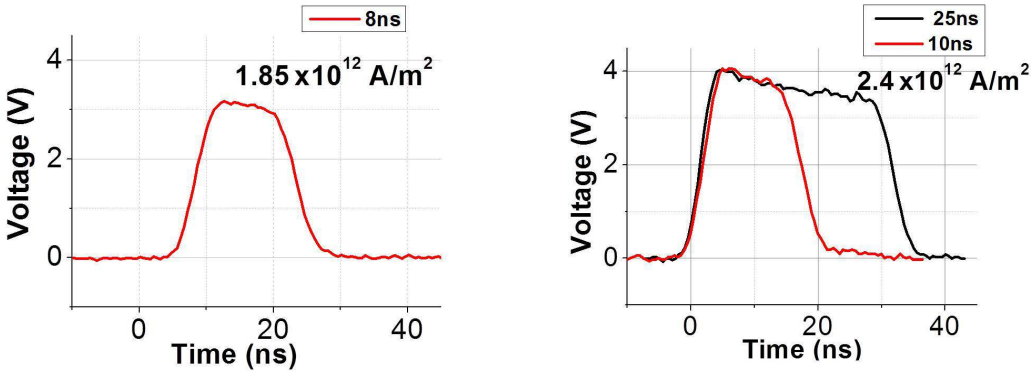

(a) (b)

Figure 5.4: Effect of Joule heating on current pulse amplitude at current densities of (a) $\sim 1.85 \times 10^{12}\,\mathrm{A/m^2}$ *and (b)* $\sim 2.4 \times 10^{12}\,\mathrm{A/m^2}$ *in* 20 µm *long and 100-*400 nm *wide Au(*2 nm*)/Py(*10 nm*)/Ir(*10 nm*)/Al*$_2$*O*$_3$*(0001) nanostripes. 6.5 to 16% decrease in the pulse amplitude at the end of the current pulses for different current densities and pulse lengths is observed.*

a 76% change of resistance (compared to the RT value) for the threshold current density of $6.7 \times 10^{11}\,\mathrm{A/m^2}$, resulting in a 150% rise of temperature (750 K) compared to RT [144]. As we observed a 13 to 40% decrease in current (resulting in a 13 to 40% increase in resistance, as both are proportional), comparing with above results, we estimated our sample temperature between 350 to 510 K.

For Py/Ir bilayers deposited on sapphire lower current densities (between 5×10^{11} and $2.45 \times 10^{12}\,\mathrm{A/m^2}$) were required to move the DWs than for Py single layers, which results into less Joule heating . Fig. 5.4(a,b) shows a 6.5 to 16% decrease in current pulse amplitude for current densities of $1.85 \times 10^{12}\,\mathrm{A/m^2}$ and $2.45 \times 10^{12}\,\mathrm{A/m^2}$, respectively. The estimated temperatures corresponding to this decrease in current values are 310 and 360 K respectively. For Py/Pt samples deposited on naturally oxidized Si no decrease in

current pulse amplitude was seen for similar current densities. This indicates the good thermal conductivity of naturally oxidized Si compared to sapphire.

5.2.2 Oersted field

The current-induced Oersted field in nanostripes is in directions transverse to the nanostripes. In Py or other soft materials the magnetization is essentially along the nanostripes length due to the shape anisotropy. Thus the Oersted field should not favour the DW motion along the nanostripes. However, the Oersted field may act on the DW configuration and, for example, make TWs wider or narrower, acting parallel or antiparallel to TW magnetization [18]. The Oersted field may thus stabilize transverse walls, preventing DW transformations. This can result in a suppression of the Walker breakdown for a given stimulus magnitude resulting in an increase of the average DW velocity, like it was observed for field induced DW motion in Py nanostripes in the presence of a transverse magnetic field [18] [111].

D. Morecroft et al. studied experimentally the effect of an Oersted field on current induced reversal in the presence of a bias field in 2.1 µm long and 270 nm wide notched Co/Cu/Py spin-valve nanostripes [90]. The micromagnetic simulations using a 3D micromagnetic model were performed to compare with experimental results. The Py reversal starts due to a bias field and the Oersted field from the current pulse helps reversal at a bias field below the switching field. The reversal process was found different from field induced reversal. It was observed that the Oersted field promotes the depinning of a DW. The spin torque effects were neglected in these measurements.

Another effect of Oersted field is a transverse tilt in the Py magnetization in the case of asymmetric Co/Cu/Py nanostripes, during current pulses. This was observed in time resolved XMCD-PEEM measurements [136]. The underlying Co layer enhances this effect, acting as a magnetic mirror for the Py layer.

We investigated the effect of the Oersted field on the DW chirality in Py/Ir bilayer nanostripes, using MFM. Using Ir instead of a spin-valve, allows separating the effect of an Oersted field from flux-closure magnetostatic interactions between the Py and Co layers or vertical spin currents [38]. The strength of the Oersted field for a given current density is varied by varying the thickness of the metallic Ir underlayer. For higher Ir thickness, there will be more current through the stripes resulting in a higher Oersted field but for a same current density. We considered the same Ir and Py resistivities and thus the same current flowing and same current densities in Ir and Py layers of equal thicknesses.

We studied two types of samples with different Ir thicknesses, Py(10 nm)/Ir(10 nm) and Py(10 nm)/Ir(15 nm) deposited on sapphire(0001) and capped by 2 nm Au. TWs were created at the bends of 10 and 20 µm long, 300 and 400 nm wide curved and S-shaped nanostripes by applying a transverse magnetic field of 50 mT. The current pulses of different current densities between 1.5 to 2.4×10^{12} A/m^2 and pulse length of 3 ns were applied. The Oersted field is not uniform over the Py thickness, thus we considered as the average Oersted field, the value calculated at the center of the Py layer. We estimated the Oersted field by using the following relation.

$$B_z = \mu_0 J z \tag{5.1}$$

where J is the current density and z is the height measured from the center of the Py/Ir bilayer structure [Fig. 5.5 (a)].

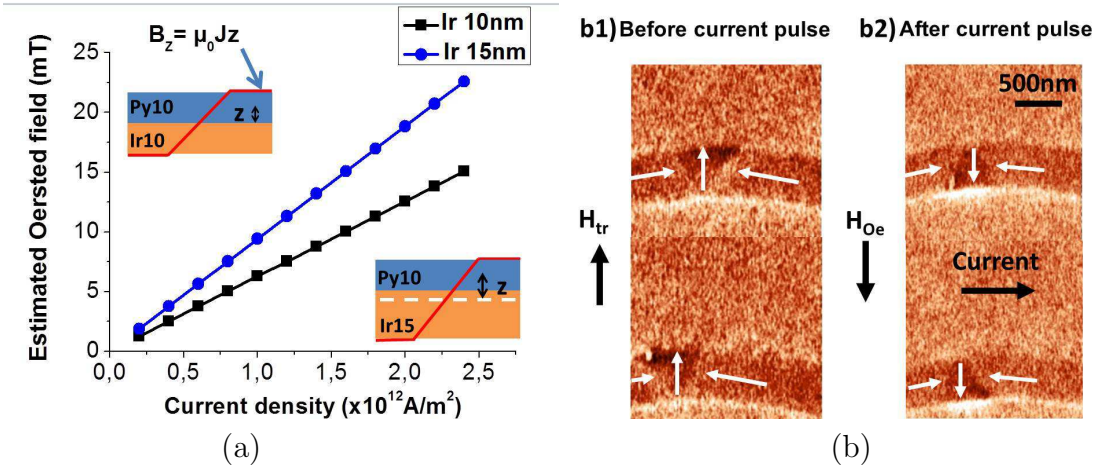

(a) (b)

Figure 5.5: (a) Oersted field profile (B_z) as a function of current density and Ir thickness. The y-axis corresponds to the estimated average Oersted field acting at the middle of the Py layer. The z is the distance from the center of the Py/Ir bilayer structure to the center of the Py layer. The red line shows the Oersted field profile acrosss the Py thickness. (b) TW chirality switching by an Oersted field in 20 µm *long and* 400 nm *wide S-shaped Au(*2 nm*)/Py(*10 nm*)/Ir(*15 nm*)/(Al_2O_3(0001) nanostripes. MFM images (b1) Initial configuration of head to head TWs (b2) after applying a* 2×10^{12} A/m^2, 3 ns *current pulse.*

Fig. 5.5(b1) shows the initial configuration of HH TWs in 400 nm wide Py(10 nm)/Ir(15 nm) nanostripes. The polarity of the current pulses was chosen such that the Oersted field was opposite to the initial magnetization direction inside the TW. After applying a current pulse of density 1.6×10^{12} A/m^2 and pulse length 3 ns, all the TWs switch their chirality with their magnetization along the Oersted field as shown in Fig. 5.5(b2). The estimated Oersted field during this pulse is $\sim$ 15 mT.

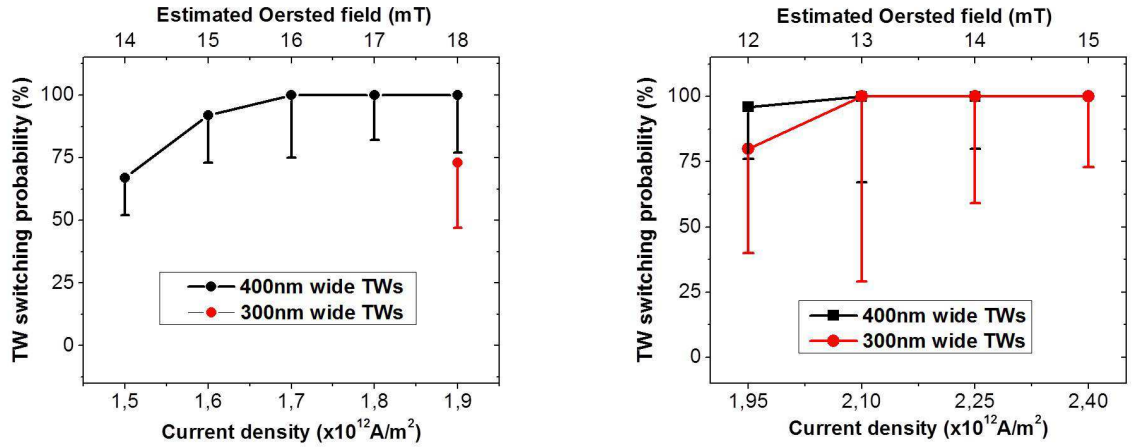

(a) (b)

Figure 5.6: TW switching probability as a function of current density and corresponding Oersted field in 300 and 400 nm *wide (a) Au(*2 nm*)/Py(*10 nm*)/Ir(*15 nm*)/Al_2O_3(0001) (b) Au(*2 nm*)/Py(*10 nm*)/Ir(*10 nm*)/Al_2O_3(0001) nanostripes.*

We measured the probability of DW chirality switching corresponding to each current density. Fig. 5.6 (a,b) shows the DW switching probability as a function of current density and corresponding Oersted field for Py(10 nm)/Ir(15 nm) and Py(10 nm)/Ir(10 nm) bilayers. The DW chirality switching probability increases with increasing current density. For the Py(10 nm)/Ir(15 nm) sample, in 400 nm wide nanostripes, TWs show a deterministic chirality switching field of 16 mT or higher as shown in Fig. 5.6(a). The 300 nm wide TWs show a higher deterministic switching field of 18 mT, as expected due to the higher demagnetizing field for narrower nanostripes.

We varied the strength of the Oersted field by changing the thickness of Ir layer from 15 nm to 10 nm. Now for the same current density, we have less Oersted field. As expected, the DW chirality switching requires higher current densities for this sample. Current densities between 1.9 and 2.4 $\times$ 10^{12} A/m^2, for pulse lengths of 3 ns, were required to switch the DW chirality with probability 100 % [Fig. 5.6(b)]. TWs in 300 and 400 nm wide nanostripes now exhibit switching fields of 15 and 14 mT respectively.

We may expect the DW chirality switching fields to be the same for both samples with different Ir thicknesses, but we observed about 25% lower switching fields for Py(10 nm)/Ir(10 nm) than Py(10 nm)/Ir(15 nm). The lower switching field is may be due to relatively good crystalline quality and surface topography of Ir and hence Py in this sample, because in our case, the best optimised thickness for Ir is 10 nm and above this value, the Ir and hence Py roughness increases (See chapter2, epitaxial Py/Ir growth). However, the Oersted field ratio between the two samples would be the same even if resistivities of Ir and Py are not the same.

We performed micromagnetic simulations in our group (Nicolas Rougemaille) to find the DW chirality switching field in nanostripes with widths between 200 to 400 nm. A homogeneous transverse field was applied for the simulations while an Oersted field with a gradient was acting in the experiments. The simulations give switching fields of 14 $\pm$ 1 mT and 9 $\pm$ 1 mT for 300 and 400 nm wide stripes, respectively. The experimental results are therefore in reasonable agreement with the simulations. We observed very rare TWs displacement due to transformation by switching their chirality under Oersted field, although DW auto-motion due to DW transformation has been reported in literature [19]. The DW pinning due to sample imperfections may be the cause of zero or very small rare displacements.

5.3 Current induced domain wall motion in epitaxial Py nanostripes

We studied the current induced DW motion in S-shaped, 12 µm long Py 15 nm single layer and 10 and 20 µm long curved and S-shaped Py(10 nm)/Ir(10 nm) bilayer nanostripes. Two different fast current pulse generators with pulse rise time $\sim$ 2 and 5 ns were used to apply short ($\leq$ 10 ns) and long ($\geq$ 10 ns) current pulses respectively. We consider only the plateau of the pulses to calculate the DW velocity. For example 5, 10 and 100 ns pulses are considered as 3, 8 and 95 ns. The current densities are corrected for the decrease in pulse amplitude due to Joule heating. We considered the average value of the current density at the middle of the current pulse. MFM was used to observe the DW position and configuration before and after each current pulse.

5.3.1 Current induced DW motion in Py single layer nanostripes

In this section I will describe the quasistatic DW motion under short (3 and 8 ns) and long (95 ns) current pulses with varying current densities from 2.5 to 3.55 $\times 10^{12}$ A/m^2 (average current densities at the middle of the current pulses, corrected due to Joule heating) in 12 µm long and 300 and 400 nm wide Au(2 nm)/Py(15 nm)/Al_2O_3(0001) nanostripes.

Critical current density

The threshold current densities required for the current-induced DW motion reported in literature are 10^{11}-10^{12} A/m^2 for single layer ferromagnetic metallic nanostripes [132][139][60]. A critical current density of 2.5 $\times 10^{12}$ A/m^2 was observed for current-induced DW motion in our nanostripes. This value is about 2 to 3 times higher than reported in the literature for single layer Py nanostripes of similar dimensions [145][146][43]. DW pinning due to the stripe edge roughness or crystallographic defects as described in section 5.1 above, can be a possible origin of the high critical current density in our nanostripes. Fig. 5.7 shows that the top VW in the 300 nm wide nanostripe moves along the electron flow by 3 µm under a 2.5 $\times 10^{12}$ A/m^2, 95 ns current pulse. The DW speed is calculated by dividing the DW displacement by the pulse length. The DW moves with an average speed of 32 m/s. The bottom VW did not move probably due to pinning.

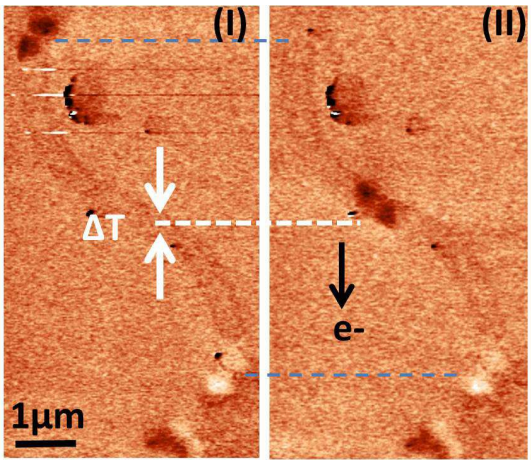

Figure 5.7: MFM image of HH and TT VWs moving along the electron flow in a 300 nm *wide Au(*2 nm*)/Py(*15 nm*)/Al_2O_3(0001) nanostripe (I) Initial configuration of VWs in* 300 nm *wide nanostripe (II) after applying a* -2.5×10^{12} A/m^2, 95 ns *current pulse. The black and white arrows corresponds to the electron-flow and temperature gradient directions respectively.*

Domain wall motion without transformation

The DW velocity increases upon increasing the current density above the threshold value. Fig. 5.8(a) shows the initial configuration of HH and TT VWs (except one HH TW in 300 nm stripe, the only one observed during all measurements, may be due to topographic defect of nanostripe at this position) in 300 and 400 nm wide nanostripes. After applying a current pulse of current density 3.4 $\times 10^{12}$ A/m^2 and pulse length of 3 ns, all the DWs

move together, along the electron flow direction. as shown in Fig. 5.8(b). Most of the DWs move over a distance of about 1.2 µm, except the top VW in the 400 nm wide stripe, resulting in an average speed of $\sim$ 400 m/s. The top VW in the 400 nm wide stripe moves about 0.4 µm, with a speed of 133 m/s. The small distance moved by this DW may be due to DW pinning. All DWs move together in the same direction and over almost the same distance, which is the expected behaviour if only STT acts on the DWs. However this expected behavior was not observed very often in our samples, and most of the time, DW transformations and motion against the electron flow took place as described below.

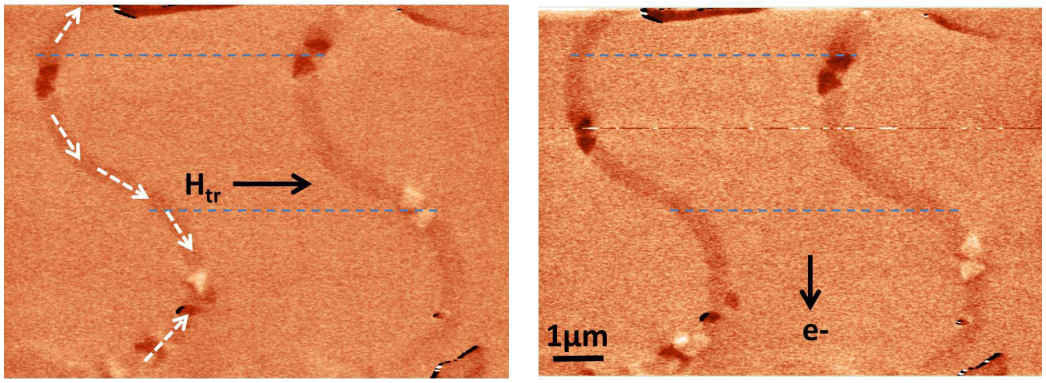

(a) (b)

Figure 5.8: MFM image of VW motion in 300 and 400 nm *wide and* 12 µm *long S-shaped Py* 15 nm *nanostripes (a) Initial configuration of HH (lower) and TT (upper) VWs. (b) After applying a* 3.4×10^{12} A/m^2 3 ns *current pulse. The black arrows indicate the direction of electron flow and the transverse magnetic field (H_{tr}) applied to create DWs at the nanostripe bends. The white arrows show the magnetization orientation in the nanostripes.*

Domain wall transformations and Joule heating

The nucleation and annihilation of double or triple vortices has been reported in 1 µm wide and 28 nm thick Py nanostripes [60]. This nucleation and annihilation of vortices occurred in the vicinity of the existing vortex. In their case, a modest rise of temperature of $\sim$ 60 K was observed for the maximum used current density, and DW pinning might be the main origin of this vortex nucleation/annihilation.

We also observed the DW transformations from single to double vortex walls (DVWs) and vice versa in both 300 and 400 nm wide nanostripes. Fig. 5.9(a) shows the initial configuration of HH and TT VWs in a 400 nm wide nanostripe. After applying a negative current pulse of current density 3.4×10^{12} A/m^2 and pulse length 3 ns, the top VW moved down against the electron flow 0.2 µm with a velocity of 67 m/s and the bottom VW transforms from a VW into a DVW without moving, as shown in Fig. 5.9(b). After the application of two more similar individual current pulses, the top VW moves down further against the electron flow by 0.2 and 0.1 µm with velocities of 33 and 67 m/s respectively, while the bottom DVW moves up, along the electron flow, by 0.4 µm with a velocity of 133 m/s and then transforms again into a single VW after the next pulse, by moving with the same velocity [Fig. 5.9(c,d)].

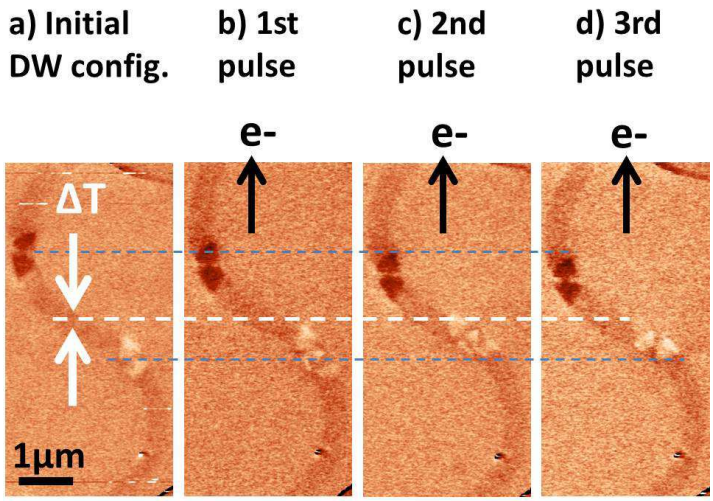

Figure 5.9: Domain wall transformations from single to double vortex and vice versa.(a) Initial configuration of HH (lower) and TT (upper) VWs in 400 nm *wide nanostripe (b-d) after each consecutive* -3.4×10^{12} A/m^2, 3 ns *current pulse. The black and white arrows indicate the direction of electron-flow and the temperature gradient respectively, in the nanostripes.*

In several cases we observed that the DWs move towards the center of the wire, against the electron flow, and this may be related to the heat gradient. The voltage resulting from a temperature difference, *"the Seebeck effect"* is a well known effect. The efficiency of the Seebeck effect is represented by Seebeck coefficient which is given by the ratio of generated voltage to the temperature difference. In the case of magnetic metals, a spin dependence of the Seebeck coefficient results into a thermoelectric spin potential named, *"the spin-dependent Seebeck effect"* [133]. Different groups have evidenced this effect in ferromagnetic conductors both experimentally and theoretically, showing that the magnonic spin currents caused by temperature gradients results in a STT comparable with current-induced torques, and can move a domain wall towards the hotter part of the stripe [50] [148].

The uni-directional DW motion towards the midddle of the nanostripes, due to a temperature gradient, has recently been reported [131]. During the current pulse, the nanostripe temperature rises instantly and uniformly. After the current pulse, during cooling, heat evacuation takes place through the substrate and the contacts. At the ends of the wire, in contact with the Au pads, the heat evacuation is faster as compared to the middle of the stripe. There exists thus a very strong temperature gradient, with a higher temperature at the middle of the stripe. As a consequence, the DW moves towards the middle of the stripe after the pulse due to the temperature gradient. It has also been shown that in the absence of pinning and DW transformations, the DW can move longer distances if temperature gradient and spin torque act in the same direction and shorter distances if they act in opposite directions [131].

In our case, the shape of the current pulses indicate significant Joule heating, leading to a 30 to 40% decrease of the pulse amplitude at the end of the current pulses. The sapphire substrate is not a good heat conductor, as compared to the normally used naturally oxidized Si substrates. If we look at Fig. 5.9(c), the DVW that moves along the electron

flow shows a 2 times larger displacement (0.4 µm) than the single vortex that moves against the electron flow (0.2 µm), even if a lower mobility of DVWs as compared to single VWs has been reported [60]. The larger displacement of the DVW can be explained by the fact that, for the DVW the temperature gradient and STT push it in the same direction, while for the single VW they oppose each other, resulting in a smaller displacement.

Statistics of domain wall motion

Fig. 5.10(a-c) shows the DW displacement and velocity distributions as a function of current density and pulse length respectively. About 60 events were analyzed for short (3 and 8 ns) current pulses for different current densities and 10 events for long (95 ns) pulses for single lower current density to avoid large Joule heating. About 62% of the VWs moved along the electron flow with 42% also moving towards the nanostripe center (29% transform to DVW and half of them moved towards the nanostripe center). The remaining 38% move opposite to the electron flow and also towards the center of the nanostripe (20% transform to DVW) as shown in Fig. 5.10(a). This means that in total, about 80% of the DWs moved towards the nanostripe center, including 62% along STT and 38% against it. 49% of VWs transform into DVWs with 35% moving towards nanostripe center and 14% away from the center. (Each percentage value corresponds to the percentage of total VWs considered in the statistics).

Fig. 5.10(b) shows that about 61% DVWs moved along the electron flow with 22% towards the stripe center (34% transfrom to VW with 13% moving towards stripe center) and remaining 39% moved opposite to the electron flow with 28% towards stripe center (22% transform to VW with 17% moving towards stripe center). So, in total, about 50% DVWs moved towards nanostripe center and 50% away from center, with 61% along STT and 39% against it. 56% of DVWs transform to VWs with 30% moving towards stripe center. (Each percentage value corresponds to the percentage of total DVWs considered in statistics).

This indicates that the temperature gradient plays a larger role in moving the DW than the STT : the DWs move more often against the electron flow than against the temperature gradient. Both higher current densities and relatively poor heat conductor sapphire substrate as compared to Si are responsible for the higher temperature gradient in our nanostripes. This confirms the uni-directional DW motion due to thermal effects as also reported in the literature [131].

Fig. 5.10(a,b) also shows that DW displacement is not proportional to the pulse length and instead there is a distribution of displacements. Furthermore, stochastic behaviour of DW propagation was found. The DW propagation probability increases with increasing the current density. This reveals the presence of pinning in our stripes, which results into smaller DW velocities for longer current pulses. We found almost similar velocities in both 300 and 400 nm nanostripes. The maximum velocities found for single VWs in Py 15 nm thick and 300 and 400 nm wide nanostripes are ~ 533 m/s under a current density of $\sim 3.4 \times 10^{12}$ A/m^2 [Fig. 5.10(c)]. This value of velocity is more than 3 times higher than reported in literature ~ 150 m/s for 200 nm wide single Py layer nanostripes for a current density of 1.6×10^{12} A/m^2 [42], two times lower than the value of the current density in our case.

Lower velocities were found for DVWs which move with maximum velocities of $\sim$ 270 m/s for a current density of $\sim 3.4 \times 10^{12}$ A/m^2 [Fig. 5.10(c)]. This value of DVW

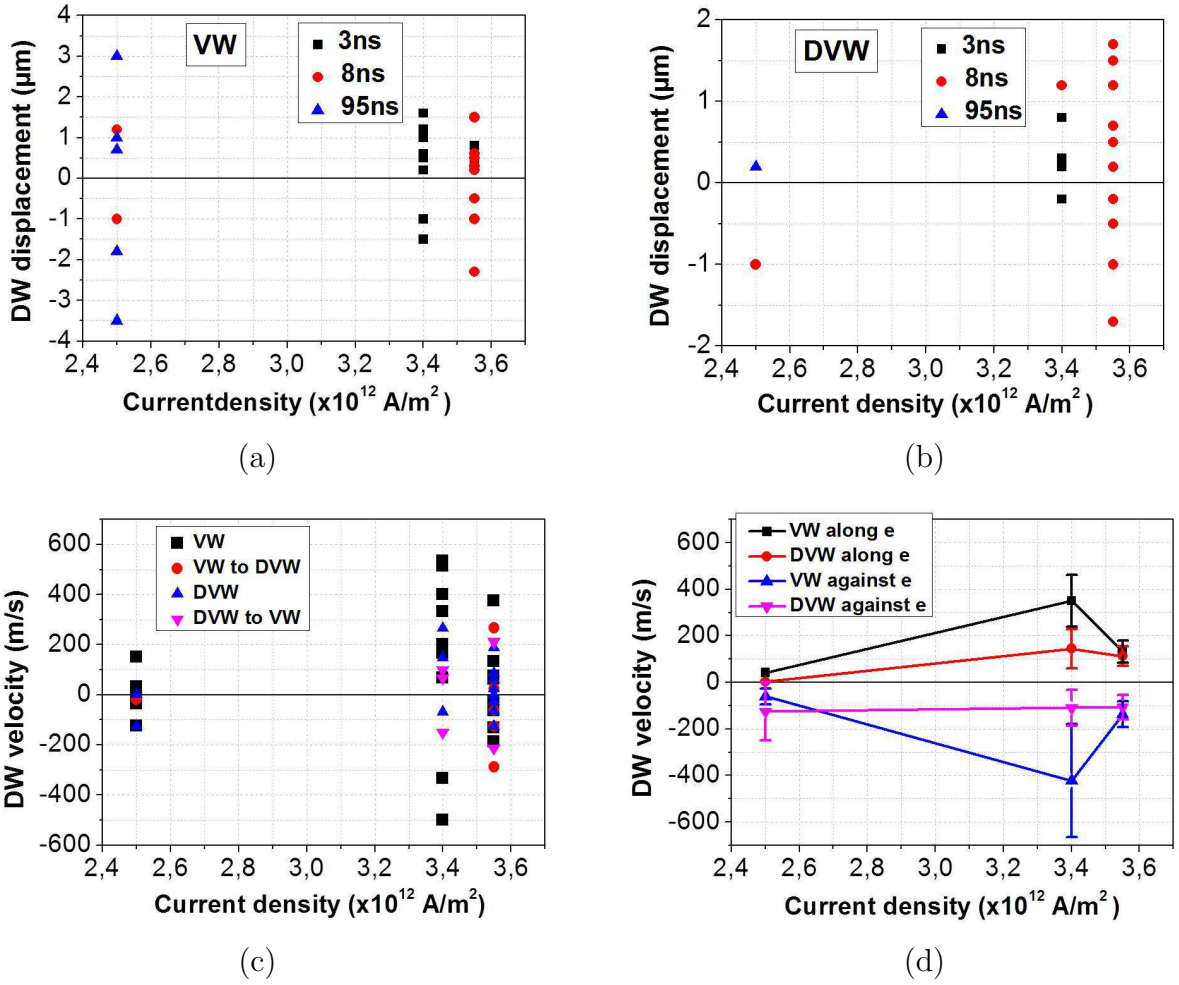

Figure 5.10: DW displacement distribution (a) single VWs (b) double VWs (c,d) DW velocity distribution and average DW velocity respectively along and opposite to the electron-flow as a function of current pulse length and current density for single and double VWs in 300 and 400 nm *wide Au(*2 nm*)/Py(*15 nm*)/Al_2O_3(0001) nanostripes. Positive and negative displacements and velocities corresponds to motion along and opposite to the electron flow respectively. About 60 events were analysed for pulse lengths 3 and* 8 ns *and 10 events for* 95 ns.

velocity is about three orders of magnitude higher than reported by Kläui et al for 28 nm thick and 1 µm wide Py nanostripes [61] using a four times lower current density. In their case, they did not observe significant Joule heating (max. rise in temperature $\sim$ 60 K), instead they observed DW pinning, so in our case higher temperature gradient due to Joule heating may also be partially responsible for the higher DVW velocities. Moreover, they used microsecond long pulses, which may result into smaller DW velocities due to DW pinning.

Fig. 5.10(d) shows that the average DW velocity increases with increasing current density. The average DW velocity along the electron flow for single VWs in 300 and 400 nm wide nanostripes is $\sim$ 350 m/s (black squares connected by solid black line) for a current density of $\sim 3.4 \times 10^{12}$ A/m^2. For DVWs the average velocity is $\sim$ 150 m/s (red disks connected by solid red line), for the same current density. By further increasing the

current density, the DWs velocities decreases due to large Joule heating.

In conclusion, we studied current induced DW motion in epitaxial Py nanostripes deposited on sapphire(0001). We observed high maximum VW velocities along the electron flow reaching 533 m/s for 3 ns short current pulses with a current density of 3.4×10^{12} A/m^2. Although, these values of DW velocities are more than 3 times higher than reported in literature but current density corresponding to these velocities is also about 2 times higher. This higher current density causes significant Joule heating resulting very often in DW transformations and DW motion against electron flow direction. The DW displacement does not scale with the current pulse length due to pinning, and longer current pulses result in smaller average DW velocities. An average DW velocity of 350 m/s is obtained with a current density of 3.4×10^{12} A/m^2. Contrary to what we expected, the DW pinning in these high-quality epitaxial films is thus higher than for most samples reported in literature, obtained by sputtering. I will discuss some possible origins of this increased pinning in the general conclusions. It is clear that a decrease of DW pinningin in order to reduce the critical current density is necessary for device applications.

5.3.2 Current induced DW motion in Py/Ir bilayer nanostripes

In contrast to single layer ferromagnetic systems, in FM/NM bilayer systems, where FM = ferromagnetic and NM = nonmagnetic, in parallel to STT there exist other effects which can influence the current induced DW motion e.g., the Oersted field due to current passing through NM layer or spin Hall effect. The SHE is acting at the interface and is thus more effective for small FM layer thickness. In our case, in the Py/Ir bilayer system, the Py thickness is 10 nm, so we expect negligible SHE. On the other hand there is an Oersted field acting on the Py layer due to the current passing through the Ir layer. Therefore, I will discuss effect of an Oersted field along with the STT on DW motion in these stripes.

We studied two types of samples with different Ir thicknesses: Py(10 nm)/Ir(10 nm) and Py(10 nm)/Ir(15 nm). The different Ir thicknesses allowed us to vary the strength of the Oersted field for the same average current density in the nanostripes. In contrast to Py single layers where VWs were observed in Py/Ir bilayer nanostripes, we observed TWs when initially prepared under an in-plane magnetic field transverse to the stripes. As for Py 10 nm thickness we are close to the phase boundary in the DW phase diagram, both metastable transverse and vortex walls may exist together. The metastable TWs can transform to VWs and vice versa by supplying some energy through external source e.g., current or thermal energy. We saw in section 5.2.2 that the Oersted field can switch the chirality of TWs. The current densities required for switching the DW chirality are of the same order of magnitude as the ones required for DW propagation in our nanostripes of width 300 and 400 nm. Here I will describe the DW propagation results in these nanostripes and will compare these results with those of single layer Py nanostripes, where the net Oersted field is zero.

Critical current density and domain wall motion with transformation

We studied DW motion in 300-400 nm wide nanostripes under different pulse widths from 1 and 25 ns and current densities between 7×10^{11} A/m^2 and 2.24×10^{12} A/m^2.

The critical current density of $7 \times 10^{11}\,\mathrm{A/m^2}$ was observed to move the DWs in Py/Ir bilayer nanostripes. This current density is about one fourth of that of our single layer Py nanostripes ($2.5 \times 10^{12}\,\mathrm{A/m^2}$) as described above and is comparable to the values reported in the literature [132][139][60].

Fig. 5.11(a) shows the scanning electrom microscope image of 20 µm long and 100 to 400 nm wide Au(2 nm)/Py(10 nm)/Ir(10 nm)/(Al_2O_3(0001) nanostripes. Fig. 5.11(b)(I) shows MFM image of initial configuration of HH (lower) and TT (upper) TWs with positive and negative asymmetries respectively in a 20 µm long and 400 nm wide S-shaped Py(10 nm)/Ir(10 nm) nanostripe. After applying a $-7 \times 10^{11}\,\mathrm{A/m^2}$, 5 ns current pulse both TWs transform into VWs moving in opposite directions. The upper TW moves up 1.6 µm, opposite to the electron flow direction, with an average speed of 320 m/s as shown in Fig. 5.11(b)(II). The lower TW moves down 0.4 µm, along the electron flow, with a speed of about 80 m/s. In many occasions these transformations were observed in these bilayer stripes resulting in DW displacements along or opposite to the electron flow direction.

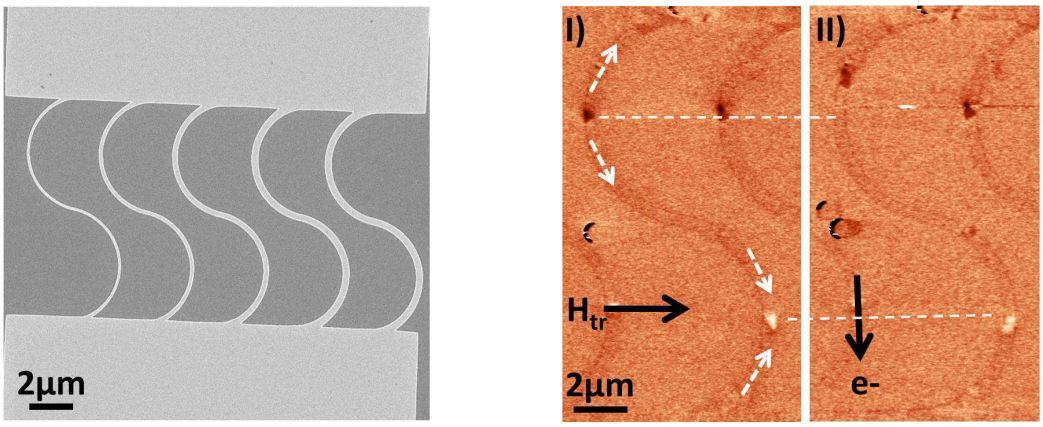

(a) (b)

Figure 5.11: (a) Scanning electron microscope image of 20 µm *long and 100 to* 400 nm *wide Au(*2 nm*)/Py(*10 nm*)/Ir(*10 nm*)/(*Al_2O_3*(0001) nanostripes (b) MFM image of (I) initial configuration of HH and TT TWs in a* 400 nm *wide nanostripe (II) and after applying a* 3 ns *current pulse with current density* $-7 \times 10^{11}\,\mathrm{A/m^2}$.

J. Y. Chauleau et al. has reported experimentally and explained analytically and numerically, that DWs can undergo a large intrinsic displacement, called auto-motion, due to the DW structural transformation. Displacements more than 3 times larger than under STT only were measured. The direction of displacement is related to the sense of change, not to the sense of triggering the transformation [19]. They studied DW transformations from asymmetric TWs to VWs in 17.5 nm thick and 450 nm wide Py nanostripes. They suggested that a typical displacement of 1 µm may occur from asymmetric TW to VW transformation and vice versa. The vortex core entered from the asymmetric edge of the TW, called half hedgehog vortex, and then moved towards the center of the nanostripe $y_c = \pm w/2$ (y_c is the position of the vortex core across the width w of the nanostripe) resulting in an extra displacement due to a change in the generalized DW magnetization angle ϕ (maximum, $\phi = \pm\pi/2$). This extra displacement, in addition to the displacement due to the STT, may result into over-estimation or under-estimation (if STT and auto-

motion act in opposite directions resulting in a smaller displacement) of DW velocities. Moreover, auto-motion does not depend on type of excitation for DW transformation (field or current).

They proposed an analytical model under assumption of a constant DW width to calculate the displacement due to auto-motion given by $q = (\pi/2)\Delta_T/\alpha$, where Δ_T is the Thiele DW width and α, the Gilbert damping parameter. They calculated the Thiele DW width from micromagnetic simulations, giving a $\Delta_T = 26\,\text{nm}$ for a 17.5 nm thick and 450 nm wide Py nanostripe. This gives $q = 2.04\,\mu\text{m}$ for $\alpha = 0.02$. This value of q is slightly larger than the maximum value 1.7 µm, that they measured experimentally.

They also demonstrated that two asymmetric HH and TT transverse walls with opposite asymmetries (positive and negative) transforming to VWs, move in opposite directions under the same current pulse. On the other hand, two asymmetric TWs with the same asymmetries moved in the same direction when transformed into a VW. The displacement due to DW transformation in both directions can be different, if it takes place along or opposite to the electron flow direction [19].

We also observed asymmetric TWs with opposite asymmetries, transformed into VWs moving in opposite directions as shown in Fig. 5.11. The upper TW moves up as expected due to auto-motion by about 1.6 µm (opposite to the electron flow direction), while the lower TW moves down along the expected direction 0.4 µm (along the electron flow as well) as shown in Fig. 5.11(b)(II). The DW may be get pinned after motion resulting in a smaller displacement along the electron flow direction.

Domain wall motion without transformation

We also observed DW motion without transformation for both vortex and transverse walls. Fig. 5.12(I) shows the initial configuration of HH TWs in 10 µm long and 300 and 400 nm wide curved-shap nanostripes. After applying a $2.2 \times 10^{12}\,\text{A/m}^2$, 3 ns current pulse, the TW in 400 nm stripe moved about 0.8 µm along the electron flow direction with a velocity of 267 m/s. The TW in the 300 nm wide stripes did not move and remains pinned [Fig. 5.12(II)].

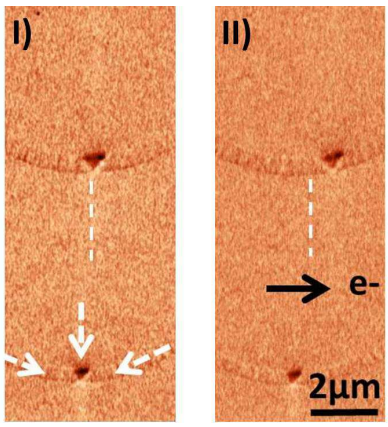

Figure 5.12: TW motion in 10 µm *long 300 and* 400 nm *wide curved-shape Au(*2 nm*)/Py(*10 nm*)/Ir(*10 nm*)/(Al_2O_3)(0001) nanostripes. (I) MFM image of initial configuration of HH TWs (II) after applying a* 3 ns *current pulse of current density* $2.2 \times 10^{12}\,\text{A/m}^2$.

Fig. 5.13(a) shows the initial configuration of HH (upper) and TT (lower) TWs and VWs in 20 µm 300, 400 and 400 nm wide nanostripes from left to right. After applying a 2.2×10^{12} A/m^2, 25 ns current pulse all four DWs in 400 nm wide nanostripes move up along the electron flow, but in the 300 nm wide stripe the DWs do not move and remained pinned as shown in Fig. 5.13(b). As all HH and TT DWs move in the same direction, this suggests that DWs move due to STT. The bottom VWs move up by about 1.8 µm, with an average velocity of 72 m/s. The upper TW and VW also move up about 1.2 and 1.8 µm along the electron flow, with velocities of about 50 and 72 m/s respectively. We noticed that these DW velocities are smaller than for shorter pulse widths with similar current densities.

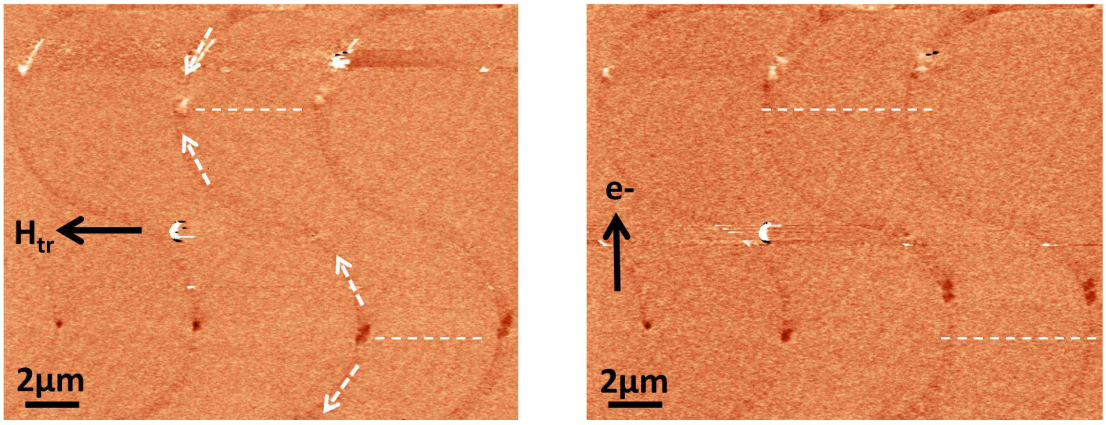

(a) (b)

Figure 5.13: TW and VW motion in 20 µm *long and 300, 400 and* 400 nm *wide S-shaped Au(*2 nm*)/Py(*10 nm*)/Ir(*10 nm*)/(Al_2O_3(0001) nanostripes from left to right (a) Initial configuration of HH and TT TWs and VWs (b) after applying* 25 ns *current pulse with current density* 2.2×10^{12} A/m^2. *The white arrows indicate the direction of magnetization in the nanostripes.*

Statistics of domain wall motion

The different DW displacements for similar current pulses in 400 nm stripes suggest the presence of DW pinning due to nanostripe edge roughness or intrinsic material defects. We observed very often DW transformations, so DW motion without and with transformation (auto-motion), may also result into different displacements. This results into a distribution of DW displacements and hence velocities as shown in Fig. 5.14(a-c). For each pulse length between 10 to 15 events were analysed.

Fig. 5.14(a) shows that in the case of initial state as TWs, about 46% moved along the electron flow (36% of total transform and as expected, moved in the direction of change of DW angle and also away from the nanostripe center, remaining 10% also moved away from the nanostripe center but without transformation). 54% TWs moved opposite to the electron flow (34% transform and moved in the expected direction and also away from the nanostripe center, remaining 20% moved towards the nanostripe center without transformation). The different transformations that occur are from TW to VW, a change of TW chirality due to the Oersted field or a change of TW asymmetry. (Each percentage value corresponds to the percentage of total TWs considered in statistics).

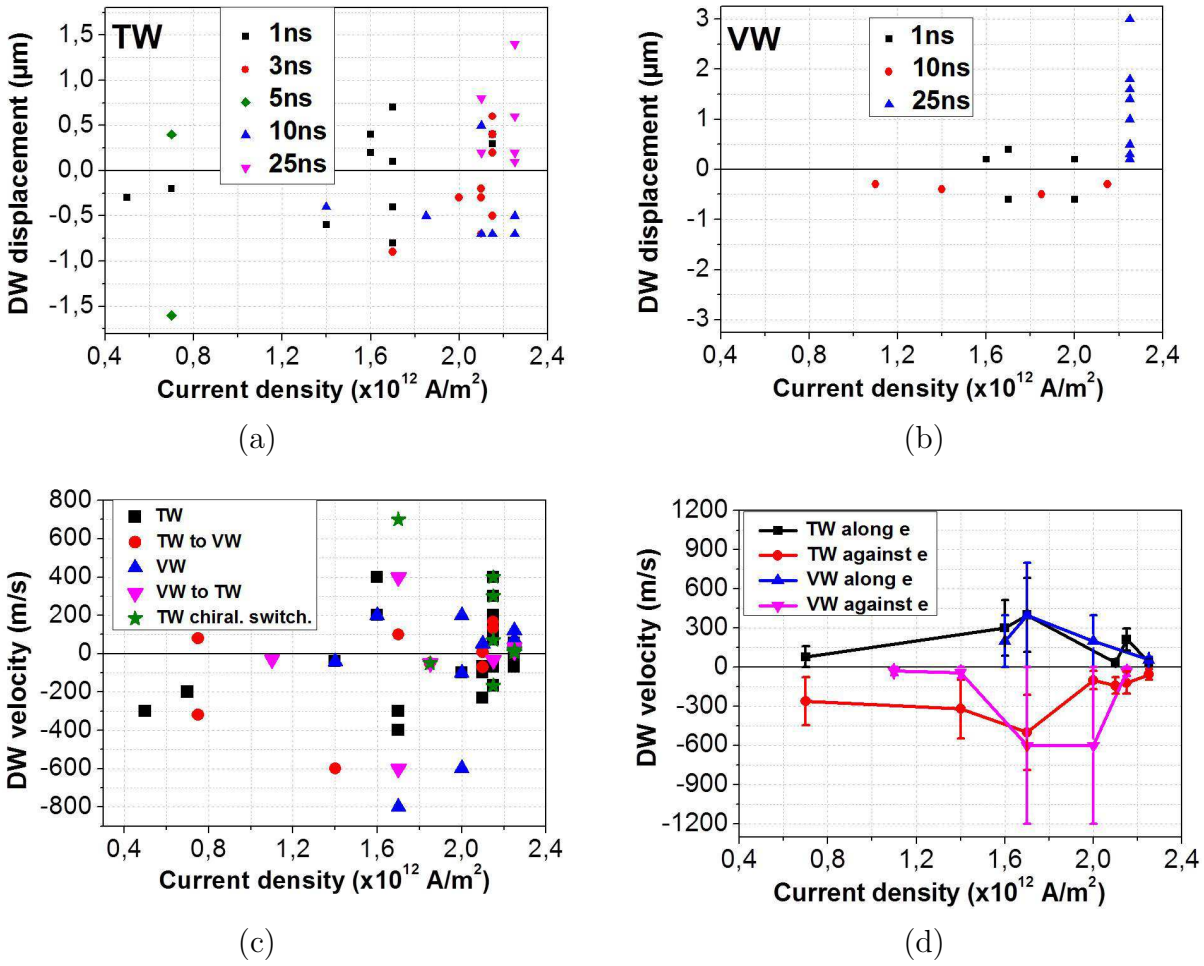

Figure 5.14: DW displacement distribution with initial state (a) TWs (b) VWs (c,d) DW velocity distribution and Average DW velocity with TWs and VWs as initial states, in 400 nm *wide Au(*2 nm*)/Py(*10 nm*)/Ir(*10 nm*)/Al_2O_3(0001) nanostripes along and opposite electron flow direction respectively as a function of current density and current pulse width. Positive and negative displacements and velocities corresponds to along and opposite electron flow respectively.*

It is clear that TW motion opposite to the electron flow is either due to TW transformation or to TW motion towards the nanostripe center due to Joule heating. As already explained, auto-motion due to DW transformations takes place in the direction of change of the DW angle and is independent of the electron flow direction, which is consistent with our measurements [19]. The displacements observed corresponding to TW transformations are between 0.1 to 1.6 µm. The higher displacement values agree well with the predicted and experimentally reported values due to auto-motion. The smaller displacements are mostly due to the DW pinning. It was observed in most of the cases that, whenever TW results into smaller DW displacement after transformation, it was initially pinned and did not move under several pulses. However, a few cases of TW motion against STT, resulting in smaller TW displacement after transformation were also seen. Secondly, the possible explanation for 20% TWs which moved against the electron flow but also towards the nanostripe center without transformation is the temperature

gradient due to Joule heating, which can result into uni-directional DW motion towards the nanostripe center [131].

36% of the TWs which moved along the electron flow direction were transformed, which can result in an extra displacement due to auto-motion and hence to over-estimation of the TW velocity, but we also observed some TWs moving without transformation. Fig. 5.14(c) shows that the maximum velocity observed for TWs in 400 nm wide nanostripes along the electron flow is 700 m/s. This value corresponds to TW transformation by changing its chirality, which may include an extra displacement due to auto-motion resulting in an over-estimation of the velocity. However, maximum TWs velocities $\sim$ 400 m/s without transformation were also observed in these stripes. Longer current pulses result again in smaller average TW velocities. Similarly higher TW velocities above 400 m/s opposite to the electron flow are also due to TW transformation, however, from transverse to vortex walls.

Fig. 5.14 (b) shows that in case of a VW as initial state, about 65% moved along the electron flow (23% transform from VW to TW with TW magnetization parallel to the Oersted field, remaining 42% moved without transformation with half towards nanostripe center and half away from center) and 35% moved opposite to the electron flow (all of them transform from VW to TW and also moved towards the nanostripe center). The VW motion due to transformation gives higher VW velocities of 400 m/s along electron flow and 600 m/s opposite to electron flow in 400 nm wide nanostripes. However, maximum VW velocities of 200 m/s without VW transformations were observed in these stripes as shown in Fig. 5.14(c). The lower VW velocities corresponding to longer current pulses and smaller DW displacements are attributed to DW pinning.

The average velocity for transverse and vortex walls is $\sim$ 365 m/s for a current density of 1.7×10^{12} A/m^2, as shown in Fig. 5.14(d). This is almost 3 times higher than reported in literature for VWs in 10 nm thick and 300 nm wide Py nanostripes for a similar current density (1.5×10^{12} A/m^2) [43]. Upon further increasing the current density, a decrease in average DW velocities is observed for both transverse and vortex walls. For higher current densities (higher voltage), we had to use a different pulse supply that did not allow applying short pulses. The pulse length is thus larger for higher current densities, resulting in smaller average DW velocities due to the influence of DW pinning.

There are issues with pinning, DW transformations and Joule heating also in these samples. However, for DWs that behave as expected under STT, the maximum velocities are higher than our and other single Py layers reported in literature, for similar current densities. A possible explanation for the higher efficiency of current-induced DW motion in our bilayer nanostripes is the influence of the Oersted field. The Oersted field during the current pulse can stabilize the DW against transformations. This can suppress the Walker breakdown resulting in higher DW velocities. We observed some transformations from transverse to vortex walls even in the presence of an Oersted field, due to the fact that VW is energetically more favourable in nanostripes of these dimensions. Less Joule heating was observed in these stripes (current densities are also lower) as compared to our single layer Py nanostripes, where the most of the DWs moved towards the nanostripe center due to strong temperature gradient, which is not the case here.

In conclusion, for 400 nm wide Py(10 nm)/Ir(10 nm) bilayer nanostripes, we obtained high maximum TW velocities (up to 400 and 700 m/s) and maximum VW velocities of (200 and 400 m/s) along the electron flow, without and with DW transformation respectively, under a current density of 1.7×10^{12} A/m^2. This value of the current density is about

half the one needed to reach similar velocities in our Py single layers. Moreover, the TW velocity is about 3 to 5 times and VW velocity is about 2 to 3 times higher than the one reported in literature 150 m/s for single layer Py nanostripes, for similar current densities [42]. For 300 nm wide Py(10 nm)/Ir(10 nm) stripes (not presented here, small number of DW motion events due to higher pinning in these stripes), maximum velocities of 300 m/s were observed for TWs for similar current density of 1.7×10^{12} A/m^2. Like Py single layers, a large distribution of velocities was observed for both transverse and vortex walls in Py/Ir bilayers. The average TW and VW velocity in 400 nm wide nanostripes for a current density of 1.7×10^{12} A/m^2 is 365 m/s.

The current induced Oersted field may be at the origin of this higher efficiency in Py/Ir stripes than in single layer Py nanostripes. Micromagnetic simulations and time-resolved measurements could give a better insight in the effect of an Oersted field on the DW dynamics. The DW transformations due to metastability of transverse and vortex walls in Py/Ir bilayers can be avoided bybdecreasing or increasing the Py thickness respectively, like we get for Py single layers in which we observed only stable VWs due to the higher Py thickness (15 nm). The Joule heating can be reduced by depositing a semiconducting layer on top of the sample covering the whole substrate, which should be a bad electrical conductor to avoid short circuiting but a good thermal conductor for better heat dissipation through this layer.

5.4 Current induced DW motion in sputtered Py/Pt bilayer nanostripes

Recently, both analytically and using micromagnetic simulations, high TW velocities $\sim$ 300 m/s due to the spin Hall effect in Py/Pt bilayer nanostripes were suggested [115]. The micromagnetic simulations were performed for 2 µm long and 80 nm wide Py(4 nm)/Pt(3 nm) bilayer nanostripes using standard Py and Pt parameters. α was choosen equal to 0.02 and β from 0.01 to 0.03. For $\alpha > \beta$, just before the Walker breakdown, they observed a maximum TW velocity of $\sim$ 240 m/s, opposite to the electron flow. This reverse DW motion was observed for only one current polarity. This DW velocity was observed for a spin Hall angle of 0.1 ° and was almost 5 times larger than for zero spin Hall angle.

For $\alpha < \beta$ considering $\alpha = 0.02$ and $\beta = 0.03$, just before the Walker breakdown, high DW velocities $\sim$ 325 m/s along the electron flow were found. In contrast with the case $\alpha > \beta$, no DW motion opposite to the electron flow was observed. In all cases, the effect of the Oersted field on the DW velocity was found to be negligible.

We studied the current induced DW motion in sputter-deposited Py(15 nm)/Pt(10 nm) bilayer nanostripes on naturally oxidized Si substrate with Ta as buffer layer and capped by Al(3 nm)/Cu(2 nm) layers to protect against oxidation. 50 µm long and 1 µm wide zigzag shaped nanostripes with zigzag angle of 90 ° [Fig. 5.15(a)] were prepared by combined electron-beam lithography and lift-off techniques. Ti(20 nm)/Au(50 nm) contact electrodes were deposited by electron-beam evaporation and lift-off techniques, to pass the current pulses through the nanostripes. HH and TT DWs were created at the bends of zigzag nanostripes by applying strong in-plane magnetic field of 50 mT transverse to the stripes. We observed VWs in these stripes as predicted by DW phase diagram in nanostripes of these dimensions [93].

In our case the Py layer is about 4 times thicker than in the work described above

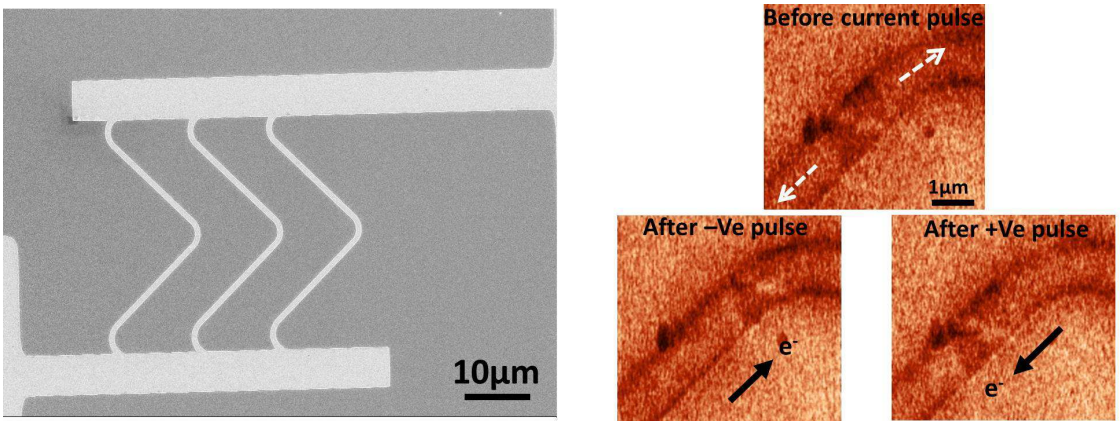

(a) (b)

Figure 5.15: Current induced VW motion in 1 µm *wide Al(*3 nm*)/Cu(*2 nm*)/Py(*15 nm*)/Pt(*10 nm*)/Ta(*3 nm*)/Si nanostripes. (a) SEM image of* 50 µm *long and* 1 µm *wide zig-zag shaped Py/Pt bilayer nanostripes (b) MFM image of initial configuration of TT vortex wall and after applying* 1×10^{12} A/m^2*, 7ns long negative and positive current pulses respectively. The white arrows indicate the direction of magnetization in the nanostripe.*

(4 nm) [115] and we expect negligible SHE acting in our Py/Pt bilayer nanostripes, since the SHE is acting at the interface and is thus more effective for small Py thickness. Instead, the effect of an Oersted field is more dominant in our stripes due to larger Pt thickness, which will be discussed along with STT.

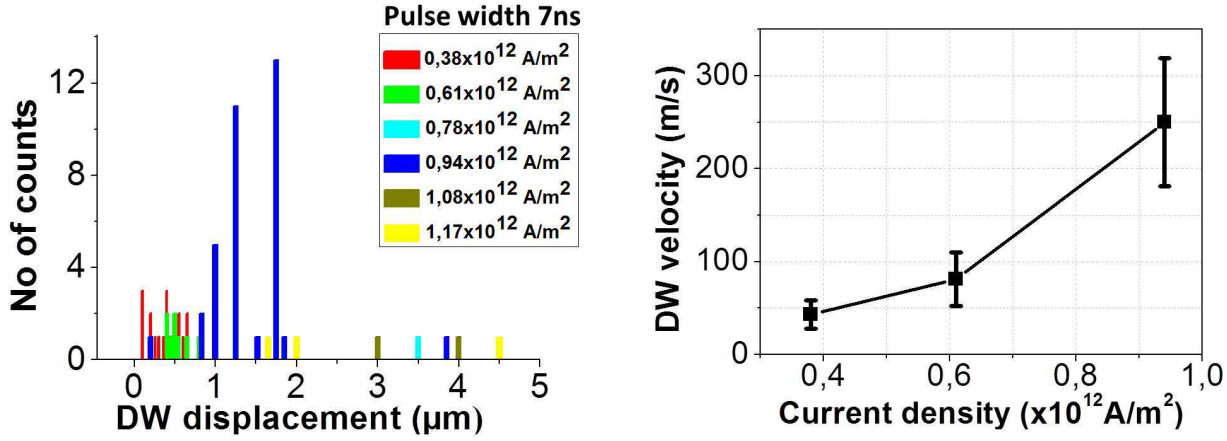

(a) (b)

Figure 5.16: Current induced VW motion in 1 µm *wide Al(*3 nm*)/Cu(*2 nm*)/Py(*15 nm*)/Pt(*10 nm*)/Ta(*3 nm*)/Si nanostripes. (a) VW displacement distribution (b) Average VW velocity, as a function of current density under* 7 ns *current pulses.*

Fig. 5.15 (b) shows the initial configuration of a TT VW in a 1 µm wide Py/Pt bilayer nanostripe. After applying the negative and the positive current pulses of current density

$1 \times 10^{12}\,\mathrm{A/m^2}$ and pulse length 7 ns, the VW moves forward and backward, respectively, each time along the electron flow between two pinning sites. The VW moves each time about 1.75 µm with a speed of $\sim 250\,\mathrm{m/s}$. We repeated 13 times applying same positive and negative pulses and observed that the DW always moves the same distance along the electron-flow. This indicates that DW motion is reproducible in our nanostripes. We do not observe transformations from vortex to transverse walls, probably because we are well above the phase boundary in the DW phase diagram, where VWs are energetically more favourable [93].

We observed different DW displacements in nanostripes at different positions under similar current pulses, which indicates the presence of DW pinning. This results into a distribution of displacements. Fig. 5.16(a) shows the VW displacement distribution as a function of current density under 7 ns current pulses. The average DW velocity corresponding to each current density is shown in Fig. 5.16(b).

The maximum DW velocity in these experiments is $\sim 250\,\mathrm{m/s}$, which is about 2 times higher with a current density 2 times lower, than for single layer Py nanostripes $\sim 150\,\mathrm{m/s}$ reported in literature [42]. A possible origin of this high efficiency in our Py/Pt bilayer system is the Oersted field. An Oersted field of $\sim 9.4\,\mathrm{mT}$ is estimated for a current density of $1 \times 10^{12}\,\mathrm{A/m^2}$, corresponding to the maximum DW velocity. The Oersted field is calculated by considering the same Py and Pt resistivities. Without the Oersted field VWs are expelled at the edge of the nanostripes above a certain threshold velocity, resulting low maximum velocity. If the STT and Oersted field act in opposite directions on the vortex core, the vortex core position may be stabilized inside the nanostripe, delaying DW transformation and hence increasing the velocity.

Micromagnetic simulations performed in our group (Nicolas Rougemaille) confirm that an Oersted field affects the vortex core within the nanostripe during VW motion. When a longitudinal field of 2 mT was applied along the nanostripe axis, the vortex core is expelled after a few nanoseconds. When a transverse field of 20 mT was applied opposite to the vortex core expulsion direction, in addition to the longitudional field along the nanostripe for VW motion, the VW displacement is 5 times larger before transformation.

In conclusion we studied current induced DW motion in Py/Pt bilayer nanostripes. We observed reproducible VW motion between two pinning sites with an average velocity of $250\,\mathrm{m/s}$ under a current density of $1 \times 10^{12}\,\mathrm{A/m^2}$ for 7 ns current pulses. This is the lower bound of the velocity, higher velocities can be possible by using shorter current pulses. The current density corresponding to this velocity is about one half the one in our epitaxial Py/Ir bilayer samples and 2 to 3 times smaller than other Py single layers reported in the literature [43][42]. We did not observe DW motion against electron-flow in Py/Pt nanostripes in contrast to epitaxial samples deposited on sapphire. In epitaxial samples some DWs moved against electron flow due to Joule heating which was negligible here due to relatively low current densities in sputtered samples deposited on Si and good thermal conductivity of Si as compared to sapphire. The high efficiency of current induced DW motion in Py/Pt bilayers may be due to the Oersted field. The micromagnetic simulations confirm the VW stabilizing effect of the Oersted field on VW motion, resulting in higher VW displacement and hence velocity before transformation. Micromagnetic simulations under current instead of field and time-resolved measurements will be performed in the near future to observe the effect of an Oersted field on the VW dynamics.

Conclusion

The goal of my Ph.D work was the optimization of single crystal epitaxial growth of Py and Su-Py films by PLD on sapphire(0001) substrate with and without Ir buffer layer, with less structural defects and surface or interface roughness, to study current-induced DW motion in nanostripes patterned from these films. The expected high crystal quality of these films was expected to lead to a reduction of the DW pinning and hence the critical current density for DW motion. Polycrystalline Py/Pt films were also prepared by sputtering on naturally oxidized Si substrate to compare the results with epitaxial samples.

High quality epitaxial fcc (111) Py and Su-Py films with very small roughness ~ 0.1 nm were obtained, however, these films are bicrystalline. They show very soft magnetic behaviour with coercive fields of 0.1, 0.3 mT for Py and Py/Ir films and 0.02, 0.07 mT for Su-Py and Su-Py/Ir films respectively. The Py films as expected to show no magnetocrystalline anisotropy but we observed weak step induced uniaxial anisotropy whose strength depends on the sapphire miscut angle and growth temperature. In the nanostripes, this small substrate-induced uniaxial anisotropy is dominated by the shape anisotropy, which keeps the magnetization direction along the nanostripe length.

MFM was used to observed the DW position and internal structure before and after the field or current pulses. Stochastic behaviour of field-induced DW depinning from natural defects in both Py(15 nm) and Py(10 nm)/Ir(10 nm) nanostripes was observed. The average DW depinning field in 400 and 300 nm wide nanostripes is ~ 2 and 2.5 mT respectively. These values of depinning fields are almost two times higher than predicted by micromagnetic simulations ~ 1 mT for 5 nm thick and 120 nm wide rough nanostripes with grain size $< D >= 10$ nm [127], probably due to extended defects and bicrystallinity. The grains size in our epitaxial bi-crystal samples is relatively large with respect to the polycrystalline samples (~ 10 nm) and is comparable to the stripe width. This may result into stronger DW pinning. On the other hand sputtered Py films show relatively smaller depinning field of 0.75 mT for 400 nm and 1.2 mT for 300 nm wide stripes.

This high pinning leads to the need for high current densities to move DWs. The minimum current density for which the DW motion was observed is 2.5×10^{12} A/m^2 in single layer Py nanostripes, which is 2 to 3 times higher than observed by other groups in similar stripes [132][139][60]. Very high DW velocities, with maximum velocity exceeding 500 m/s were found for current density 3.4×10^{12} A/m^2 in these stripes. The highest DW velocities were found quite rarely. The DW displacement does not scale directly with the pulse length and the DWs get pinned before the end of the pulse, making that higher velocities were obtained for shorter current pulses. Moreover, the high current density required for higher DW velocities gives rise to significant Joule heating resulting sample temperature 510 K. This results into DW transformations [60] and very often DW motion

against the electron flow or towards the stripe center due to strong temperature gradient present in the nanostripes, as also reported in the literature [19].

In contrary to Py single layers, small critical current density of 7×10^{11} A/m^2, comparable to reported in literature was observed in Py(10 nm)/Ir(10 nm) bilayer nanostripes. However, DW motion was found to be stochastic due to DW pinning and very rare reproducible events were observed. This results in a distribution of velocities with maximum very high velocities of 400 and 700 m/s for Vortex and transverse walls respectively with a current density of 1.7×10^{12} A/m^2, in 400 nm wide nanostripes. These values of velocity are 3 to 5 times higher than observed in single layer Py nanostripes having similar dimensions, for similar current densities, reported in the literature [43][46]. DW transformations from transverse to vortex and vice versa were also observed after applying current pulses. Joule heating was small with a maximum rise of temperature up to 360 K due to smaller current densities required for DW motion as compared to single layer Py nanostripes.

For sputtered deposited Py/Pt bilayer nanostripes, we observed critical current density of 4×10^{11} A/m^2, lower than for both epitaxial Py single and Py/Ir bilayer nanostripes. Motion of VWs in sputtered 1 µm wide Py(15 nm)/Pt(10 nm) nanostripes bilayers is much more reproducible, leading to high DW velocities (above 250 m/s) for moderate current densities ($\sim$) 1×10^{12} A/m^2). This value of current density is 2 to 3 times lower and velocity 2 times higher than for typical values reported in literature for single Py layers [43][27]. In contrast to epitaxial Py and Py/Ir nanostripes, no Joule heating was observed in these stripes, but, current density was also smaller than epitaxial samples for maximum velocities. However, even for current densities comparable to that used for Py/Ir bilayers, negligible Joule heating was observed. Another reason of the higher Joule heating in epitaxial stripes is the poor thermal conductivity of the sapphire substrate as compared to the naturally oxidized Si.

The current-induced Oersted field may be at the origin of the high efficiency of Py/Ir and Py/Pt bilayer systems, while net Oersted field is zero in Py single layers. The Oersted field favour TWs of one chirality, like it has been shown in the literature that transverse field stabilize the one chirality of TWs during field induced DW motion, preventing DW transformations [18]. This can result in a suppression of the Walker breakdown for a given stimulus magnitude resulting in an increase of the average DW velocity. We studied the effect of Oersted field on TW chirality in Py/Ir nanostripes with different Ir thicknesses and clearly observed TW chirality switching by Oersted field under positive and negative current pulses. The current densities required for TW chirality switching are of same order of magnitude as required for DW motion. The Oersted field might also modify the TW shape by widening or narrowing the TWs. For wider TWs, depinning becomes easier and this might explain the lower critical current densities for bilayer nanostripes.

In case of VWs, the Oersted field may stabilize the vortex core in the center of nanostripe by supressing the core expulsion to the nanostripe edge and hence preventing the VW transformation. This can result in a suppression of the Walker breakdown resulting in an increase of the average DW velocity. Micromagnetic simulations performed in our group by Nicolas Rougemaille confirm that the transverse magnetic field can stabilize the vortex core at the center of the nanostripe during VW motion. When a transverse field of 20 mT was applied opposite to the vortex core expulsion direction, in addition to the longitudional field along the nanostripe for VW motion, the VW move with 5 times higher displacement before transformation.

Time-resolved XMCD-PEEM measurements will be performed in near future to con-

firm the effect of Oersted field on VW mobility. For the Py/Pt bilayers, the relative contribution of STT and Oersted field can be tuned by tuning the Pt thickness. Time-resolved measurements on different Py/Pt bilayers will be performed to observe the vortex core motion under current. Best ratio would be when the action of STT and Oersted field on the core cancel each other.

High quality epitaxial Su-Py films with negligible magneto-striction have also been prepared, which may show less pinning than Py. We could not really measure them until now since DWs in nanostripes pattrened from these films were very easily dragged even by the 3 nm $Co_{80}Cr_{20}$ tips. Even further low moment tips (with less magnetic material) are needed to measure them. This indicates very low DW propagation field in these stripes, hence small critical current densities for current-induced DW are expected. This result is encouraging, and measurements will be done in near future with even lower moment magnetic tips.

Appendix A

Experimental techniques

A.1 Pulsed laser deposition (PLD)

Pulsed laser deposition (PLD) is a thin film deposition (specifically a physical vapour deposition) technique where a high power pulsed laser beam is focused inside a vacuum chamber to strike a target of the desired composition. Material is then vapourised from the target and deposited as a thin film on a substrate, such as a silicon wafer facing the target. This process can occur in ultra high vacuum (UHV) or in the presence of a background gas, such as oxygen which is commonly used when depositing oxides to fully oxygenate the deposited films. PLD is for instance a common technique for the fabrication of high-Tc superconductors. On the reverse, PLD is rarely used for the epitaxy of metals. Some specificities arise with respect to molecular beam epitaxy, some with advantages, some with drawbacks [116].

PLD is very simple technique and produces films with the same composition as the target. It is fast and cost effective. The advantages of pulsed laser ablation are flexibility, fast response, congruent evaporation and energetic evaporants. The main drawback of PLD is the formation of droplets in thin film growth, specially when using high fluence.

While the basic setup is simple relative to many other deposition techniques, the physical phenomena of laser-target interaction and film growth are quite complex. When the laser pulse is absorbed by the target, energy is first converted to electronic excitations and then into thermal, chemical and mechanical energy resulting in evaporation, ablation, plasma formation and even exfoliation. The ejected species expand into the surrounding vacuum in the form of a so called plume containing many energetic species including atoms, molecules, electrons, ions, clusters, before depositing on the typically hot substrate The process of PLD can schematically be divided into four stages:

- Laser ablation of the target material and creation of a plasma
- Dynamic of the plasma under vacuum (expansion, cooling)
- Deposition of the ablated material on the substrate
- Nucleation and growth of the film on the substrate surface

Each of these steps is crucial for the crystallinity, uniformity and stoichiometry of the resulting film.

The ultra high vaccum chambers

The UHV setup in our lab and its schematics are shown in the figures A.1 and A.2 respectively. It consist of three main chambers connected to each other under UHV.

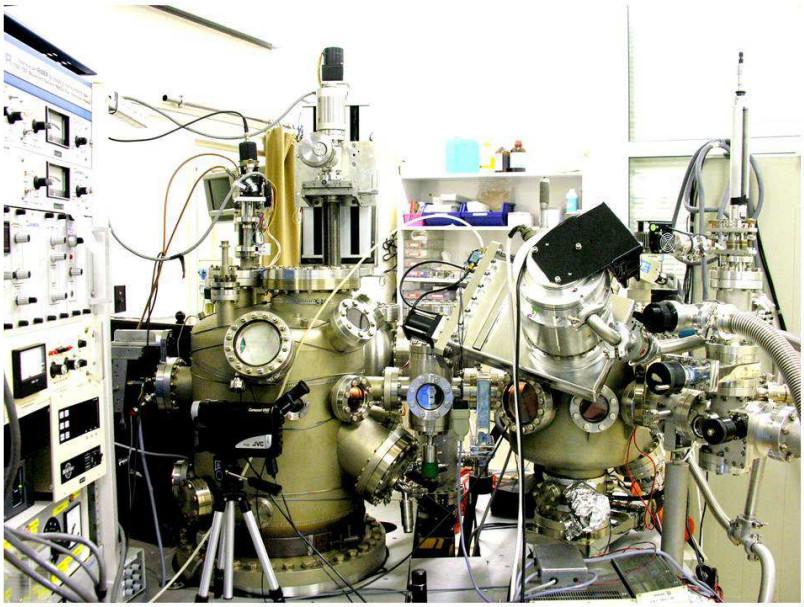

Figure A.1: Photo of ultra high vacuum setup in our lab.

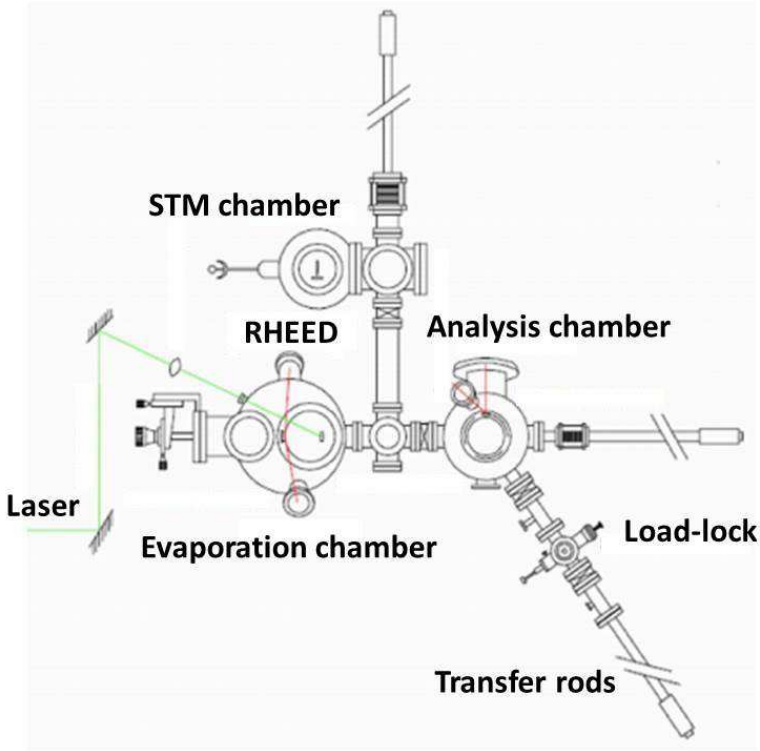

Figure A.2: Schematic view of ultra high vacuum setup.

The evaporation chamber contains a rotatable substrate holder with a heating filament, a 10-20 keV electron gun coupled to a fluorescent screen equipped with a 10 bit CCD camera for reflection high energy electron diffraction (RHEED) measurements, a multi-target holder, a quartz microbalance for estimating the speed of deposition and a moveable mask for varying the thickness of deposits.

The analysis or preparation chamber contains an argon etching gun, Auger electron spectroscopy (AES), a home made electron bombardment (0.2 mm diameter Ta wire) heated sample holder. Samples temperatures are measured with a pyrometer. It also provides a dozen storage positions for targets and substrates.

The STM chamber contains an Omicron scanning tunneling microscope (STM), for studying the samples surface topography. We used non conducting sapphire substrate for thin film deposition. A wobble-stick in the STM chamber is used to make an electrical contact for imaging, by turning the metallic clamp used to fix the sample on the Omicron plaquette onto the metallic layer. A home made etched tungston (W) tip is used for STM imaging. I t can be moved horizontally on the sample and hence is able to image samples with variable thicknesses.

In general, the vacuum is of the order of a 4×10^{-11} Torr in the evaporation chamber and of a 3×10^{-10} Torr in the analysis and STM chamber. During my thesis the quality of vacuum was good,with a base pressure of $\sim 4 \times 10^{-11}$ Torr, leading to a pressure of 4×10^{-10} Torr during the deposition.

All parts of UHV chamber are isolated by valves. The introduction and removal of substrates, targets, samples etc. are done via a mini chamber called load-lock kept under a vacuum of $\sim 10^{-6}$ Torr. The manipulation of samples between the chambers is performed with transfer rods through 1 inch molyblocks containing Omicron plaquettes compatible with the Omicron system. The samples are fixed on plaquettes with the help of Mo clamps.

Laser and Speed of deposition

We used a pulsed Quantel Nd-YAG laser with a pulse duration of 10 ns, repetition frequency of 10 Hz and a maximum energy per shot of 150 mJ. The initial frequency is doubled using a non linear crystal, to reach the wavelength of 532 nm. The laser average power is $\sim$ 1 W, leading to an instantaneous power of $\sim$ 10 MW, which is sufficient to melt the surface of any light absorbing material, in our case metals.

It is important to know and control the speed of deposition to control the thickness of the material deposited. Furthermore, the growth of material will be different according to the speed at which we deposit. A quartz balance in evaporation chamber is used for this purpose. It is a quartz plate whose shear resonance frequency varies depending on rigidity and inertia. The rigidity is a second order modification whereas inertia is proportional to quantity of material deposited. Thus, the frequency evolution of the resonance inform us about the quantity of material deposited. Before each deposition, the quartz is placed in front of the target on which laser beam is sent to check the speed of deposition. The speed can be adjusted by modifying any of the following two parameters.

- The total power of the beam in J/pulse which changes the fluence while the surface of evaporation is kept constant. The rate of evaporation versus fluence displays a threshold above which the rate of evaporation increases sharply. This is achieved by varying the time delay between the oscillator and amplificatory stages of the laser.

- Before entering the deposition chamber the beam has a diameter of about 0.5 cm^2. The beam is then focused on a target by a converging lens with a focal length of $f = 500$ mm. The target is placed between f/5 and f/3 focal point. By playing with the focus, it adjusts power (or energy) per unit surface called the fluence. Moving towards focus increases the fluence and thus the rate of evaporation per unit area, however the total area of evaporation is reduced. Typically we work between 0.1-1 Joule per meter-square, leading a typical deposition rate of 0.05 nm/min at 10 Hz. The distance between the substrate and target is 140 mm.

Epitaxial thin film growth modes

The growth of epitaxial thin films under thermodynamic equilibrium at higher temperatures during the initial stages is determined by the balance of the different surface free energies involved and follows one of the three well-known mechanisms:

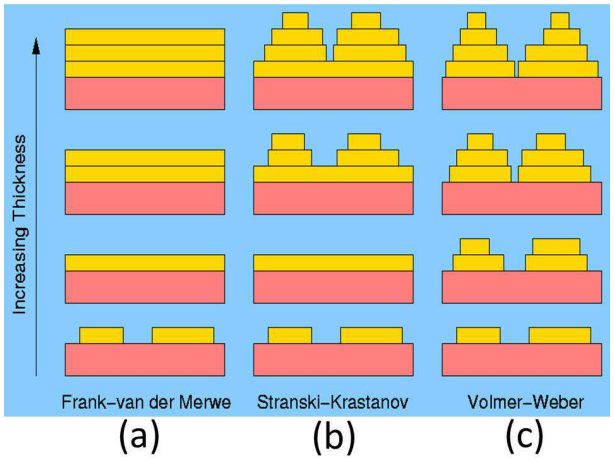

Figure A.3: Schematic representation of three epitaxial growth modes. (a) Frank-van der Merwe, layer by layer growth (b) Volmer-Weber, island growth (c) Stranski-Krastanov, layer by layer plus island growth [J.J. de Miguel].

- Frank-van der Merwe mode : This growth mode is characterized by a layer by-layer deposition. Each monolayer start to grow after the completion of previous layer. The interaction between the atoms of the deposited material and the substrate is stronger than the mutual interaction of deposited material atoms. This mode is favourable for materials with same lattice parameters or small lattice mismatch with the substrate.

- Volmer-Weber mode : This growth process corresponds to the formation of three dimensional (3D) islands growth. The interaction between the atoms of deposited material and the substrate is weaker than the mutual interaction of the deposited material atoms.

- Stranski-Krastanov mode : This growth mode corresponds to the nucleation of 3D islands after a layer by layer growth of one or several monolayers.

However, at lower temperatures in non equilibrium conditions this is not the case. In this case some roughness so called *"mounds"* is created which can be overcome by tuning the temperature. The schematic representation of these growth modes is shown in Fig. A.3.

A.2 Reflection high energy electron diffraction (RHEED)

A RHEED system requires an electron source (gun), photoluminescent detector screen and a sample with a clean surface, although modern RHEED systems have additional parts to optimize the technique. The electron gun generates a beam of electrons with an energy in the range 10-20 keV that strike the sample at a very small angle relative to the sample surface, typically 0-5° degree.

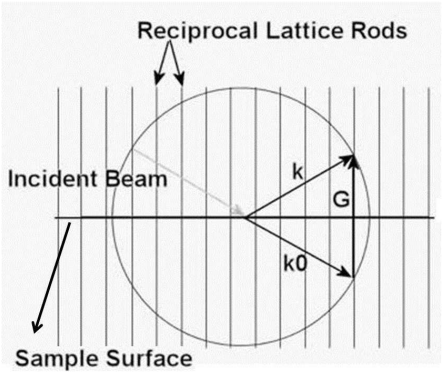

Figure A.4: Schematic view of the RHEED construction of the Ewald's Sphere at the sample surface. The radius of the Ewald's sphere is equal to the magnitude of the k_0 vector, which is the reciprocal of the wavelength of the incident electrons. The k vector, corresponds to an allowed diffraction condition, and the G vector is the difference between the k and k_0 vectors called scattering vector [Wikimedia].

In the RHEED setup, only the top-most plane of atoms contribute to the RHEED pattern. Atoms at the sample surface diffract (scatter) the incident electrons due to the wavelike properties of electrons. The reciprocal lattice of 2D network is an array of rods perpendicular to this network as shown in RHEED schematics (Fig. A.4). Owing to the high energy of the electrons the Ewald sphere has a large radius. Thus the diffraction pattern is essentially a set of streaks (the rods) perpendicular to the sample surface. The diffracted electrons interfere constructively at specific angles according to the crystal structure and spacing of the atoms at the sample surface and the wavelength of the incident electrons.

The azimuthal angle is the angle at which the incident electrons impinge on the surface of the sample. Inspecting RHEED patterns and spacing of streaks as a function of the azimuth, the reciprocal space of the surface can be reconstructed, and so its crystallographic structure. RHEED also yields information on the morphology of the surfaces (flat, rough, facetted etc) through the analysis of the shape of the streaks.

A.3 Scanning tunneling microscopy

In scanning tunneling microscopy (STM), a fine metallic conducting tip is scanned back and forth close (a few Å) to a conductive sample, without a physical contact between the tip and the sample. A voltage (few volts) is applied between the tip and the sample resulting in a small electric current (nA) from sample to tip or vice versa due to electron tunneling, a quantum mechanical effect.

There are different mode of operation of STM. In constant current mode, using a feedback loop, the tip is vertically adjusted in such a way that the current always stays constant. A topographic image of the surface is obtained by recording the vertical position of the tip. In constant height mode, the tip is attached to a piezoelectric tube and voltage applied to the piezo rod is changed to maintain a constant distance for the tip from the sample surface. The resulting current depends upon the distance between the tip and sample surface. The changes in voltage generates a topographic image of the sample surface.

The lateral resolution is about 1 Å whereas a vertical resolution down to 0.01 Å can be achieved. The STM can be used in ultra high vacuum, air or other environments. A schematic view of STM is shown in Fig. A.5.

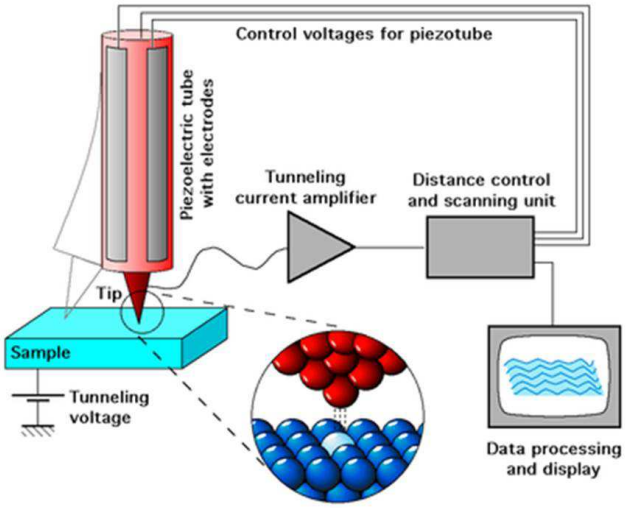

Figure A.5: Schematic view of scanning tunneling microscopy [M. Schmid].

A.4 Superconducting Quantum Interference Device Magnetometry

Superconducting Quantum Interference Devices (SQUID) are very sensitive magnetometers used to measure extremely small magnetic fields. Nowadays, this instrument is widely used worldwide in research laboratories. The system is designed to measure the magnetic moment of a sample, from which the magnetization may be derived.

They are based on superconducting loops containing Josephson junctions. The superconducting loops is a solenoid made of superconducting wire. This solenoid is kept

at liquid helium temperature in a liquid helium chamber. The uniform magnetic field is produced along the axial cylindrical core of the coil. A bipolar supply is used to operate the superconducting magnet. A superconducting detection coil which is a single piece of superconducting wire is placed in the uniform magnetic field region of the solenoidal superconducting magnet. This superconducting detection coil is coupled inductively to the sample.

The SQUID device functions as an extremely sensitive current-to-voltage-converter. The measurements are done in SQUID by moving the sample through the superconducting detection coil. Hence, the magnetic moment of the sample induces an electric current in the pick-up coil system. A change in the magnetic flux in these coils changes the persistent current in the detection circuit. So, the change in the current in the detection coils produces a variation in the SQUID output voltage proportional to the magnetic moment of sample. The measurement of magnetic moment as a function of applied magnetic field, produced by the current passing through the superconducting coil, is used to derive the hysteresis loops.

A.5 Kerr magnetometry and Microscopy

Both Kerr magnetometry and microscopy are based on the *"Magneto-Optical Kerr Effect"* (MOKE), which deals with the interaction of polarised light with the internal magnetic field of the magnetic sample. Through this interaction, the polarization of the light reflected from the surface of a magnetic sample changes. This effect is similar to the *"Faraday effect"*, which describe the changes of polarised light transmitted through a optically transparent magnetic sample.

In order to detect the changes introduced into the polarization state of the light by reflection from a magnetized surface, a pair of nearly crossed polarizers is located in the optical path. The linear polarizer on the incident beam restricts the polarization to one direction. Through the interaction of the light with the magnetized surface polarization components perpendicular to that of the incident beam are generated. The reflected beam is passed through an analyzer which is nearly crossed with the incident light polarizer. As a result, the component of the light that maintained its original polarization state after the interaction with the magnetized surface is attenuated, while the component generated through the magneto-optical (Kerr) interaction is allowed to pass to the detector. Maximum attenuation of the incident light is achieved when the polarizers are perfectly crossed, however Kerr component of the light is very weak and would require an extremely sensitive detector. By allowing some of the incident light to reach the detector the Kerr signal and the background (incident) signal are allowed to add coherently, contributing to a higher signal which is easily registered by conventional detectors.

This general principle is the one used in our microscope. The schematic representation of this principle is shown in Fig. A.6 (b). However, in our focused Kerr magnetometer, we use a Wollaston prism, which divides the beam into two orthogonally polarized beams, which are monitored by a pair of photodiodes as shown in Fig. A.6 1.5(a). Thus monitoring the relative intensity on the two diodes allows to obtain the polarization of the reflected light as a function of an applied field, allowing to derive a hysteresis loop. In the magneto-optical microscope the sensitive signal detector is the CCD camera. This allows us to perform imaging of nucleation and propagation of domain walls.

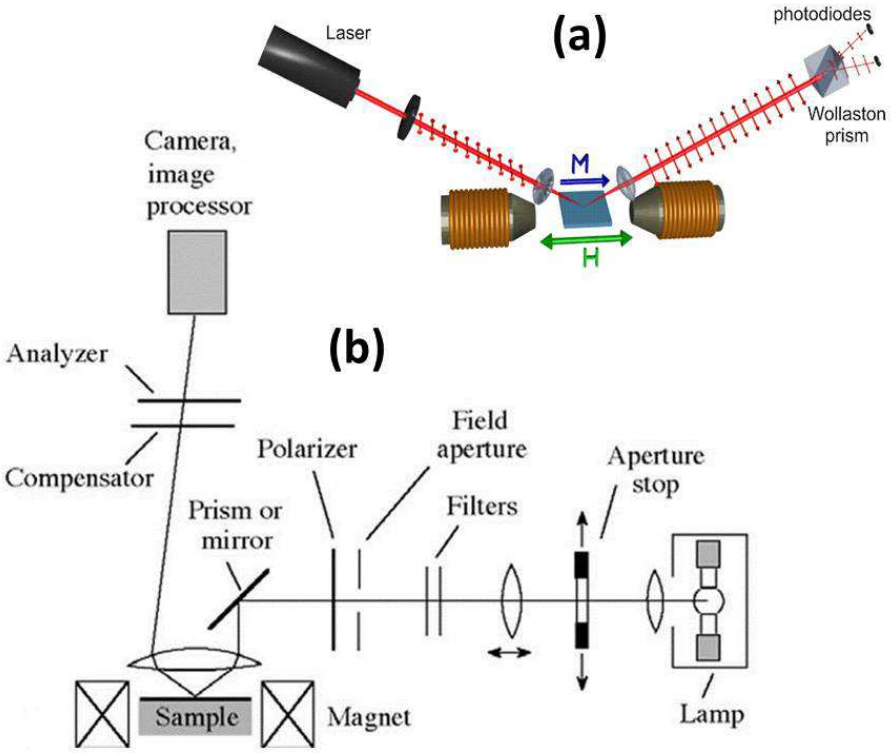

Figure A.6: (a) Schematic view of Kerr magnetometry [B. Hillebrands] (b) Kerr microscopy [53].

A.6 Ferromagnetic resonance

(Ferromagnetic resonance (FMR) is a spectroscopic technique to measure magnetic properties via precessional motion of the magnetization in ferromagnetic materials, in an external magnetic field. The external (continuous) magnetic field orients the magnetization direction, while the (small) microwave field, oriented perpendicular to the static field, causes the precession. The precession frequency will depend on the static field, and when it resonates with the microwave field, the microwave absorption will be maximum.

FMR experimental setup consist of a microwave resonant cavity with a fixed resonance frequency and an electromagnet. A detector is placed at the end of the cavity to detect the microwaves. The magnetic sample is placed between the poles of the electromagnet. The schematic representation of basic FMR setup is shown in Fig. A.7. In our case, FMR measurements were taken using a fixed frequency 9.77 GHz cavity. The electromagnet field strength lies between 0-2 T. The sample is mounted on a goniometer with the magnetic field applied parallel to the surface of the film. The goniometer can rotate the sample, allowing to study angular dependence of the resonance field and line-width from in-plane to out-of-plane of the sample suraface. The magnetic field is sweep while the resonant absorption intensity of the microwaves is detected. When the magnetization precession frequency and the resonant cavity frequency are the same, absorption increases sharply which is indicated by a decrease in the intensity at the detector.

Usually the absorption derivative is measured. The resonance field position H_{res} depends on the angles, anisotropy parameters, g-factor, and magnetization of the sample.

The linewidth ΔH is directly connected to the relaxation processes. In ultrathin films, Gilbert damping is commonly used to describe the relaxation.

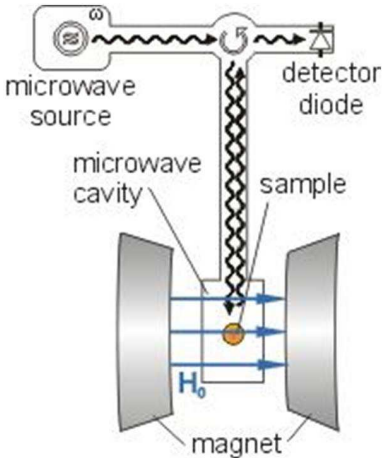

Figure A.7: A conventional FMR spectrometer setup [W. Kuch].

A.7 X-ray magnetic circular dichorism and Photo-emission electron microscopy

To study the Domain wall (DW) configurations in both Py and Co layers in spin-valve nanostripes, we used the element selective X-ray magnetic circular dichroism (XMCD) and Photo-emission electron microscopy (PEEM). XMCD is the difference of the absorption between the left and right circularly polarized X-rays in a magnetic material. The absorption edges have energies which are characteristic for each element. The X-ray absorption results in transition of a core-electron to empty states above the fermi level, leaving behind empty core levels which are then filled by electrons relaxing from higher energy levels. The difference of energy is provided to Auger electrons which are emitted out of the atoms. These Auger electrons can be scattered and give rise to secondary electrons. The final number of photoelectrons (Auger and secondary electrons) emitted is proportional to the X-ray absorption intensity.

The total number of secondary electrons emitted from the material for a fixed circular polarization gives us a map of the magnetization in the sample, imaged by PEEM as shown in Fig. A.8 (a). The secondary electrons are extracted by the objective lens kept at a high potential, focused and expanded by a set of projection electrostatic lenses. The image is formed on a fluorescent screen combined with a microchannel plate and captured on a CCD camera.

We performed measurements at the Nanospectroscopy beamline at the synchrotron ELETTRA (Trieste, Italy). For XMCD, the x-ray energy was tuned to the maximum of the Fe L_3-absorption-edge (707 eV) for the Py layer and of the Co L_3-edge (778 eV) for the Co layer. A spatial resolution below 40 nm was obtained, being limited in particular by the extraction voltage and magnetic lens aberrations.

Fig. A.8 (b) shows the map of magnetization in a square element with a flux-close domain structure. The domains with a magnetization parallel to incoming X-rays will

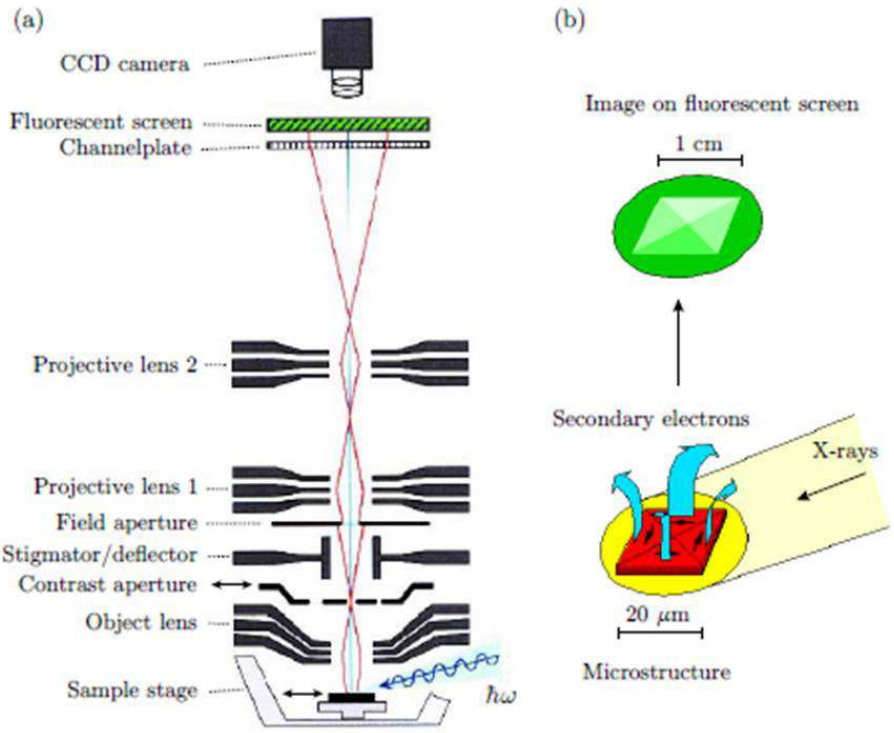

Figure A.8: Schematic view of (a) the internal configuration of the PEEM microscope. The incident X-ray beam excites secondary electrons which form (b) a magnified XMCD absorption image on the fluorescent screen and CCD camera [W. Kuch].

absorb more photons and therefore emit more secondary electrons (bright contrast) than in the antiparallel case (dark contrast). The intermediate intensity will be found for domains with a magnetization perpendicular to the incoming X-rays.

Usually what we do is that we take two images, one with left and one with right-circularly polarized x-rays, and then we take the asymmetry (the difference divided by the sum of the two images). This increases the magnetic contrast and decreases the topographic contrast.

A.8 Sample patterning techniques

Different lithography techniques are used for patterning of samples e.g. optical, electron-beam or focused ion beam lithography etc. We used optical and electron beam lithography for patterning magnetic nanostripes to study current-induced domain wall motion in these stripes.

A.8.1 Optical lithography

In optical lithography ultra-violet (UV) or deep ultra-vilot (DUV) light is used as a radiation source. An UV lamp is used to insulate the polymer resist sensitive to UV light, through a mask partially transparent to light. For positive resist, the insulated part of the resist is removed using a photoresist developper, leaving behind the desired pattern.

These patterns are used as template for deposition of required materials. The resolution and quality of the patterns depend on the wavelength of the light used, the UV lamp power, time exposure, material of the mask and type of the resist. There is a minimum limit of the pattern size that can be achieved by UV lithography of about ($\sim$ 500 nm), due to diffraction limit of the light wavelength.

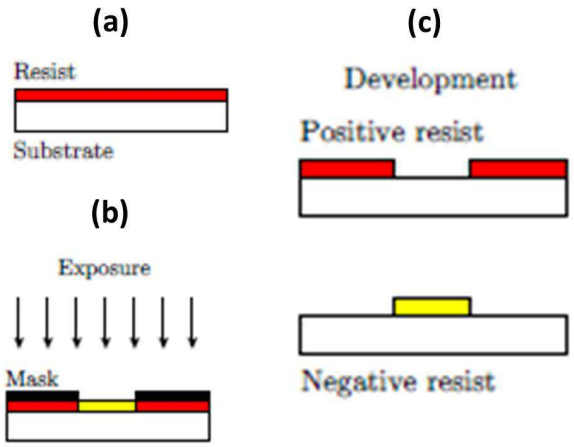

Figure A.9: Schematics UV lithography. After insulation by UV light using a mask, the exposed part of positive resist is removed in a developper, while negative resist becomes harder after insulation and remains there [135].

We used DUV lithography for depositing Au(50 nm)/Ti(20 nm) contact electrodes for passing current pulses through the metallic nanostripes. First 500 nm thick, S1818 polymer photo resist is deposited by spin coating on sapphire substrate. The resist is then exposed to DUV light for 60 seconds through a partially transparent Cr mask containing desired patterns to fabricate. The exposed part is then removed by rinsing in a photo-resist micro-developer solution for 90 seconds and then in water for 30 seconds. The Au/Ti layers were deposited on this template. Finally, the remaining parts of the resist are removed by putting in a acetone solution using the lift-off process. The schematic of DUV lithography is shown in Fig. A.9.

A.8.2 Electron-beam lithography

The e-beam lithography technique uses an electron beam in a scanning electron microscope, to expose an electron-sensitive positive resist, usually polymethylmethacrilate (PMMA). Patterns with lateral dimensions of the order of tens of nanometers can be fabricated by this technique. The main disadvantage of electron-beam lithography is that it is slow and time consuming due to sequential scanning of the electron beam. It is therefore suitable for small area patterns.

In our case, first continuous thin Py and Py/Ir films were deposited on a sapphire (0001) substrate by pulsed laser deposition. Later, these magnetic films were patterned into S-shaped and zig-zag shaped nanostripes of width between 100-600 nm using combined electron-beam lithography and lift-off techniques at Nanofab, Institut Néel by Stefania Pizzini.

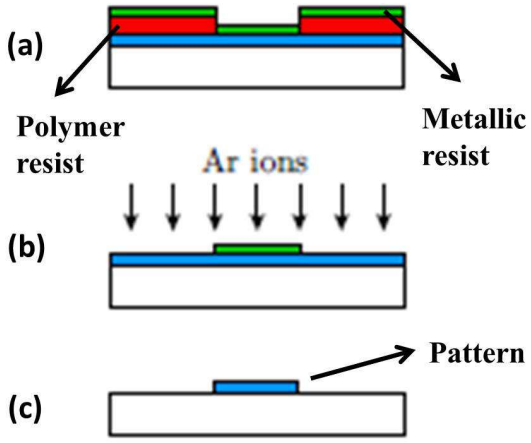

Figure A.10: Ion beam etching technique using a metallic mask which is prepared by standard lift-off technique. Etching of the metallic mask is monitored by a SIMS signal of a reference layer [135].

Fig. A.10 shows the schematics of the lift-off and electron-beam lithography process. A pattern is first created using UV lithography and lift-off process on a magnetic layer to be patterned as described above. A reference metallic layer with calibrated thickness having etching times larger than the magnetic layer is evaporated on a separate substrate. A metallic mask (in our case, Ti) with a thickness 2-3 nm larger than reference layer is evaporated on the magnetic layer. The two sample layers are then etched using ion beam etching technique simultaneously. The etching is stopped when the reference layer is fully etched, resulting in a 2-3 nm Ti metallic mask on the magnetic pattern.

Appendix B

List of Publications

B.1 Papers

1. V. Uhlir, J. Vogel, N. Rougemaille, O. Fruchart, M. Z. Ishaque, V. Cros, J. Camarero, J. C. Cezar, F. Sirotti and S. Pizzini. *Current-induced domain wall motion and magnetization dynamics in CoFeB/Cu/Co nanostripes.* J. Phys.: Condens. Matter, **2**4, (2012) 024213.

2. V. D. Nguyen, C. Naylor, L. Vila, A. Marty, P. Laczkowski, C. Beigné, L. Notin, Z. Ishaque and J. P. Attané. *Magnon magnetoresistance of NiFe nanowires: Size dependence and domain wall detection.* Appl. Phys. Lett., **9**9, 262504 (2011)

B.2 Presentations

1. M. Z. Ishaque, S. Perl, S. Pizzini , O. Fruchart, Nicolas Rougemaille, J. C. Toussaint, J. Vogel. *Effects of Oersted field on current induced domain wall motion and domain wall chirality in bilayer (FeNi/Ir) nanostripes.* Poster presentation in Joint MMM-Intermag conference 2013, Chicago, Illinois, USA.

2. M. Z. Ishaque, J. Vogel, S. Pizzini, D. Berling, L. Ranno, E. Mossang, O. Fruchart. *Development of epitaxial Permalloy (FeNi) and supermalloy (FeNiMo) films for current induced domain wall motion.* Poster presentation in Joint European Magnetic Symposia 2012, Parma, Italy.

3. M. Z. Ishaque, S. Perl, S. Pizzini , O. Fruchart, Nicolas Rougemaille, J. C. Toussaint, J. Vogel. *Effects of Oersted field on current induced domain wall motion and domain wall chirality in bilayer (FeNi/Ir) nanostripes.* Poster presentation in Joint European Magnetic Symposia 2012, Parma, Italy.

4. M. Z. Ishaque, O. Fruchart, J. Vogel, S. Pizzini, N. Rougemaille, J. C. Toussaint, V. Uhlir, Z. Kassir-Bodon, A. Masseboeuf, P. Bayle-Guillemaud, A. Locatelli, O. Mentes, M. Urbanek. *Enhanced stability of transverse domain walls in spin-valve nanostripes.* Oral presentation in Colloque Néel 2011, Brest, France.

5. M. Z. Ishaque, J. Vogel, O. Fruchart, S. Pizzini, N. Rougemaille. *Development of epitaxial permalloy (FeNi) films for current induced domain wall motion.* Poster presentation in Colloque Néel 2010, Strasbourg, France.

6. M. Z. Ishaque, J. Vogel, O. Fruchart, S. Pizzini, N. Rougemaille. *Development of epitaxial permalloy (FeNi) films for current induced domain wall motion.* Poster presentation in Journée de la Matiere Condensé (JMC12) 2010, Troyes, France.

Appendix C

List of Abbreviations

AFM - Atomic Force Microscope
AMR - Anisotropic Magnetoresistance
DW - Domain Wall
FMR - Ferromagnetic Resonance
FCC - Face Centered Cubic
FM - Ferromagnetic
FWHM - Full Width at Half Maximum
GMR - Giant Magnetoresistance
HH - Head to Head
MFM - Magnetic Force Microscope
MOKE - Magneto Optical Kerr Effect
NM - Non Magnetic
OOMMF - Object Oriented Micromagnetic Framework
PEEM - Photoemission Electron Microscope
PMA - Perpendicular Magnetic Anisotropy
PMMA - Polymethyl Methacrylate
RHEED - Reflection High Energy Electron Diffraction
RAM - Random Access Memory
RKKY - Ruderman Kittel Kasuya Yosida
RMS - Root Mean Square
RT - Room Temperature
SEM - Scanning Electron Microscope
STM - Scanning Tunneling Microscope
STT - Spin Transfer Torque
SV - Spin Valve
SQUID - Superconducting Quantum Interferrence Device
TT - Tail to Tail
TW - Transverse Wall
TBIIST - Transverse Bias Initial Inverse Susceptibility and Torque
UV - Ultraviolet
UHV - Ultra High Vacuum
VW - Vortex Wall
XMCD - X ray Magnetic Circular Dichroism

Bibliography

[1] M. Albrecht, T. Furubayashi, M. Przybylski, J. Korecki, and U.Gradmann. Magnetic step anisotropies. *Phys. Rev. B*, 113:207–220, 1992.

[2] D. Allwood, G. Xiong, C. Faulkner, D. Atkinson, D. Petit, and R. Cowburn. Magnetic domain-wall logic. *Science*, 309:1688, 2005.

[3] D. Atkinson, D. A. Allwood, G. Xiong, M. D. Cooke, C. C. Faulkner, and R. P. Cowburn. Magnetic domain-wall dynamics in a submicrometre ferromagnetic structure. *Nature Mater.*, 2:85, 2003.

[4] M. N. Baibich, J. M. Broto, A. Fert, F. Nguyen Van Dau, F. Petroff, P. Etienne, G. Creuzet, A. Friederich, and J. Chazelas. Giant magnetoresistance of (001)Fe/(001)Cr magnetic superlattices. *Phys. Rev. Lett.*, 61:2472–2475, 1988.

[5] L. Baselgia, M. Warden, and F. Waldner. Derivation of the resonance frequency from the free energy of ferromagnets. *Phys. Rev. B*, 38:2237–2242, 1988.

[6] Ya. B. Bazaliy, B. A. Jones, and S. Zhang. Modification of the Landau-Lifshitz equation in the presence of a spin-polarized current in colossal- and giantmagnetoresistive materials. *Phys. Rev. B*, 57:R3213–3216, 1998.

[7] G. S. D. Beach, C. Knutson, C. Nistor, M. Tsoi, and J. L. Erskine. Nonlinear domain-wall velocity enhancement by spin-polarized electric current. *Phys. Rev. Lett.*, 97:057203, 2006.

[8] G. S. D. Beach, C. Nistor, C. Knutson, M. Tsoi, and J. L. Erskine. Dynamics of field-driven domain-wall propagation in ferromagnetic nanowires. *Nat. Mater.*, 4:741, 2005.

[9] G.S.D. Beach, C. Knutson, M. Tsoi, and J.L. Erskine. Field and current driven domain wall dynamics: An experimental picture. *J. Magn. Magn. Mater.*, 310:2040, 2007.

[10] L. Berger. Dragging of domains by an electric-current in very pure, noncompensated, ferromagnetic metals. *Phys. Lett.*, 46, 1973.

[11] L. Berger. Prediction of a domain-drag effect in uniaxial, noncompensated, ferromagnetic metals. *J. Phys. Chem. Solids*, 35, 1974.

[12] L. Berger. Exchange interaction between ferromagnetic domain walls and electric current in very thin metallic films. *J. Appl. Phys.*, 55, 1984.

[13] L. Berger. Emission of spin waves by a magnetic multilayer traversed by a current. *Phys. Rev. B*, 54, 1996.

[14] D. Berling, S. Zabrocki, R. Stephan, G. Garreau, J. L. Bubendorff, A. Mehdaoui, D. Bolmont, P. Wetzel, C. Pirri, and G. Gewinner. Accurate measurement of the in-plane magnetic anisotropy energy function in ultrathin films by magneto-optics. *J. Magn. Magn. Mater.*, 297:118–140, 2006.

[15] G. Binasch, P. Grünberg, F. Saurenbach, and W. Zinn. Enhanced magnetoresistance in layered magnetic structures with antiferromagnetic interlayer exchange. *Phys. Rev. B*, 39:4828–4830, 1989.

[16] L. Bocklage, B. Kruger, T. Matsuyama, M. Bolte, U. Merkt, D. Pfannkuche, and G. Meier. Dependence of magnetic domain-wall motion on a fast changing current. *Phys. Rev. Lett.*, 103:197204, 2009.

[17] P. Bruno and C. Chappert. Ruderman-kittel theory of oscillatory interlayer exchange coupling. *Phys. Rev. B*, 46:261–270, 1992.

[18] M. T. Bryan, T. Schrefl, D. Atkinson, and D. A. Allwood. Magnetic domain wall propagation in nanowires under transverse magnetic fields. *J. Appl. Phys.*, 103:073906, 2008.

[19] J. Y. Chauleau, R. Weil, A. Thiaville, and J. Miltat. Magnetic domain walls displacement: Automotion versus spin-transfer torque. *Phys. Rev. B*, 82:214414, 2010.

[20] V. V. Chi. Epitaxial graphene prepared by chemical vapor deposition on single crystal thin iridium films on sapphire. *Appl. Phy. Lett.*, 98:181903, 2011.

[21] R. Eason. *Pulsed laser deposition of thin films*. Wiley and New York, 2006.

[22] M. Eltschka, M. Wotzel, J. Rhensius, S. Krzyk, U. Nowak, M. Klaui, T. Kasama, R. E. Dunin-Borkowski, L. J. Heyderman, H. J. van Driel, and R. A. Duine. Nonadiabatic spin torque investigated using thermally activated magnetic domain wall dynamics. *Phys. Rev. Lett.*, 105, 2010.

[23] C. Burrowes et al. Non-adiabatic spin-torques in narrow magnetic domain walls. *Nat. Phys.*, 6:11, 2010.

[24] D. Ravelosona et al. Nanometer scale observation of high efficiency thermally assisted current-driven domain wall depinning. *Phys. Rev. Lett.*, 95, 2005.

[25] J. P. Attané et al. Thermally activated depinning of a narrow domain wall from a single defect. *Phys. Rev. Lett.*, 96:147204, 2006.

[26] Kirilyuk et al. Magnetization reversal in ultrathin ferromagnetic films with perpendicular anisotropy. *J. Magn. Magn. Mater.*, 171, 1997.

[27] S. S. P. Parkin et al. Magnetic domain-wall racetrack memory. *Science*, 320:190–194, 2008.

[28] S. Foss, R. Proksch, E. D. Dahlberg, B. Moskowitz, and B. Walsh. Localized micromagnetic perturbation of domain walls in magnetite using a magnetic force microscope. *Appl. Phys. Lett.*, 69:3426, 1996.

[29] P. Freitas and L. Berger. Observation of s-d exchange force between domain walls and electric current in very thin permalloy films. *J. Appl. Phys.*, 57, 1985.

[30] H. Fritzsche, J. Kohlhepp, and U. Gradmann. Epitaxial strain and magnetic anisotropy in ultrathin Co films on W(110). *Phys. Rev. B*, 51, 1995.

[31] O. Fruchart, S. Jaren, and J. Rothman. Growth modes of W and Mo thin epitaxial [110] films on [1-120] sapphire. *Appl. Surf. Sci. 135(1-4), 218-232 (1998).*, 135:218–232, 1998.

[32] O. Fruchart, P. O. Jubert, M. Eleoui, F.Cheynis, B. Borca, P. David, V. Santonacci, A. Liénard, M. Hasegawa, and C. Meyer. Growth modes of Fe(110) revisited: a contribution of self-assembly to magnetic materials. *Journal of Physics: Condensed Matter*, 19, 2007.

[33] S. Fukami, T. Suzuki, N. Ohshima, K. Nagahara, and N. Ishiwata. Micromagnetic analysis of current driven domain wall motion in nanostrips with perpendicular magnetic anisotropy. *J. Appl. Phys.*, 103, 2008.

[34] I. Garate, K. Gilmore, M. D. Stiles, and A. H. MacDonald. Nonadiabatic spin-transfer torque in real materials. *Phys. Rev. Lett.*, 79, 2009.

[35] J. M. Garcia, A. Thiaville, J. Miltat, K. J. Kirk, and J. N. Chapman. Magnetic force microscopy imaging of patterned permalloy elements under an external applied field. *J. Magn. Magn. Mater.*, 242-245:1267–1269, 2002.

[36] J.M. Garcia, A. Thiaville, and J. Miltat. Magnetic force microscopy imaging of nanowires and elongated patterned elements. *J. Magn. Magn. Mater.*, 249:163–169, 2002.

[37] T. L. Gilbert. A phenomenological theory of damping in ferromagnetic materials. *IEEE Trans. Magn.*, 40, 2004.

[38] J. Grollier, P. Boulenc, V. Cros, A. Hamzic, A. Vaurčs, A. Fert, and G. Faini. Switching a spin valve back and forth by current-induced domain wall motion. *Appl. Phys. Lett.*, 83:509, 2003.

[39] J. Grollier, D. Lacour, V. Cros, A. Hamzic, A. Vaurčs, A. Fert, D. Adam, and G. Faini. Switching the magnetic configuration of a spin valve by current-induced domain wall motion. *J. Appl. Phys.*, 92:4825, 2002.

[40] G. Gutekunst, J. Mayer, and M. Ruhle. Atomic structure of epitaxial Nb-Al2O3 interfaces. *Philosophical magazine A*, 75:1329–1355, 1997.

[41] X. Z. Hao, Z. J. Cheng, Z. Z. Fen, Z. Q. Wei, D. H. Tao, and H. Yue. The effects of vicinal sapphire substrates on the properties of AlGaN/GaN heterostructures. *Chinese Physics B*, 18:5457–05, 2009.

[42] M. Hayashi, L. Thomas, R. Moriya, C. Rettner, and S. S. P. Parkin. Current-controlled magnetic domain-wall nanowire shift register. *Science*, 320:209–211, 2008.

[43] M. Hayashi, L. Thomas, C. Rettner, R. Moria, Y. B. Bazaliy, and S. S. P. Parkin. Current driven domain wall velocities exceeding the spin angular momentum transfer rate in permalloy nanowires. *Phys. Rev. Lett.*, 98:037204, 2007.

[44] M. Hayashi, L. Thomas, C. Rettner, R. Moriya, X. Jiang, and S. S. P. Parkin. Dependence of current and field driven depinning of domain walls on their structure and chirality in permalloy nanowires. *Phys. Rev. Lett.*, 97:207205, 2006.

[45] M. Hayashi, L. Thomas, C. Rettner, R. Moriya, and S. S. P. Parkin. Direct observation of the coherent precession of magnetic domain walls propagating along permalloy nanowires. *Nat. Phys.*, 3:21, 2007.

[46] M. Hayashi, L. Thomas, C. Rettner, R. Moriya, and S. S. P. Parkin. Real time observation of the field driven periodic transformation of domain walls in permalloy nanowires at the larmor frequency and its first harmonic. *Appl. Phys. Lett.*, 92, 2008.

[47] J. He, Z. Li, and S. Zhang. Current-driven vortex domain wall dynamics by micromagnetic simulations. *Phys. Rev. B*, 73, 2006.

[48] L. Heyne, M. Klaui, D. Backes, T. A. Moore, S. Krzyk, U. Rudiger, L. J. Heyderman, A. Fraile Rodriguez, F. Nolting, T. O. Mentes, M. A. Nino, A. Locatelli, K. Kirsch, and R. Mattheis. Relationship between nonadiabaticity and damping in permalloy studied by current induced spin structure transformations. *Phys. Rev. Lett.*, 100:066603, 2008.

[49] L. Heyne, J. Rhensius, A. Bisig, S. Krzyk, P. Punke, M. Klaui, L. J. Heyderman, L. Le Guyader, and F. Nolting. Direct observation of high velocity current induced domain wall motion. *Appl. Phys. Lett.*, 96:032504, 2010.

[50] D. Hinzke and U. Nowak. Domain wall motion by the magnonic spin seebeck effect. *Phys. Rev. Lett.*, 107:027205, 2011.

[51] J. C. A. Huang, T. E. Wang, C. C. Yu, Y. M. Hu, P. B. Lee, and M. S. Yang. Epitaxial growth and characterization of (100) and (110) permalloy films. *J. Cryst. Growth*, 171:442–446, 1997.

[52] A. Hubert, W. Rave, and S. L. Tomlinson. Imaging magnetic charges with magnetic force microscopy. *Phys. Stat. Sol. (b)*, 204:817–828, 1997.

[53] A. Hubert and R. Schäfer. *Magnetic domains : The analysis of magnetic microstructures*. Springer, Berlin, 1999.

[54] C.-Y. Hung and L. Berger. Exchange forces between domain wall and electric current in permalloy films of variable thickness. *J. Appl. Phys.*, 63:4276, 1988.

[55] Mi-Young Im, Lars Bocklage, Peter Fischer, and Guido Meier. Direct observation of stochastic domain-wall depinning in magnetic nanowires. *Phys. Rev. Lett.*, 102:147204, 2009.

[56] Y. Jang, S. Yoon, K. Lee, S. Lee, C. Nam, and B. K. Cho. Current-induced domain wall nucleation and its pinning characteristics at a notch in a spin-valve nanowire. *Nanotechnology*, 20:125401, 2009.

[57] S. W. Jung, W. Kim, T. D. Lee, K. J. Lee, and H. W. Lee. Current-induced domain wall motion in a nanowire with perpendicular magnetic anisotropy. *Appl. Phys. Lett.*, 92:202508, 2008.

[58] T. Kasuya. A theory of metallic ferro- and antiferromagnetism on zener's model. *Prog. Theor. Phys.*, 16:45–57, 1956.

[59] A. V. Khvalkovskiy, K.A. Zvezdin, Ya. V. Gorbunov, V. Cros, J. Grollier, A. Fert, and A. K. Zvezdin. High domain wall velocities due to spin currents perpendicular to the plane. *Phys. Rev. Lett.*, 102:067206, 2009.

[60] M. Kläui, P.O. Jubert, R. Allenspach, A. Bischof, J. A. C. Bland, G. Faini, U. Rudiger, C. A. F. Vaz, L. Vila, and C. Vouille. Direct observation of domain-wall configurations transformed by spin currents. *Phys. Rev. Lett.*, 95:026601, 2005.

[61] M. Kläui, M. Laufenberg, L. Heyne, D. Backes, and U. Rüdiger et al. Current-induced vortex nucleation and annihilation in vortex domain walls. *Appl. Phys. Lett.*, 88:232507, 2006.

[62] K. Kobayashi, Nabuyuki Inaba, N. Fujita, Y. Sudo, T. Tanaka, M. Ohtake, M. Futamoto, and F. Kirino. Damping constants for permalloy single-crystal thin films. *IEEE Trans. magn.*, 45:2541–2544, 2009.

[63] J. C. S. Kools, A. J. Devasahayam, K. Rook, C. L. Lee, and M. Mao. Effect of microstructure on the oscillating interlayer coupling in spin-valve structures. *J. Appl. Phys.*, 93:7921, 2003.

[64] W. Kuch, L. I. Chelaru, K. Fukumoto, F. Porrati, F. Offi, M. Kotsugi, and J. Kirschner. Layer-resolved imaging of magnetic interlayer coupling by domain-wall stray fields. *Phys. Rev. B*, 67:214403, 2003.

[65] L. Landau and E. Lifshits. On the theory of the dispersion of magnetic permeability in ferromagnetic bodies, 8, 153 (1935). *Phys. Z. Sowjet.*, 8, 1935.

[66] S. Laribi, V. Cros, M. Munoz, J. Grollier, A. Hamzic, C. Deranlot, A. Fert, E. Martinez, L. L. Daz, L. Vila, G. Faini, S. Zoll, and R. Fournel. Reversible and irreversible current induced domain wall motion in CoFeB based spin valves stripes. *Appl. Phys. Lett.*, 90:232505, 2007.

[67] S. Laribi, V. Cros, M. Munoz, J. Grollier, A. Hamzic, C. Deranlot, A. Fert, E. Martnez, L. L. Diaz, L. Vila, G. Faini, S. Zoll, and R. Fournel. Reversible and irreversible current induced domain wall motion in CoFeB based spin valves stripes. *Appl. Phys. Lett.*, 90:232505, 2007.

[68] S. LaShell, B. A. McDougall, and E. Jensen. Spin splitting of an Au(111) surface state band observed with angle resolved photoelectron spectroscopy. *Phys. Rev. Lett.*, 77:3419–3422, 1996.

[69] M. Laufenberg, W. Buhrer, D. Bedau, P.-E. Melchy, M. Klaui, L. Vila, G. Faini, C. A. F. Vaz, J. A. C. Bland, and U. Rudiger. Temperature dependence of the spin torque effect in current induced domain wall motion. *Phys. Rev. Lett.*, 97:046602, 2006.

[70] S. Lepadatu, A. Vanhaverbeke, D. Atkinson, R. Allenspach, and C. H. Marrows. Dependence of domain-wall depinning threshold current on pinning profile. *Phys. Rev. Lett.*, 102:127203, 2009.

[71] P. M. Levy, S. Maekawa, and P. Bruno. Range dependence of interlayer exchange coupling. *Phys. Rev. B*, 58:5588–5593, 1998.

[72] S. P. Li, D. Peyrade, M. Natali, A. Lebib, Y. Chen, U. Ebels, L. D. Buda, and K. Ounadjela. Flux closure structures in cobalt rings. *Phys. Rev. Lett.*, 86:1102–1105, 2001.

[73] Z. Li and S. Zhang. Domain-wall dynamics and spin-wave excitations with spin-transfer torques. *Phys. Rev. Lett.*, 92:207203, 2004.

[74] Z. Li and S. Zhang. Domain-wall dynamics driven by adiabatic spin-transfer torques. *Phys. Rev. B*, 70, 2004.

[75] C. K. Lim, T. Devolder, C. Chappert, J. Grollier, V. Cros, A. Vaurčs, A. Fert, and G. Faini. Domain wall displacement induced by subnanosecond pulsed current. *Appl. Phys. Lett.*, 84:2820, 2004.

[76] R. Loloee and M. A. Crimp. Effect of growth temperature on the structure and magnetic properties of sputtered biepitaxial (111) permalloy films. *J. appl. Phy.*, 92:4541–4544, 2002.

[77] G. Malinowski, A. Lorincz, S. Krzyk, P. Mohrke, D. Bedau, O. Boulle, J. Rhensius, L. J. Heyderman, Y. J. Cho, S. Seo, and M. Klaui. Current-induced domain wall motion in Fe20Ni80 nanowires with low depinning fields. *J. Phys. D: Appl. Phys.*, 43:045003, 2010.

[78] A. P. Malozemoff and J. C. Slonczewski. Magnetic domain walls in bubble materials. *Academic Press, New York*, 1979.

[79] H. J. Mamin, D. Rugar, J. E. Stern, R. E. Fontana, and P. Kasiraj. Magnetic force microscopy of thin permalloy films. *Appl. Phys. Lett.*, 55:318, 1989.

[80] R. D. McMichael and M. J. Donahue. Head to head domain wall structures in thin magnetic strips. *IEEE Trans. Magn.*, 33:4167–4169, 1997.

[81] F. Michelini, L. Ressier, J. Degauque, P. Baulés, A. R. Fert, J. P. Peyrade, and J. F. Bobo. Permalloy thin films on MgO(001): Epitaxial growth and physical properties. *J. Appl. Phys.*, 92:7337–7340, 2002.

[82] I. M. Miron. *Study of interaction between spin polarised current and a magnetic domain wall in material with perpendicular anisotropyI. M.* PhD thesis, Ecole doctrale de physique Grenoble, 2009.

[83] I. M. Miron, G. Gaudin, S. Auffret, B. Rodmacq, A. Schuhl, S. Pizzini, J. Vogel, and P. Gambardella. Current-driven spin torque induced by the rashba effect in a ferromagnetic metal layer. *Nat. Mater.*, 2010.

[84] I. M. Miron, T. Moore, H. Szambolics, L. Daniel, B. Prejbeanu, S. Auffret, B. Rodmacq, S. Pizzini, J. Vogel, M. Bonfim, A. Schuhl, and G. Gaudin. Fast current-induced domain-wall motion controlled by the rashba effect. *Nat. Mater.*, 2011.

[85] I. M. Miron, P.J. Zermatten, G. Gaudin, S. Auffret, B. Rodmacq, and A. Schuhl. Domain wall spin torquemeter. *Phys. Rev. Lett.*, 102, 2009.

[86] S. Mizukami, Y. Ando, and T. Miyazaki. The study of FMR linewidth for NM/FeNi/NM (NM = Cu, Ta, Pd and Pt) films. *Jpn. J. Appl. Phy.*, 40:580–585, 2001.

[87] S. Mizukami, Y. Ando, and T. Miyazaki. Effect of spin diffusion on Gilbert damping for a very thin permalloy layer in Cu/Py/Cu/Pt films. *Phys. Rev. B*, 66:104413, 2002.

[88] T. A. Moore, M. KLaui, L. Heyne, P. Mohrke, D. Backes, J. Rhensius, U. Rudiger, L. J. Heyderman, J.-U. Thiele, G. Woltersdorf, C. H. Back, A. Fraile Rodrguez, F. Nolting, T. O. Mentes, M. A. Nino, A. Locatelli, A. Potenza, H. Marchetto, S. Cavill, and S. S. Dhesi. Scaling of spin relaxation and angular momentum dissipation in permalloy nanowires. *Phys. Rev. B 80*, 80:132403, 2009.

[89] T. A. Moore, I. M. Miron, G. Gaudin, G. Serret, S. Auffret, B. Rodmacq, A. Schuhl, S. Pizzini, J. Vogel, and M. Bonfim. High domain wall velocities induced by current in ultrathin Pt/Co/AlOx wires with perpendicular magnetic anisotropy. *Appl. Phys. Lett.*, 93:262504, 2008.

[90] D. Morecroft, I. A. Colin, F. J. Castańo, J. A. C. Bland, and C. A. Ross. Current-induced magnetization reversal in NiFe/Cu/Co/Au notched mesoscopic bars. *Phys. ReV. B*, 76:054449, 2007.

[91] A. Mougin, M. Cormier, J. P. Adam, P. J. Metaxas, and J. Ferré. Domain wall mobility, stability and walker breakdown in magnetic nanowires. *Europhys. Lett.*, 78:57007, 2007.

[92] Y. Nakatani, A. Thiaville, and J. Miltat. Faster magnetic walls in rough wires. *Nat. Mater.*, 2, 2003.

[93] Y. Nakatani, A. Thiaville, and J. Miltat. Head-to-head domain walls in soft nanostrips: a refined phase diagram. *J. Magn. Magn. Mater.*, 290-291:750–753, 2005.

[94] J. M. B. Ndjaka, A. Thiaville, and J. Miltat. Transverse wall dynamics in a spin valve nanostrip. *J. Appl. Phys.*, 105:023905, 2009.

[95] L. Neel. *Compt. Rend.*, 241:500, 1955.

[96] L. Néel. Sur un nouveau mode de couplage entre les aimantations de deux films. *C.R. Acad. Sci.*, 255:1676, 1962.

[97] J. Nogučs and I. K. Schuller. Exchange bias. *J. Magn. Magn. Mater.*, 192:203, 1999.

[98] M. Ohtake, T. Tanaka, F. Kirino, and M. Futamoto. Preparation of hcp-Ni(11-20) epitaxial thin films on Au(100) single-crystal underlayers. *Journal of Physics: Conference Series*, 200:072072, 2010.

[99] M. Ohtake, T. Tanaka, K. Matsubara, F. Kirino, and M. Futamoto. Epitaxial growth of permalloy thin films on MgO single crystal substrates. *Journal of Physics: Conference Series*, 303, 2011.

[100] T. Ono, H. Miyajima, K. Shigeto, K. Mibu, N. Hosoito, and T. Shinjo. Propagation of a domain wall in a submicrometer magnetic wire, science 284, 468 (1999). *Science*, 284, 1999.

[101] S. S. P. Parkin. Systematic variation of the strength and oscillation period of indirect magnetic exchange coupling through the 3d, 4d, and 5d transition metals. *Phys. Rev. Lett.*, 67:3598–3601, 1991.

[102] S. S. P. Parkin. *US patent no 6834005*, 2004.

[103] S. S. P. Parkin, R. Bhadra, and K. P. Roche. Oscillatory magnetic exchange coupling through thin copper layers. *Phys. Rev. Lett.*, 66:2152–2155, 1991.

[104] S. S. P. Parkin, N. More, and K. P. Roche. Oscillations in exchange coupling and magnetoresistance in metallic superlattice structures: Co/Ru, Co/Cr, and Fe/Cr. *Phys. Rev. Lett.*, 64:2304, 1990.

[105] F. Petroff, A. Barthélemy, D. H. Mosca, D. K. Lottis, and A. Fert. Oscillatory interlayer exchange and magnetoresistance in Fe/Cu multilayers. *Phys. Rev. B*, 44:5355, 1991.

[106] H. N. Pishkenari, M. Behzad, and A. Meghdari. Nonlinear dynamic analysis of atomic force microscopy under deterministic and random excitation. *Chaos, Solitons and Fractals*, 37:748–762, 2008.

[107] S. Pizzini, V. Uhlir, J. Vogel, N. Rougemaille, S. Laribi, V. Cros, E. Jiménez, J. Camarero, C. Tieg, E. Bonet, M. Bonfim, R. Mattana, C. Deranlot, F. Petroff, C. Ulysse, G. Faini, and A. Fert. High domain wall velocity at zero magnetic field induced by low current densities in spin valve nanostripes. *Appl. Phys. Express*, 2:023003, 2009.

[108] K. Richter, R. Varga, and A. Zhukov. In uence of the magnetoelastic anisotropy on the domain wall dynamics in bistable amorphous wires. *J. Phys.: Condens. Matter*, 24:296003, 2012.

[109] N. Rougemaille, V. Uhlir, O. Fruchart, S. Pizzini, J. Vogel, and J. C. Toussaint. Phase diagram of magnetic domain walls in spin valve nano-stripes. *Appl. Phys. Lett.*, 100:172404, 2012.

[110] M. A. Ruderman and C. Kittel. Indirect exchange coupling of nuclear magnetic moments by conduction electrons. *Phys. Rev.*, 96:99–102, 1954.

[111] R. Mattheis S. Glathe and D. V. Berkov. Direct observation and control of the walker breakdown process during a field driven domain wall motion. *Appl. Phys. Lett.*, 93:072508, 2008.

[112] E. Salhi and L. Berger. Current-induced displacements and precession of a bloch wall in NiFe thin films. *J. Appl. Phys.*, 73:6405, 1993.

[113] B. D. Schrag, A. Anguelouch, S. Ingvarsson, G. Xiao, Y. Lu, P. L. Trouilloud, A. Gupta, R. A. Wanner, W. J. Gallagher, P. M. Rice, and S. S. P. Parkin. Néel "orange-peel" coupling in magnetic tunneling junction devices. *Appl. Phys. Lett.*, 77:2373–2375, 2000.

[114] N. L. Schryer and L. R. Walker. The motion of 180 degree domain walls in uniform dc magnetic fields. *J. Appl. Phys.*, 45:5406, 1974.

[115] S. M. Seo, K. W. Kim, J. Ryu, H. W. Lee, and K. J. Lee. Current-induced motion of a transverse magnetic domain wall in the presence of spin hall effect. *Appl. Phys. Lett*, 101:022405, 2012.

[116] J. Shen, Z. Gai, and J. Kirschner. Growth and magnetism of metallic thin films and multilayers by pulsed-laser deposition. *Surf. Sci. Rep.*, 52:163–218, 2004.

[117] J. C. Slonczewski. Theory of bloch line and bloch wall motion. *J. Appl. Phys.*, 45:2705, 1974.

[118] J. C. Slonczewski. Current-driven excitation of magnetic multilayers. *J. Magn. Magn. Mater.*, 159, 1996.

[119] J. C. Slonczewski. Current-driven excitation of magnetic multilayers. *J. Magn. Magn. Mater.*, 159, 1996.

[120] J. Smit and H. G. Beljers. *Philips Res. Rep. 10*, 113, 1955.

[121] G. Tatara and H. Kohno. Theory of current-driven domainwall motion: Spin transfer versus momentum transfer. *Phys. Rev. Lett.*, 92, 2004.

[122] G. Tatara, T. Takayama, H. Kohno, J. Shibata, Y. Nakatani, and H. Fukuyama. Threshold current of domain wall motion under extrinsic pinning and non-adiabaticity. *J. Phys. Soc. Jpn.*, 75, 2006.

[123] A. Thiaville and Y. Nakatani. *Micromagnetic simulation of domain wall dynamics in nanostrips.* Springer Berlin Heidelberg, 2007.

[124] A. Thiaville and Y. Nakatani. *Nanomagnetism and Spintronics.* Elsevier, Oxford, 2009.

[125] A. Thiaville, Y. Nakatani, J. Miltat, and Y. Suzuki. Micromagnetic understanding of current driven domain wall motion in patterned nanowires. *Europhys. Lett.*, 69, 2005.

[126] A. Thiaville, Y. Nakatani, J. Miltat, and N. Vernier. Domain wall motion by spin-polarized current: a micromagnetic study. *J. Appl. Phys.*, 95, 2004.

[127] A. Thiaville and Y.Nakatani. *Domain-wall dynamics in nanowires and nanostrips*, chapter 5, pages 161–205. Springer Berlin Heidelberg, 2006.

[128] L. Thomas, R. Moriya, C. Rettner, and S. S. P. Parkin. Dynamics of magnetic domain walls under their own inertia. *Science*, 30, 2010.

[129] L. Thomas, M. G. Samant, and S. S. P. Parkin. Domain-wall induced coupling between ferromagnetic layers. *Phys. Rev. Lett.*, 84:001816, 2000.

[130] Y. Togawa, T. Kimura, K. Harada, T. Akashi, T. Matsuda, A. Tonomura, and Y. Otani. Domain nucleation and annihilation in uniformly magnetized state under current pulses in narrow ferromagnetic wires. *Jpn. J. Appl. Phy.*, 45:1322–1324, 2006.

[131] J. Torrejon, G. Malinowski, M. Pelloux, R. Weil, and A. Thiaville. Unidirectional thermal effects in current-induced domainwall motion. *Phys. Rev. Lett.*, 109:106601, 2012.

[132] M. Tsoi, R. E. Fontana, and S. S. P. Parkin. Magnetic domain wall motion triggered by an electric current. *Appl. Phys. Lett.*, 83:2617, 2003.

[133] K. Uchida, S. Takahashi, K. Harii, J. Ieda, W. Koshibae, K.Ando, S. Maekawa, and E. Saitoh. Observation of the spin seebeck effect. *Nature (London)*, 455:778, 2008.

[134] W. C. Uhlig, M. J. Donahue, D. T. Pierce, J. Unguris, W. C. Uhlig, M. J. Donahue, D. T. Pierce, and J. Unguris. Direct imaging of current-driven domain walls in ferromagnetic nanostripes. *J. Appl. Phys.*, 105:103902, 2009.

[135] V. Uhlir. *Current induced magnetization dynamics in nanostructures.* PhD thesis, Ecole doctrale de physique, Grenoble, 2010.

[136] V. Uhlir, S. Pizzini, N. Rougemaille, V. Cros, E. Jiménez, L. Ranno, O. Fruchart, M. Urbanek, G. Gaudin, J. Camarero, C. Tieg, F. Sirotti, E. Wagner, and J. Vogel. Direct observation of oersted-field-induced magnetization dynamics in magnetic nanostripes. *Phys. Rev. B*, 83:020406, 2011.

[137] V. Uhlir, S. Pizzini, N. Rougemaille, J. Novotný, V. Cros, E. Jiménez, G. Faini, L. Heyne, F. Sirotti, C. Tieg, A. Bendounan, F. Maccherozzi, R. Belkhou, J. Grollier, A. Anane, and J. Vogel. Current-induced motion and pinning of domain walls in spin-valve nanowires studied by XMCD-PEEM. *Phys. Rev. B*, 81:224418–224427, 2010.

[138] V. Uhlir, J. Vogel, N Rougemaille, O. Fruchart, Z. Ishaque, V. Cros, J. Camarero, J. C. Cezar, F. Sirotti, and S. Pizzini. Current-induced domain wall motion and magnetization dynamics in CoFeB/Cu/Co nanostripes. *J. Phys.: Condens. Matter*, 24:024213, 2012.

[139] N. Vernier, D. A. Allwood, D. Atkinson, M. D. Cooke, and R. P. Cowburn. Domain wall propagation in magnetic nanowires by spin-polarized current injection. *Europhys. Lett.*, 65:526–532, 2004.

[140] J. Vogel, S. Cherifi, S. Pizzini, F. Romanens, J. Camarero, F. Petroff, S. Heun, and A. Locatelli. Layer-resolved imaging of domain wall interactions in magnetic tunnel junction-like trilayers. *J. Phys. : Condens. Matter*, 19:476204, 2007.

[141] J. Vogel, W. Kuch, R. Hertel, J. Camarero, K. Fukumoto, F. Romanens, S. Pizzini, M. Bonfim, F. Petroff, A. Fontaine, and J. Kirschner. Influence of domain wall interactions on nanosecond switching in magnetic tunnel junctions. *Phys. Rev. B*, 72:220402, 2005.

[142] K. Weerts, P. Neutens, L. Lagae, and G. Borghs. Influence of pulse amplitude and rise time on field-induced domain wall propagation in NiFe nanowires,. *J. Appl. Phys.*, 103, 2008.

[143] P. Weiss. *J.Phys.*, 6:401, 1907.

[144] A. Yamaguchi, S. Nasu, H. Tanigawa, T. Ono, and K. Miyake et al. Effect of joule heating in current-driven domain wall motion. *Appl. Phy. Lett.*, 86:012511, 2005.

[145] A. Yamaguchi, T. Ono, S. Nasu, K. Miyake, K. Mibu, and T. Shinjo. Real-space observation of current-driven domain wall motion in submicron magnetic wires. *Phys. Rev. Let.*, 92:077205, 2004.

[146] A. Yamaguchi, K. Yano, H. Tanigawa, S. Kasai, and T. Ono. Reduction of threshold current density for current-driven domain wall motion using shape control. *Jpn. J. Appl. Phy.*, 45:3850–3853, 2006.

[147] K. Yosida. Magnetic properties of Cu-Mn alloys. *Phys. Rev.*, 106:893–898, 1957.

[148] Z. Yuan, S. Wang, and K. Xia. Thermal spin-transfer torques on magnetic domain walls. *Solid State Commun.*, 150:548–551, 2010.

[149] M. Zhu, C. L. Dennis, and R. D. McMichael. Temperature dependence of magnetization drift velocity and current polarization in py by spin-wave doppler measurements. *Phys.Rev. B*, 81:140407, 2010.

[150] A. Zhukov, J. M. Blanco, M. Ipatov, A. Chizhik, , and V. Zhukova. Manipulation of domain wall dynamics in amorphous microwires through the magnetoelastic anisotropy. *Nanoscale Research Letters*, 7:223, 2012.

Résumé

L'objectif de cette thèse est de optimiser la croissance épitaxiale de couches minces magnétiques Py et Su-Py avec faible rugosité de surface et d'interface, peu de défauts structurels. Cela peut réduire le piégeage de parois et donc diminuer la densité de courant de seuil pour déplacement de parois. Deuxièmement d'étudier l'effet du champ magnétique Oersted sur le déplacement de parois de domaines magnetiques induit par courant dans des nanobandes asymétrique de bicouches Ir\Py et Ir\Su-Py. Nous avons réussi à préparés couches minces épitaxiale sur des substrats sapphire(0001) avec bonne propriétés surface, structurale et magnétiques. Nanobandes polycristallines Pt\Py préparées par pulvérisation sur Si ont également été étudiées pour comparer les résultats avec des échantillons épitaxiés. Un mouvement de parois stochastique a été observé en raison du piégeage, ce qui donne lieu à une large distribution de vitesses de paroi de domaine. Les grains de grande taille (comparable à la largeur de bande) dans nos couches minces épitaxiales bi-cristallins par rapport aux échantillons polycristallins (~5-10nm) peuvent être une source possible du fort piégeage. Des déplacements de paroi opposés au flux d'électrons et des transformations de paroi ont également été observés en raison de chauffage Joule. Nous avons observé le changement de chiralité des parois transverses sous champ Oersted avec des impulsions de courant en utilisant la microscopie à force magnétique. Néanmoins, des vitesses de parois maximales (jusqu'à 400 et 250m/s) sans transformation de paroi pour des densités de courant relativement faibles (1.7 $x10^{12}$ and 1 $x10^{12}A/m^2$) ont été observées dans échantillons épitaxiales et pulvérisées respectivement. Le champ Oersted est peut-être à l'origine de la grande efficacité du couple de transfert de spin dans ces bandes en bicouche. Il peut stabiliser les parois transverses, empêchant des transformations. Cela peut conduire à une décalage du seuil de Walker vers des courants plus élevés, résultant en une augmentation de la vitesse de paroi. Des premier mesures XMCD-PEEM résolues en temps sur nanobandes de Pt\Py montrent également le mouvement du coeur du vortex vers la direction du champ Oersted, mais d'autres mesures sont nécessaires avec épaisseurs différents de Pt de quantifier et de séparer l'effet du champ Oersted de couple de transfert de spin.

Mots Clés : Paroi de domaine, mouvement induit par courant de parois de domaines, Couple de transfert de spin, Champ Oersted, Systèmes magnétiques épitaxiés

Abstract

The aim of this thesis is to optimize the epitaxial growth of magnetic thin films Py and Su-Py with less structural defects and surface or interface roughness. This can reduce the domain wall (DW) pinning and hence threshold current density to move the DW. Secondly, to study the effect of the magnetic Oersted field on current-induced DW motion in asymmetric Ir\Py and Ir\Su-Py bilayer nanostripes. We managed to prepared epitaxial thin films on sapphire (0001) substrates with good surface, structural and magnetic properties. Polycrystalline Pt\Py nanostripes prepared by magnetron sputtering on Si were also studied to compare the results with epitaxial samples. DW motion was found to be stochastic due to DW pinning, which results in a distribution of velocities. The large grain size (comparable to the stripe width) in our epitaxial films with respect to the polycrystalline samples (~5-10nm) may be a possible source of pinning. DW motion opposite to the electron flow and DW transformations were also observed due to Joule heating. We observed chirality switching of transverse walls induced by the Oersted field due to current pulses using magnetic force microscopy. Nevertheless, high maximum DW velocities (up to 400 and 250m/s) without DW transformation for relatively low current densities (1.7 $x10^{12}$ and 1 $x10^{12}A/m^2$) were observed in epitaxial and sputtered samples respectively. The Oersted field may be at the origin of the high efficiency of the spin transfer torque in these bilayer stripes. It can stabilize transverse walls, preventing DW transformations. This can result in a shift of the Walker breakdown to higher currents, resulting in an increase in DW velocity. Initial results of time-resolved XMCD-PEEM measurements on Pt\Py nanostripes show the vortex core motion along the Oersted field direction but further measurements are required with different Pt thicknesses to quantify and separate the effect of Oersted field from spin transfer torque.

Key words : Domain wall, Current-induced domain wall motion, Spin transfer torque, Oersted field, epitaxial magnetic systems